Modèles de minimisation d'énergies discrètes pour la cartographie cystoscopique

Thomas Weibel

Modèles de Minimisation d'Énergies Discrètes pour la Cartographie Cystoscopique

THÈSE

présentée et soutenue publiquement le 9 juillet 2013

pour l'obtention du

Doctorat de l'Université de Lorraine

Mention : Automatique, Traitement du Signal et des Images, Génie Informatique

par

Thomas WEIBEL

Composition du jury :

Président :	Jean-Marc CHASSERY	DR CNRS, GIPSA-Lab, Grenoble.
Rapporteurs :	Fabrice HEITZ	PU, Université de Strasbourg, ICube.
	Joachim OHSER	PU, Hochschule Darmstadt, Allemagne.
Examinateurs :	François GUILLEMIN	PUPH, Université de Lorraine, CRAN/ICL, Nancy.
	Ronald RÖSCH	PhD, Fraunhofer ITWM, Kaiserslautern, Allemagne.
Directeur de thèse :	Christian DAUL	PU, Université de Lorraine, CRAN, Nancy.
Co-Directeur de thèse :	Didier WOLF	PU, Université de Lorraine, CRAN, Nancy.

CRAN

To Michael Jordan. And Henrike.

Acknowledgements

Contents

CONTENTS

CONTENTS

Introduction

This thesis was written at the CRAN laboratory (Centre de Recherche en Automatique de Nancy, UMR 7039 CNRS/Université de Lorraine) in the department SBS (Santé-Biologie-Signal). The thesis framework is a scientific cooperation between the CRAN and the department of image processing at the Fraunhofer Institute for Industrial Mathematics (ITWM), which also provided the financial support. One field of research within the SBS department aims at facilitating bladder cancer diagnosis. The thesis is situated in this context. Medical expertise and data is supplied by Prof. François Guillemin from the ICL (Institut de Cancérologie de Lorraine), which is a comprehensive cancer center located in Nancy.

The reference clinical procedure for bladder cancer diagnosis is cystoscopy. The purpose of such an examination is to visually explore the internal epithelial wall of the human bladder using a cystoscope (a rigid or flexible endoscope specifically designed for bladder examination). The organ is filled with an isotonic saline solution during the examination, which temporarily rigidifies the bladder's internal walls. The cystoscope is then inserted through the urethra, and the surface of the epithelium is systematically scanned for cancerous or other lesions. These can then be surgically removed using tools inserted through an operative channel of the instrument. The surface is illuminated using either white or fluorescence light. On the one hand, the white light modality corresponds to the standard and reference modality, which results in a natural appearance of the epithelium. The fluorescence light modality, on the other hand, can be used after injection of a marker substance to facilitate early cancer detection, at the expense of a natural epithelium appearance. For these reasons, fluorescence illumination is never used solely. Clinicians (urologists and surgeons) perform their diagnosis by observing a video-sequence on a monitor.

The main limitation of a cystoscopic examination is the small field of view (FOV) of cystoscopes, which complicates endoscope navigation and scene interpretation for the clinicians. Furthermore, bladder tumours, which appear on the first skin layers, are often multi-focal (they appear as multiple spots on the epithelial surface). Due to the small FOV of the cystoscope, it is therefore not possible to observe, in one single image, the entire spatial distribution of lesions (tumours, scars, etc.), as well as their localization with respect to anatomical landmarks (such

as the ureters or air bubbles). Because it is difficult to interpret the acquired data at a later point without the physical feedback of navigating the cystoscope, video-sequences are currently not archived for patient follow-up. Instead, regions of interest are annotated on an anatomical sketch of the bladder, and print-outs corresponding to these regions are archived with this sketch. Such a print out also shows a surface area limited by the FOV of the images. The archived data (small FOV and no anatomical landmarks visible) does not facilitate diagnosis, lesion follow-up preparations, and treatment traceability.

These limitations can be overcome with the aid of two- and three-dimensional cartography algorithms. Indeed, large FOV maps, constructed with the images of cystoscopic video-sequences, allow for archiving the recorded sequence in an intuitive format, i.e. a single two-dimensional panoramic image or a three-dimensional textured mesh. Such maps (also referred to as mosaics) can be used to compare lesion evolution side-by-side, while greatly reducing data redundancy. During a follow-up examination, these maps also facilitate navigation inside the organ (both lesions and anatomical landmarks are visible) and minimize the risk of missing regions of interest observed in a previous examination. They also enable a second diagnosis (after the examination) by the clinician who acquired the data or by other clinicians.

Two-dimensional cartography algorithms allow for constructing large FOV panoramic images from conventional cystoscopic video-sequences. However, due to the non-planar shape of the bladder and the varying cystoscope viewpoints during the examination, the resolution of the panoramic image is often severely "distorted" for larger FOVs. Techniques used in classical panoramic imaging to overcome this problem (e.g. by using spherical coordinates) do not apply in this context, as they require a stationary camera rotating around its optical center. Furthermore, clinicians are still required to mentally project the two-dimensional map onto the organ's three-dimensional shape. Both difficulties can be overcome with the aid of three-dimensional cartography algorithms. These allow to reconstruct a textured mesh of the observed part of the bladder, whose resolution depends only on the distance between cystoscope and epithelium. However, the downside of three-dimensional cartography is that the bladder's poor local depth variation requires modified instruments to robustly construct three-dimensional maps.

The *general aim* of this thesis is to design and implement both two- and three-dimensional cartography algorithms in order to facilitate bladder lesion diagnosis and follow-up. Such algorithms consist of several steps. Overlapping images of the video-sequence must be registered (superimposed) in a robust and accurate fashion and then placed into a common coordinate system. Crossing cystoscope trajectories create multiple overlapping map parts, requiring global optimization to achieve coherent data superimposition. Finally, once the transformation parameters are estimated, the texture for each pixel/face in the map must be selected from the redundant data available in the video-sequence.

Previous contributions showed the feasibility of two-dimensional cartography of hollow organs. However, these methods work only robustly and reliably with regard to the registration of consecutive image pairs, which are normally related by small viewpoint changes. This is a

strong limitation, as small registration errors (between consecutive image pairs) accumulate to larger global cartography errors. This leads to visible misalignments (texture discontinuities) between non-consecutive images when the cystoscope returns to a previously visited location (i.e. for crossing endoscope trajectories or loops). Robust and accurate registration of these non-consecutive image pairs is most often not possible with existing contributions, as the images are related by large viewpoint differences. Moreover, up to this point, no method to automatically detect and correct accumulated errors for the cartography of cystoscopic video-sequences has been proposed. Therefore, previous contributions only presented "strip"-shaped maps with a large FOV in one main direction. One *aim* of this thesis is to design and implement an algorithm that automatically detects and corrects accumulated errors. This requirement immediately leads to another *aim*: the development of a registration algorithm that is able to systematically register images related by larger viewpoint changes. Reaching both aims will allow for constructing fully large FOV maps (e.g. multiple overlapping strips).

Once the transformations that place each image of the sequence into the common map coordinate system have been computed, panoramic images without strong texture discontinuities can be constructed. However, small bladder texture misalignments (for instance due to temporal local bladder deformations) and visible color gradients (due to vignetting and different exposure of the images) remain perceptible and must be corrected for a seamless and visually coherent appearance. Additionally, many images suffer from motion blur and camera de-focus. Previous contributions, based on (non-)linear interpolation, tend to produce blurry bladder texture, as they do not consider the quality of the individual images. Hence, another *aim* of the thesis is to correct small texture misalignments and exposure gradients without blending, and to prefer well contrasted images over blurry data when available.

The *global scientific aim* of this thesis is to show the feasibility of discrete energy minimization techniques in the context of cystoscopic cartography and to develop algorithms that solve the goals formulated in the previous paragraphs. In particular, it should be shown that such methods can be a robust and elegant approach for the core stages of the cartography pipeline. Recent advances in this field (e.g. higher-order inference, minimization strategies) potentially allow to achieve more accurate and robust results than those obtained with existing bladder cartography approaches. Of particular interest are techniques based on the st-mincut/maxflow theorem, which allow to solve discrete labeling problems using specifically constructed graphs. Such algorithms, often referred to as graph-cuts in the computer vision context, have been successfully applied to many image processing applications, such as image segmentation, image de-noising, or the estimation of disparity and optical flow. Only a few contributions also apply these techniques to image registration and image compositing. However, these approaches cannot be directly applied in the context of cystoscopic cartography due to the limitations discussed previously.

Another *aim* of this thesis is to design the algorithms in such a way that they can be applied to two-dimensional cartography and be extended to three-dimensional cartography. There, the

challenge is to find the geometric link between local coordinate systems, which correspond to different viewpoints of the instrument. These links allow for reconstructing the cystoscope trajectory and the three-dimensional shape of the epithelium. Only a few approaches can be found in the literature concerned with three-dimensional cartography of endoscopic data. These contributions are either based on a priori knowledge, active-stereo principles, structure from motion, or external navigation systems. As will be discussed, the poor local geometry of the bladder and the small FOV observed in each viewpoint impedes the use of these approaches to robustly recover viewpoints and three-dimensional structure. It was however shown in a previous thesis written at the CRAN laboratory, that an active-stereo-vision system, guided by two-dimensional image registration, allows to recover the cystoscope trajectory and a set of three-dimensional measurements on the epithelium. This approach is based on hypotheses derived from two-dimensional cartography. However, these hypotheses do not hold in general for arbitrary viewpoint changes in three-dimensional cartography. Consequently, the existing approach is not able to register non-consecutive acquisitions. As is the case for previous contributions to two-dimensional cartography, only "strip"-shaped three-dimensional bladder reconstructions were presented. Furthermore, it was not shown how the (sparse) three-dimensional bladder reconstruction can be textured using the images of the video-sequence. Therefore, the last *aim* of this thesis is to show the feasibility of energy minimization techniques for three-dimensional bladder reconstruction. Viewpoint estimation should not depend on 2D hypotheses and arbitrary viewpoint links should be estimated robustly and accurately. Finally, a triangulated mesh must be obtained from the reconstructed points. This mesh should be textured from the available images, ensuring seamless alignment of vascular structures, while maximizing contrast of the observed scene and removing any exposure related gradients.

To reach these goals, the thesis is structured as follows.

Chapter 1: Cystoscopic Cartography. This chapter first introduces the medical context of the thesis. Then, previous contributions towards two- and three-dimensional endoscopic cartography are discussed. A particular focus is laid on state-of-the-art techniques for bladder cartography. Each step of the cartography pipeline is described, and advantages and drawbacks of existing methods are discussed. The chapter concludes with a more detailed formulation of the scientific and medical objectives of this thesis.

Chapter 2: Graph-Cut Optimization. The second chapter introduces the mathematical and algorithmic framework of graph-based discrete energy minimization techniques. The described discrete energy minimization principles and algorithms build the basis for the methods proposed in Chapters 3 and 4. It is shown how energy functions whose variables may take arbitrary values (such as displacement vectors in $\mathbb{R}^2$) can be minimized, and how higher-order interaction between variables can be incorporated into a pairwise (graph-representable) form. Then, previous applications of graph-cut approaches towards image registration and image

compositing are presented. The chapter concludes with a proposition of a first modification of a reference graph-cut based image registration technique. A qualitative comparison with state-of-the-art white light bladder image registration algorithms demonstrates the feasibility of discrete energy minimization for the registration of video-sequences acquired in the white light modality.

Chapter 3: 2D Cartography. In Chapter 3, a complete two-dimensional cartography pipeline is presented. To overcome the limitations of existing state-of-the-art registration techniques, higher-order potential functions are proposed. These allow to compute image similarity and regularization costs invariantly of the underlying geometric transformations linking partly overlapping small FOV images of the epithelium. The proposed cost functions allow to robustly register both consecutive and non-consecutive image pairs of a video-sequence with high accuracy. The transformations of non-consecutive image pairs are are required to globally correct accumulated errors between different trajectories. Furthermore, a technique to detect overlapping trajectories and to select a small subset of additional (non-consecutive) image pairs is presented. It is then shown how the combined set of consecutive and non-consecutive transformation parameters can be used to globally optimize the placement of all images into a common global coordinate system. Lastly, an energy minimization based map compositing algorithm is proposed. The method allows to correct small remaining misalignments of vascular structures in overlapping image regions in a first step, and at the same time maximizes the map's texture quality by favouring contrasted images over blurry ones. In a second step, exposure related artefacts are removed without blurring or interpolation, and the corrected map retains both contrast and hue of the original input images. Finally, the proposed methods are evaluated both quantitatively and qualitatively on realistic phantom data as well as on clinical data acquired at the ICL. Furthermore, results on non-medical applications, such as consumer photography stitching and high-dynamic-range imaging, demonstrate that the proposed methods are also applicable in more general scenarios.

Chapter 4: 3D Cartography. The last chapter describes extensions made to the algorithms proposed in Chapter 3, which allow to construct three-dimensional large FOV textured meshes. As previously discussed, the bladder's three-dimensional structure cannot be robustly reconstructed without modified cystoscopes. The results presented are a proof-of-concept, obtained from realistic bladder phantoms and two cystoscope prototypes developed at the CRAN laboratory. It is shown that only minor modifications of the two-dimensional cartography algorithms are necessary in order to construct large FOV textured meshes. Besides registration and global map correction adaptation, the compositing algorithm is modified to work on triangular surface meshes instead of a pixel level. This formulation allows to achieve the same goals as in two dimensions, namely to maximize the contrast of the texture and remove exposure related artefacts. The results show the potential of the proposed methods on several acquisition scenarios, including non-medical scenes captured with the Kinect sensor.

Chapter 1

Cystoscopic Cartography

1.1 Medical Context

1.1.1 Bladder Cancer

Bladder cancer is the 7th most common type of cancer in the world (TP03), the fourth most common malignant lesion among males in industrialized countries (Soc08), and the second most common urinary disease. Ninety-five percent of bladder tumours originate on the first cell layers of the epithelial surface of the internal bladder wall. Epithelial tumour tissue occurs when some cells start to abnormally multiply (i.e. without control). Figure 1.1 illustrates the genesis of epithelial tumours.

After bladder cancer detection, tests are necessary to check the lesions' degree of evolution. These tests are referred to as *staging*, and are helpful in guiding future treatment and follow-up. Bladder cancer stages are classified using the TNM (primary Tumour, lymph Nodes, distinct Metastasis) staging system. Figure 1.2 shows the major stages of primary tumours.

Research results suggest lifetime monitoring of patients after surgical removal of cancerous tumours to avoid recurrence (HLCB+04).

1.1.2 Cystoscopic Examination

Since bladder lesions usually appear in an early stage on the internal epithelial surface, potential cancers can be visualized and detected with cameras. Bladder monitoring is conducted in a cystoscopic examination, where a rigid or flexible cystoscope (an endoscope designed for bladder examination), see Figures 1.3b-c, is inserted through the urethra into the bladder. The textured epithelial surface of the bladder wall is classically visualized on a monitor (see Figure 1.3a). During the examination, the bladder is filled with an isotonic solution, which temporarily inflates the bladder and limits bladder wall movements and shape changes. However, the bladder
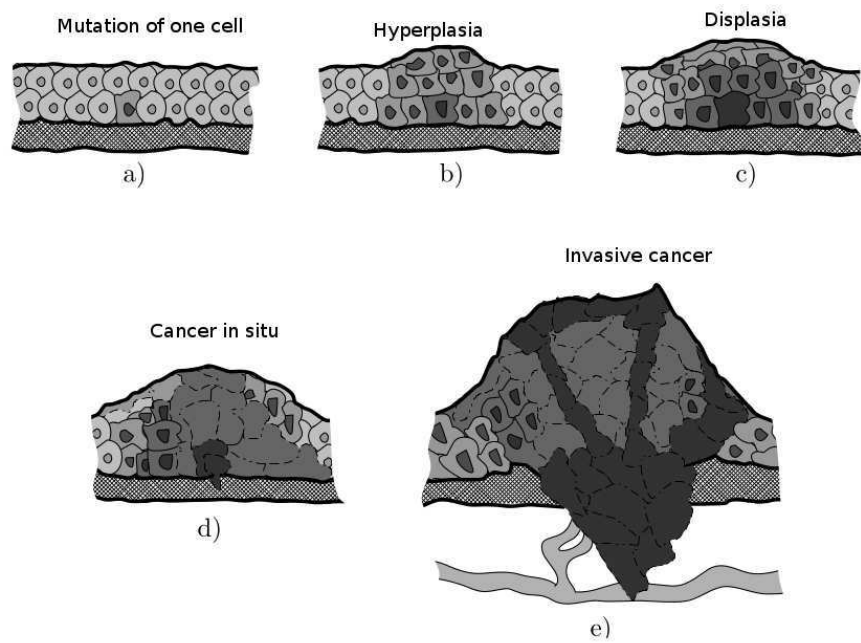
Figure 1.1: Simplified representation of the different stages leading to bladder tumours. This illustration of the epithelial tissue evolution is taken from (HM07). (a) Mutation of a single cell. (b) Abnormal augmentation of the number of cells and increasing cell size. (c) Abnormal development of the tissue (dysplasia). (d) Cancer *in situ*. (e) Propagation of the tumorous tissue.
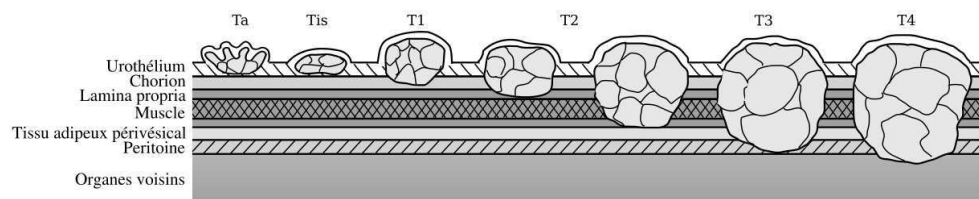
Figure 1.2: Degrees of invasion (stages) of bladder cancer (illustration taken from (HM07)). The detailed stages are defined as follows: **Ta** Non-invasive papillary carcinoma. **Tis** Carcinoma *in situ* ('flat tumour'). **T1** Tumour invades subepithelial connective tissue. **T2** Tumour invades the muscle of the bladder. **T3** Tumour invades the adipose perivesical tissue. **T4** The tumour invades a neighboring organ (prostate, uterus, vagina, pelvic wall or abdominal wall).
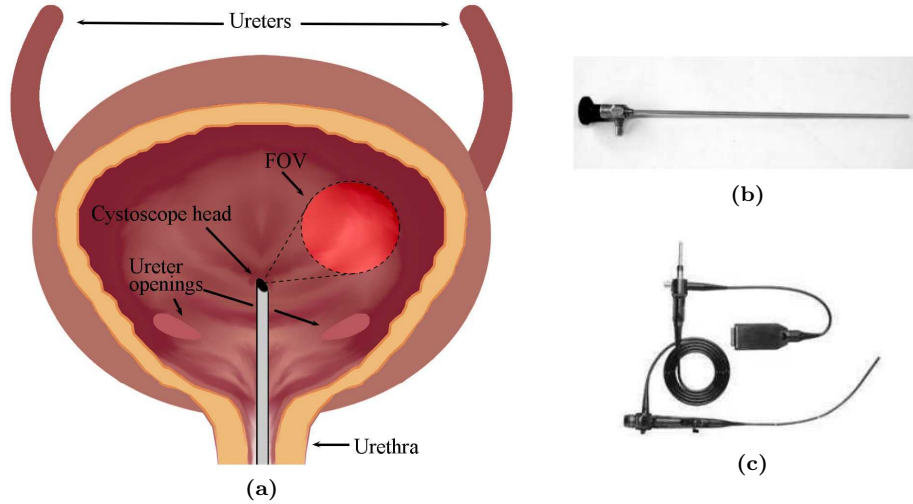
Figure 1.3: (a) Schematic examination overview. A cystoscope is inserted into the bladder through the urethra. During the examination, the cystoscope is moved along the epithelial surface, and the clinicians scan the bladder for lesions using the limited field of view (FOV). Visual-spatial orientation is difficult, as multi-focal lesions can neither be viewed from a single point of view, nor with respect to anatomical landmarks, such as the urether openings. (b) Rigid cystoscope, Karl Storz 27005BA. (c) Flexible cystoscope, Olympus EndoEYE.

can be "deformed" due to contact with other neighboring organs, or due to bending caused by movements of a rigid cystoscope. The clinician (urologist or surgeon) then navigates the cystoscope along the epithelial surface to scan the bladder for lesions, such as tumour tissue or scars (indicated in Figure 1.3a). The standard imaging modality is to use white light illumination (Figure 1.4a), while fluorescence light together with tumour marker substances allows for earlier localization of tumorous tissue (Figure 1.4b). In this modality, the marker substances, excited by a narrow band illumination source, emit a red fluorescence light. However, the scene does not appear natural and complicates orientation inside the bladder for the clinicians. For these reasons, white light being the reference modality, fluorescence is sometimes used in addition, alternating between white and fluorescence illumination.

The main restriction during a cystoscopic examination is the limited field of view (FOV) of the cystoscope (area of one up to several cm^2). Small FOVs are required to obtain sufficiently exposed and contrasted images at a high frame rate (25 frames per second). Figures 1.5a-c show images extracted from a cystoscopic video-sequence at different time steps. The limited FOV complicates navigation, orientation and identification of tumorous tissue for the clinicians during the examination (CM00), as well as the re-identification of tumour tissue during follow-up examinations. Moreover, bladder cancer is often multi-focal (tumour tissue is spread over large areas of the bladder wall), which makes it neither possible to visualize the lesions' spatial distribution, nor to localize them with respect to anatomical landmarks (such as the urethra,
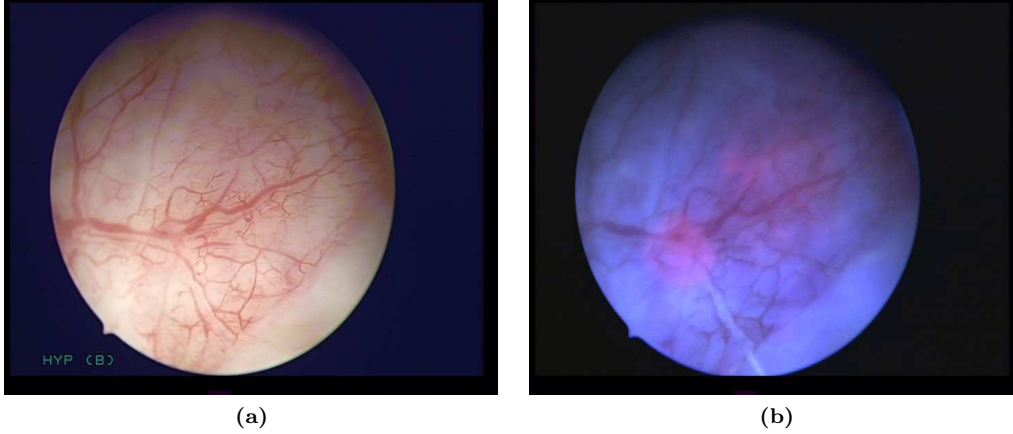
Figure 1.4: Different imaging modalities. (a) The reference white light modality, facilitating navigation inside the bladder. (b) Fluorescence modality. Tumours can be detected at an earlier stages.

the ureters, air bubbles, etc.) from a single point of view (see also Figure 1.3a).

A widely used clinical procedure is therefore to draw a sketch of the bladder that includes anatomical landmarks. During the examination, clinicians then mentally visualize the three dimensional structure of the organ and keep track of the instrument's current position inside the bladder. When a region of interest is found, its position is noted on the bladder sketch, and sometimes (when the clinicians find it necessary) a screen-shot of the current FOV is printed and archived with this sketch. This procedure is tedious and makes it very difficult for other clinicians to use the archived information in a follow-up examination. Furthermore, analyzing the lesions' evolution over time by comparing two video-sequences is difficult, or even impossible, as the movement of the cystoscope is unlikely to follow the same path and/or with the same scanning speed.

For these reasons, clinicians have expressed their interest in using panoramic images (or mosaics) showing a large FOV surrounding lesions and landmarks for their diagnosis and follow-ups. Indeed, such large FOV maps can overcome the limitations presented in the previous paragraphs. They facilitate navigation in bladder cancer follow-up examinations, and help to re-identify multi-focal lesions. They allow to compare lesion evolution from previous examinations, and can be helpful in surgery planning. In addition, these large FOV maps allow to archive the examination in a single, high-resolution image, making it accessible to other clinicians. Figure 1.5 shows an example for such a large FOV mosaic. The result, given in Figure 1.5d, has been composed from a 27 second video-sequence. Figures 1.5a-c show some image examples extracted from the sequence.

While two-dimensional panoramic images greatly facilitate lesion diagnosis and follow up, the depth information is lost in such representations. However, clinicians mentally visualize

(a)   **(b)**   **(c)**

(d)
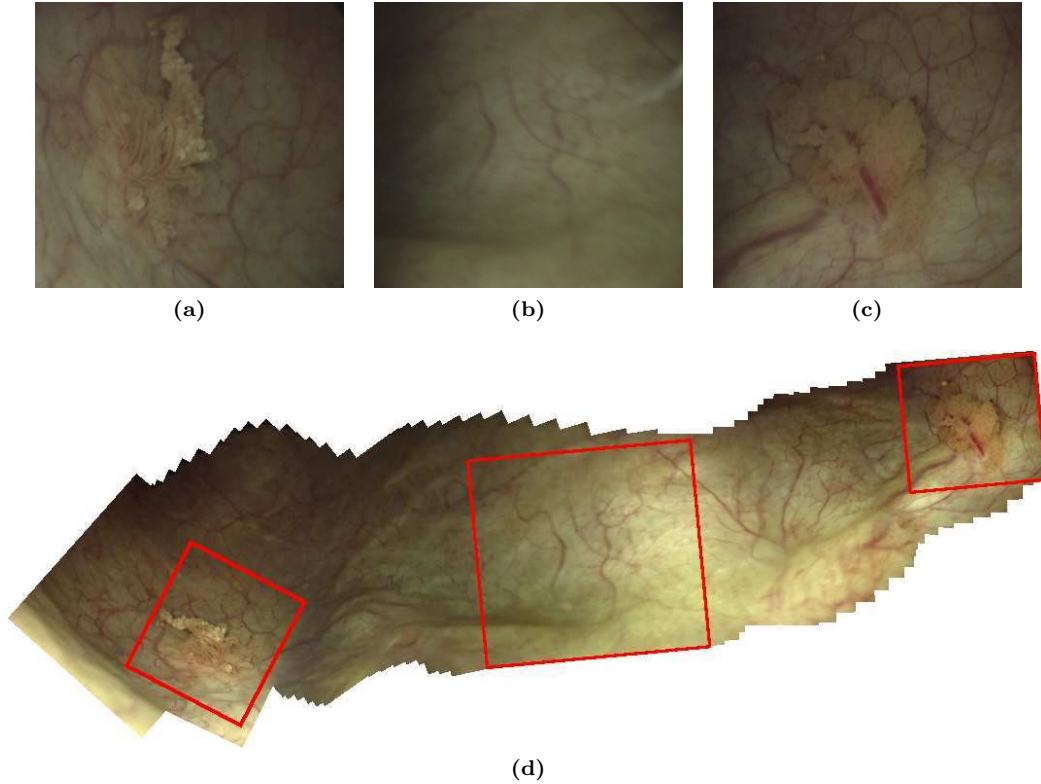
Figure 1.5: Large FOV map example on clinical data. (a) First image of the sequence. Its position in the map is indicated by the leftmost quadrangle in d). (b) Central image of the sequence (center quadrangle in d)). (c) Last image of the sequence (rightmost quadrangle in d)). (d) Large FOV textured map, built using the methods proposed in this thesis.

the anatomy of organs (like the bladder) in three dimensions. Three-dimensional panoramic surfaces (superimposed by the texture of the images) are consequently also of interest. For this reason, the work presented in this thesis deals both with two- and three-dimensional bladder map construction.

Section 1.2 sketches a general overview of the cartography process and illustrates such techniques for both general and medical applications. In Section 1.3, endoscopic cartography applications are reviewed, with a focus on cystoscopic cartography and the specific steps involved in the process. The mathematical terminology, models and formulations used throughout this thesis are also introduced. Previous contributions along with their advantages and limitations are also presented. Finally, Section 1.4 deals with previous approaches towards three-dimensional endoscopic cartography, which are fundamental for the methods developed in Chapter 4.
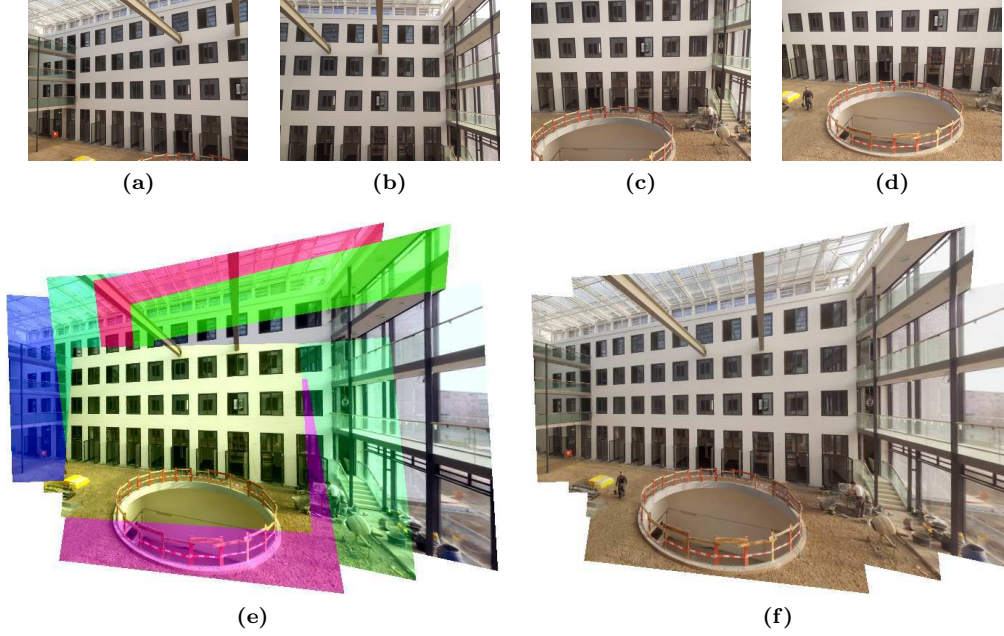
Figure 1.6: Mosaicing example. (a)-(d) A set of partly overlapping images, taken with a smartphone camera. The viewpoint changes correspond mainly to camera orientation along its x- and y-axes. (e) Images (colorized for visualization purposes) registered into a common coordinate system. (f) Large FOV panoramic image, showing no structure inconsistencies or brightness changes across image seams. Results have been created using the methods proposed in this thesis.

1.2 Image Mosaicing

In order to compute large FOV mosaics from the data of a video-sequence, all overlapping images need to be placed into a common global coordinate system.

This process, often called *mosaicing* or *panoramic stitching*, is based on registration algorithms. The purpose of image registration is to find the geometrical transformation that superimposes the overlapping and homologous parts of two images. A thorough survey on registration methods for various image modalities can be found in (Bro92, ZF03). Figure 1.6 illustrates this mosaicing process. For a set of images (Figures 1.6a-d show a few samples), the transformations that align the images are determined, and all images are placed into a common coordinate system (see Figure 1.6e). Then, appropriate seam positions[1] are determined and brightness differences crossing image borders are corrected. The final mosaic then shows neither structure inconsistencies nor visible brightness differences. The result in Figure 1.6f has been created using the methods proposed in this thesis.

---

[1]As will be explained later, seams determine the positions on the panoramic image where the transition between overlapping images is performed.

1.2.1 General Applications of Image Mosaicing

Image mosaicing has been successfully applied in various applications. In consumer photography, wide-angle panoramas are stitched fully automatically from a set of pictures (SS97, BL03, SPS05, d07). These pictures do not necessarily need to be taken in a certain order, but it simplifies the process. In such applications, the data usually contains sufficient information to facilitate speed and accuracy of the registration process. Indeed, primitives facilitating the registration step can usually be robustly extracted from the images. Today, most smart-phones and consumer cameras are equipped with panoramic stitching software.

Another application where mosaicing algorithms are applied is video-stabilization (LKK03, MOG$^+$06). Temporal subsets of images are aligned in order to reduce the trembling effect occurring with hand-held cameras. Such methods are also known as software-stabilization in consumer camcorders, and are a popular alternative to expensive optical stabilization hardware.

Obtaining images with super-resolution is another application which benefits from mosaicing algorithms (ZP00, CZ03, Cap04). Overlapping images are registered with sub-pixel accuracy, and this quasi-redundant information is exploited to construct images with increased (super-)resolution.

In radio-astronomy, large FOV mosaics of the small Magellanic cloud were created from multiple pointings of a telescope (SSSB96). In the same application field, the work presented in (PMR$^+$03) observes 40 square degrees of sky using mosaics created from multiple overlapping pointings.

In areal imaging (FFKM02, ZHR04, CMFO06, MWC$^+$06, BMG10), image mosaicing can be used to reduce both lens/sensor weight and bandwidth when streaming images from an Unmanned Aerial Vehicle (UAV). Resolution and FOV of the images sent can thereby be increased, and an operator on ground is able to keep features of interest in view for a longer period of time.

1.2.2 Medical Applications

The registration of medical images is a well studied field (for a thorough overview, the reader is referred to (MV98, PMV03)), and the versatility of image mosaicing algorithms for different scene types has been demonstrated. Despite these two observations, far less research can be found in the literature concerning the cartography of medical data consisting of large sequences of images affected by a great information variability. However, in many medical applications, existing stitching techniques could be easily adapted to the scenes.

In confocal microscopy, globally consistent panoramic maps of a live mouse colon are created using a robust estimator based on statistics for Riemannian manifolds (VPPA05). Non-rigid deformations and irregular sampling are tackled by efficient fitting of scattered data.

In opthalmology, in order to assist the diagnosis and treatment of retinal diseases, the work proposed in (CSRT02) registers pairs of images of the curved human retina acquired with a fundus microscope. Vascular landmarks are extracted, and matched using a 12-parameter non-linear transformation model that approximates the curved human retina. Another approach (STR03) uses a generalization of the Iterative Closest Point (ICP) algorithm (Zha94) to superimpose overlapping retinal images. This method needs only an appropriate local estimate (matches only in a small sub-region of the overlapping area), which are called bootstrap regions. The transformation of these local matches is first refined, and then expanded to larger regions until it covers the entire overlapping region. Also for retinal image registration, in (YS04), the authors use global constraints to jointly estimate the global transformations in an iterative fashion, by minimizing the Mahalanobis distance between matching features using transformation parameter error covariance matrices.

Other medical applications of image mosaicing are mammography (JMHL96) or X-ray angiography (CQWS97). It is noticeable, that for these two applications (like for many others) mosaics are computed with only a few images.

1.3 2D Endoscopic Cartography

The medical applications mentioned in the previous section either rely on the use of a priori knowledge of the geometric transformations between overlapping images, or are not fully automated. In endoscopy in general, and in cystoscopy in particular, no *a priori* knowledge is available, as the instrument is moved freely during the examination. Additionally, the organ is only temporarily rigid, and is deformed by other neighboring organs. Temporarily means here that between consecutives images of small sequence parts (e.g. some few seconds) the bladder wall movement or deformation can be considered as negligible, but that over a longer time, the organ is not motionless. This point is discussed later in detail. Moreover, cystoscopic images present several challenges to the registration algorithm. Both intra- and inter-patient image (e.g. texture) variability demand robust algorithms that don't require parameter adjustments for each patient, or even parameter adjustments during an examination.

Some images are well illuminated and show highly contrasted vascular structures (see Figure 1.7a-c). Other images suffer from motion blur due to rapid cystoscope movements along the organ wall (Figure 1.7d), or from de-focus if the cystoscope is too close to the bladder surface (Figure 1.7g) or has not yet re-focused after rapid movements (Figure 1.7h). The images also exhibit strong illumination differences caused by vignetting and the angle and distance of the cystoscope towards the bladder surface (see Figure 1.7e-f). In addition, rapid fluid motions cause blurring artifacts when passing the FOV of the cystoscope (Figure 1.7i). Moreover, the displacement between partly overlapping images can be quite severe (small percentage of overlap, strong perspective displacements), which can be a significant problem for algorithms that
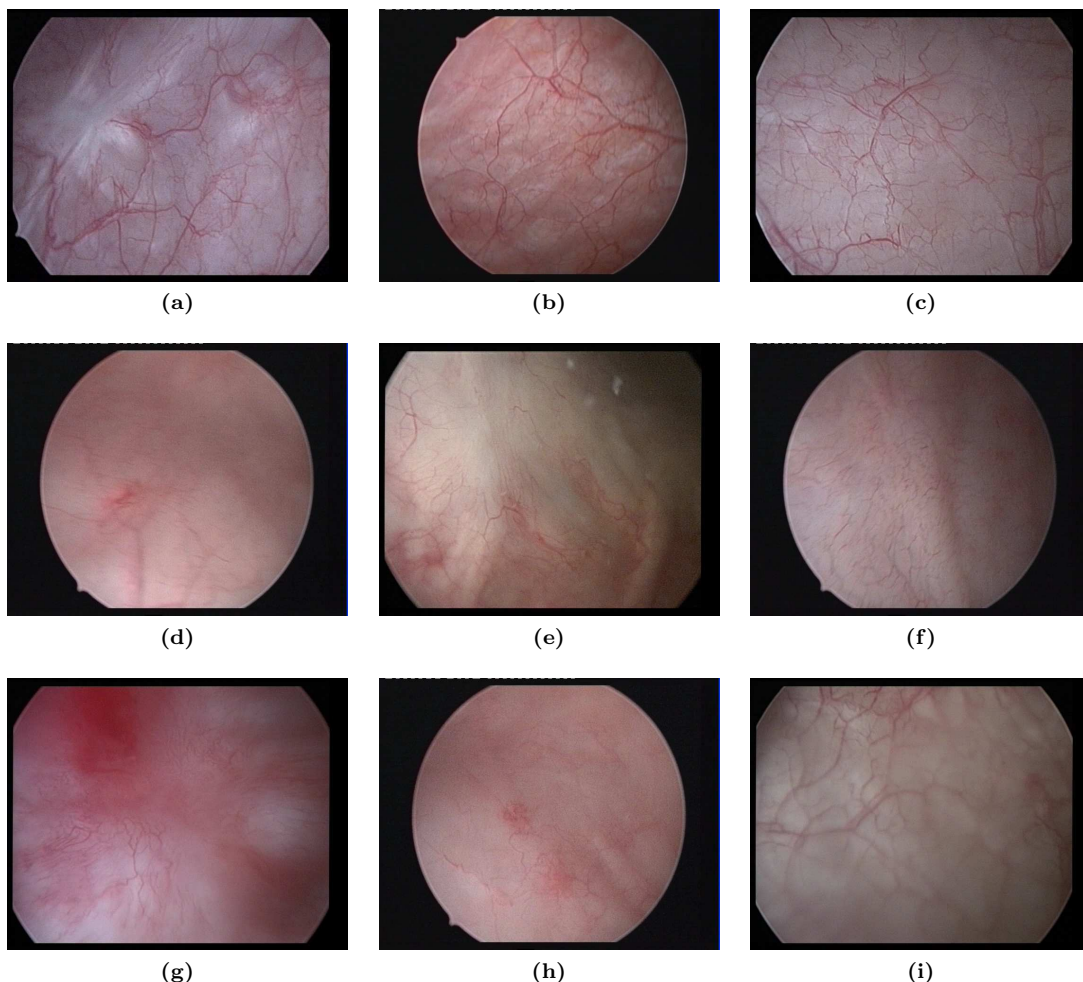
Figure 1.7: Image samples extracted from five cystoscopic video-sequences, demonstrating the image variability. (a)-(c) Sharp images with well-contrasted vascular structures. (d) Image suffering from motion blur due to rapid cystoscope movement. Small vascular structures are removed by the blurriness. (e)-(f) Images with inhomogeneous illumination due to vignetting and non-orthogonal angle towards the bladder surface. Small and only local vascular structures are present. (g) The cystoscope is too close to the bladder surface and unable to focus. (h) The camera's auto-focus delay leads to a short period of blur. (i) Blurry image due to rapid fluid motion.

need an initial estimate close to the solution to produce robust and accurate results, or those that are not invariant to perspective transformations.

These challenges demand for robust algorithms that do not require inter-patient parameter tuning, and that can handle the image variability (see section above) occurring in a cystoscopic video-sequence as best as possible. The following sections sketch the different steps of the

cystoscopic cartography process, present previous contributions and discuss their strengths and weaknesses with regard to the mentioned challenges. These sections also introduce the required mathematical formulations for the methods proposed in Chapters 3 and 4. Specific models for three-dimensional cartography (Chapter 4) will be introduced in Section 1.4.

1.3.1 Pre-Processing

Images taken by an endoscope suffer from several degradations and have to be attenuated before the actual cartography algorithm is applied. These degradations include lens distortion, vignetting, or spatially periodic patterns induced by optical fibers of flexible cystoscopes. Vignetting leads to brightness gradients, so that the image center is more illuminated than the peripheral regions. Furthermore, different angles of the light source towards the bladder surface lead to inhomogeneous illumination in the image, and varying distances and angles with regard to the bladder surface lead to illumination and contrast differences between partly overlapping images. Additionally, only an ellipse-shaped region shows valid foreground regions due to the cystoscope's optical system (the black regions in Figure 1.7 do not contain information). Most contributions discard the black pixels by thresholding them (BSGA09, BBS$^+$10, MLHMD$^+$04, MLDB$^+$08) and use a region of interest (ROI) for subsequent calculations. This can be done either using a constant threshold, or using Otsu's method (Ots75). Other contributions work on rectangular subregions, extracted from within the valid foreground region (HMBD$^+$10). The latter will be used for all methods proposed in this thesis, as it simplifies the algorithms, at the expense of a small loss of FOV.

Distortion Correction

Lens distortion correction requires calibrating the endoscope's intrinsic parameters, which are usually modelled with an internal camera matrix and distortion coefficients (Zha00). The internal camera matrix is defined as

$$\mathrm{K} = \begin{bmatrix} \frac{f}{S_x} & 0 & c_x \\ 0 & \frac{f}{S_y} & c_y \\ 0 & 0 & 1 \end{bmatrix} = \begin{bmatrix} f_x & 0 & c_x \\ 0 & f_y & c_y \\ 0 & 0 & 1 \end{bmatrix}. \tag{1.1}$$

f is the focal length and $(S_x,\ S_y)$ are the pixel side lengths along the x- and y-axes of the image, all three usually given in micrometers, whereas the coordinates $(c_x,\ c_y)$ correspond to the projection of the optical center on the image plane with regard to the x- and y-axes. The distortion parameters given in Equation (1.2) represent the image deformation with respect to $(c_x,\ c_y)$.

$$\kappa = \begin{bmatrix} \kappa_1 & \kappa_2 & \kappa_3 & p_1 & p_2 \end{bmatrix}. \tag{1.2}$$

Radial distortion factors $(\kappa_1, \kappa_2, \kappa_3)$ are responsible for "barrel" or "fish-eye" effects, while tangential distortion factors (p_1, p_2) occur because the lens is not perfectly parallel to the imaging plane. Distorted pixel locations can be corrected using

$$x_c = x_u(1 + \kappa_1 r^2 + \kappa_2 r^4 + \kappa_3 r^6) + 2p_1 x_u y_u + p_2(r^2 + 2x_u^2)$$
$$y_c = y_u(1 + \kappa_1 r^2 + \kappa_2 r^4 + \kappa_3 r^6) + 2p_2 x_u y_u + p_1(r^2 + 2y_u^2),$$

where (x_u, y_u) and (x_c, y_c) depict uncorrected (distorted) respectively corrected (undistorted) pixel coordinates, and r is the Euclidean distance between (x_u, y_u) and the optical center projection (c_x, c_y). The intrinsic calibration parameters can be estimated using Zhang's method (Zha00), requiring only a few images of a simple planar calibration pattern (such as a checkerboard or blob pattern). In (MLHMD+04), it was shown for cystoscopes that the tangential distortion is negligible and that only two radial coefficients allow for a precise distortion correction. This distortion correction is applied by all contributions to bladder cartography, with the exception of (HMBD+10), where the authors chose to use a central 400×400 pixels sub-region within the valid foreground region of the images. They argue that access to the cystoscope for calibration is not always possible, and the distortion correction of each image adds up to the computation time[1]. But, since cystoscopes can only be used one time per day (they have to be sterilized after each examination), they are accessible usually for a fast calibration procedure. Nonetheless, tests in (HMBD+10) showed that radial distortion in this central part is small enough to be negligible. This approach also facilitates most processing steps, as no ROI information needs to be incorporated into the algorithms, albeit with a small loss of FOV.

Vignetting and Inhomogeneous Background Exposure

Vignetting is an optical phenomenon, most evident with wide-angle lenses. In the case of endoscopes, there is an illumination gradient from the image center to its borders (the center being the most illuminated). This gradient is constant for a given setup, and can be calibrated offline using a reference pattern with constant reflectance. Vignetting correction leads to homogeneous illumination, but only when the cystoscope is moved orthogonal to the bladder surface. The illumination changes due to the cystoscope's angle and distance towards the bladder surface cannot be directly calibrated, as the instrument's position within the organ is unknown. Figures 1.8a-b demonstrate the vignetting effect, where the exposure gradient in the peripheral image regions is clearly visible. Figure 1.8c shows an example of inhomogeneous illumination and varying contrast due to different angle and distance to the bladder wall in partly overlapping images. Both effects can influence registration and compositing algorithms, depending on the methods used.

As registration algorithms based on feature correspondences (described in Section 1.3.3.1) are often invariant to illumination changes, there is no need to correct vignetting and exposure differences at this stage. These approaches postpone vignetting and exposure correction to

---

[1]Correcting distortion is fast, but can be an issue if images need to be processed at frame-rate.

the blending part of the cartography process (see Section 1.3.4), since these effects have to be attenuated after placing (stitching) the registered images into the global map.

Registration algorithms based on iconic data (see Section 1.3.3.2) directly rely on the color or grey value information of the images. Therefore, inhomogeneous illumination strongly influences registration robustness and accuracy. In (HMBD+10), images are homogenized by subtracting a band-pass filtered image from the original image. This band-pass filter is designed to eliminate both low frequencies due to vignetting (frequency of illumination gradients are supposed to be much lower than the interesting bladder textures), as well as high frequencies due to the fiber-pattern of flexible cystoscopes (the regular optical fiber pattern consists of frequencies being higher than the bladder textures). In the corrected image, all vascular structures remain visible, while exposure gradients and fiber-patterns are strongly attenuated. This pre-processing can potentially also facilitate the map compositing process (see Section 1.3.4). However, since it also removes the background color from the images, these pre-processed images do not look "natural", and were not used for the final map creation in (HMBD+10). In Figures 1.8d-e, illumination corrected (band pass filtered) images can bee seen.

The data being preprocessed, the next step of the cartography process is to register pairs of overlapping images. In order to give the prerequisites for understanding the existing registration
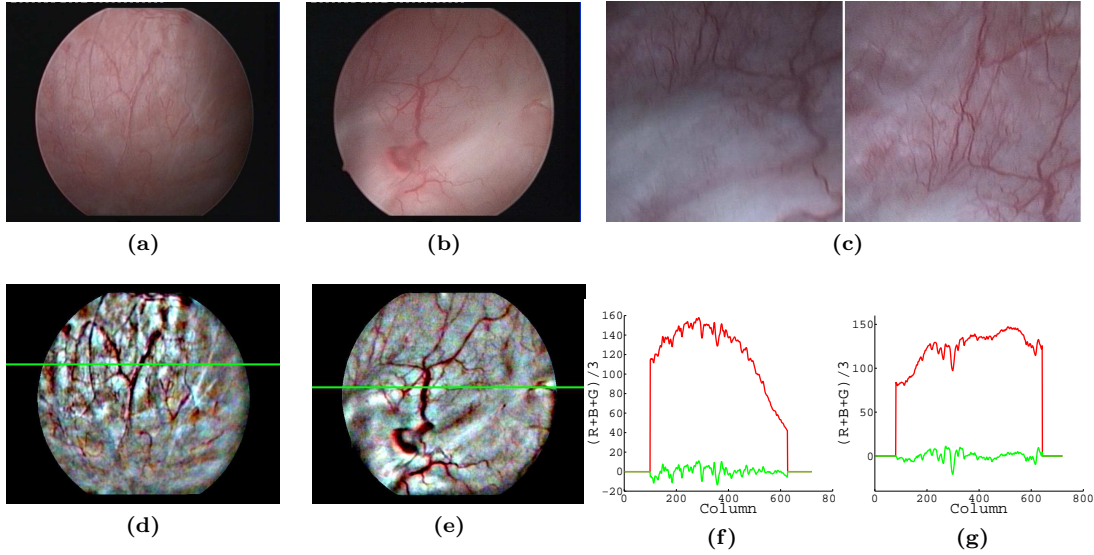
Figure 1.8: Illumination and contrast variability in cystoscopic images. (a)-(b) Example of the vignetting effect: the brightness in the peripheric image regions is lower than in the central regions due to the wide-angle lens of the cystoscope. (c) Different angles of the instrument towards the bladder surface and the auto-exposure mode of the camera lead to different exposure levels in the overlapping image regions. (d)-(e) Illumination-corrected versions of a) and b), using the method proposed in (HMBD+10). (f)-(g). Corresponding line profiles of a) and b) (in red) and d) and e) (in green). While the global exposure gradients have been removed, local structures have been preserved.

algorithms (explained in Section 1.3.3), 3D and 2D geometrical considerations are first provided to the reader in Section 1.3.2.

1.3.2 Geometry of Cystoscopic Image Acquisition Systems

The displacement of the cystoscope between two image acquisitions has first to be mathematically defined to understand the geometrical link between the pixels of the images acquired from two different viewpoints. For this reason, the instrument displacement is first shortly discussed and the geometrical transformation parameters linking the images are then presented.

Three-dimensional Cystoscope Displacement

While the clinicians freely move the cystoscope inside the organ, the instrument's displacement between two acquisitions i and j corresponds exactly to a rigid 3D transformation

$$T_{i \to j}^{3D} = \left[\begin{array}{cc} R_{i \to j}^{3D} & t_{i \to j}^{3D} \\ \vec{0} & 1 \end{array} \right]. \tag{1.3}$$

$R_{i \to j}^{3D} = R_X(r_X) \, R_Y(r_Y) \, R_Z(r_Z)$ is a 3D rotation matrix composed by 3 rotations with angles r_X, r_Y, r_Z around the axes $\vec{X}_i, \vec{Y}_i$ and $\vec{Z}_i$ of the camera of acquisition number i, centered at the camera's optical center C_i, with

$$R_X(r_X) = \left[\begin{array}{ccc} 1 & 0 & 0 \\ 0 & \cos(r_X) & -\sin(r_X) \\ 0 & \sin(r_X) & \cos(r_X) \end{array} \right]; \quad R_Y(r_Y) = \left[\begin{array}{ccc} \cos(r_Y) & 0 & \sin(r_Y) \\ 0 & 1 & 0 \\ -\sin(r_Y) & 0 & \cos(r_Y) \end{array} \right];$$

$$R_Z(r_Z) = \left[\begin{array}{ccc} \cos(r_Z) & -\sin(r_Z) & 0 \\ \sin(r_Z) & \cos(r_Z) & 0 \\ 0 & 0 & 1 \end{array} \right].$$

$t_{i \to j}^{3D} = [t_X \ t_Y \ t_Z]^T$ is a translation vector, where t_X and t_Y are parallel to the image plane, and t_Z is orthogonal to the image plane.

Two-dimensional Image Geometry

As the cystoscope is moved closely to the bladder wall at a high acquisition rate, the geometry of the bladder combined with the small FOV leads to the typical assumption made about the 2D relationship between overlapping images. Indeed, since the bladder is filled with an isotonic liquid and the time between two acquisitions is very short, the epithelial surface can be considered as rigid (without movements and deformations) for small image sequences. Moreover, in many regions of the filled bladder, the small FOV (the cystoscope is close to the epithelium) visualizes quasi-planar surface parts. With such assumptions (which were confirmed by the results of (BSGA09, HMBD$^+$10, MLDB$^+$08, BHDS$^+$10)), the 2D geometrical link between

homologous pixels of two acquisitions i and j can be modelled as a homogeneous perspective transformation (or homography). This transformation is defined as

$$\mathrm{T}^{2\mathrm{D}}_{i \to j} = \left[\begin{array}{ccc} S_x \cos \phi & -s_x \sin \phi & t_x \\ s_y \sin \phi & S_y \cos \phi & t_y \\ h_x & h_y & 1 \end{array} \right], \tag{1.4}$$

where (S_x, S_y) correspond to scale changes, (s_x, s_y) are shearing factors, and ϕ models the in-plane rotation. Translations are given by (t_x, t_y), and (h_x, h_y) correspond to out-of-plane rotations. Subscripts denote the x- and y-axes of the image plane.

A homogeneous position $p^{2\mathrm{D}}_{i,k} = [x_{i,k}, y_{i,k}, 1]^T$ of pixel k in the (source) image I_i is transformed to its corresponding homogeneous sub-pixel position $p^{2\mathrm{D}}_{j,k'} = [x_{j,k'}, y_{j,k'}, 1]^T$ in the (target) image I_j by

$$p^{2\mathrm{D}}_{j,k'} = \nu_k \, \mathrm{T}^{2\mathrm{D}}_{i \to j} p^{2\mathrm{D}}_{i,k}, \tag{1.5}$$

where ν_k is a normalizing factor, ensuring that the third element of $p^{2\mathrm{D}}_{j,k'}$ is equal to 1. The use of indices k and k' denotes homologous pixel positions, displaced from the coordinate system of acquisition i into that of acquisition j. We will also use the terminology $\mathrm{T}^{2\mathrm{D}}_{i \to j}(I_i)$ to describe the transformation (perspective warping) of an image I_i into the coordinate system of image I_j. This transformation is computed using back-warping and bi-cubic interpolation.

Global perspective transformations (that transform pixel positions expressed in the local coordinate system of acquisition i into a common global coordinate system) can be computed via concatenation:

$$\mathrm{T}^{2\mathrm{D}}_{0 \to i} = \prod_{k=0}^{i-1} \mathrm{T}^{2\mathrm{D}}_{k \to k+1}. \tag{1.6}$$

Equation (1.6) assumes (without loss of generality) that the coordinate system of the first acquisition is used as the reference coordinate system.

Note that some contributions (BSGA09, BBS+10) use an affine version of Equation (1.4), i.e. h_x and h_y are equal to zero and no perspective transformations are applied. While this has a negligible visual effect for the registration of two subsequent images, concatenated global transformations are changed noticeably due to accumulated errors, as the cystoscope displacement is indeed fully perspective.

Cylindrical and Spherical Projections

It should be noted that for many cartography applications (i.e. consumer photography), it is generally recommended to use cylindrical or spherical coordinates when constructing the final panorama. This is due to the fact that the map tends to get deformed severely once the FOV extends 90 degrees when using planar coordinates (Sze06). This effect is demonstrated in Figure 1.9a. Using cylindrical or spherical coordinates, three-dimensional rotation of the camera around its optical center simplifies the 2D geometry between images to translations and in-plane rotations. As a consequence, images do not shrink/expand or get deformed perspectively, and

Figure 1.9: Planar vs. spherical coordinates. (a) Map created using the original images and a perspective projection model. The large FOV of the sequence leads to severe size differences between the images. (b) Map created using spherical projection model. Camera panning reduces to translations of the projected images, leading to a panoramic image more pleasing to the eye.

the final panorama is more pleasing to the eye, as shown in Figure 1.9b. As the bladder is (roughly) spherical, a spherical projection appears to be the ideal surface to project the images onto. However, these models assume that the camera is only rotating around its own optical center, and is not translated. This rules out using spherical coordinates for cystoscopic cartography, as the instrument is mostly translated along the bladder wall. In practice, the endoscope displacement does not correspond at all to a scenario where spherical coordinates may be used.

Estimating $\mathrm{T}^{2\mathbf{D}}_{i \to j}$

A homogeneous perspective transformation, as given by Equation (1.4), has eight degrees of freedom. From Equation (1.5), we get two equations for each point correspondence:

$$x_{j,k'}(h_{31}x_{i,k} + h_{32}y_{i,k} + 1) = h_{11}x_{i,k} + h_{12}y_{i,k} + h_{13}$$
$$y_{j,k'}(h_{31}x_{i,k} + h_{32}y_{i,k} + 1) = h_{21}x_{i,k} + h_{22}y_{i,k} + h_{23}, \tag{1.7}$$

where $h_{lm}(l, m \in \{1, 2, 3\})$ are the elements of $\mathrm{T}^{2\mathrm{D}}_{i \to j}$ (see Equation (1.4)). These equations are linear with respect to the elements of $\mathrm{T}^{2\mathrm{D}}_{i \to j}$, so that four point correspondences are sufficient to determine $\mathrm{T}^{2\mathrm{D}}_{i \to j}$ up to scale. Using Equation (1.7), a homogeneous equation system to solve for $\mathrm{T}^{2\mathrm{D}}_{i \to j}$ can be written:

$$A\vec{h} = \vec{0}, \tag{1.8}$$

with $\vec{h}$ containing the elements of $\mathrm{T}^{2\mathrm{D}}_{i \to j}$. For exactly four point correspondences, A is an 8x9 matrix with rank 8 and has a one-dimensional Null-space that gives the exact solution for $\vec{h}$. When more than four point correspondences are available, Equation (1.8) is overdetermined and has no exact solution, due to errors in the correspondences leading to a rank of $A \neq 8$. Using the Singular Value Decomposition (SVD) technique (GR70), $\vec{h}$ can be approximated in a least squares fashion.

In a similar way, the rigid 3D transformations $\mathrm{T}^{3\mathrm{D}}_{i \to j}$ can be estimated, which will be explained in Chapter 4.

1.3.3 Registration of Cystoscopic Images

The geometry of the cystoscopic acquisition system being introduced, and the geometric model used for superimposing overlapping images being defined, it is now possible to present existing contributions for the assessment of $\mathrm{T}^{\mathrm{2D}}_{i \to j}$ in the case of bladder images. The process of superimposing the common area of partly overlapping images is called registration.

Feature Based Registration

Feature based approaches extract locations (*key-points*) in both images that are likely to be discriminative, such as points located on corners or line segments. One of the early examples for such a key-point extraction method is the Harris corner detector (HS88). For these key-points, feature vectors are computed and can be used to measure the similarity between key-points in different images. A variety of descriptors exist in the literature. Well known examples are Scale Invariant Feature Transform (SIFT) (Low99) and Speeded Up Robust Features (SURF) (BTVG06) features. These descriptors are scale and rotation invariant. More recently, Affine Scale Invariant Robust Features (ASIFT) were proposed (MY09), which extend SIFT features for affine transformation invariance. Other common feature descriptors are ORB (RRKB11), or Histograms of Oriented Gradients (HoG) (DT05). Once key-points and descriptor vectors have been computed for a pair of images, a search for corresponding key-points is performed. The typical procedure is to find the best descriptor match for each key-point in the source image to all descriptors of the target image's key-points. From these initial matches, only those whose score is by a certain factor better[1] than the second best match are kept. Alternatively, another initial outlier rejection is to also compute the best matches for all descriptors in the target image, and only keep matches that agree in both directions (i.e. both from image I_i to image I_j and vice versa). Since these initial matches still contain outliers, robust outlier rejection methods, such as RANSAC (FB81) or LMedS (Rou84)), are performed to remove outliers and fit the transformation.

This feature based image registration approach was used in (BSGA09, BBS⁺10) for images acquired in the fluorescence modality. In (BSGA09), SIFT features are computed for a set of key-points, while in (BBS⁺10), SURF features were used to decrease computation time in order to work in a real-time framework. Both in (BSGA09) and in (BBS⁺10), RANSAC was applied to estimate the affine transformation that registers consecutive images of cystoscopic video-sequences. Images acquired in the fluorescence modality usually show strong vascular contrast, so that image primitives (key-points in this case) can be robustly segmented and matched in consecutive images throughout the sequence.

---

[1]In (Low99), a threshold of 0.8 is suggested.

Feature Based Registration in the White Light Modality

In the more widespread (and standard) white light modality, less contrast is available, and image primitives cannot be robustly extracted throughout the video-sequence systematically. Figures 1.7a-c show cystoscopic images with contrasted vascular structures, which can robustly be segmented and used for image registration. The remaining images do not contain enough sufficient vascular structures (or they are only bundled in a small sub-region), and are (partly) blurry due to de-focusing or the angle towards the bladder surface. When a well exposed scan leads to well-contrasted images, registration using SURF features and RANSAC robust fitting of a perspective transformation is feasible. Figure 1.10a shows the successful matching of two consecutive images from a cystoscopic video-sequence. In the top row of each sub-figure, the two input images that have to be registered are shown. In the middle row, green lines depict reliable feature point correspondences, while red lines show rejected outliers. In the bottom row, the first (source) image (left hand side) is warped onto the target image using the estimated perspective transformation. Point correspondences are well spread in the overlapping image regions, and consequently the superimposed source image is well aligned with the target image. Figure 1.10b shows a pair of consecutive images from another cystoscopic sequence. However, the images suffer from slight motion blur, and are less contrasted. These effects are often caused by slow auto-exposure and auto-focus of the camera, or when the cystoscope is further away from the bladder wall. The middle row of Figure 1.10b shows much more rejected outliers, which indicates that feature correspondences are less unique when the images' quality decreases. While the estimated perspective transformation using inliers still leads to a visually acceptable perspective warping of the source image, inliers are less well spread and are focused on the vascular structure in the center of the images. Between two images the alignment errors are usually not perceptible, but theses errors accumulate during the placement of the data in a global map and often become visible in the map, as will be discussed latter.

Finally, Figure 1.10c shows a pair of non-consecutive images. While no previous contribution to bladder cartography tries to register non-consecutive image pairs, they play an important role in this thesis for global correction of the image placement in the common map coordinate system, as will be shown later in Chapter 3. Only a few correspondences could be obtained after initial outlier rejection, because the feature vectors are not invariant to perspective transformations or strong appearance differences. Only 8 valid inliers were determined after RANSAC fitting, and the superimposed images are incorrectly aligned. The results from Figure 1.10c demonstrate that feature based registration cannot be robustly used for white light bladder cartography. If only one pair of images is incorrectly superimposed, the final map will also be incorrectly stitched.

| (a) | (b) | (c) |
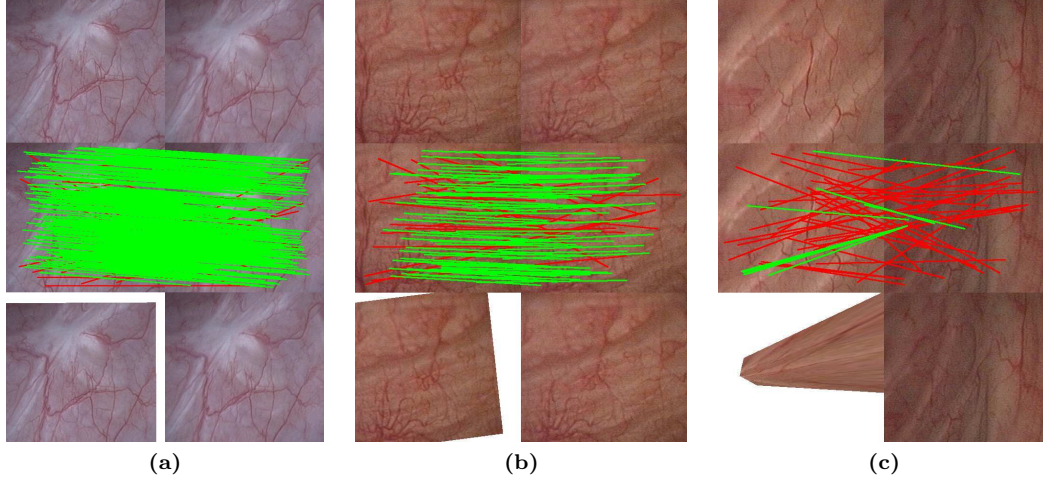
Figure 1.10: Feature based registration in the white light modality. (a) Well contrasted consecutive images without motion blur. Enough homologous SURF keypoints can be extracted and matched with RANSAC. Green lines depict reliable feature point correspondences, red lines show rejected outliers. (b) Consecutive images, suffering from motion blur, de-focus and weak exposure. More rejected outliers and altogether less matches show that descriptors are less unique when image quality decreases. The estimated perspective transformation still leads to an acceptable (visually coherent) superimposition of the images, but inliers are focused on the vascular structures in the center of the images. (c) Registration of non-consecutive images, which differ both in contrast and exposure due to different angle and distance to the bladder surface. Only a few (mostly incorrect) correspondences could be obtained after initial outlier rejection. Such a lack of positive matches arises since feature vectors are not invariant to perspective transformations and the strong appearance difference. Eight valid inliers were determined by RANSAC, but the superimposed images using the estimated transformation are incorrectly aligned.

Registration Based on Iconic Data

Two approaches based on iconic data were previously developed at the CRAN laboratory for robustly registering bladder images in the white light modality. In (MLHMD$^+$04, MLDB$^+$08), $\mathrm{T}^{2\mathrm{D}}_{i \to j}$ is obtained by maximizing the mutual information between the target image I_j and the source image I_i transformed by $\mathrm{T}^{2\mathrm{D}}_{i \to j}(I_i)$. This work is based on EMpirical entropy Manipulation and Analysis (EMMA), proposed in (VWI97). The mutual information is a statistical measurement which combines the grey-level entropies $E(I_j)$ and $E(\mathrm{T}^{2\mathrm{D}}_{i \to j}(I_i))$ of the overlapping parts of the images I_j and $\mathrm{T}^{2\mathrm{D}}_{i \to j}(I_i)$ and the joint grey-level entropy $E(I_j, \mathrm{T}^{2\mathrm{D}}_{i \to j}(I_i))$. This measurement can be written as

$$S_{MI}(I_j, \mathrm{T}^{2\mathrm{D}}_{i \to j}(I_i)) = E(I_j) + E(\mathrm{T}^{2\mathrm{D}}_{i \to j}(I_i)) - E(I_j, \mathrm{T}^{2\mathrm{D}}_{i \to j}(I_i))$$

and is maximized by a stochastic gradient descent algorithm, optimizing the transformation parameters of $\mathrm{T}^{2\mathrm{D}}_{i \to j}$. The grey-level entropies are computed using grey-level probability density functions. Each probability density function is analytically modelled by the sum of about 300

Gaussian functions with the same standard deviation. The value of the latter is optimized together with the perspective matrix parameters. A large number of iterations is needed to reach convergence, so consequently, this approach needs several hours to compute a panoramic image from a video-sequence.

As discussed in detail in Section 1.5, the computation time is the least important aspect (registration quality being the most important one), as maps are mainly used for a second diagnosis (after the actual examination) and bladder cancer follow-up. However, it is still desirable to be able to make a the second diagnosis shortly after the examination. To achieve a fast cartography algorithm, (HMBD$^+$10) proposed to use a Baker-Matthews optical flow approach that minimizes the sum of squared distances (SSD) of grey-values between overlapping images. In order to increase the speed of convergence, they first compute an initial transformation using cross-correlation in the Fourier domain, thereby obtaining an initial estimate of translation only (parameters t_x and t_y in Equation (1.4)). The lack of strongly discriminative texture prevents the computation of all transformation parameters of $T^{2D}_{i \to j}$ directly in the Fourier domain, otherwise the method from (JJ06) might possibly be applied directly. Formally, the optical flow approach of (HMBD$^+$10) can be written as

$$S_{BM}(I_j, T^{2D}_{i \to j}(I_i)) = \sum_{p \in I_j \cap T^{2D}_{i \to j}(I_i)} (I_j(p) - (T^{2D}_{i \to j}(I_i))(p))^2$$

In (HSB$^+$09), a study concerning robustness and accuracy of both optical flow and mutual information based methods was conducted. For endoscope displacements consisting mainly of translations, the two exiting methods register the images accurately. However, for $T^{2D}_{i \to j}$ dominated by rotations, scale changes and/or perspective changes, both methods perform significantly worse (the registration accuracy is up to ten times worse than for pure translations). While this has only small visible effects on the registration of two subsequent images, the global error accumulates drastically and is often visible in the maps. These results will be discussed in more detail at the end of Chapter 2, where we compare the results of (HSB$^+$09) with an initial proof of concept for graph-cut based image registration, as published in (WDBH$^+$na).

1.3.4 Map Compositing

The *local* $T^{2D}_{i \to i+1}$ matrices registering consecutive images I_i and I_{i+1} can be used to determine the *global* matrices $T^{2D}_{0 \to i}$, as defined in Equation (1.6), which place each image I_i in the map coordinate system (here that of image I_0). Once theses global transformations $T^{2D}_{0 \to i}, i \in \{0, ..., N-1\}$ have been estimated for all N images, the panoramic image can be composed. This compositing process will also be referred to as *stitching*.

Often, this process is divided into several steps (Sze06). First, seams can be computed. These seams determine the locations of transition between overlapping images in the global map. This is equivalent to a labelled image, where each pixel p is assigned an image index $l_p \in \{0, ..., N-1\}$, where l_p means that image I_{l_p} is used to obtain the color for pixel p in

the map. The position of these seams should be determined so that visible texture and color discontinuities in the map are removed, or at least minimized. Such discontinuities can occur due to small misalignments, or ghosting (moving objects in a static scene). Once these seams are detected, blending methods try to correct exposure differences over seam borders. While seam detection plays an important role in many stitching applications, hitherto, all previous contributions to bladder cartography (MLHMD$^+$04, MLDB$^+$08, WRS$^+$05, BBS$^+$10, BGS$^+$10, BGS$^+$11) omitted this seam detection step, even though such methods are of great interest also for bladder cartography. The methods proposed in (BRM$^+$09, MLHMD$^+$04, MLDB$^+$08) directly compose the panoramic image by overwriting existing pixel values with those from the current image. This leads to too dark maps when vignetting is strongly present, and to visible exposure artefacts, as can be seen in Figure 1.11a. Other contributions perform blending techniques to minimize composition artefacts at pixels in overlapping image regions.

Alpha-Blending

The most basic blending method is known as linear alpha-blending (PD84, Bli94). The pixels p in the overlapping area $I_{I_i \cap I_j}$ between two images I_i and I_j (or the current panoramic image and the next image to be stitched) are linearly interpolated using

$$I_{I_i \cap I_j}(p) = \alpha I_i(p) + (1 - \alpha) I_j(p). \tag{1.9}$$

This very simple linear interpolation method may work sufficiently when scene exposure variations are small. For cystoscopic images however, the vignetting-induced exposure differences are still clearly visible after linear alpha-blending, as can be seen in Figure 1.11b, and also introduces blurring across overlapping images.

Feathering

Slightly better results can be obtained by substituting the weighting parameter α of Equation (1.9) with a weighting function $\alpha(p)$, which weights pixels near the images' center more strongly than those in the peripheral regions (WRS$^+$05). The weights can be computed using any distance transformation (e.g the Euclidean distance transformation (ST94)), or the grass-fire transformation (B$^+$67). A similar method was proposed in (HMBD$^+$10), where weights are computed using the Gaussian function $\alpha(p) = 0.9e^{-r/(2\sigma)} + 0.1$, with σ equal to one quarter of the image's width, and r the distance of p to the image center. The result using a Euclidean distance-weighted alpha-blending can be seen in Figure 1.11c. While artefacts due to vignetting are mostly removed, a significant amount of blur is visible. Another possibility to chose the weighting function is to use offline-calibrated endoscopic illumination characteristics, as proposed in (BGS$^+$10), which also reduces the vignetting-induced exposure loss at the peripheral image regions.
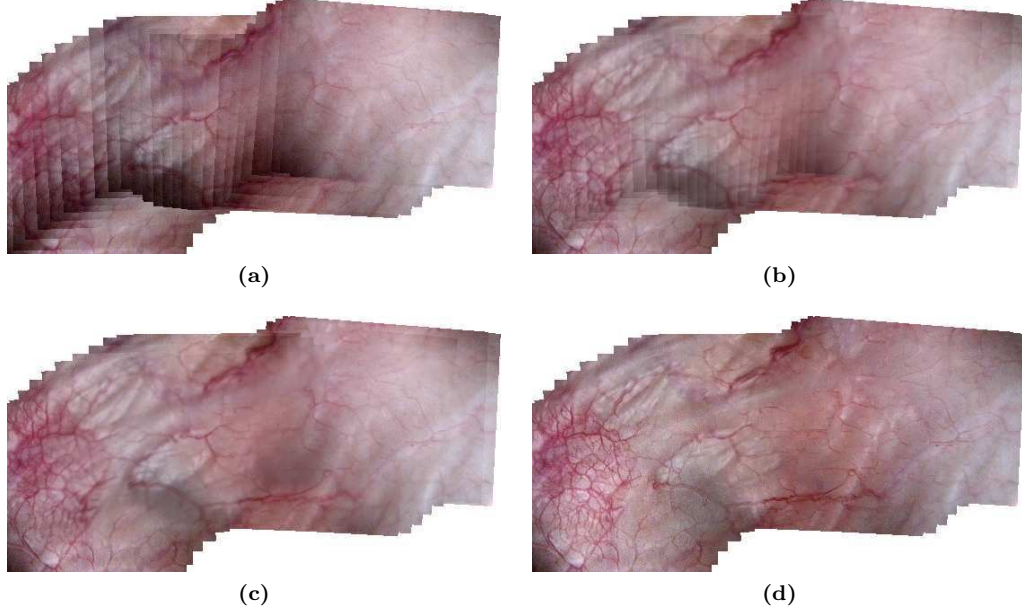
Figure 1.11: Examples of different map compositing techniques. The registration was performed using the methods proposed in Chapter 3. (a) The map is iteratively overwritten with the current image, as applied in (BRM$^+$09, MLHMD$^+$04, MLDB$^+$08). Artefacts due to the exposure differences and vignetting are clearly visible at the images' borders. (b) Alpha-blending (PD84, Bli94) with $\alpha = 0.75$. Exposure artefacts are reduced compared to those in a), but still visible. Blurring artefacts are introduced. (c) Distance based alpha-blending (HMBD$^+$10). Artefacts are mostly removed, but the degradation due to blur is stronger than in b). (d) Outlook and comparison to the compositing techniques proposed in Chapter 3 of this thesis. No artefacts can be seen, and the map's contrast is greatly enhanced.

Multi-Scale Blending

Due to the freely moving cystoscope, individual images of a cystoscopic video-sequence often show strong variations in map resolution (an image taken close to a lesion usually has a higher panoramic resolution than an image captured from a larger distance when the clinicians try to locate anatomical landmarks). Images also differ in exposure due to the distance and orientation of the cystoscope with regard to the bladder surface. In the fluorescence modality, the rapidly decaying fluorescence must also be taken into account when stitching the final panorama. If images, acquired at a late stage of the examination, dominate the texture of the map, the reddish glowing tumour tissue visible in earlier images will be lost. In order to obtain well illuminated maps showing a maximum of fluorescence and resolution, a multi-scale blending method was proposed in (BGS$^+$10), and later extended to a non-linear multi-scale blending method in (BGS$^+$11). It is argued that well exposed images can only be acquired when the cystoscope is moved at close distance to the bladder wall. For such acquisitions, bright images correspond both to high fluorescence emission as well as to high resolution. The aim of the

multi-scale blending method is to exploit the images acquired close to the bladder wall to build maps with high resolution and strong fluorescence signal.

This multi-scale non-linear blending method produces well exposed textured maps showing fine vascular structures, as can be seen in (BGS$^+$11). However, it does not consider the influence of motion blur or de-focus, as images taken from similar viewpoints will have similar mean brightness, independent of their contrast or sharpness. Furthermore, images taken from close range are always preferred over images taken from further away, even if the former are blurry. The image sequence shown in Figure 1.11 contains images taken all from approximately the same distance to the bladder epithelium, so the multi-scale blending approach of (BGS$^+$11) has no apparent advantages over feathering methods in the white light modality.

1.3.5 First Assessment of Existing Endoscopic Cartography Approaches

As a first and brief evaluation of the published cartography approaches (see Section 1.5 for a detailed discussion), it is possible to notice that the automatic registration of a large number of images without a priori knowledge is an open problem in endoscopic applications in general, and in cystoscopy in particular. Indeed, several steps of the existing endoscopic cartography methods do not satisfy all conditions for automatic and visually coherent bladder map creation.

- The robust white light registration algorithms usually require large overlapping regions between consecutive images (often at least 90% of the image area) and well contrasted data (without blur). Feature-based approaches may not robustly estimate the geometric relationship systematically, as sequences are often blurry or of weak contrast.

- There is no automatic detection of non-consecutive images with strong overlapping and common regions (e.g. due to crossing endoscope trajectories). Such a detection is required to correct the visual aspect of the maps.

- Blending algorithms minimizing the texture and color discontinuities are often not efficient enough. Moreover, they also do not optimize the contrast of the maps, nor do they detect optimal transitions (seams) between overlapping images.

1.4 3D Endoscopic Cartography

Two-dimensional cartography greatly facilitates diagnosis, preparation of follow-up examinations, surgery planning and archiving of the recorded video in a single high resolution picture (see Section 1.1). However, the organ is three-dimensional, and the mental orientation and representation performed by the clinicians is intuitively done in 3D. In addition, three-dimensional data presents valuable information during surgical interventions, especially for locating lesions

with respect to anatomical landmarks or for roughly measuring the dimension of lesions. Consequently, it can also be helpful to construct three-dimensional maps (or textured surfaces) from the video-sequence acquired during a cystoscopic examination.

Unfortunately, as explained previously, the small FOV and the close distance of the cystoscope towards the bladder surface impedes the direct estimation of 3D data from the video-sequence (using only the two-dimensional images, showing quasi-planar scenes). As shown in the literature related to the few attempts of 3D analysis of endoscopic data, either a priori information about the parametric surface of the organ, or additional 3D data is necessary to robustly reconstruct the organ's three-dimensional shape. In the following sections, we will review the literature regarding the 3D reconstruction of endoscopic medical data.

1.4.1 2D Endoscopic Cartography with 3D a priori Knowledge

When the observed scene can be represented as a parametric surface of known shape, the images can be registered using the known surface geometry as an a priori information. This reduces distortions due to the projection of the three-dimensional scene onto the image plane. In (CS09), this approach was used to construct maps of the inner oesophagus wall using tubular 3D shapes. The method computes both the endoscope trajectory T^{3D} and a 2D panoramic image. Although not done in (CS09), the registered images could be projected onto the tubular shapes to obtain a 3D representation of parts of the inner oesophagus wall.

More specific for bladder cartography, the method of (BSGA09) represents the bladder surface using "hemicube" planes. Each hemicube plane approximates a part of the bladder's surface (back wall, left and right lateral wall, upper wall and ostium) as a plane. For each of these regions, a seperate scan is performed by the clinician, and the computed 2D map is associated with this hemicube. The justification for this procedure is to prevent severe perspective distortions arising when projecting the entire spherical bladder surface on a single planar map (see also Figure 1.9). Using seperate hemicubes, distortions remain low, and the entire bladder map can be displayed by unfolding all hemicube planes. The main disadvantage is the fact that the clinicians must manually select the corresponding hemicubes while scanning the bladder, and must scan each hemicube separately. This may impede the clinicians' own standard procedure of scanning the organ's surface, and does not guarantee seamless transitions from one hemicube to the other. Additionally, the map is constructed only up to scale and does not allow for the measurement of dimensions in world coordinates. Nonetheless, it depicts an interesting approach of a semi-3D cartography approach, which can be easily archived in a single high resolution (unfolded) image.

1.4.2 3D Endoscopic Cartography

In a calibrated stereo (or multi-camera) setup (i.e. with known intrinsic and extrinsic parameters), 3D points can be reconstructed if their homologous 2D pixel positions can be detected and matched between two or more viewpoints. However, as the instrument is moved freely, its trajectory (i.e. the extrinsic parameters, encapsulated in $T_{i \to j}^{3D}$) is unknown. Structure from motion (SfM,(PKG99, HZ03)) approaches, which are based on bundle adjustment (TMHF00), tackle this problem by simultaneously estimating 3D points and camera displacement from several viewpoints. This approach was used to estimate the surface of the bladder in (SPS12). As a first step, images are registered using SIFT and RANSAC, and the 2D map is globally corrected to obtain more accurate transformation between consecutive and non-consecutive images. While this is theoretically possible using iconic data registration, it implies very long computation times and a robust automatic detection of non-overlapping images (which is still an open problem). In (SPS12), an initial 3D point reconstruction is then computed with the constraint that the 3D points must lie on a sphere (a geometric constraint that is not fulfilled in practice). Finally, an incremental bundle adjustment step iteratively moves the reconstructed points towards the true surface shape. The final 3D map is obtained by fitting a surface on the reconstructed points, and projecting the 2D images onto it.

The algorithm was tested on a pig bladder phantom injected with contrast dye. This dye strongly increases the contrast of vascular structures and ensures the presence of image primitives which can be easily segmented. As was argued before, image primitive extraction cannot be systematically guaranteed with human bladder tissue in realistic (clinical) conditions. Nonetheless, the estimated perspective transformations $T_{i \to j}^{2D}$ could be used to create artificial correspondences for the bundle adjustment step. However, a main restriction is the fact that the cystoscope must be close to perpendicular at all times during the acquisition to ensure the convergence of the method. More specific, in (SPS12), a specifically designed instrument (an ultra-thin optical fiber) was placed near the center of the phantom, and was automatically rotated by a robotic system around its origin to scan the entire phantom from the same viewpoint. This ensures both perpendicular orientation to the bladder wall, as well as enough three-dimensional structure (non-planar) in each image. These assumptions do not hold with rigid endoscopes for practical reasons (the clinician cannot manoeuvre a rigid cystoscope to be in such a situation). Even with fiber-scopes, this is a challenging task for clinicians and would require intensive training. In addition (for both rigid and flexible cystoscopes), the instrument must be displaced much closer to the bladder surface in order have sufficient brightness and texture resolution in the images, which loses valuable three-dimensional structure (FOV shows quasi-planar structures). Furthermore, bundle adjustment is sensitive to the initial solution, and the bladder is often not spherical, as other organs warp it. Moreover, this approach requires the entire bladder to be scanned and globally registered, which is a challenging (and still open) problem with clinical cystoscopic data.

1.4.3 3D Endoscopes

The methods presented in the previous section only use 2D images to recover the organ surfaces. Alternatively, endoscopes that also provide 3D information could allow for a more robust estimation of the surface geometry. Most solutions described in the literature are based on the active stereo-vision principle. In comparison to passive stereo-vision, the use of a light projector facilitates the matching and reconstructions steps in the case of complex medical scenes. For two channel endoscopes, there is a direct way to implement the active stereo-vision principle. One channel projects light patterns (such as lines, scattered points, or structured light patterns) onto the surface, while the other channel acquires the projected patterns. When both projector and camera are calibrated, the projected pattern can be used to determine 3D positions in the camera coordinate system. In (CLZQ03), it was shown that for a relatively small baseline (distance between projector and camera channel axes) of 2 mm, points on test objects can be reconstructed with sub-millimeter accuracy. This system was also used to reconstruct the surface of the oral cavity. In (ADG09), the authors have used the same principle to reconstruct the abdominal cavity using a coded pattern that facilitates the matching between the pattern and its projection. While these two approaches lead to very robust estimation of dense surfaces for small FOV endoscopes, the projected patterns suppress the color information of the organ and are not suitable for cystoscopic cartography. In addition, the almost planar surface seen in each FOV in a cystoscopic setup impedes a robust registration. For instance, if the cystoscope is displaced along the bladder wall, while its distance and (out-of-plane) orientation towards it remains constant for two acquisitions, the same planar surface will be recovered. In such a scenario, the endoscope displacement is ambiguous and cannot be recovered robustly.

This ambiguity can be overcome by guiding the 3D registration using 2D textures. At the CRAN laboratory, an active stereo-vision prototype (whose implementation on a one-channel endoscope is currently in progress) for two-channel endoscopes was proposed using an eight laser dot structured light pattern (BHDS$^+$10). After projector-camera calibration (BHSD$^+$10), 3D positions of these eight laser dots in the camera coordinate system are acquired in addition to each color image. The rigid 3D cystoscope displacement $T_{i \rightarrow j}^{3D}$, given in Equation (1.3), is estimated together with the corresponding $T_{i \rightarrow j}^{2D}$ perspective transformation registering consecutive image pairs. As detailed in (BHDS$^+$10), the inner 3D bladder surface construction is guided by the registration of 2D images. This algorithm exploits some constraints relating to the 3D and 2D prototype geometry and the 3D/2D laser point correspondences to ensure a robust 3D surface construction. After the surface has been built, the 2D image textures can be projected onto it.

Recently, in (PHS$^+$09), a 3D endoscope was built with a time-of-flight (ToF, (LSKK10)) camera. Each pixel of a ToF camera provides a distance from the surface. This system was used to reconstruct surfaces of the inner wall of a pig stomach using a laparascope. The modulated infrared light was emitted through an optical fiber, and the distance images were acquired

through the endoscope channel. Similar to the dense active stereo-vision systems described in the first paragraph, using almost planar surfaces in each FOV, the ambiguity (due to poor geometrical information) impedes a robust estimation of the endoscope displacement since the 3D shapes cannot be registered without additional texture information.

However, as described in Chapter 4, the ToF based surface measurement principle can be implemented on one-channel endoscopes (such as cystoscopes equipped with color cameras) using commercially available beam splitters. This would allow to simultaneously acquire the distance images from the ToF camera and the color images of a CCD camera. After offline stereo calibration of both cameras, these distances can be transformed into 3D positions in the color camera coordinate system. Such a system could therefore supply a high resolution color image and a low resolution 3D point cloud. 2D image registration algorithms can then be used to guide either 3D-3D data superimposition algorithms or to solve 2D-3D point correspondence problems with the aim to find the $T_{i \to j}^{3D}$ rigid transformation (see Equation (1.3)) linking two endoscope positions.

1.4.4 First Assessment of Existing 3D Endoscopic Cartography Approaches

The literature (SPS12) shows that the complexity and inherent variability of endoscopic data complicates a robust construction of 3D bladder maps. However, the publications of active stereo-systems (CLZQ03, ADG09) dedicated to endoscopy have shown that this measuring principle can be a solution to recover 3D organ information in a robust way. Moreover, it was shown in (BHDS⁺10) that 3D cartography of textured large FOV data is possible and can be guided by 2D image registration.

1.5 Objectives of the thesis

The main and general aim of this thesis is to robustly build 2D large FOV textured maps from the images of a cystoscope acquired for unknown and realistic (crossing) trajectories, which were not handled in previous contributions. The existing algorithms lead to visually incoherent panoramic images for such instrument displacements. A second goal of this thesis is to show the feasibility of 3D cystoscopic cartography. To do so, the 2D algorithms have to be adaptable to 3D cartography. To meet these objectives, different and challenging problems have to be solved. The following sections summarize the scientific and medical objectives of this dissertation.

1.5.1 Scientific Objectives

The main scientific objectives (in bold) addressed in Chapters 3 and 4 are formulated as follows.

Globally Coherent Transformations

No previous contribution automatically handles the case of partly overlapping, non-consecutive image pairs. However, as the examination progresses, clinicians regularly return to previously visited locations on the bladder surface (e.g. to regularly locate the cystoscope with respect to an anatomical landmark, or to scan the epithelium in a systematic way). Possible instrument trajectories are zig-zag-paths (the cystoscope performs multiple overlapping line-scans), or loop-scenarios. In these cases, small local registration errors accumulate to larger global cartography errors, leading to visible misalignments in the map when returning to previously scanned areas. Without global correction of the local and global transformation matrices, the final map will be incoherently stitched. Global correction thus requires registration of additional (non-consecutive) image pairs.

The authors of (MLDB$^+$08) have proposed a method to correct such misalignments, by equally distributing the global errors between first and last image in loop scenarios using steepest gradient optimization. However, no means of automatically detecting these loops is given, and their algorithm is unable to register pairs of images with less than 90% of overlap, which is seldom the case in such scenarios.

In (BTGA11), a system to detect gaps (e.g. missed parts in zig-zag- and loop-scenarios) was proposed. Using this information, clinicians could potentially be able to re-scan these unseen regions to fill holes in the panoramic image. However, only phantom image sequences were used in (BTGA11), which significantly reduces global errors. Consequently, the authors did not deal with correction of global errors. Clinical studies are currently conducted by the authors of (BTGA11), and probably global errors will be an issue there.

One aim of this thesis is the design of an automatic overlap detection algorithm. For this purpose, overlapping non-consecutive image pairs must be detected and registered accurately. Accumulated errors have to be distributed equally over all possible image pairs, so that globally coherent panoramic maps can be composed. The corresponding contributions are presented in Section 3.2.

Robust and Accurate Image Registration

As stated in Sections 1.3 and 1.3.3, the intra- and inter-patient texture variability, as well as motion blur and camera de-focus, involve several challenges to image registration algorithms (see again Figure 1.7). Feature based image registration methods (BSGA09, BBS$^+$10) on the one hand are able to estimate the transformations that superimpose partly overlapping images in an accurate fashion. However, such an approach is only feasible when the images are well focused and do not exhibit strong perspective, focus, or exposure differences. This directly rules out the registration of non-consecutive images (see previous section), because these effects are almost always present due to the freely moving cystoscope (causing strong perspective changes) and the auto-focus and auto-exposure mode of the camera attached to the instrument. It also impedes the registration of images taken while the cystoscope is displaced rapidly, as the motion

blur removes valuable vascular structures and prevents the extraction of enough homologous key-points.

Approaches based on iconic data on the other hand (MLDB$^+$08, HMBD$^+$10) do not rely on the segmentation of image primitives and work more robustly in the mentioned scenarios, but their accuracy suffers when rotations, scale and/or perspective changes become more dominant (HSB$^+$09). While consecutive image pairs are often related mainly by translations, the other parameters are dominant when the endoscope changes its direction, and especially on non-consecutive image pairs. Furthermore, these methods usually need a large percentage of overlap (90% or more). While this is a reasonable assumption for consecutive image pairs, the overlap percentage is often much less than 65% between non-consecutive images.

For these reasons, another objective of this thesis is to design and implement a registration algorithm that works equally robustly and accurately, independent of the transformations involved. It must be able to register non-consecutive image pairs with a low amount of overlap, so that global map correction (see previous section) can be achieved. This objective is addressed in Section 3.3.

Map Compositing

As was stated in Section 1.3.4, all previous contribution omit the step of detecting optimal seam lines for the composition of the final panoramic image. Instead, overlapping images are directly blended into a global textured map. While some of these methods are able to produce maps without visually visible artefacts (and enhance the map in the fluorescence modality based on the images' intensities), blending-induced blurring and ghosting are the direct consequences of the previously proposed methods.

Another aim is therefore to superimpose overlapping images while maximizing the contrast of the textured maps. Seam lines must be selected so that no visible artefacts due to misaligned vascular structures are present, images with good focus are preferred over blurry ones, and the final map must not show any exposure related artefacts. This objective is met in Section 3.4.

Extendibility to 3D Cystoscopic Cartography

The main focus of this thesis is 2D cystoscopic cartography, because clinical data providing additional 3D measurements (see Section 1.4) are not available yet. However, it is another aim of the thesis to develop and implement the algorithms in a way that they can be extended to work on 3D data. The algorithms must be modular in a sense that only the formulas explicitly based on 2D data need to be re-implemented for 3D, while remaining steps and the global algorithmic approach should not need modifications. Initial tests on phantom data (simulated and acquired in the laboratory) should show the potential for clinical applications in the future. These extensions to three-dimensional cartography are addressed in Chapter 4.

1.5.2 Medical Interest and Time Constraints

Although real-time cartography algorithms could be of interest for online wide FOV visualization (e.g. to show clinicians whether they have missed/overseen some parts of the bladder wall), building a map offline (i.e. the methods proposed in this thesis cannot be used in a real-time application) can also lead to real medical progress. The following reasons strengthen this point.

- Recording a large FOV map is an efficient way to archive important examination information. It is recalled that currently only a bladder sketch and a small FOV picture are archived. Videos are not recorded since they are usually not exploitable by clinicians who did not perform the examination. Even the clinicians who did it lose the ability to understand the video after some time has passed. A wide FOV panoramic image, both including the whole lesion and anatomical landmarks, allows for scene understanding (e.g. lesion type, lesion localisation in the bladder, lesion state) for all clinicians. This fact ensures the traceability of examinations and surgical treatments over time for a disease that usually requires a long time follow-up. This aspect of the work rather demands accurate and robust cartography algorithms than fast ones.

- The other interest of large FOV bladder maps lies in the fact that other clinicians than the urologist or surgeon who performed the examination can pose a second or third diagnosis. Again, the confronting of several diagnoses does not require real-time cartography.

- As mentioned, to facilitate a diagnosis, the maps should be built in a robust and precise way, rather than at image acquisition rate. However, computation times not exceeding a quarter or a half hour enable clinicians to pose a second diagnosis, without requiring the patient to stay for a long time at the hospital. The clinician/patient discussion (interview) can then take place after the second diagnosis.

- Comparing visually (or automatically) two maps built with data acquired in intervals of some weeks or months potentially facilitates lesion evolution assessment. Such an assessment also does not require real-time cartography.

1.5.3 Global Approach: Discrete Energy Minimization as a Framework for Cystoscopic Cartography Algorithms

As described in detail in Chapter 2, the use of graph-cuts to solve discrete energy minimization problems has shown great potential in many applications of image processing and computer vision. Such techniques have been successfully applied in various areas (segmentation, pre-processing, disparity estimation, object detection, and many more) due to the flexibility they allow in formulating tailored energy functions. Results are generally of high quality, which made graph-cuts a popular field of research since the late 90s. We believe these techniques can be used

for many steps of the cystoscopic cartography process, and can outperform many of the existing approaches. The final (but not least important) goal of the thesis is therefore to demonstrate the potential of discrete energy minimization models for difficult image registration problems and for producing high quality panoramic images and textured surfaces. While these algorithms can hardly be implemented at acquisition rate, they should fulfil the third constraint of the previous paragraph, so that the clinician/patient interview after the examination can benefit from a large FOV textured map.

Chapter 2

Graph-Cut Optimization

This chapter presents an overview of discrete energy minimization using graph-cuts, and aims at providing a self contained introduction to the topic. Basic notations used throughout this dissertation will be introduced.

2.1 Discrete Energy Minimization in Computer Vision

Many problems that arise in image processing and computer vision, such as image segmentation (BJ01, BFL06, BRB$^+$04, RKB04), de-noising (BVZ01, Ish09), disparity estimation (BVZ98, KZ01, BVZ01, KZ02, WAB03, LRR08, GHN$^+$10), or photomontage and stitching (KSE$^+$03a, ADA$^+$04, LI07), can be solved using discrete energy minimization techniques. A typical form for such an energy function to be minimized is given in Equation (2.1):

$$E(\mathrm{x}) = \sum_{p \in \mathcal{V}} E_p(x_p) + \sum_{(p,q) \in \mathcal{N}} E_{pq}(x_p, x_q), \tag{2.1}$$

where $\mathrm{x} : \mathcal{V} \to \mathcal{L}$ is a configuration (or *labeling*) that maps every $p \in \mathcal{V}$ to an element $\mathrm{x}(p)$ from a set of labels $\mathcal{L}$, and $\mathcal{N} \subseteq \mathcal{V} \times \mathcal{V}$ is a neighborhood system defined on the set $\mathcal{V}$. To enhance readability, we define $x_p := \mathrm{x}(p)$. Often, an image $I : \mathcal{V} \to \mathbb{R}^m$ maps the set of pixels $\mathcal{V} \subset \mathbb{Z}^2$ defined on a finite grid to $\mathbb{R}^m$ (e.g. $m = 1$ for gray-scale, $m = 3$ for RGB color images), and $\mathcal{N}$ denotes a neighborhood system defined on this grid. The configuration x then corresponds to a certain assignment of labels (e.g. grey-values) to each pixel. In discrete optimization, the set of labels $\mathcal{L}$ is finite, as opposed to continuous optimization, where $\mathcal{L} \subseteq \mathbb{R}$. While algorithms may internally represent $\mathcal{L}$ as a set of (linearly ordered) integer values, each discrete label may map to a real value, or may be associated with a symbolic meaning. For example, in disparity estimation, the labels are displacement vectors in $\mathbb{R}^n$, while for binary segmentation, the set of labels is $\mathcal{L} = \{$"background", "foreground"$\}$.

2.1.1 Order and Interaction

In Equation (2.1), E_p is often referred to as a *unary term*, while E_{pq} is known as a *pairwise term*, due to the number of dependent variables. We say a function $E(\text{x})$ is of order k when it consists of terms with at most $k+1$ interdependent variables. Following this definition, Equation (2.1) is of order 1, or a *first-order* energy function, since it involves at most two dependent variables p and q. In general, a kth-order energy function

$$E(\text{x}) = \sum_{c \in \mathcal{C}} E_c(x_c) \tag{2.2}$$

consists of a set of *cliques* $\mathcal{C}^1$ whose number of variables in each clique c is at most $k+1$, where $x_c = \{x_p \mid \forall p \in c\}$ encodes the configuration of the variables in the clique. Equation (2.1) consists of cliques of size 1 (e.g. the unary terms) and of size 2 (e.g. the pairwise terms). The functions $E_c(x_c)$ are also called *potential functions*. Direct neighbours of a variable p are defined in the set $\mathcal{N}_p$.

In practice, $E_p(x_p)$ often measures a similarity to observed data (i.e. how likely pixel p is to be labeled x_p). Therefore it is often referred to as the *data term*. With $E_{pq}(x_p, x_q)$, one usually models spatial coherence, such as piece-wise smooth disparity fields. Consequently, it is often called *interaction* or *smoothness* term. However, data terms may also be expressed using first- or higher-order potential functions, as will be seen in Chapters 3 and 4.

2.1.2 Markov Random Fields

Energy functions, such as those in Equations (2.1) and (2.2), are closely related to probability distributions of *Markov Random Fields* (Li95). A *random field* $X = [X_1, ..., X_p, ...X_N]$ consists of N random variables, and $X = \text{x}$ is the before mentioned configuration, where every variable may be assigned a value $x_p \in \mathcal{L}$. All possible configurations, given a label set $\mathcal{L}$, are defined as the set $\mathcal{X}$. Each assignment can be associated with a probability $\Pr(X_p = x_p)$, or in short $\Pr(x_p)$. The joint probability for a configuration of the entire random field is then defined as $\Pr(X = \text{x}) = \Pr(\text{x})$. If X is a Markov Random Field, it satisfies the following properties (for a given $\mathcal{N}$):

$$\Pr(\text{x}) > 0, \forall \text{x} \in \mathcal{X} \qquad \text{(Positivity property)}$$
$$\Pr(x_p | \{x_q : q \in \mathcal{N}_p\}) = \Pr(x_p | \{x_q : q \in \mathcal{V} \setminus \{p\}\}) \quad \text{(Markovian property)}$$

Then, according to the Hammersley-Clifford theorem (HC71, Bes74), the joint probability distribution can be written as a Gibbs distribution:

$$\Pr(\text{x}) = \frac{1}{Y} \, e^{-\sum_{c \in \mathcal{C}} E_c(x_c)} \text{ with } Y = \sum_{\text{x} \in \mathcal{X}} e^{-\sum_{c \in \mathcal{C}} E_c(x_c)}$$

---

[1] In graph theory, a clique in an (undirected) graph $\mathcal{G} = (\mathcal{V}, \mathcal{E})$ is a subset of the set of vertices $\mathcal{C} \subseteq \mathcal{V}$, so that every pair of vertices in $\mathcal{C}$ is connected by an edge $e \in \mathcal{E}$. Here, the term clique will be used also informally to group the number of interdependent variables of an energy function.

where Y is known as the partition function. The corresponding Gibbs energy can be obtained from the negative logarithm of its distribution:

$$E_{\text{Gibbs}}(\text{x}) = -\log\left(\Pr(\text{x})\right) = -\log\left(\frac{1}{Y}\right) + \sum_{c\in\mathcal{C}} E_c(x_c) = \text{const} + E(\text{x}).$$

Therefore, the maximum a posteriori solution (i.e. the most probable labeling) x^* of X, given by

$$\text{x}^* = \arg\max_{\text{x}\in\mathcal{L}^N} \Pr(\text{x}),$$

can be found by minimizing $E(\text{x})$.

2.2 Energy Minimization using Graph-Cuts

MRFs as a framework for modelling energy functions such as those of Equation (2.1) have been known to the computer vision community since the seminal work presented in (GG84) in the mid-eighties. At that time however, a lack of efficient optimization techniques impeded a broad use. Deterministic algorithms, such as iterated conditional modes (Bes86) or highest confidence first (CB90), often only converge to poor local minima. A stochastic method like simulated annealing (KGJV83) is theoretically able to obtain the minimum cost solution, but in practice, the temperature decrease process demands great attention to be paid to the algorithm's parameters, which impedes practical use on large datasets. Other used methods include max-product loopy belief propagation (Pea88) and tree-reweighted message passing (WJW02).

In the late nineties, the use of max-flow/min-cut algorithms (FF56, FF62) to solve pairwise MRFs revived the interest of energy minimization for many computer vision problems. They have been shown to outperform other related methods in both quality and speed (see also (SZS$^+$08) for a thorough comparative study of different energy minimization techniques on a set of representative benchmarks). Most of the algorithms developed in this dissertation use this graph-cut framework to minimize energy functions designed for solving the objectives formulated in Chapter 1. Therefore, the following sections are devoted to the introduction of basic formulations. It will be shown how energy functions like that of Equations (2.1) and (2.2) can be expressed in a graph-cut framework and minimized efficiently.

2.2.1 The st-Mincut/ Maxflow Theorem

General Definitions

In graph theory, a *network flow* can be used to model systems in which resources travel from one location to another (Cor01). Examples are traffic along roads, fluids in pipes, or data sent over a
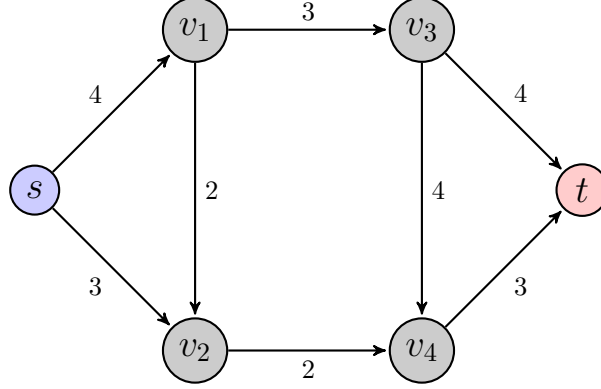
Figure 2.1: Example of a network $\boldsymbol{N}$. $\boldsymbol{V} = \{v_1, v_2, v_3, v_4\}$. Resource may travel from the source vertex s to the sink vertex t. Numbers depict maximum edge capacities.

local area network (LAN). A *network* $\boldsymbol{N}$ is assumed to be a directed graph $\boldsymbol{G} = (\boldsymbol{V} \cup \{s, t\}, \boldsymbol{E}, c)$, consisting of a set of vertices $\boldsymbol{V}$ and a set of edges $\boldsymbol{E} \subseteq \boldsymbol{V} \cup \{s, t\} \times \boldsymbol{V} \cup \{s, t\}$. In addition, a capacity function $c : \boldsymbol{E} \to \mathbb{R}^+$ assigns a non-negative capacity (or weight) to each edge. This weight represents the maximal amount of data that can flow along each edge. Two special vertices have to be distinguished, namely a *source s* and a *sink t*, and we assume that for each $v \in \boldsymbol{V}$, there exists a path $s \rightsquigarrow v \rightsquigarrow t$. Figure 2.1 shows an example of a network.

A flow $f : \boldsymbol{E} \to \mathbb{R}^+$ on a network $\boldsymbol{N}$ assigns each edge a non-negative value $f(u, v)$ that represents the amount of data passing through the edge linking vertices u and v, so that

$$0 \leq f(u, v) \leq c(u, v), \forall (u, v) \in \boldsymbol{E} \text{ (capacity constraint)} \tag{2.3}$$

and

$$\sum_{u \in \boldsymbol{V}|_{(u,v) \in \boldsymbol{E}}} f(u, v) = \sum_{u \in \boldsymbol{V}|_{(v,u) \in \boldsymbol{E}}} f(v, u), \ \forall v \in \boldsymbol{V} \text{ (flow conservation)} \tag{2.4}$$

The value of a flow f_{val} is equal to the total data leaving the source s, which according to Equations (2.3) and (2.4) is in turn equal to the total data entering the sink t, i.e.

$$f_{\text{val}} = \sum_{u \in \boldsymbol{V}, (s,u) \in \boldsymbol{E}} f(s, u) = \sum_{u \in \boldsymbol{V}, (u,t) \in \boldsymbol{E}} f(u, t)$$

Given a network $\boldsymbol{N}$, how does one find the maximum amount of flow $f_{\text{val}}^{\text{max}}$ that can pass through it? For this, we need to introduce the residual capacity c_f of an edge, which is defined as the difference between its capacity and the current flow passing through it:

$$c_f(u, v) = c(u, v) - f(u, v).$$

The residual capacity along a (simple) path p (e.g. $\mathsf{p} = \{s, v1, v3, t\}$) from s to t is then given by

$$c_f(\mathsf{p}) = \min \{c_f(u, v) : (u, v) \in \mathsf{p}\}.$$
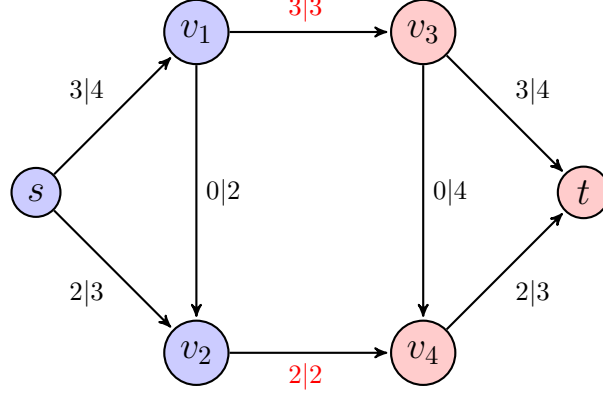
Figure 2.2: Maximum flow of the network shown in Figure 2.1. Edge numbering depict $f(u,v)|c(u,v)$. The bottleneck (red edge numbers) is equivalent to the minimum cut, separating the vertices into $\boldsymbol{S}$ (blue) and $\boldsymbol{T}$ (red). The flow along edges linking the source set with the sink set is equivalent to the amount of flow leaving the source / entering the sink, and equivalent to the maximum flow of the network. Note that the distribution of flow (unlike the maximum flow) is not unique, other valid flows with equal min-cut/max-flow are possible.

If $c_f(\mathsf{p})$ is strictly positive $(c_f(\mathsf{p}) > 0)$, then p is called an augmenting path, and $c_f(\mathsf{p})$ more data could flow along p without voiding Equations (2.3) and (2.4). Consequently, if there exists an augmenting path in $\boldsymbol{N}$, the flow is not maximal. A cut C of $\boldsymbol{N}$, formally

$$C = (\boldsymbol{S}, \boldsymbol{T}), \boldsymbol{S} \cup \boldsymbol{T} = \boldsymbol{V} \cup \{s, t\}, s \in \boldsymbol{S}, t \in \boldsymbol{T}$$

is a partition of the vertices into two disjoint subsets $\boldsymbol{S}$ and $\boldsymbol{T}$, where $\boldsymbol{S}$ is called the *source set*, and $\boldsymbol{T}$ is called the *sink set*. The capacity (or cost) of such a cut C_{val} is the sum of capacities of all edges (u, v) from the source set that are part of the cut:

$$C_{\mathrm{val}} = \sum_{u \in \boldsymbol{S}, v \in \boldsymbol{T}, (u,v) \in \boldsymbol{E}} c(u, v).$$

The cut, for which the capacity is minimal, is called the minimum cut (or st-min-cut). It is intuitive to see in Figure 2.2 that this cut represents the global bottle-neck of the network $\boldsymbol{N}$, and that its capacity $C_{\mathrm{val}}^{\min}$ is equal to the maximum flow $f_{\mathrm{val}}^{\max}$ passing through the network. The next sections will introduce algorithms for solving the st-mincut/maxflow problem.

Mincut/Maxflow Algorithms

Augmenting Path Algorithms

The basic augmenting-path algorithm (FF56, FF62) iteratively pushes flow along augmenting paths until the maximum flow is reached. Initially, there is no flow going from the source to the sink, e.g. $f_{\mathrm{val}} = 0$. In each iteration, the algorithm finds an augmenting path p and pushes $c_f(\mathsf{p})$

more flow through it, thereby saturating it and removing it from the list of augmenting paths. In the original Ford-Fulkerson version (FF56, FF62), augmenting paths are searched using a depth-first strategy. This implies that each path of the graph is explored as far as possible before backtracking. The maximum flow is reached when no augmenting path can be found, which means each path p crosses as least one saturated edge. These saturated edges represent the minimum cut boundary. When edge capacities are integers, the algorithm complexity is bounded by $O(|\boldsymbol{E}| \ f_{\text{val}}^{\max})$ because each augmenting path can be found in at maximum $O(|\boldsymbol{E}|)$ time using depth-first search, and the flow is increased by at least 1 for each augmenting path. For irrational flow values, convergence is not guaranteed (not even convergence towards the maximum flow) (Zwi95).

Improved versions, independently published in (Din70) and (EK72), find shortest paths using a breadth-first search (as opposed to depth-first search in (FF56, FF62)). These methods are guaranteed to converge independently of $f_{\text{val}}^{\max}$. First, all shortest paths of a fixed length l[1] are found and augmented. Then, a new breadth-first search for paths of length $l+1$ using the remaining unsaturated edges are searched from scratch. In this way, theoretical complexity is strongly diminished. Indeed, the worst case complexity of (Din70) is $O(|\boldsymbol{E}| \ |\boldsymbol{V}|^2)$, and $O(|\boldsymbol{E}|^2 \ |\boldsymbol{V}|)$ for (EK72).

Push-Relabel Algorithms

A different approach is used in push-relabel algorithms. These do not maintain a valid flow throughout the computation, since active vertices may have a positive flow excess. Excess flow is then pushed towards active vertices with a smaller distance to the sink. Un-pushable flows are eventually pushed back to the source. The general push-relabel algorithm has a complexity of $(O(|\boldsymbol{V}|^2|\boldsymbol{E}|)$. An implementation of (GT88) has a complexity of $O(|\boldsymbol{V}|^3)$ when using a queue (FIFO) based vertex selection rule, and $O(|\boldsymbol{V}|^2\sqrt{|\boldsymbol{E}|})$ when using a highest active vertex based selection rule.

Boykov-Kolmogorov Algorithm

In practice, the max-flow algorithm proposed by Boykov and Kolmogorov in (BK04) is the most efficient version when applied to dense 2D or 3D graph structures, which are commonly used in computer vision problems. It can be seen as a heuristic variation of the augmenting-path algorithms (FF62, Din70, EK72). Indeed, the difference is that in (BK04), new paths from the source to the sink are not searched from scratch in each iteration, but previously found paths are stored in a search tree structure. This structure contains two search trees, a source tree and a sink tree. These trees contain the vertices associated with each terminal ("labeled vertices"). Vertices not associated with a search tree are called "unlabeled". In addition, a flag for each vertex stores its state (active or passive). Initially, only the source and the sink are labeled and marked as active (i.e. all other vertices are initially unlabeled and marked as passive). The

---

[1]For the breadth-first search, unit length edges are used. The shortest path of length l is therefore a path from s to t that spans l edges.

algorithm then iteratively performs the three stages refered to as "growing stage", "augmenting stage" and "adopting stage". These stages are described in the next paragraphs.

Growing stage. Active vertices add passive and unlabeled neighboring vertices to their search tree if their connecting edge has a residual capacity greater than zero. These newly acquired vertices in turn become active. Once all neighboring vertices and their edges to the current vertex have been evaluated, the current vertex is marked as passive (but retains its label). This step is repeated with the remaining active vertices of the trees until either no more active vertices remain, in which case the algorithm terminates and the st-mincut is found. Or until an active vertex finds an unsaturated edge to a vertex from the other search tree, which means a that an augmenting path p from the source to the sink is found.

Augmenting stage. If an augmenting path p was found in the previous stage, it is augmented by increasing the flow by $c_f(p)$ along all of its edges, similar as in (FF62). In this stage however, the search trees may transform into forests (i.e. a vertex can become the root of a new tree). A new tree maybe be generated, since at least one saturated edge is created during the augmenting step. If such a saturated edge lies between a vertex and its associated vertex terminal, the former cannot be reached from the the terminal vertex, according to the search tree criteria allowing only unsaturated edges.

Adopting stage. In this stage, the search trees are rebuilt. For each *orphan* (a labeled vertex that can be reached from its associated terminal only through saturated edges after the augmenting stage), new parents are searched. If through an edge to a neighboring vertex, an unsaturated path to the same terminal can be found, this vertex becomes the new parent in the search tree. If no parent can be found, the vertex is marked as unlabeled, and its *children* are marked as orphans. These steps are repeated until no orphans are left.

An illustration of the different steps of the Boykov-Kolmogorov maxflow algorithm is shown in Figure 2.3. In the initial stage (Figure 2.3a), only s and t are active (blue and red indicates active vertices of the source/sink trees. Light blue and red vertices are passive vertices of their tree, white vertices are unlabeled. Red edges are saturated and cannot be used in search trees). In the following growing stage (starting with the source tree, see Figure 2.3b), s finds in p and q passive, unlabeled vertices, and adds them to its search tree. Then s becomes passive. The next step is the growing stage from the sink tree (Figure 2.3c). t finds in p a vertex from the opposite search tree. This starts the augmenting stage, where the path $\{s, p, t\}$ is augmented by the bottleneck residual capacity 1. In the following adoption stage, no orphan vertex is found, as p is still connected to its terminal through an unsaturated edge. Then the growing stage of the sink tree is continued (t had not explored all of his neighbors yet), and t finds in q another vertex from the opposite search tree. In the augmenting stage (Figure 2.3d), the path $\{s, q, t\}$ is augmented by 1. At the adoption stage, q is now an orphan, but through p, an
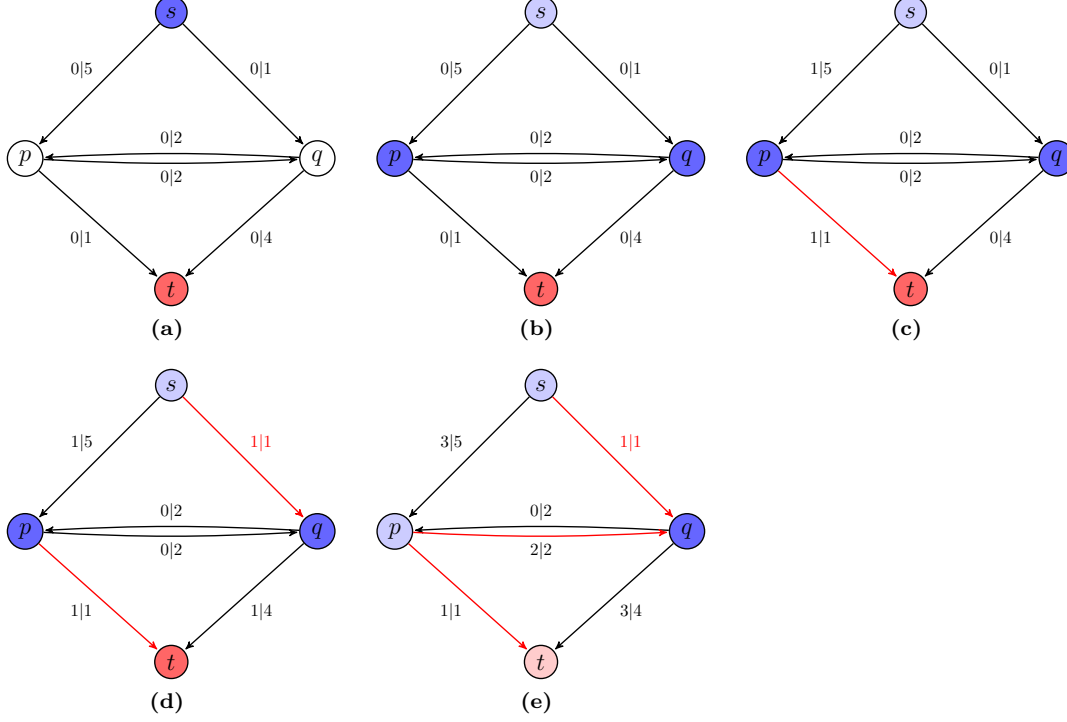
Figure 2.3: Boykov-Kolmogorov max-flow algorithm. (a) Initial stage. Only s and t are active (blue and red indicates active vertices of the source/sink trees. Light blue and red vertices are passive vertices of their tree, white vertices are unlabeled. Red edges are saturated and cannot be used in search trees). (b) Growing stage (source tree): s finds in p and q passive, unlabeled vertices, and adds them to its search tree. Then s becomes passive. (c) Growing stage (sink tree): t finds in p a vertex from the opposite search tree. This starts the augmenting stage, where the path $\{s, p, t\}$ is augmented by the bottleneck residual capacity 1. In the following adoption stage, no orphan vertex is found. (d) Growing stage (sink tree): t finds in q another vertex from the opposite search tree. In the augmenting stage, the path $\{s, q, t\}$ is augmented by 1. At the adoption stage, q is now an orphan, but through p, an existing unsaturated path to s exists. (e) Growing stage (source tree): from p, no unlabeled vertex can be found, so it becomes passive. q finds in t a vertex from the opposite search tree, so the path $\{s, p, q, t\}$ is augmented by 2. In the adoption stage, q is again an orphan, but no unsaturated path to s can be found. Therefore, q becomes unlabeled. No active vertices remain, and the algorithm terminates. The saturated edges from $\boldsymbol{S}$ to $\boldsymbol{T}$ depict the minimum cut of the network, and its cost is equal to the maximum flow.

existing unsaturated path to s is found. Then, in the growing stage of the source tree, from p, no unlabeled vertex can be found, so p becomes passive. q finds in t a vertex from the opposite search tree, so the path $\{s, p, q, t\}$ is augmented by 2. In the adoption stage, q is again an orphan, but no unsaturated path to s can be found. Therefore, q becomes unlabeled. No active vertices remain, and the algorithm terminates. The saturated edges from $\boldsymbol{S}$ to $\boldsymbol{T}$ depict the minimum cut of the network, and its cost is equal to the maximum flow.

There exists no polynomial upper bound for the algorithm of (BK04), and a trivial upper

bound is $O(|\boldsymbol{E}||\boldsymbol{V}|^2|f_{\max}|)$, because augmenting paths found are not necessary shortest paths. This means, in theory, the algorithm complexity is worse than augmenting paths or push-relabel algorithms. However, exhaustive tests on several typical vision graphs (2D and 3D grids) showed that it outperformed the methods of (Din70) and (GT88) by 2-5 times. The implementation of (BK04) is by far the most widely used software for computer vision related applications dealing with maximum flow problems. Recently in (JSH12), the Boykov-Kolmogorov algorithm was implemented in a cache-friendly manner for grid-like graph structures to reduce memory bandwidth bottlenecks.

2.2.2 Graph-Cut Examples for Two-Label Problems

This section will show how the concept of network flows and the st-mincut/maxflow theorem can be applied to two image processing problems - binary image de-noising and binary image segmentation. Both applications have in common that their result is of binary nature. If we can express these problems in terms of energy minimization, as given by Equation (2.1) with $x : \mathcal{V} \to \{0, 1\}$, then these energies can be minimized using st-mincut algorithms, and this minimum corresponds to the most probable binary labeling in an MRF.

Binary Image Restoration

Consider the application of de-noising the binary image $I : \mathcal{V} \to \{0, 1\}$, as shown in Figure 2.4a, which is suffering from salt and pepper noise. Ideally, we want to preserve the object and background structures (i.e. remove pepper inside the object, and salt in the background).

If we assume that the noise-free image is similar to the observed one, we can formulate the data (unary) term for a given pixel as

$$E_p(x_p) = |I(p) - x_p|.$$

If this was not the case, i.e. the restored values must not be similar to the observed noisy observation, then there is little chance of restoring the image. Of course, minimizing only this energy does not require any optimization framework, as its minimum is the noisy input I itself. In order to remove the noise, some sort of regularization (smoothness) is needed. Assuming (as before) that a sufficient number of pixels is noise-free, we can suppress outliers (noisy pixels) by minimizing the following energy:

$$E_{pq}(x_p, x_q) = |x_p - x_q|,$$

This assumes that neighboring (noise-free) pixels most probably have the same intensity. Putting both terms together and applying them to the entire image domain using the 8-connectivity neighborhood system $\mathcal{N}^8$, we get the energy function

$$E(\mathrm{x}) = \sum_{p \in \mathcal{V}} E_p(x_p) + \lambda \sum_{(p,q) \in \mathcal{N}^8} E_{pq}(x_p, x_q), \tag{2.5}$$
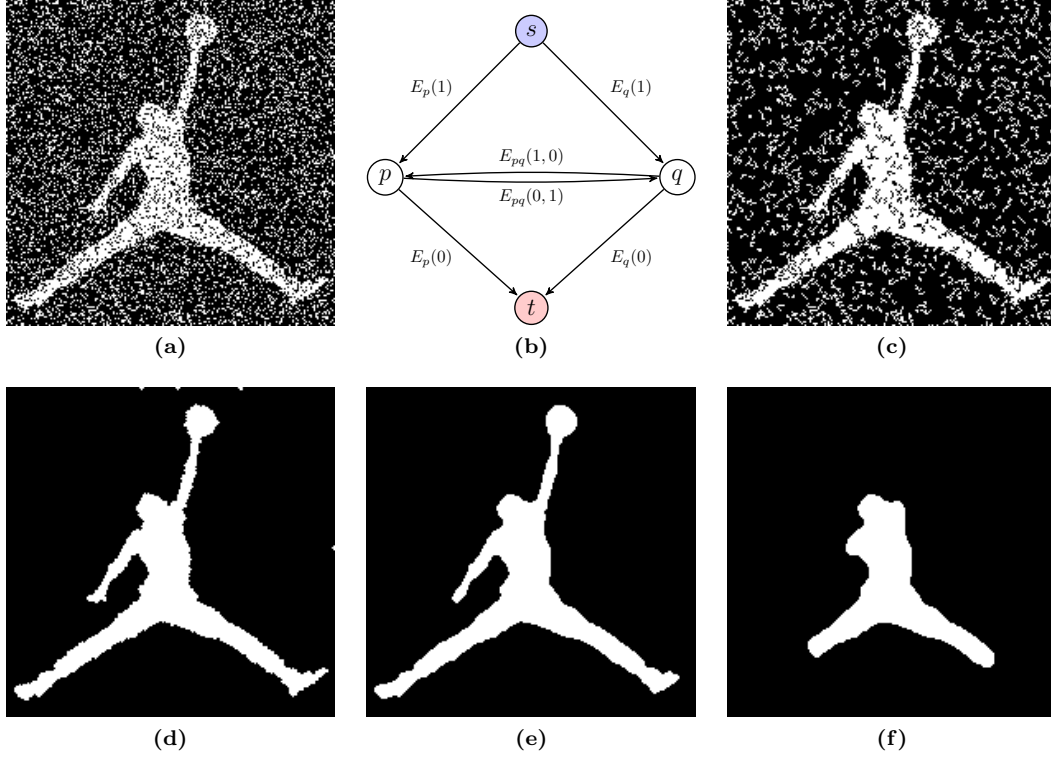
Figure 2.4: Binary image denoising using st-mincuts. (a) Input image suffering from salt and pepper noise, affecting ≈ 40% of the pixels. (b) St-mincut graph construction. (c)-(f) Obtained results using $\lambda = \{0.15, 0.3, 0.6, 1.2\}$. Higher regularization leads to smoother, but shrinking object boundaries.

which will be minimized. The parameter λ weights the relative importance between regularization and data terms (generally more noise requires higher λ). Assembling the energy costs into an st-mincut solvable graph is straightforward. For each pixel $p \in \mathcal{V}$, we add a vertex[1] to the graph $\boldsymbol{G}$. We associate the source vertex with background, the sink vertex with foreground, and add the capacities $c(s, p) = E_p(1)$ and $c(p, t) = E_p(0)$ to the edges connecting each pixel p with both terminal vertices. If, after an st-mincut, a vertex is in the source set, we label the corresponding pixel as "background", else as "foreground". Regularization is incorporated by adding two directed edges (p, q) and (q, p) with capacities equal to λ (equivalent to an undirected edge) between each pair of pixels in an 8-neighborhood configuration. The graph structure for two neighboring pixels is shown in Figure 2.4b. If we recall, that the cost C_{val} of an st-cut is equal to the sum of capacities of all edges going from the source set to the sink set, it is obvious to see that the cost of each possible st-cut is equal to the corresponding energy cost of Equation (2.5). Figures 2.4b-e show the labelings corresponding to the energy

---

[1]For simplicity, the words vertex and pixels are used interchangeably here.

minimum with different regularization weights. Higher regularization leads to smoother object boundaries, but shrinking can also be observed with high values of λ.

Binary Image Segmentation

As with the example shown in the previous section, the problem of segmenting an image into foreground and background can equally be computed optimally using st-mincuts. The image $I : \mathcal{V} \rightarrow \{0, ..., 255\}$ to be segmented is shown in Figure 2.5a, where the object/foreground corresponds to dark pixel intensities, while the background corresponds to brighter pixel intensities. Using a global and constant threshold t_{otsu} (computed using Otsu's method (Ots75)) leads to unsatisfactory object/background segmentation, as shown in Figure 2.5b. The same segmentation can also be computed via energy minimization:

$$E^{\mathrm{otsu}}(\mathrm{x}) = \sum_{p \in \mathcal{V}} E_p^{\mathrm{otsu}}(x_p) \tag{2.6}$$

$$E_p^{\mathrm{otsu}}(x_p) = (-1)^{x_p}(I(p) - t_{\mathrm{otsu}}) + \max(I). \tag{2.7}$$

Adding the constant offset $\max(I)$ (maximal observed intensity in I) in Equation (2.7) ensures strictly positive edge capacities. As before, minimizing Equation (2.6) is straightforward. The result can be improved with the aid of regularization

$$E_{pq}^{\mathrm{reg}}(x_p, x_q) = \omega_{p,q} \, T(x_p \neq x_q)$$
$$\omega_{p,q} = \exp\left(1 - \frac{|I(p) - I(q)|}{\sigma}\right),$$

where $T(\cdot)$ is an indicator function, equal to 1 if its argument is true, and 0 otherwise. This ensures that only neighboring pixels that have been assigned different labels will add $\omega_{p,q}$ to the total energy of the segmentation. The use of indicator functions is often observed in graph-cut based segmentation algorithms. The parameter $\sigma = 20$ ensures that small intensity differences, which are not assumed to be a part of the object boundaries, have a very small impact on the regularization term. The energy function to be minimized thus becomes

$$E^{\mathrm{otsu + reg}}(\mathrm{x}) = \sum_{p \in \mathcal{V}} E_p^{\mathrm{otsu}}(x_p) + \lambda \sum_{(p,q) \in \mathcal{N}^8} E_{pq}^{\mathrm{reg}}(x_p, x_q).$$

The st-mincut solvable graph structure is the same as that of the previous section (i.e. that of Figure 2.4b). Data terms compute the capacities of edges to the terminal vertices. Capacities between neighboring pixels p and q will be set to $c(p,q) = c(q,p) = \lambda \, \omega_{pq}$[1], now varying with the underlying observed intensities (e.g. small at image gradients, high in constant regions).

---

[1] As before, this is de-facto equivalent to using an undirected graph. By using different capacities for the edges (p,q) and (q,p), it is possible to extend the segmentation model. For instance, if the object is known to be brighter or darker than the background, this knowledge can be incorporated as a hard constraint (BFL06) by setting edges oriented from the source set to the sink set to infinity for unwanted pixel intensity combinations. Other possibilities are star-shape priors (Vek08), or adding balloon forces to overcome the shrinking bias observed in Figure 2.4d.
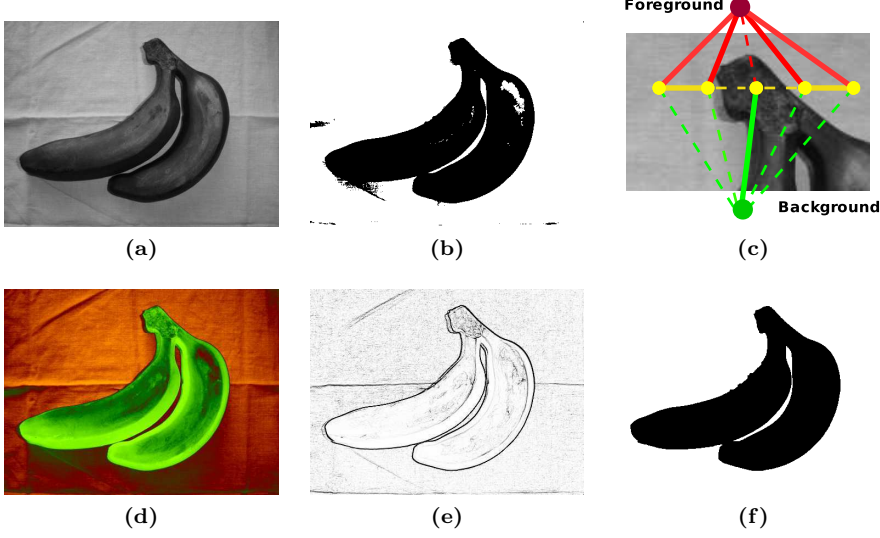
Figure 2.5: An example of binary image segmentation using graph-cuts. (a) Input image. (b) Result using $\lambda = 0$, which is equivalent to the basic thresholding operation, insufficient to separate object from background. (c) Exemplary graph setup. Red and green edges depict costs for assigning foreground and background, respectively. Yellow edges depict pairwise costs. Edge thickness is proportional to their capacity. Dashed edges corresponds to the minimum cut, separating the object from its background. (d) Data terms visualized for the entire image, same colors as in c). Intensity is proportional to the capacity. (e) Pairwise terms visualized. Dark intensity corresponds to low pairwise costs. (f) Segmentation obtained with $\lambda = 1$.

An exemplary 1-dimensional graph construction is shown in Figure 2.5c. Red and green edges correspond to data terms, while yellow edges correspond to regularization terms. The thickness of the edges is proportional to their capacities. The st-mincut for this graph is indicated with dashed lines, seperating the object from its background. Data costs for the entire image are shown in Figure 2.5d (same color as in Figure 2.5c, intensity is proportional to the capacities), while potential pairwise costs are shown Figure 2.5e (intensity is proportional to the capacity). Using $\lambda = 1$, the object can be satisfyingly separated from its background, as can be seen in Figure 2.5f.

2.2.3 Submodular and Non-Submodular Energy Functions

In the previous sections, it was shown how energy minimization problems with functions of binary labels can be transformed into a flow network and solved via st-mincuts. Before we can proceed to energy functions with more than two labels (e.g $\mathcal{L} = \{l_1, ..., l_k\}, k > 2$), we need to provide a general-purpose graph construction and define which kind of energy functions it can minimize. Solving a kth-order function of discrete variables is in general NP-hard (BVZ01, BKR11). However, there are certain subclasses that can be solved in polynomial time.
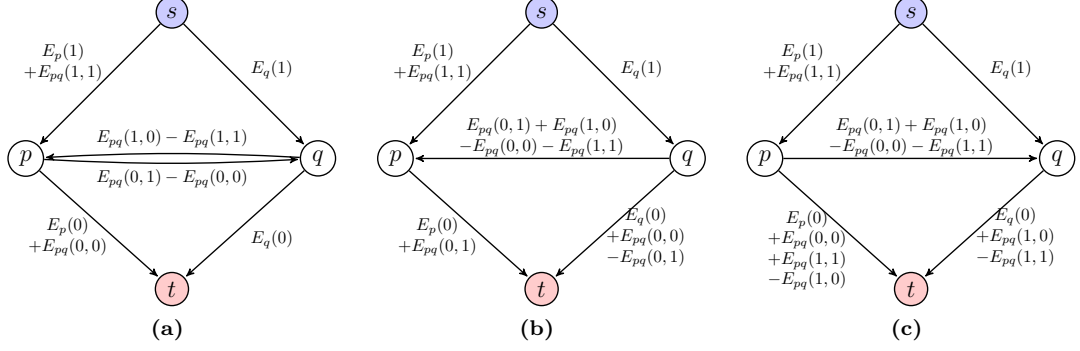
Figure 2.6: General first order st-mincut graph construction for a two variable energy function, as given by Equation (2.1), which satisfies the submodularity constraint of Equation (2.8). In order to have edge capacities ≥ 0, three different constructions are necessary. (a) Graph construction for the case $E_{pq}(0,1) - E_{pq}(0,0) \geq 0$ and $E_{pq}(1,0) - E_{pq}(1,1) \geq 0$. (b) Graph construction for the case $E_{pq}(0,1) - E_{pq}(0,0) < 0$. (c) Graph construction for the case $E_{pq}(1,0) - E_{pq}(1,1) < 0$. It is easy to check that the cost of any st-cut is equal to the energy of the corresponding label assignments.

Submodular functions are an example for such a subclass, and they can be seen as the analogy of convex functions in continuous optimization. As was shown in Section 2.2.1, in order to find the st-mincut of a network $\boldsymbol{N}$, all edges in the graph must have non-negative weights. This restricts the class of energy functions that can be solved. Consider again the case of a first-order energy function $E(\mathrm{x})$, with x : $\mathcal{V} \rightarrow \{0,1\}$, e.g. $E(\mathrm{x})$ is a function of binary variables, or a *quadratic pseudo boolean function* (QPBF). Quadratic here corresponds to the order $k = 1$, and pseudo boolean indicates that the function's variables are binary, but the energy it returns is real valued. This function is *graph-representable* (or submodular) if and only if for all $(p,q) \in \mathcal{N}$ the inequality

$$E_{pq}(0,0) + E_{pq}(1,1) \leq E_{pq}(0,1) + E_{pq}(1,0) \tag{2.8}$$

holds. Such functions are also called *regular*. Note that unary terms are always regular[1]. The construction of a graph for a two-variable submodular QPBF is given in Figure 2.6. Different constructions are necessary in order to ensure edge capacities ≥ 0. Multiple energies are merged into single edges by adding their costs. In the previous two examples, $E_{pq}(0,0) = E_{pq}(1,1) = 0$, so submodularity was ensured, and the graph construction was equal to that of Figure 2.6a.

However, in many computer vision problems, Equation (2.8) does not hold. This is also the case for the registration and map compositing problems presented in the next chapters. To take such a situation into account, one strategy, as applied in (KSE+03b, ADA+04, RKKB05), is to truncate non-submodular terms, i.e. by replacing each pairwise term violating Equation (2.8) with a submodular approximation that satisfies Equation (2.8). In these applications (KSE+03b, ADA+04, RKKB05), this approach gives acceptable results, mainly because the

---

[1]The only restriction is given by $E_p(x_p) \geq 0, \forall p \in \mathcal{V}$, but this can easily be ensured.

number of non-submodular terms is small and the energy function is not changed significantly by the truncation. In Section 2.3.1, an example for a truncation scheme will be given. However, when non-submodular terms become more dominant, truncation alters the energy function drastically, and results decrease in quality accordingly (CG06).

More recently in (KR07), built upon a work from (BH02), it was shown that non-submodular energy functions can still be *partially* minimized using graph-cuts. The output of this algorithm, which we will refer to as BHS[1], is a *partial* labeling x : $\mathcal{V} \rightarrow \{0, 1, \emptyset\}$, where $x_p = \emptyset$ means the optimal label cannot be computed (x_p is "unlabeled"). In all other cases, i.e. where $x_p = \{0, 1\}$, the resulting label for p is guaranteed to be a *part* of the global minimum (*partial optimality*). The *persistence property* ensures that the energy of the partial labeling does not increase (more on that in Section 2.3.1). The BHS algorithm works by transforming the energy into a so called *normal form* using re-parametrization of the original energy function. This re-parametrization scheme can be found in (KR07). The number of "unlabeled" variables is strongly related to the number of non-submodular terms in the energy function. This number is small in many applications (often less than 1%). The reason for this is that the cost of assigning neighboring variables (p, q) the same label (e.g. $x_p = x_q$) should (on average) be much smaller than assigning different labels ($x_p \neq x_q$). For instance, for the functions of binary variables illustrated in Section 2.2.2, there are no submodular terms possible, as $E_{pq}(0, 0) = E_{pq}(1, 1) = 0$. We will come back to this issue in Section 2.3. Finally, certain search heuristics can be used to further label unlabeled pixels (BHT06, RKLS07, WTRF08).

2.2.4 Higher-Order Energy Functions

So far, it was explained how general first-order (non-)submodular quadratic pseudo boolean energy functions of up to two variables in each term (see Equation (2.1)), can be transformed into a flow network and minimized using graph-cuts. Now consider a function of binary variables with individual terms of three variables:

$$E(\mathrm{x}) = \sum_{(p,q,r) \in \mathcal{C}} E_{pqr}(x_p, x_q, x_r). \tag{2.9}$$

Equation (2.9) is of order 2, and clearly, terms of three variables cannot be expressed directly in a flow network, as defined in Section 2.2.3. In (KZ04), it was first shown how to construct a graph for such energy functions using *auxiliary* vertices. For each second-order term, one auxiliary vertex a is added to the graph $\boldsymbol{G}$, as shown in Figure 2.7, which depicts one of two possibilities to construct st-mincut-solvable graphs of a second-order pseudo boolean energy function. As with the first-order graph construction shown in Figure 2.6, the actual graph capacities depend on the energy function. A second construction that must be distinguished is

---

[1]This algorithm is often referred to as Quadratic Pseudo Boolean Optimization (QPBO). This, as suggested in (BKR11), is however misleading, as the problem itself is already called QPBO. We therefore refer to the algorithm by BHS, wich are the initials of the original authors.

omitted and can be found in (KZ04). The graph construction of Figure 2.7 requires the energy function to be submodular, and in the case of second-order energy functions, this requirement is fulfilled if all its projections on two variables are submodular. A projection of a function on n variables means fixing all but n of its variables. For instance, the projection

$$E_{pq}^{'x_r=1}(x_p, x_q) = E_{pqr}(x_p, x_q, 1)$$

fixes the variable $x_r = 1$, and this projection can now be examined for submodularity (Equation (2.8)). A second-order energy function E_{pqr} has six projections on two variables (three binary variables that can take two values each). The edge capacities of the graph construction in Figure 2.7 are based on mappings of all possible combinations of a pseudo-boolean function to real numbers. This mapping is defined in (KZ04) as

$$\pi(E_{1...n}) = \sum_{x_1 \in \{0,1\},...,x_n \in \{0,1\}} \prod_{i=1}^{n} (-1)^{x_i} E_{1...n}(x_1, ..., x_n).$$

For instance, the capacities of the edges connecting p, q and r with a (and a with t) correspond to the mapping of the full second-order energy function $E_{pqr}(x_p, x_r, x_r)$:

$$\pi(E_{pqr}) = \begin{array}{l} E_{pqr}(0,0,0) - E_{pqr}(0,0,1) - E_{pqr}(0,1,0) + E_{pqr}(0,1,1) \\ - E_{pqr}(1,0,0) + E_{pqr}(1,0,1) + E_{pqr}(1,1,0) - E_{pqr}(1,1,1) \end{array}.$$

Similarly, the edge capacity between p and q correspond to $-\pi(E_{pq}^{'x_r=0})$.

The technique presented in (KZ04) is one possibility of reduction of a second-order binary function to its equivalent pairwise form (i.e. with the same energy minimum). In general, any higher-order pseudo boolean energy function can be reduced to an equivalent first-order form (BHS91, BH02), and several strategies have been proposed. For instance, in (FD05) a strategy referred to as *reduction by minimum selection* is used. On the other hand, *reduction by substitution* was employed in (AFG08). The most commonly used technique, as published in (Ish09, Ish10), is also based on the minimum selection scheme, as reduction by substitution leads to a very large percentage of non-submodular terms. Recently, in (GBP11), the reduction of a kth order pseudo boolean function to its equivalent first-order form was formulated as an optimization problem itself, which allows to select the best reduction method for each term. This allows to minimize the number of non-submodular terms in the reduced pairwise form.
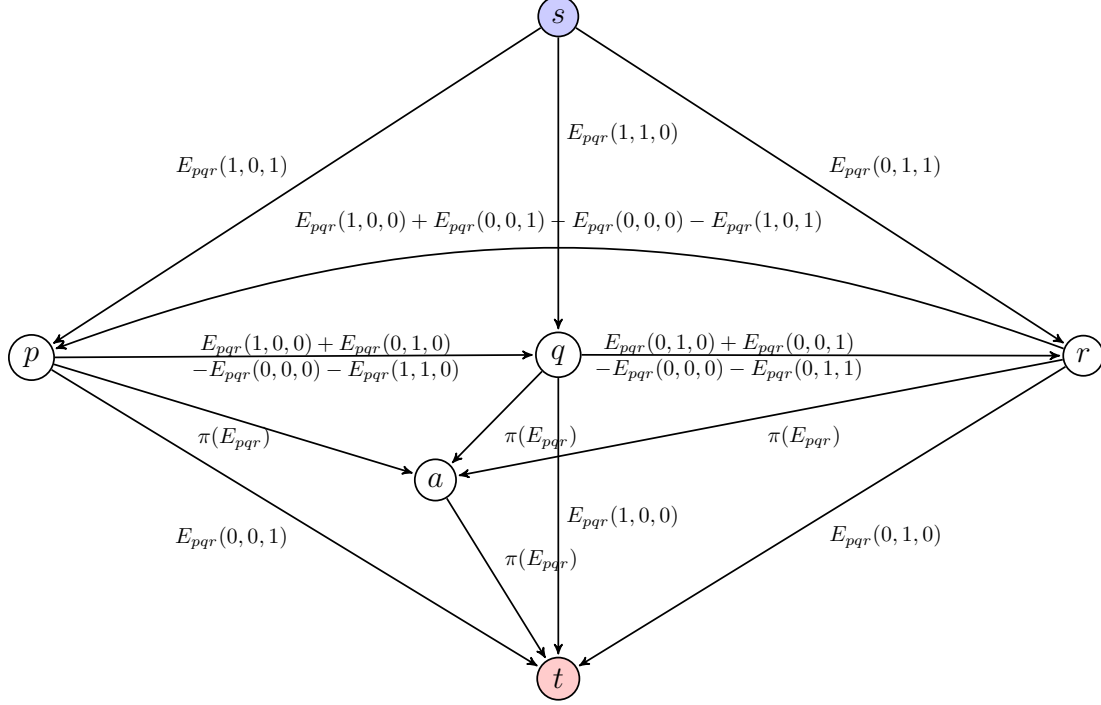
Figure 2.7: General second order graph construction for the case $\pi(E_{pqr}) \geq 0$. In addition to the cost of an st-mincut, a constant energy $E_{pqr}^{\text{const}} = E_{pqr}(1,1,1) - E_{pqr}(0,1,1) - E_{pqr}(1,0,1) - E_{pqr}(1,1,0)$ must be added in order to obtain the correct energy for a given st-mincut labeling. Similar as in Figure 2.6, there exists a second construction method for the case $\pi(E_{pqr}) < 0$. The reader is referred to (KZ04) for this construction. More details are found in the text.

2.3 Graph-Cuts for Multi-Label Problems

Minimizing energy functions of non-binary variables, i.e. $\mathcal{L} = \{l_1, ..., l_k\}, k > 2$, using graph-cuts can be divided into two groups, namely transformation methods and move-making algorithms (BKR11). On one hand, transformation methods transform the energy function into one that uses a set of boolean variables for each "multi-state" variable x_p, where a certain assignment of this boolean set represents the assignment of a label in $\mathcal{L}$. For certain subclasses of discrete energy functions, such as first-order submodular functions, the global energy minimum can be found in polynomial time. Move-making algorithms on the other hand decompose the minimization problem into a sequence of binary-valued problems, which can be solved efficiently using st-mincut algorithms. Although global minima can not be guaranteed, most publications use move-making algorithms to minimize their energy functions, as the classes of functions that can be minimized using transformation methods are restricted and transformation methods require a large amount of computer memory. As will be seen in Section 2.3.3, move-making algorithms are better suited than transformation methods for solving the problems of Chap-

ter 3 and 4. For this reason, we will detail move-making algorithms in this section, whereas the principle of transformation methods is only given briefly at the end of this section.

2.3.1 Move-Making Algorithms

Introduced in (BVZ01), the alpha-expansion and the alpha-beta swap are two popular approaches for solving labeling problems $x : \mathcal{V} \rightarrow \mathcal{L}$, where the set of possible labels $\mathcal{L}$ $(|\mathcal{L}| > 2)$ is finite. Finding optimal discrete labelings belongs in the field of combinatorial optimization, as the set of all possible solutions is countable. Such an approach is in general not a limitation, as $\mathcal{L}$ can be made arbitrarily large to encode the necessary numerical accuracy, or altered during the optimization. The computation however increases at least linearly with the size of the label set $|\mathcal{L}|$. For submodular energy functions, move-making algorithms converge to *strong* local minima[1] in polynomial time.

Alpha-Expansion

Starting with an initial solution x^0 (for example, the observed noisy image), the alpha-expansion works by iteratively computing a binary min-cut over all possible labels in $\mathcal{L}$. In each iteration, an *expansion-move* for a label α increases (expands) the set of pixel that are given this label in the current solution x^c:

$$x_p \leftarrow \left\{ \begin{array}{ll} \alpha & \text{if } x_p^c = \alpha \\ \alpha \text{ or } x_p^c & \text{otherwise.} \end{array} \right.$$

One cycle of alpha-expansion iterates over all $\alpha \in \mathcal{L}$. The algorithm usually converges after two cycles (no expansion-move, for any label $\alpha \in \mathcal{L}$, can further decrease the energy $E(x)$), but only minor changes occur after the first cycle. It is easy to see that each expansion-move can be computed with an st-mincut, by associating one of the terminal vertices with the current solution x^c, and the other terminal vertex with label α. Figure 2.8a shows the unary term setup for one alpha-expansion move. Pairwise (or reduced higher-order) costs are merged into the graph structure according to the criteria illustrated in Figures 2.6 and 2.7. Initially in (BVZ01) it was shown that the alpha-expansion can be applied to energy functions where E_{pq} is a metric. It was later shown (KZ04) that it can be applied if for all labels α, β, γ and pairs (p, q) the inequality

$$E_{pq}(\alpha, \alpha) + E_{pq}(\beta, \gamma) \leq E_{pq}(\alpha, \gamma) + E_{pq}(\beta, \alpha) \tag{2.10}$$

holds. In this case, the energy function is said to be submodular with regard to alpha-expansion. Equation (2.10) is the triangle inequality if, for all α, $E_{pq}(\alpha, \alpha) = 0$. In (BVZ01), it was shown that the strong local minimum obtained using alpha-expansions is within a known factor of the global minimum. Let c be the ratio of the largest non-zero value of E_{pq} to the smallest non-zero value of E_{pq} for all labels in $\mathcal{L}$ and pairs (p, q), i.e.

---

[1] A strong local minimum is much lower than the theoretical upper bound, and often equal to the global minimum, although this cannot be theoretically justified.

$$c = \max_{(p,q) \in \mathcal{N}} \left(\frac{\max_{\alpha \neq \beta \in \mathcal{L}} E_{pq}(\alpha, \beta)}{\min_{\alpha \neq \beta \in \mathcal{L}} E_{pq}(\alpha, \beta)} \right),$$

and $\hat{x}$ be the local minimum obtained with alpha-expansion, and x^* be the global minimum. Then it can be shown that $E(\hat{x}) \leq 2cE(x^*)$. In practice however, the energy is generally much closer to the global minimum, often even reaching it exactly (see also Section 2.3.3) as long as all terms are submodular.

If some of the terms in the energy function are non-submodular with respect to Equation (2.10), the energy can either be truncated in such a way that the energy is guaranteed not to increase (RKKB05), for example by replacing each $E_{pq}(x_p, x_q)$ with

$$E'_{pq}(x_p, x_q) = \min \left\{ E_{pq}(x_p, x_q), E_{pq}(\alpha, x_q) + E_{pq}(x_p, \alpha) - E_{pq}(\alpha, \alpha) \right\}.$$

Alternatively, or if the energy function contains a sufficiently large number of non-submodular terms, resulting in a strong alteration of the original energy function using truncation, the BHS algorithm can be used. If the unlabeled variables keep their current label, the *persistence property* of the BHS algorithm guarantees that the energy does not increase, i.e. $E(\mathrm{x}) \leq E(\mathrm{x}^c)$ and $E(\mathrm{x}) \leq E(\mathrm{x}^p)$. Therefore, if enough variables get labeled in each expansion-move, the solution will still be driven towards a strong local minimum. We will give an example shortly on the example of the fusion-move.

Alpha-Beta-Swap

The alpha-beta-swap algorithm also starts with an initial solution x^0, and iteratively computes *swap-moves* over all possible pairs of labels in $\mathcal{L}$. A swap-move allows the subset of variables currently assigned the label α to switch to label β, and vice-versa (see also Figure 2.8b):

$$x_p \leftarrow \begin{cases} \alpha \text{ or } \beta & \text{if } x_p^c = \alpha \text{ or } x_p^c = \beta \\ x_p^c & \text{otherwise.} \end{cases}$$

An alpha-beta-swap cycle iterates over all possible pairs of labels $\alpha, \beta \in \mathcal{L}$. The algorithm converges when no swap-move can further decrease the energy. An energy is submodular with regard to alpha-beta-swaps when, for all labels α, β and pairs (p, q), the following constraint holds

$$E_{pq}(\alpha, \alpha) + E_{pq}(\beta, \beta) \leq E_{pq}(\alpha, \beta) + E_{pq}(\beta, \alpha).$$

This constraint is less restrictive than with alpha-expansions (it corresponds to the special case of $\beta = \gamma$ of Equation (2.10)), but more moves need to be computed ($|\mathcal{L}|^2$ instead of only $|\mathcal{L}|$ with alpha-expansion). As with the alpha-expansion, non-submodular energies can either be truncated or still be efficiently minimized if a sufficiently large number of variables get labeled in each swap-move when using the BHS algorithm.
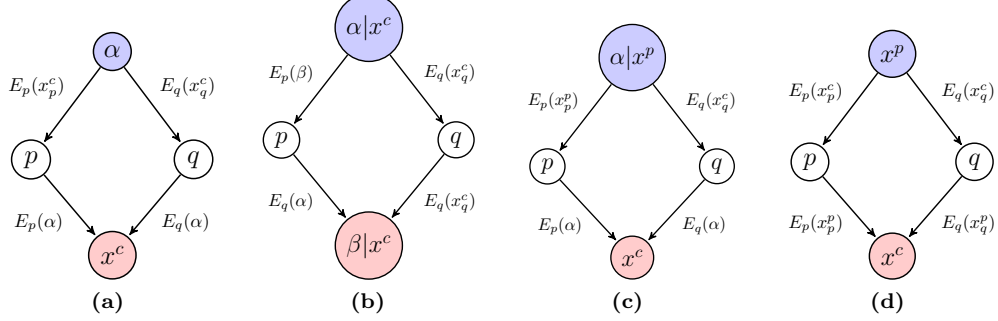
Figure 2.8: Graph construction (unary terms only) for different move-making algorithms. Pairwise terms are setup according to the criteria defined in Figure 2.6. (a) Alpha-Expansion. Any variable can either keep its current label, or switch to α. (b) Alpha-Beta-Swap. Any variable currently labeled either as α or β, can switch. Variables labeled $\neq \alpha, \beta$ must retain their current label, but they must stay in the graph for the pairwise terms. (c) Alpha-Expansion-Contraction. Variables currently labeled as α can keep their label, or switch to the label of the proposition x^p. All other variables may keep their current label, or switch to α. The Alpha-Expansion-Beta-Shrink algorithm is a special case of the Alpha-Expansion-Contradiction algorithm, where the proposition x^p is equal to β everywhere. (d) Fusion-Move. The most general move-making algorithm. Each variable p can either retain its current label x_p^c, or switch to the label x_p^p of the proposition.

Alpha-Expansion-Contraction and Beta-Shrink

Recently, two methods that generalize alpha-expansion for multi-label energy minimization problems were proposed. First, in (SA11), the authors introduce the *alpha-expansion-beta-shrink-move*. As with a standard alpha-expansion move, any variable may keep its current label, or switch to α. In addition however, variables currently assigned the label α may also "shrink" to the label β:

$$x_p \leftarrow \begin{cases} \alpha \text{ or } \beta & \text{if } x_p^c = \alpha \\ \alpha \text{ or } x_p^c & \text{otherwise.} \end{cases}$$

It is argued in (SA11) that these moves *dominate* both alpha-expansion and alpha-beta-swap in a sense that more (or equal, but not less) variables may change in one move, possibly leading to lower energies and faster convergence rate. At the same time, they require no additional constraints on the energy function (only the submodularity constraint of Equation (2.8) must be satisfied). Depending on the application, β can be chosen in either random or heuristic fashion for each move, resulting in the same number of moves than with alpha-expansions. Alternatively, β can also be iterated over all labels for each α, resulting in the same number of moves than with alpha-beta-swaps.

The method proposed in (WPM⁺12), called *alpha-expansion-contradiction*, is a generalization of the alpha-expansion-beta-shrink-move. Instead of allowing the variables assigned the label α to shrink to the label β, they may now "contract" to arbitrary labels of a proposition x^p:

$$x_p \leftarrow \begin{cases} \alpha \text{ or } x_p^p & \text{if } x_p^c = \alpha \text{ (contradiction)} \\ \alpha \text{ or } x_p^c & \text{otherwise (alpha-expansion).} \end{cases}$$

This allows more flexibility than using a constant β. For instance, x_p^p can be chosen from the lowest unary costs for each variable, which intuitively performs best when observations are not very noisy or when the regularization (pairwise terms) is low relative to the unary costs. On the other hand, either constant propositions x^p (same β everywhere) or smoothly varying x^p may perform better if regularization ratio is high or the expected result is piecewise smooth. Figure 2.8c illustrates the unary term graph setup for alpha-expansion-contradiction. Alpha-expansion-beta-shrink is obtained by simply substituting x_p^p with β for each variable p.

Fusion-Move

The move-making algorithms explained in the previous sections work by proposing constant solutions at each iteration. An exception is (WPM$^+$12), which proposes arbitrary labels for each variable labeled α. These methods generally perform well in a broad range of applications, and will finish in a deterministic number of moves (e.g. in a multitude of $|\mathcal{L}|$ moves for alpha-expansion). However, these constant propositions are less suitable when the expected energy minimum is not composed of piecewise constant (e.g. multi-label segmentation, frontal baseline stereo) or piecewise smooth (e.g. small displacement optical flow, denoising) labelings. This can be justified using Equation (2.8) - as long as assigning the same labels leads to lower energies than assigning different labels, proposing constant labelings will result in many submodular terms. When the energy minimum corresponds to mostly non-smooth/non-constant labelings (e.g. large displacement stereo/optical flow with many strong disparity gaps), proposing constant labelings will lead to more non-submodular terms ($E_{pq}(x_p, x_q = x_p)$ may be high, voiding Equation (2.8)), and generally to local minima further away from the global minimum. In order to circumvent this issue, a generalization of all move-making algorithms was first introduced in (LRR08), called *fusion-move*. It was later expanded to a broader range of applications in (LRRB10). Its principle is to *fuse* two suboptimal solutions (or labelings) x^c (e.g. the current solution), and x^p (the proposed solution) into a solution with lower or equal energy. In this solution, the label x_p of each variable is either taken from x^c or x^p:

$$x_p \leftarrow x_p^c \text{ or } x_p^p.$$

As before, this move can be expressed as an st-mincut, but now both x^c and x^p can be chosen more appropriately given the energy function to be minimized, as shown in Figure 2.8d. The fusion-move is a generalization of the other move-making algorithms. For example, one alpha-expansion move can be realized by setting x^c to the current solution, and $\mathrm{x}^p = \{\alpha, \forall p \in \mathcal{V}\}$. The binary problems shown in Section 2.2.2 can be solved by setting x^c to 0, and x^p to 1 for all variables. It provides the most flexibility, as propositions can be created in almost any way, without restriction (for example, amongst other propositions, pixel-wise random solutions were used in (Ish09)). Just as before, the fused solution might only be partially optimal when non-submodular terms are present in the energy function. In the example given in (Ish09, Ish10), it can also be observed that the solution is driven towards a strong local minimum, even if
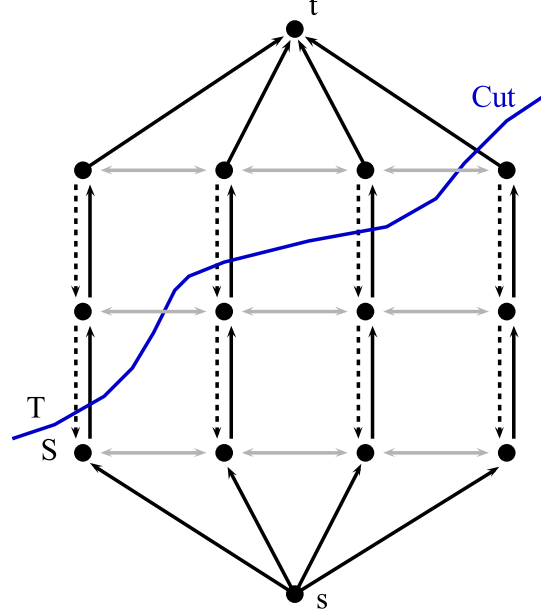
Figure 2.9: Example of a graph construction for convex (w.r.t. $\mathcal{L}$) energy functions where labels can be expressed as consecutive integers. Black edges represent the data terms. Dashed edges carry an infinite weight, preventing multiple cuts per variable. Grey edges encode the linear interaction term $E_{pq}(x_p, x_q) = |x_p - x_q|$. The cut represents the solution x $= \{x_1 = 1, x_2 = 2, x_3 = 2, x_4 = 3\}$. Any convex interaction term can be realized by adding more grey edges.

significant numbers of variables (varying between 30% and 70% in the initial stages) remain unlabeled in each fusion-move. When the algorithm comes closer to convergence, the number of labeled variables increases greatly. However, the fusion-move approach does not provide deterministic convergence, so heuristic stopping criteria, such as minimal energy decrease during a certain number of moves, are usually used.

2.3.2 Transformation Methods

When the label set $\mathcal{L}$ can be expressed as a linearly ordered set (e.g. consecutive integers), and the interaction term $E(x_p, x_q)$ is convex with respect to $\mathcal{L}$, it is possible to compute the exact solution in polynomial time using a single binary graph-cut (Ish03). Application examples leading to a convex, integer-representable label set are image de-noising or stereo-disparity estimation, where the pairwise terms are computed with the L1 or L2 norm. A graph-construction for the L1 norm is illustrated in Figure 2.9, where for each variable, $|\mathcal{L}| - 1$ vertices (not counting source and sink) will be added to the graph. As all labels that are used in this dissertation cannot be represented by ordered integers (e.g. 2D disparity vectors, unordered image indexes), we will not go into any more detail. Instead the reader is referred to the original work, published in (Ish03), or to the corresponding chapter in (BKR11).

It should be noted that there exist more general transformation methods (SF06, Sch07), which are able to find the global minimum of multi-label submodular pairwise energies, also in polynomial time. These energies, given in the form of

$$E(\mathbf{x}) = \sum_{p \in \mathcal{V}} E_p(x_p) + \sum_{(p,q) \in \mathcal{N}} \omega_{pq} E(x_p, x_q), \qquad (2.11)$$

need not be representable as consecutive integers. While these methods could be used for minimizing some of the energy functions defined later in this thesis, they require the allocation of a graph with $|\mathcal{V}|(|\mathcal{L}| - 1)$ nodes (excluding s and t) and $|\mathcal{V}|(|\mathcal{L}| - 2) + |\mathcal{E}|(|\mathcal{L}| - 1)^2$ edges, which impedes optimization of problems with even a moderately large label set on a current desktop computer. The example given in the next section will illustrate the disadvantages of transformation methods, and show that the energies obtained with move-making algorithms are almost identical for submodular energy functions.

2.3.3 Example for Multi-Label Problems: Image De-Noising

In this section, on the example of grey-value image de-noising, several of the previously mentioned concepts will be illustrated. A submodular first-order energy function will be minimized using both move-making algorithms and transformation methods. The original (noise-free) image for all experiments is shown in Figure 2.10a. In the experiments, in each iteration, a noisy image $I^n : \mathcal{V} \to \mathbb{R}$, corrupted by increasing Gaussian noise ($\sigma_{\text{noise}} \in \{2, 4, ..., 60\}$) (see Figure 2.10b for one example with $\sigma_{\text{noise}} = 30$) is generated to allow for variations in the energy function. As usual, the first-order energy function to be minimized is given by

$$E(\mathbf{x}) = \sum_{p \in \mathcal{V}} E_p(x_p) + \lambda \sum_{(p,q) \in \mathcal{N}^4} E_{pq}(x_p, x_q), \qquad (2.12)$$

using a 4-connected neighborhood system $\mathcal{N}^4$, to reduce memory necessary for the transformation method proposed in (SF06). The labeling now corresponds to grey-value intensities, i.e. $\mathbf{x} : \mathcal{V} \to \{0, ..., 255\}$. Similar to the binary denoising example, given in Section 2.2.2.1, the data term ensures that the minimized solution stays as closely as possible to the observed data, while the regularization penalizes intensity differences across neighboring pixels linearly:

$$E_p(x_p) = |I^n(p) - x_p| \quad E_{pq}(x_p, x_q) = |x_p - x_q|.$$

Move-Making vs. Transformation

The following first experiment compares the multi-label submodular optimization algorithm presented in (SF06) with the standard alpha-expansion procedure, iterating over the allowed range of grey-value intensities for two cycles. Due to the exhaustive memory requirements of the method of (SF06), the grey-value intensity range have to be subsampled by a factor of 5, e.g.
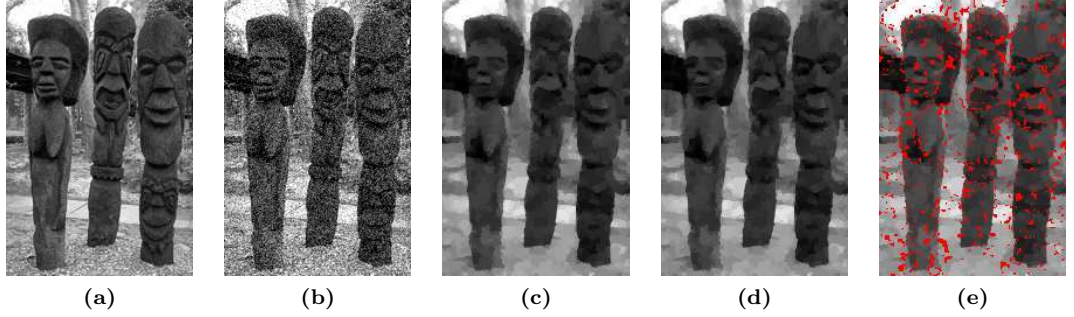
Figure 2.10: Alpha-expansion vs. transformation method. (a) Noise-free original grey-value image. (b) Noisy input image I^n ($\sigma_{\mathrm{noise}} = 30$). (c) Result obtained with the method of (SF06). (d) Result obtained after one cycle of alpha-expansion. Both methods reach the global energy minimum ($E(\mathrm{x}) = 1123147$), but there are small differences in the ratio between data term and regularization, due to the possibility of multiple st-mincuts with equal cost. (e) Pixel-wise difference between b) and c).

$\mathcal{L} = \{0, 5, ..., 250, 255\}$[1]. While this already shows the applicability limitations of the method of (SF06) for problems with even moderately sized label sets, the purpose of this experiment is to compare quality in terms of energy costs. Surprisingly, both methods result in the same final energy costs in each iteration, which demonstrates that move-making algorithms are well suited to find strong local, or in this case, even global energy minima of submodular energy functions. Figure 2.10c shows the result (for the iteration with $\sigma_{\mathrm{noise}} = 30$) obtained using the method of (SF06) ($E(\mathrm{x}) = 1123147 = 873105 + 250042$), Figure 2.10d that of the alpha-expansion approach ($E(\mathrm{x}) = 1123147 = 873300 + 249847$). Figure 2.10e shows the pixelwise difference. While the final energies of both methods are identical, they differ slightly in the relative ratio between unary and pairwise energies (recall that there maybe several st-mincuts with the same cost). These results coincident with results obtained in (MYW05) for a stereo-vision application. The authors conclude that move-making based graph-cuts obtain energies that are at worst 3.6% higher than the global minimum.

Heuristics for Generating Propositions

The second experiment demonstrates that heuristics can be employed to decrease computation time without significant loss in quality. Working on the full range of grey-value intensities, e.g. $\mathcal{L} = \{0, 1, ..., 255\}$, we define as the gold-standard an alpha-expansion algorithm running until convergence. Convergence can only be determined after no energy decrease has been observed in $|\mathcal{L}|$ alpha-expansion moves. In all iterations of this experiment however, the energy minimum was obtained after no more than one cycle. As the previous experiment assessed, this energy corresponds to the global minimum of Equation (2.12). We therefore compare

---

[1]On a Desktop computer with 8GB main memory.
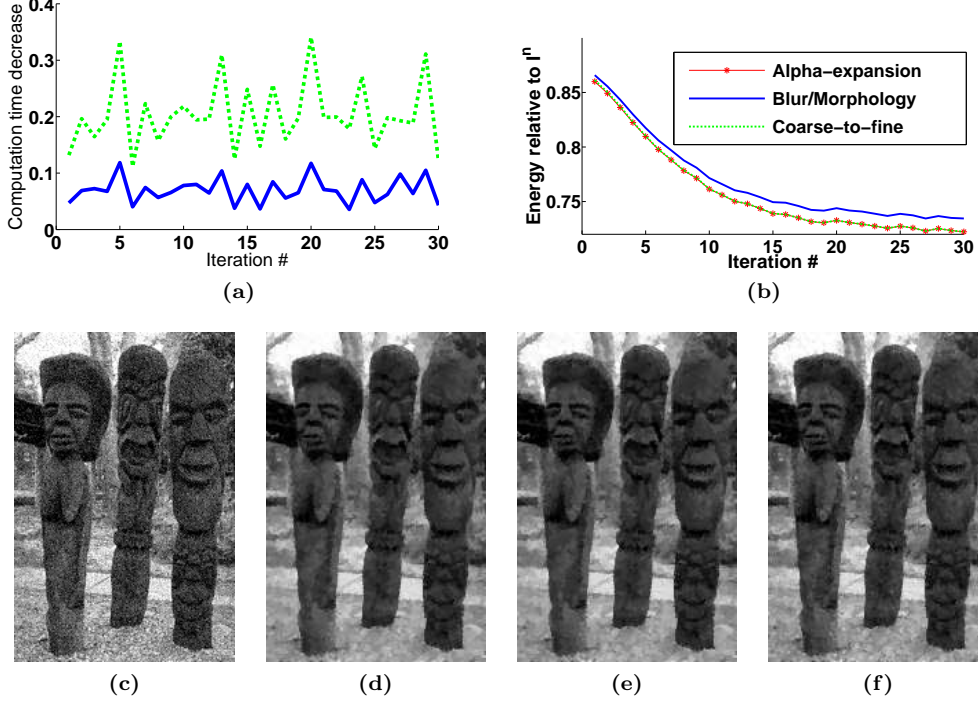
Figure 2.11: Performance improvement using heuristic propositions. We compare a standard one-cycle alpha expansion over the full range of intensities with a coarse-to-fine approach, and one that offers blurred and morphologically processed versions of I^n. See text for more details. (a) Computation time, relative to the standard alpha-expansion. Both variations decrease the computation time significantly. (b) Energies after termination, relative to the energy of I^n. While the variations hardly reach the global minimum, achieved with the standard method, they come very close and the coarse-to-fine method even reaches this minimum from time to time. (c) I^n with noise of $\sigma_{\mathrm{noise}} = 20$. (d) Result using standard alpha-expansion. (e) Result using coarse-to-fine approach. (f) Result using proposition based on blurring and morphology. The differences between d) and e) are hard to spot, but present.

a single cycle alpha-expansion algorithm with two variations in terms of both quality and computation time. In the first variation, an initial alpha-expansion cycle over a subsampled range $\{0, 10, ..., 240, 250, 255\}$ is performed. The obtained result is then used as the initial solution x^c, which is refined using pixelwise offsets in the range $\{-10, -9, ...10\}$ using fusion-moves. This variation therefore computes a total of 48 expansion-/fusion-moves. The second variation works solely with fusion-moves. First, six blurred versions of I^n with a gaussian kernel of sizes $\sigma_{\mathrm{blur}} = \{0.1, 0.3, ..., 1.1\}$ are proposed. These propositions are suitable in regions of smooth grey-value transitions. Then, a set of morphologically processed images (median filter, closing and opening) with kernel sizes $\{2, 3, 4\}$ are proposed, offering better propositions close to object borders. This results in a total of only 15 fusion moves to be computed. The experiment was run for 30 iterations, and in each iteration, a new I^n with increasing σ_{noise} was

generated. Each variation starts with the noisy image as its initial solution x^0. In addition, the order in which the propositions were offered were randomly selected, which generally offers slightly better results than iterating linearly over the set of labels[1].

As can be expected, the computation time compared to the standard, one-cycle alpha-expansion approach is reduced by about 80% for the first variation ($48/256 \simeq 0.19\%$), while the second variation runs roughly 20 times faster ($15/256 \simeq 0.06\%$). Figure 2.11a shows the running times for each iteration, relative to the time of the standard, one-cycle alpha-expansion. In Figure 2.11b, a plot of the energy ratio between the original noisy image I^n and the final energies are plotted for each iteration. The second variation performs noticeably worse (but still only by 1%) than the one-cycle full alpha-expansion. However, the first variation's energy comes very close to the global minimum, in some iterations even reaching it. A similar observation can be made by looking at the images from one of the iterations. Figure 2.11c shows the noisy input image I^n with $\sigma_{\mathrm{noise}} = 20$. Figures 2.11d-f show the result of the standard one-cycle alpha-expansion, the coarse-to-fine and the blur/morphology variations, respectively. Visual differences are difficult to spot, but present.

Conclusion

We can conclude this section with the fact that move-making algorithms allow a greater flexibility, and require much less memory than transformation methods. While transformation methods are able to find the global minimum of certain energy functions, the strong local minima obtained with move-making algorithms are usually very close to the global minimum. While this cannot be theoretically proven, and the theoretical upper bound of alpha-expansions is quite far away from the optimum, the results of the first experiment show that reaching the global minimum, at least for submodular terms, is possible. In addition, the large number of vertices and edges needed by transformation methods will not generally lead to faster results than can be obtained with iterative move-making algorithms (see algorithm complexities in Section 2.2.1.2). Furthermore, memory requirements grow exponentially with the number of labels, which prevents the applicability to problems with large label sets (which we will need for the registration algorithms in Chapter 3 and 4). Higher-order energy functions (also used in Chapters 3 and 4), reduced to pairwise terms, are generally partly non-submodular and can also not be expressed using Equation (2.11) (there exists no pairwise ω_{pq}, and $E(x_p, x_q)$ of Equation (2.11) only depends on the label combination, whereas reduced higher-order functions depend both on the specific variables of the clique, as well as on the clique's label combination, which both are not of pairwise nature). The map compositing algorithms proposed in this thesis cannot be represented either as convex pairwise terms (needed for (Ish03)), nor in the form of Equation (2.11) (ω_{pq} depends on the label combination as well).

---

[1]This has no effect on the one-cycle standard alpha-expansion, as it converges to the global minimum, but produces slightly better results for the two other variations (BVZ01).

Having justified the preference of move-making algorithms compared to transformation methods, a second conclusion can be made. When the label set is significantly large, huge improvements regarding the computation time are possible by selecting propositions in a fusion-move approach. However, such heuristic selection requires careful adaptation to the specific energy function to prevent significant loss in the quality of the results. Global minima are still possible with such approaches, but as not as likely as with standard alpha-expansion.

2.4 Graph-Cuts for Image Registration and Map Compositing

2.4.1 Image Registration using Graph-Cuts

As was discussed in Chapter 1, the algorithm being in the center of the cartography process is the registration of partly overlapping images. Several contributions have been devoted to formulating this problem in terms of discrete energy minimization. This section will outline the basic ideas of these works. In Section 2.5, we will conclude this chapter with an initial proof-of-concept that uses a sparse graph structure to efficiently register overlapping cystoscopic images.

The energy of a non-rigid deformation field can be written as

$$E(\mathrm{x}_{i\to j}) = \sum_{p\in\mathcal{V}} E_p^{\mathrm{data}}(x_p) + \lambda \sum_{(p,q)\in\mathcal{N}^8} E_{pq}^{\mathrm{reg}}(x_p, x_q), \qquad (2.13)$$

where now the configuration $\mathrm{x}_{i\to j} : \mathcal{V} \to \mathcal{L} \subset \mathbb{R}^2$ corresponds to 2D displacement vectors, estimated for each pixel p in the source (floating) image $I_i : \mathcal{V} \to \{0, ..., 255\}$. The data term measures the similiarity of pixels p in the source image to sub-pixels $p + x_p$ in the target (reference) image $I_j : \mathbb{R}^2 \to \{0, ..., 255\}$[1]:

$$E_p^{\mathrm{data}}(x_p) = D\left(I_i(p), I_j(p + x_p)\right). \qquad (2.14)$$

The choice of D in Equation (2.14) is application specific. In (TC07), a simple squared difference between observed intensity values $I_i(p)$ and $I_j(p + x_p)$ was used. The authors of (SC10) use a mutual information based data term.

The regularization term of Equation (2.13) used in (TC07, SC09, SC10) penalizes the first derivative in the displacement field

$$E^{\mathrm{reg}}(x_p, x_q) = \|x_p - x_q\|_2. \qquad (2.15)$$

To allow user interaction, landmarks were included to Equation (2.13) by the authors of (LSC07). Pixels declared as a landmark add hard constraints to the energy function, as these

---

[1]Grey-values at sub-pixel locations $I_j(x + x_p)$ are obtained via bi-cubic interpolation and Dirichlet boundary extension.

pixels must be transformed as indicated by the user. Other pixels are influenced by nearby landmarks based on their Euclidean distance. In (LSC07), on images from a coronary angiogram, the registration converges to an incorrect local minimum without landmarks, but converges to the correct solution when adding them. While this landmark-based approach can be helpful in the case of strong, non-linear deformations, it is not feasible on a large image database or video-sequence due to the exhaustive amount of user interaction needed. However, it could be added in a semi-automatic setup, where registration results are checked automatically for their reliability, and only unreliable image pairs are sent to the user after processing the entire image sequence.

As the computation time increases linearly with the size of the label set $\mathcal{L}$, a multi-level approach was proposed in (SC09). Starting from the coarsest level (lowest resolution) in a Gaussian pyramid, an alpha-expansion based image registration algorithm is applied to the images until convergence with a reduced label set. The result (the labeling representing the displacement at the current level) is propagated up (resized) to the next level, and this scheme continues until the finest (original) level of the pyramid is reached.

In comparison to a "direct" registration of the source and target images, the pyramidal approach leads to a processing time reduction of 54%, whereas the data superimposition robustness and accuracy are similar for both approaches. This result shows the potential of multi-scale approaches with graph-cut optimization. However, the time needed to superimpose two images (538 seconds on average) for the multi-scale approach of (SC09), with $\mathcal{L} = \{0, \pm1, ..., \pm17\}^2$, also shows that dense[1] graph-cut based registration with a large two-dimensional label set leads to high processing times, which is not feasible for the registration of a video-sequence that contains hundreds or thousands of images.

This issue can be overcome using the methods proposed in (GKT$^+$08). Displacements of control points in a regular grid (instead of dense representation) are optimized via MRFs, which leads to a dimensionality reduction on the variables. Registration costs are still computed on the entire image domain via non-linear interpolation of the control point displacements. The authors also apply a multi-scale coarse-to-fine scheme, and are able to estimate the displacement field in 10-50 seconds[2] (depending on the similarity measure used) on 256×256 pixel image resolution. However, this method assumes that an initial pre-alignment (translation and rotation) has been performed beforehand, greatly reducing the search space encapsulated in $\mathcal{L}$. In Section 2.5, we also use a set of control points to reduce the number of variables, but these points are selected based on image texture. This allows to compute registration costs without interpolation on the entire image domain, leading to faster registration times. At the same time, no pre-alignment is required, allowing to directly estimate the underlying image transformations.

Proposed in (GHN$^+$10), second-order cliques, obtained from triangulated meshes, allow to compute (local) image (dis-)similarity using affine approximations. This approach is more

---

[1]Here, dense means that each pixel is represented by a vertex in the graph.
[2]C++ program running on a 2.16 GHz CPU.

robust than pixel-wise similarity measurements in texture-homogeneous image regions, and invariant to affine transformations (as opposed to block matching approaches, which are only invariant to translations). Like the method of (GKT$^+$08), triangulated meshes greatly reduce the number of variables, but the higher-order potentials infer more complexity on MRF optimization.

Graph-Cuts for Stereo and Optical Flow Estimation

While there exist only a few publications (see previous section) specifially contributed to image registration (superimposing two images as best as possible) using discrete energy minimization, the energy formulation of stereo or optical flow estimation in terms of discrete energy minimization is closely related to non-rigid registration. In both applications, the minimized energy should correspond to the most probable displacement field that maps pixels of the source image onto their displaced position in the target image. However, optical flow results are used for motion or object segmentation, not explicitly for image superimposition. Similar, stereo disparity estimation is used to obtain the depth of a scene, visualized by two (or more) cameras from different viewpoints. Consequently, the problems one faces and the attempts to solve them are significantly different between optical flow and image registration/superimposition. In stereo or optical flow estimation, one faces the problem of occlusions, photometric inconsistencies, large displacements of foreground objects with respect to the movement of the background, or the preservation of thin object structures. On the other hand, cystoscopic image registration algorithms do not pose the problem of occlusions or large displacements of foreground objects (apart from small tissues flowing along the FOV, which have to be ignored, not matched). However, they must be able to register images accurately under strongly varying image conditions (see again Section 1.3 for details). While stereo and optical flow methods usually have a large amount of image overlap, cystoscopic image pairs may overlap by less than 50%, requiring careful attention to be paid to border conditions.

A detailed listing of corresponding publications regarding optical flow and stereo estimation would therefore go beyond the scope of this thesis, even though the Middlebury Stereo and Optical Flow databases[1] contain several contributions based on graph-cuts, which were, at the time of their publication, among the top performing methods ((LRR08, GHN$^+$10) represent two interesting approaches). The evaluation pages of these websites are therefore a good starting point to explore various approaches towards stereo and optical flow methods.

2.4.2 Map Compositing using Graph-Cuts

The last step of the cartography process consists of composing the globally aligned images into a single global textured map. Unlike classical blending/interpolation methods (see Section 3.4), formulating this goal as an MRF optimization problem can overcome the issue of blurring and

---

[1]http://vision.middlebury.edu/stereo/, http://vision.middlebury.edu/flow/

ghosting. This approach allows to optimize the location of "hard" transitions between overlapping images, instead of (non-)linear interpolation between the images in superimposed areas. Pairwise MRFs were first used in (KSE$^+$03b) to optimize texture synthesis between overlapping images. Given N (usually superimposed) images, the configuration x $: \mathcal{V} \rightarrow \{0, ..., N-1\}$ assigns each pixel p in the map an image index x_p, which determines the grey/color value to be used for the texture of the map. In other words, the color of a pixel in the map is selected among all images in which this pixel is visible, with the aim to optimize the visual quality in the map. Optimal transitions are obtained by minimizing a sum of pairwise potential costs

$$E(\text{x}) = \sum_{(p,q) \in \mathcal{N}} E_{p,q}(x_p, x_q)$$
$$\text{with } E_{p,q}(x_p, x_q) = T(x_p \neq x_q) \Gamma \left(I_{x_p}(p), I_{x_q}(q) \right),$$

where $\Gamma(\cdot)$ measures the dissimilarity across image transitions (where $x_p \neq x_q$). This idea was extended by several combinations of unary and pairwise potential functions in (ADA$^+$04). The authors refer to this approach by "Interactive Digital Photomontage", and via user interaction, several problems are addressed. Examples are *selective composites*, where the user selects best elements in several images of a changing scene, and the composed map shows the optimal fusion of these images.

The idea of (KSE$^+$03b, ADA$^+$04) was extended to the problem of texturing triangulated three-dimensional surfaces in (LI07). Vertices represent faces of the surface mesh, and pairs of vertices represent faces which share a common edge. Unary potentials capture the "quality" of a face being textured by its projection in the image I_{x_p}, while pairwise potentials again penalize dissimilarities across image transitions.

All approaches (KSE$^+$03b, ADA$^+$04, LI07) assume image exposure and white balance not to vary too drastically, and remove any remaining exposure differences via gradient-domain fusion (ADA$^+$04) or seam levelling (LI07) in a second step after initial seams have been obtained. An exception is the "relighting" technique of (ADA$^+$04), where the images are taken under different unknown lighting conditions, but the images are expected to be perfectly aligned. Both assumptions do not hold in a cystoscopic cartography application, as images differ strongly in terms of exposure and are usually slightly misaligned due to local bladder movements. At the same time, the quality of each image varies strongly. In Chapter 3, we modify the ideas proposed in (KSE$^+$03b, ADA$^+$04, LI07) to optimize contrast, texture alignment, and exposure/white-balance differences for cystoscopic video-sequences. This approach is extended to three-dimensional cartography in Chapter 4.
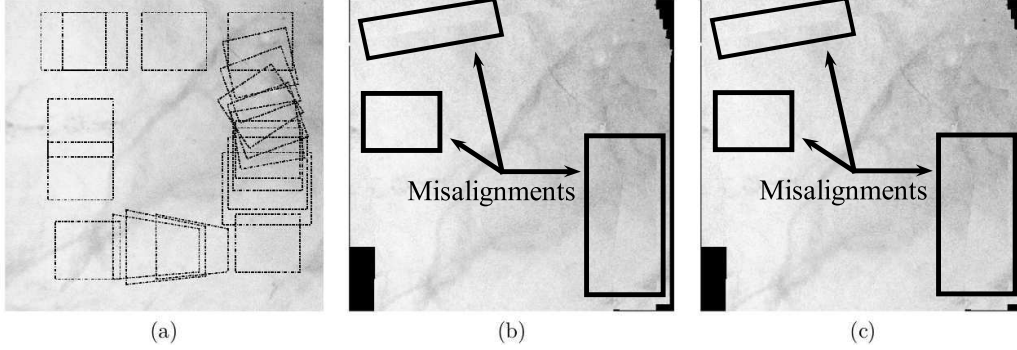
Figure 2.12: Pig bladder phantom used in (HSB[+]09) for the accuracy evaluation. (a) Original high resolution picture. The simulated transformations are illustrated with the successive image positions and their shapes. (b) Map obtained with the method of (MLDB[+]08). (c) Map obtained with the method of (HMBD[+]10). In both maps, local registration errors accumulate and lead to to misaligned structures at several map positions.

2.5 Sparse Graph-Cuts for Cystoscopic Image Registration: a Proof of Concept

2.5.1 Cystoscopic Image Registration Assessment

This section will show preliminary developments regarding the possibility/potential of graph-cut based optimization approaches towards the registration of cystoscopic video-sequences. First, results of existing state-of-the-art registration methods for cystoscopic image registration are presented. A comparison with these results will show the potential of an initial assessment of graph-cut based image registration in Section 2.5.3. In a comparative study (HSB[+]09), the methods of (MLDB[+]08, HMBD[+]10), described in Section 1.3.3.2, were compared in terms of accuracy, robustness and computation time. This comparison was performed with a realistic phantom consisting of images simulating a cystoscopic video-sequence. A pig bladder (which is visually very similar to human bladder tissue[1]) was incised, opened and put flat on a table to capture a high resolution photograph of it. This photograph was used to simulate known transformations that typically occur during a cystoscopic examination, and to obtain a ground truth cystoscopic image sequence. To do so, a sequence of sub-images were extracted from the digital high resolution picture. The simulated perspective transformations are visible on Figure 2.12a[2]. They are symbolized by the displacement and shape change of consecutive images, which are drawn onto the bladder picture and represent the camera movement.

---

[1]Even experienced urologists state that pig bladder texture is visually very close to human bladders.

[2]While color images are used in Chapters 3 and 4, previous registration algorithms do not incorporate color information. The comparison in this chapter is therefore performed on grey-level images.

(a)   (b)   (c)
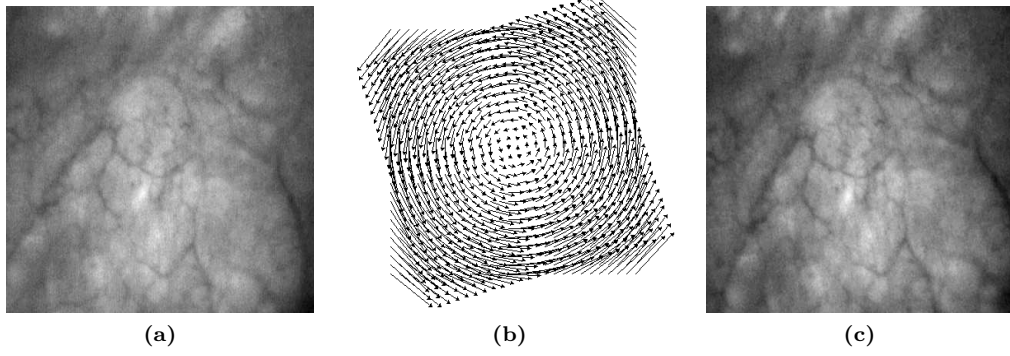
Figure 2.13: Image registration using dense graph-cuts. (a) and (c) Input images, geometrically linked by a pure in-plane rotation. (b) Result using the authors' implementation of (TC07). For visualization purposes, only for each 5th vertex, an arrow is drawn. The resulting flow field is smooth, and produces a mean local registration error of $\epsilon_{i\rightarrow i+1} = 0.06$ pixels. This shows that graph-cuts are well suited for cystoscopic image registration in terms of registration accuracy. However, the large label set (all possible 2D displacements) leads to a computation time of several minutes, unsuitable for large video-sequences.

To assess registration accuracy, the mean local registration error is defined as

$$\epsilon_{i\rightarrow i+1} = \frac{1}{|\mathcal{V}|} \sum_{p\in\mathcal{V}} ||\hat{\mathrm{T}}^{2\mathrm{D}}_{i\rightarrow i+1}p - \mathrm{T}^{2\mathrm{D}}_{i\rightarrow i+1}p||, \tag{2.16}$$

where $\hat{T}^{2\mathrm{D}}_{i\rightarrow i+1}$ and $T^{2\mathrm{D}}_{i\rightarrow i+1}$ are respectively true (known) and estimated homographies placing pixels from the coordinate system of image I_i into the coordinate system of image I_{i+1}. Figures 2.12b-c show the final map composed by the methods of (MLDB$^+$08) and (HMBD$^+$10) respectively. While local errors[1] are small, they accumulate to large errors and result in visible misalignments when the sequence returns to the first image, clearly visible by comparing with Figure 2.12a (in Figures 2.12b-c, a visible seam is present at the top left hand side, and the vascular structure in the bottom left hand side is positioned incorrectly due to the accumulating registration errors).

2.5.2 Cystoscopic Image Registration using Standard Graph-Cuts

A method, similar to that described in (TC07) and defined in Equation (2.13), was implemented and tested for assessing the adequacy of graph-cut techniques to register cystoscopic images. The data terms consist of squared intensity differences, and the regularization penalizes the first derivative in the displacement vector field, as defined in Equation (2.15). The method produces small local registration errors (mean registration error $\epsilon_{i\rightarrow i+1}$ less than 0.2 pixels)

---

[1] It is recalled that local errors or local homographies refer to registration errors or transformations between consecutive images, while global errors are the cartography errors due to placement (with the global homography) of image I_i in the global map coordinate system (typically that of the first image).

on all perspective transformations tested on the phantom of Figure 2.12a. These small errors allow to assume that graph-cuts can be a well suited approach when image registration quality (accuracy) is the main goal. Figure 2.13 shows two input images geometrically related by a pure in-plane rotation, which becomes visible through the computed dense vector flow $x_{i \to j}$ shown in Figure 2.13b. The registration time of several minutes is similar to that of (MLDB$^+$08), but far higher than the two seconds needed to superimpose the images with the method of (HMBD$^+$10). As discussed in Chapter 1, the computation time is the least important aspect, as the maps are mainly used for surgery planning and follow-up examinations. Even if is desirable to build panoramic maps shortly after the examination, or even in real-time, map construction accuracy and robustness remain the most important evaluation criteria for the registration quality. Any improvements made towards a possible real-time usage must therefore not sacrifice this registration quality.

2.5.3 Sparse Graph-Cuts with Locally Refined Vertex and Edge Selection

In order to obtain $\mathrm{T}_{i \to j}^{2\mathrm{D}}$, it is not necessary to compute a dense deformation field, but only a few homologous pixel positions (at least 4) are needed to estimate a homography (recall Section 1.3.2 for the estimation of $\mathrm{T}_{i \to j}^{2\mathrm{D}}$ from a set of homologous points). A sparse sampling $\mathcal{V}^s \subset \mathcal{V}$ in image $I_i : \mathcal{V} \to \{0, ..., 255\}$ can speed up the computation time significantly. However, more attention needs to be paid to the data term evaluation. Indeed, when data terms are only computed for sparsely sampled vertices, the optimization is likely to converge to a poor local minimum because the *implicit* influence of neighboring pixels in a dense sampling $\mathcal{V}$ is lost. To reduce loss of information, data terms must be more robust and should consider the intensity distribution of a local neighborhood of each vertex. Therefore, the original pixelwise squared difference is now measured in an 11x11 squared window centered on each vertex p:

$$E_p^{\mathrm{sparse}}(x_p) = \sum_{p' \in \mathcal{N}_p^{11}} |I_i(p') - I_j(p' + x_p)|^2 .$$

Again, $I_j : \mathbb{R}^2 \to \{0, ..., 255\}$ and grey-values at sub-pixel locations are obtained via bi-cubic interpolation and Dirichlet boundary conditions. As will be shown in Section 2.5.4, this vertex sub-sampling reduces the computation time by some orders of magnitude.

However, as can be seen from Figure 2.14b, where a "winner-takes-all" result is shown (in other words, optimization with $\lambda = 0$), data terms show several outliers (displacement vectors which significantly deviate from their true displacement) when an equally spaced grid $\mathcal{V}^s$ is used. This observation complicates convergence towards the global minimum, and is due to the fact that an equidistant sub-sampling will place many vertices into regions with poor intensity variations (almost homogeneous). Indeed, if such regions are selected in the source image by the vertex subsampling, they can be "matched" with several regions in the target image containing similar homogeneous intensity values. This situation often arises in cystoscopic bladder images.

(a)	(b)	(c)
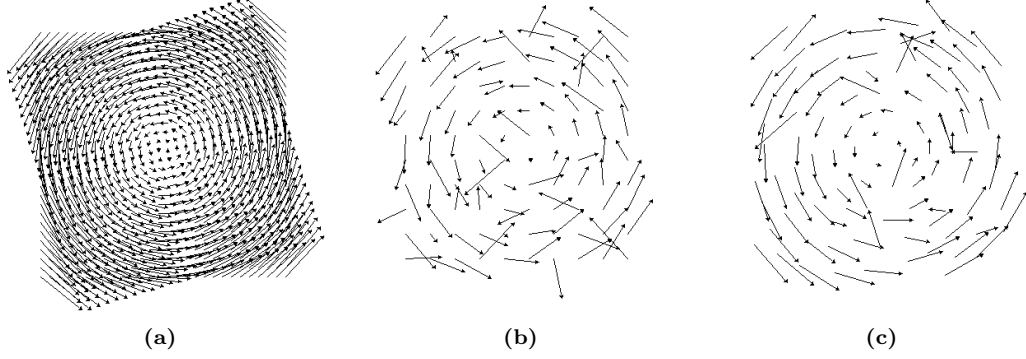
Figure 2.14: (a) Dense displacement vector field of Figure 2.13a used as reference. (b) The use of a sub-sampled grid of vertices speeds up the computation by some orders of magnitude. However, data terms become less distinctive and show several outliers, making convergence towards the energy minimum more complicated (reprojection error $\epsilon_{i,i+1} = 2.91$ pixels including regularization term). (c) Using the proposed vertex selection scheme (WDBH$^+$na), where potential locations are computed using the Harris corner detector (HS88) and thinned using ANMS (BSW05), vertices are locally moved to more distinctive locations. This improves the data terms, reduces outliers, and leads to a reprojection error of $\epsilon_{i \to i+1} = 0.26$.

The idea of the proposed algorithm is to prefer image regions with more texture in order to facilitate the registration, while still retain a sparse set of vertices.

To obtain more discriminative data terms, vertices are locally moved to positions with more texture. To do so, possible vertex positions are first determined with the Harris corner detector (HS88). The response map threshold is set low to obtain key-points also in (almost) homogeneous image regions. Then, these points are thinned using Adaptive Non-Maximal Suppression (ANMS), see (BSW05). The strongest key-point (strongest response of the Harris detector) is first selected, and all key-points in a fixed radius around it are removed from the list. Then, the second strongest key-point is selected, and the process is iterated until no more key-points can be removed. This locally refined sampling $\mathcal{V}^s$ ensures that key-points are well spread over the image (due to the low threshold), while locally, they are positioned at the most discriminative locations, such as those corresponding for example to vascular structures. This vertex selection scheme is illustrated in Figure 2.15a, and its improvement regarding the data terms can be seen in Fig 2.14c (now "winner-takes-all" shows less outliers, thereby facilitating a correct minimum).

The neighborhood system for the selected vertices can be obtained with a k-nearest neighbor approach, or by looking in a fixed radius around each vertex. The drawback of the latter approach is that the significance of the interaction term varies for each vertex depending on the number of neighbors within the radius. Consider for example a vertex that is more likely to be labeled incorrectly, then the interaction penalty for assigning a false label will be less expensive when it has only a few distant neighbors, and zero when it is not close to other vertices. On the other hand, the k-nearest neighbor approach can result in an edge system with

(a)   **(b)**
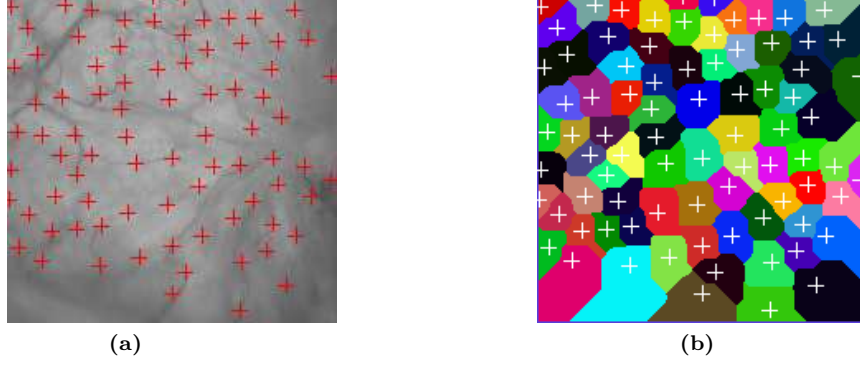
Figure 2.15: Sparse Graph-Cut method. (a) Nodes selected using Harris corner detector and Adaptive Non-Maximal Suppression. (b) Neighborhood system based on the seeded watershed transform. An edge is added to the graph between two nodes if the influence zones correspond to 8-connected neighbors.

I   II   III

(a)
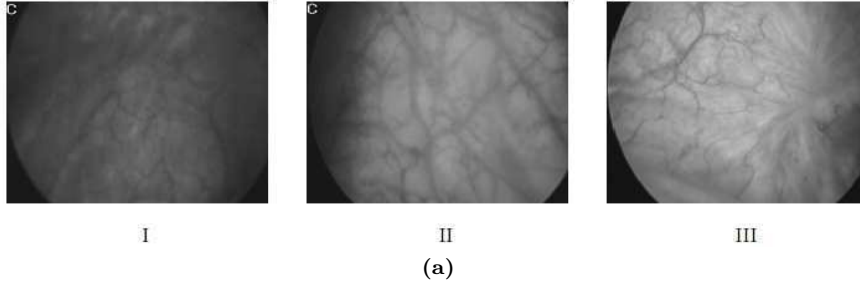
	$\phi = 10°$	$S_x = S_y = 1.2$	$\phi = 5°, S_x = S_y = 1.1$ $(t_x, t_y) = (-4, 3)$
Dense	0.06	0.02	0.09
Sparse, Harris	0.26	0.26	0.24
Sparse, equally	2.91	0.94	1.51

(b)

Figure 2.16: (a) I - III Input images used to evaluate the performance differences between dense, equally rastered and Harris-ANMS-based vertex selection. (b) Comparison of mean registration errors, as given by Equation (2.16). Applied image transformations (parameters of Equation (1.4)) are given in the first line of the table. The errors are measured in pixels.

holes. Therefore, we propose a neighborhood system that takes the spatial distribution of the selected vertices into account. Using the selected vertices as basins, the watershed transform (Soi03) computes the influence zone of each vertex. These influence zones can be used to generate a natural neighborhood system for the vertices. Figure 2.15b illustrates this approach. The neighborhood system $\mathcal{N}^s$ consists of all vertex pairs whose influence zones are 8-connected

(a)

(b)
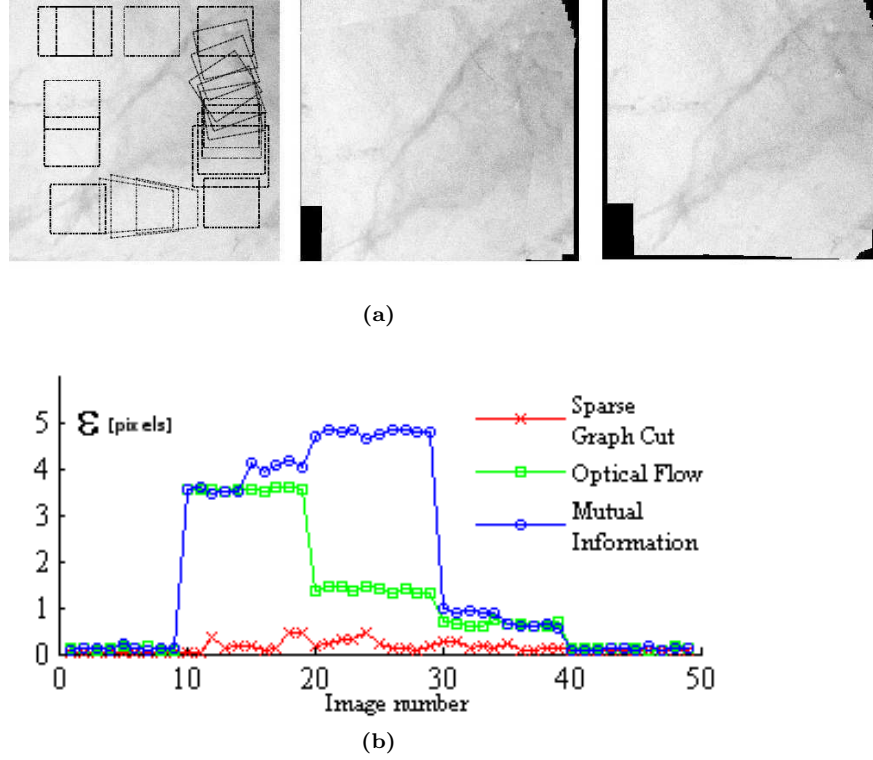
Figure 2.17: Pig bladder phantom and registration error comparison for different methods. (a) Left: camera movement and the imaged area for each acquisition indicated. Middle: Result obtained with the mutual information based registration. Right: Result obtained using sparse graph-cuts. Note the missing visible image borders and the properly reconstructed structures on the left. (b) Local registration errors. The sparse graph-cut method is able to register all image pairs robustly, almost invariant to the variations of the perspective transformation parameters.

neighbors. The final energy function is then given by

$$E^{\text{sparse}}(\mathbf{x}_{i \to j}) = \sum_{p \in \mathcal{V}^s} E_p^{\text{sparse}}(x_p) + \sum_{(p,q) \in \mathcal{N}^s} \|x_p - x_q\|_2 \,,$$

and is minimized using alpha-expansion.

2.5.4 Initial Results

The performances of both the dense and the sparse methods were first evaluated on three reference images, extracted from real cystoscopic sequences. These images were chosen to take into account intensity and texture variability of cystoscopic images. Known transformations were applied to the images to create target images. Figure 2.16a shows the three input images, and the applied transformations are listed in Figure 2.16b together with the obtained mean registration errors $\epsilon_{i \to i+1}$ defined in Equation (2.16). Best results are achieved with the dense

graph-cut ($\epsilon_{i \rightarrow i+1} \leq 0.1$ pixels for each image pair). This approach takes 154 seconds on average to converge to the final solution. Both regularly and locally refined "sparse methods" take 5 seconds to converge on average, but the locally refined selection scheme is 4 up to 10 times more accurate.

Next, the Harris-ANMS-based graph-cut registration algorithm is compared with the methods of (MLDB$^+$08, HMBD$^+$10). By observing the literature (Section 1.3.3.2), these methods can be considered as the reference algorithms for white light bladder image registration. Figures 2.17a-b show the final panoramic image stitched with the method of (MLDB$^+$08) and the proposed algorithm (WDBH$^+$na) respectively. Unlike with the methods of (MLDB$^+$08, HMBD$^+$10), our result correctly aligns the images with respect to the first image (again, compare with Figure 2.12a), as the accumulated global errors become smaller with more accurate transformations linking consecutive images. Figure 2.17b quantifies the $\epsilon_{i \rightarrow i+1}$ errors occurring during the sequence. While both (MLDB$^+$08) and (HMBD$^+$10) are $4 - 10$ times less accurate when in-plane rotations (images 10-20) or scale changes (images 20-30) occur, the proposed method performs equally well ($\epsilon_{i \rightarrow i+1} \leq 0.3$ pixels) independent of the transformations involved. Compared to the registration accuracy of the dense graph-cut ($\epsilon_{i \rightarrow i+1} = 0.2$ pixels on average for this sequence), the computational speed-up of more than one order of magnitude clearly favors the use of the proposed method (the accuracy of the proposed method remains comparable to that of the dense graph-cut, while the computation time decreases significantly).

2.6 Conclusions

This chapter presented a general overview of energy minimization techniques using methods based on the st-mincut/maxflow theorem. Basic notations were introduced, and core algorithms necessary to solve the scientific problems formulated in Chapter 1 were explained. It was shown how discrete pairwise energy functions whose variables take binary values (such as those used for image segmentation) can be solved efficiently to obtain the global minimum using graph-cuts. Furthermore, it was shown how these techniques can be extended for functions whose variables may take on real numbers. Such functions will be used in Chapters 3 and 4. If the set of possible values is countable and the energies are submodular, global minima can be found. In non-submodular cases, strong local minima close to the optimum can be obtained. It was shown how the algorithms can be extended to minimize functions with individual terms of size greater than two, and it was assessed that proposal generation tailored for a specific energy function allows for significant computation time decrease in fusion-move based approaches. Last, but not least, it was shown that these concepts show great potential for image registration under difficult conditions and for panoramic image compositing. These applications define the core of the scientific problems formulated in Chapter 1. First tests showed the potential of graph-cuts

to register images with high accuracy, independent of the transformation that geometrically links overlapping image pairs.

Contributions

- Established a state-of-the-art literature on discrete energy minimization techniques using graph-cuts, with a particular focus on problems typical of cystoscopic cartography applications.

- Determined that fusion-moves benefit from significant computation time reduction without noticeable quality decrease if propositions are generated smartly and adapted to the specific energy function.

- Initial implementation and proof of concept that show the potential of graph-cuts regarding cystoscopic cartography. Accurate results outperforming state-of-the art methods were achieved and the algorithm performs independently of the geometric transformation linking overlapping images.

- A novel locally refined vertex and edge selection scheme for graph-cut based image registration. This allowed to reduce the computation time of image registration by two orders of magnitude, without significant loss in registration accuracy, independent of the geometric transformation relating overlapping images.

Publication

- T. Weibel, C. Daul, A. Ben Hamadou, D. Wolf, and R. Rösch. Endoscopic bladder image registration using sparse graph cuts. In *17th IEEE International Conference on Image Processing (ICIP)*, pages 157–160, September 2010. Hong Kong, China (oral presentation)

Chapter 3

2D Cartography

In the previous chapter, it was shown that graph-cuts can be a promising registration technique for white light cystoscopic video-sequences. Accuracy and robustness of consecutive image registration using graph-cut methods are superior to those of the tested state-of-the-art methods (MLHMD$^+$04, MLDB$^+$08, HMBD$^+$10). On the phantom cystoscopic video-sequence provided by (HSB$^+$09), the accuracy remains relatively constant independent of the parameter values of the perspective transformation linking consecutive images.

3.1 Problem Description and Chapter Overview

Despite the initial improvements on image registration accuracy, errors still accumulate visibly during image placement in a common coordinate system. This fact remains a problem, even for registration methods more accurate than that proposed in the previous chapter. This is particularly true for clinical data, since the phantom data of (HSB$^+$09) used in the evaluation of Section 2.5.4 leads to registration errors much smaller than observed with patient data. As clinicians regularly return to previously visited locations on the bladder surface during the examination, this will lead to visible and strong misalignments.

Figure 3.1a shows this effect on a sequence where the cystoscope trajectory performs a loop. Apart from brightness gradients due to exposure differences and vignetting, the superimposition of consecutive images leads to visually coherent texture transitions in image regions without closing or crossing endoscope trajectories. However, when observing the first and last image of the sequence (indicated by the red and green quadrangles in Figure 3.1a), the global misalignment is evident, both in scale and spatial position. This is illustrated in the top image of Figure 3.1b, where both first and last images are superimposed (these images should be perfectly superimposed when registration errors during the sequence are 0). In order to provide visually coherent panoramic images, these errors need to be detected and corrected automatically.
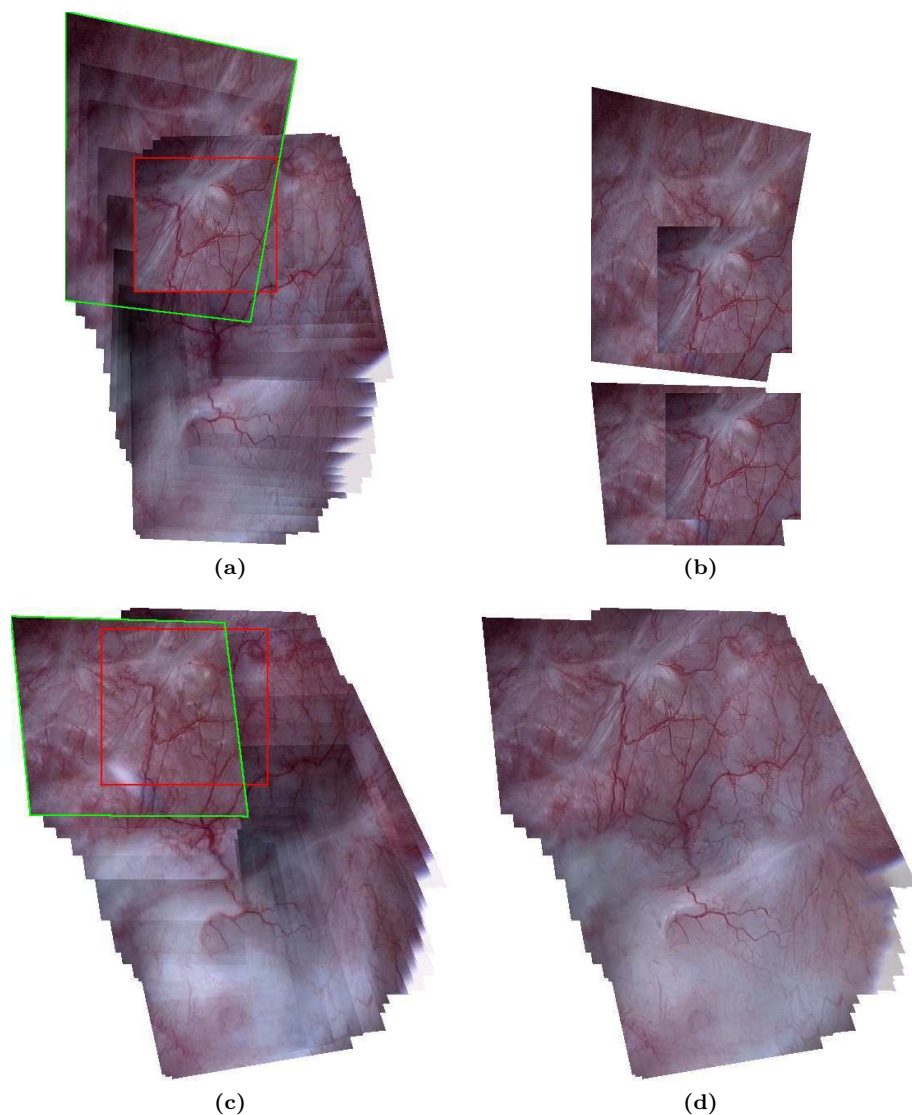
Figure 3.1: Effects of accumulated cartography errors and map improvements presented in this chapter. (a) While superimposed consecutive images show visually coherent transitions (except for exposure and vignetting induced brightness gradients), accumulated errors lead to visible misalignments when the instrument returns to previously visited locations on the bladder surface. This is indicated by the red (first image of the sequence) and green (last image) quadrangles, which are visibly misaligned. (b) Top: first and last image superimposed before correction. Bottom: after correction, the images are now correctly superimposed. (c) Map after correcting global misalignments. Small texture misalignments may still be present due to the non-planar surface and local warping. Furthermore, images suffering from motion blur decrease the visual quality of the map. (d) Stitching techniques can correct small misalignments, increase the contrast of the panoramic map, and remove blending induced gradients. The contrast in d) is strongly enhanced, and exposure/texture gradients are removed, as can be seen by comparing with with c).

State-of-the-art contributions devoted to bladder cartography have not presented methods to detect accumulated errors, and usually show maps without loop trajectories or crossing paths. An exception is (MLDB$^+$08), where the authors have proposed a method to correct global misalignment by jointly adjusting the local transformations between first and last image of a loop using a steepest gradient optimization. However, they present no method to automatically detect these loops, and their algorithm cannot be easily extended to multiple overlapping images (the adjustment is only performed on consecutive images). Feature-correspondence based approaches (e.g. (BBS$^+$10)) could directly employ traditional methods of globally registering the entire sequence using bundle-adjustment techniques (see (Sze06) for an introductory overview). The advantage of feature based methods lies both in the fast image pair registration and in the possible automatic detection of non-overlapping images. However, as discussed in Chapter 1, in the white light modality, iconic data registration must be used for robust image superimposition, which impedes registering all possible pairs of the sequence (as required for classic bundle adjustment) due to time constraints.

The effects of error accumulation can also be understood by comparing Figure 3.1a with the corrected map (corrected image positions in the map) of Figure 3.1c. Figure 3.1c is visually more coherent in terms of texture discontinuities, even if small texture misalignments remain. In this corrected map, the first and last images are adequately superimposed, as shown in the bottom image of Figure 3.1b. The remaining texture misalignments are due to the spherical bladder surface projected onto a flat panoramic coordinate system[1], local warping of the surface due to physical contact to other organs, and bending of the bladder caused by the movement of the rigid cystoscope. These small texture misalignments can be corrected by finding optimal seam locations between overlapping images. As opposed to blending techniques, seams depict a hard border between parts of partly overlapping images. For misaligned texture, the former approach leads to ghosting and blur, while seams allow for sharp transitions. Such seams may also be used to increase the contrast of the map (by discarding blurry images), as shown in Figure 3.1d.

To sum up Figure 3.1, the map correction proposed in this thesis consist of two steps: the first step corrects small misalignments and maximizes the texture contrast in the map. Exposure differences are then corrected in a second step, while retaining the obtained contrast of step one.

The remainder of this chapter is organized as follows. While the chronological order of the proposed cartography pipeline starts with the registration of consecutive image pairs, we will first explain the proposed method to detect a meaningful subset of non-consecutive image pairs in Section 3.2. These will then be used to globally correct accumulated cartography errors. In Section 3.3, higher-order cost functions that are invariant to perspective transformation parameter values will be presented. In addition, a coarse-to-fine minimization scheme that

---

[1]As will be shown in Chapter 4, without additional information, such as the distance of the instrument from the surface, the parametric surface model cannot be used as a-priori information for registration or surface compositing.

allows to reduce computation time significantly is proposed. This registration algorithm will be used for both consecutive and non-consecutive image pairs. For consecutive image pairs, it leads to more accurate and robust solutions. For non-consecutive image pairs, the proposed terms authorize a successful registration where other methods fail. Lastly, a combined stitching and exposure correction technique is proposed in Section 3.4. It allows to correct small local texture misalignments (remaining after global correction in Section 3.2) and is able to create visually coherent panoramic images with minimal loss of information (maximum contrast). These different algorithm steps are evaluated in Section 3.5, both quantitatively on realistic phantom data, as well as qualitatively on patient data. In addition, we demonstrate that the proposed algorithms may also be used in more traditional applications, such as seamless stitching of a set of images captured with consumer cameras, or high dynamic range image composition.

Parts of this chapter previously appeared in (WDWRum, WDW$^+$12, WDW$^+$an).

3.2 Global Map Correction

Feature correspondence based algorithms (e.g. such as the one presented in(BBS$^+$10)) are fast, so registering all possible image pair combinations of a sequence is possible within application time limits (i.e. shortly after the examination). If all pairs of images with a minimum overlap could be registered in a robust fashion, rejecting non-overlapping pairs would be simple. A rejection criterion could be a minimum percentage (threshold) of inlier matches after RANSAC fitting. All valid feature correspondences between overlapping image pairs could then be used to compute global transformations using bundle adjustment techniques (Sze06). In such an approach, global transformation matrices are adjusted by minimizing the sum of distances between homologous pixel positions in all registered image pairs.

However, as was justified in Chapter 1, feature correspondences cannot be robustly estimated in the white light modality. Iconic data registration methods are slower than feature based approaches and therefore registering all possible image pair combinations requires too much computation time. To overcome this problem, we propose to use the initial global transformations $T^{2D}_{0 \to i}$ (placing the images in the global map coordinate system) obtained by concatenating local transformations $T^{2D}_{i \to i+1}$ between consecutive pairs to detect overlapping non-consecutive image pairs $(i, j \neq i+1)$ automatically. From these overlapping additional image pairs, a useful subset must be selected and registered[1]. The computed additional transformations $T^{2D}_{i \to j \neq i+1}$ can then be used to correct accumulated errors globally. Global transformations must be adjusted so that local registration errors (for all computed $T^{2D}_{i \to j}$) are minimized, which leads to visually coherent superimposition.

---

[1] Again, due to time constraints, the registration of all available overlapping image pairs is infeasible.

To sum up, the method detailed in this section is a bundle adjustment method. The difference to classical methods is that, instead of using all image pair combinations, only an automatically selected subset of image pairs needs to be registered, and no image primitives have to be extracted from the images. This subset of image pairs is then used during the iterative and global map correction process.

3.2.1 Detecting Additional Image Pairs

Once all local transformations $T^{2D}_{i \to i+1}$ between consecutive images are computed, the global matrices $T^{2D}_{0 \to i}$ relating each image I_i with the coordinate system of a reference image can be obtained by concatenation. For simplicity (and without loss of generality), we will use the first image (I_0) as the reference image:

$$T^{2D}_{0 \to i} = \prod_{k=0}^{i-1} T^{2D}_{k \to k+1}. \tag{3.1}$$

This straightforward approach (a global matrix is a simple product of consecutive local matrices) yields visually coherent maps (MLDB$^+$08, HMBD$^+$10, BBS$^+$10, WDBH$^+$na) between consecutive images. However, small registration errors accumulate, and when the cystoscope comes back to previously visited locations (e.g. when a loop is closed or during a "zig-zag"-path), the misalignment is evident (see again Figure 3.1b). In order to correct these misalignments, the local transformations between non-consecutive but overlapping image pairs need to be taken into account when computing global transformations $T^{2D}_{0 \to i}$. Using the initial map constructed with Equation (3.1) as a starting point, we can estimate the overlap ratio $\delta^{2D}_{i,j}$ between any two (consecutive and non-consecutive) image pairs (I_i, I_j) of the sequence using:

$$\delta^{2D}_{i,j} = \min\left(\frac{\mathcal{A}_{i,j}}{\mathcal{A}_i} \cdot \frac{\mathcal{A}_{i,j}}{\mathcal{A}_j} \right), \tag{3.2}$$

In Equation (3.2), $\mathcal{A}_i, \mathcal{A}_j$ are the areas in pixels of the transformed images I_i and I_j in the panoramic image (i.e. the map coordinate system), and $\mathcal{A}_{i,j}$ is the area of overlap in pixels between images I_i and I_j. Areas $\mathcal{A}_i$ and $\mathcal{A}_j$ are computed by perspective warping of quadrangles into the global coordinate system, and $\mathcal{A}_{i,j}$ is computed using the area of polygon overlap (i.e. $\mathcal{A}_i \cap \mathcal{A}_j$). For two completely superimposed images, $\delta^{2D}_{i,j} = 1$, while for non-overlapping image pairs, $\delta^{2D}_{i,j} = 0$. Theoretically, we could compute $T^{2D}_{i \to j}$ for all pairs of images with an overlap $\delta^{2D}_{i,j}$ greater than a minimally allowed overlap t_δ (i.e. $\delta^{2D}_{i,j} > t_\delta$). This is however computationally expensive and therefore not recommended for iconic data based registration algorithms. Instead, a greedy algorithm similar to (MFM04) allows us to select a meaningful subset of possible additional image pairs $((i,j) : \delta^{2D}_{i,j} > t_\delta, \ j \neq i + 1)$. We create a weighted, undirected initial graph $G = (V, E, w)$ in which every image I_i is represented by a node v_i, and existing consecutive

---

Algorithm 1: Determining additional image pairs.

Input: Overlap threshold t_δ, short-cut threshold t_ϑ
Output: Indices of additional transformation pairs S
// Set of initial (i.e. consecutive) pair indices
$S_c \leftarrow \{(i,j) : j = i + 1\}$;
// Set of non-consecutive indices
$S_{nc} \leftarrow \{(i,j) : j > i + 1\}$;
$S \leftarrow \emptyset$;
// Compute overlap for all pairs
foreach $(i,j) \in S_c \cup S_{nc}$ **do**
   | compute $\delta^{2D}_{i,j}$;
// Remove non-consecutive pairs with too low overlap
$S_{nc} \leftarrow S_{nc} \setminus \{(i,j) : \delta^{2D}_{i,j} < t_\delta\}$;
while $S_{nc} \neq \emptyset$ **do**
   | Create $G(E, V, w)$ from S_c;
   | // Compute material shortcut
   | **foreach** $(i,j) \in S_{nc}$ **do**
   | | compute $\vartheta_{i,j}$;
   | // Discard pairs with $\vartheta_{i,j} < t_\vartheta$
   | $S_{nc} \leftarrow S_{nc} \setminus \{(i,j) : \vartheta_{i,j} < t_\vartheta\}$;
   | // Add pair with largest $\vartheta_{i,j}$ to the set of additional pairs ...
   | $S \leftarrow S \cup \{(i,j) : \max(\vartheta_{i,j})\}$;
   | // ... and remove it before the next iteration.
   | $S_{nc} \leftarrow S_{nc} \setminus \{(i,j) : \max(\vartheta_{i,j})\}$;
   | // Update combined set (consecutive and additional pair indices)
   | $S_c \leftarrow S_c \cup S$;

---

transformations $T^{2D}_{i \to i+1}$ will create an edge $e_{i,i+1}$ with weight $w_{i,i+1} = 1 - \delta^{2D}_{i,i+1}$ that links nodes v_i and v_{i+1}. Let the "material shortcut" be

$$\vartheta_{i,j} = 1 - \frac{w_{i,j}}{\sum_{i \rightsquigarrow j} w},$$

where $\sum_{i \rightsquigarrow j} w$ is the sum of image overlap along the shortest path from v_i to v_j, found using Dijkstra's algorithm (Dij59). Note that for consecutive pairs $(i, i + 1)$, $\vartheta_{i,i+1}$ is always 0, while it is close to 1 for pairs whose shortest path spans many images. At each iteration of the proposed algorithm, we add a new edge $e_{i,j}$ (again with weight $w_{i,j} = 1 - \delta^{2D}_{i,j}$) to G for the pair with the highest $\vartheta_{i,j}$. Adding the image pair with the highest "material shortcut" ensures that accumulated errors can be attenuated for a large number of images (i.e. many images can be reached using a significantly shorter path after adding $e_{i,j}$ to G). In the next iteration, $\vartheta_{i,j}$ is then recomputed for all remaining pairs $((i,j) : \delta^{2D}_{i,j} > t_\delta)$. These steps are repeated until no pairs with a minimum amount of "material shortcut" t_ϑ are left. A schematic overview of the algorithm is given in Algorithm 1. The final graph then consists of edges between consecutive image pairs (for which the transformations are already computed), and

edges between additional, non-consecutive image pairs. Before continuing with the next section, these image pairs must be registered using the methods that will be explained in Section 3.3.

3.2.2 Bundle Adjustment

Both consecutive and non-consecutive local transformation matrices $\mathrm{T}^{2\mathrm{D}}_{i\to j}$ can now be combined to obtain the best possible global matrices $\mathrm{T}^{2\mathrm{D}}_{0\to i}$. Similar to Section 3.2.1, we construct a weighted graph $G = (E, V, w)$ using all available transformations. The weights are defined as

$$w_{i,j} = \frac{1}{|\mathrm{T}^{2\mathrm{D}}_{i\to j}(I_i)|} \sum_{p\in \mathrm{T}^{2\mathrm{D}}_{i\to j}(I_i)} \left\| I_j(p) - \mathrm{T}^{2\mathrm{D}}_{i\to j}(I_i)(p) \right\|_2^2,$$

and represent the mean sum of squared differences (SSD, divided by the number of valid pixel positions $|\mathrm{T}^{2\mathrm{D}}_{i\to j}(I_i)|$) of the colors of homologous pixels between image I_j and image $\mathrm{T}^{2\mathrm{D}}_{i\to j}(I_i)$, i.e. image I_i transformed into the coordinate system of I_j. A color difference is given by the Euclidean distance between two RGB vectors, and the mean SSD is obtained by dividing the sum of all distances by the number of homologous pixels. The pre-processing method used in (HMBD^{+}10) is applied before computing the weights $w_{i,j}$, so that the SSD is not biased by different levels of exposure or vignetting. We observed that images differing in contrast have less influence on the mean SSD (due to the pre-processing step applied) than small registration inaccuracies have. Thus, using the mean SSD as the edge weights will ensure that when several paths with comparable numbers of transformations are available for computing the global transformation for an image, the one with the best overall registration quality is chosen. The global transformation $\mathrm{T}^{2\mathrm{D}}_{0\to i}$ for each image I_i is then obtained by concatenation along the shortest path in G.

While this reduces the accumulated error for each image that has "shortcut"-transformations (e.g. loops will now be closed, see Figure 3.1a), smaller local errors still remain. Consider for example consecutive images (I_i, I_{i+1}) that have a different shortest path to the reference image I_0. This implies independently accumulated errors when placing I_i and I_{i+1} into the global map. These errors are corrected using a modified bundle adjustment algorithm, similar to that presented in (MFM04). A regularly spaced grid of points $\mathcal{G}$ that covers the entire map is created. If two overlapping images (I_i, I_j) are perfectly aligned in the reference coordinate system, their local transformation $T^{2\mathrm{D}}_{i\to j}$ should be equal to the product of their global transformations, i.e. $\mathrm{T}^{2\mathrm{D}}_{i\to j} = \mathrm{T}^{2\mathrm{D}}_{0\to j}\mathrm{T}^{2\mathrm{D}}_{0\to i}{}^{-1}$. This property allows to create the cost function

$$E = \sum_{g\in \mathcal{G}} \left(\frac{1}{|L_g|} \sum_{i,j\in L_g} \left\| g - \mathrm{T}^{2\mathrm{D}}_{0\to j}{}^{-1}\mathrm{T}^{2\mathrm{D}}_{i\to j}\mathrm{T}^{2\mathrm{D}}_{0\to i}g \right\|_2 \right), \tag{3.3}$$

which can be minimized using non-linear least squares. In Equation (3.3), g is a grid point of the set $\mathcal{G}$, and L_g is the set of image pairs for which a local transformation $\mathrm{T}^{2\mathrm{D}}_{i\to j}$ exists and g

is visible in both images. The cost for each grid point is normalized by the number of image pairs $|L_g|$.

Because each grid point is only visible in a small subset L_g of available image pairs (I_i, I_j), Equation (3.3) is highly sparse (between 1% and 5% of non-zero elements in the Hessian matrix in out experiments) and can therefore be minimized with a sparse Levenberg-Marquardt routine (Lou10). The sparse Jacobian matrix is obtained using automatic differentiation (GJM$^+$99) because an analytic Jacobian is difficult to obtain.

3.3 Image Registration using Perspective-Invariant Cost Functions

While consecutive images are often linked by translation-dominated perspective transformations and generally share a large percentage of overlap (90% or more), non-consecutive pairs (as needed for global corrections proposed in the previous section) may be linked by arbitrary perspective transformations[1] and low overlap percentage. State-of-the-art methods (MLHMD$^+$04, MLDB$^+$08, HMBD$^+$10) require at least 90% of overlap, and as was shown in the previous chapter, perform significantly worse on transformations that deviate from almost pure translations. Furthermore, the proposed data terms in (WDBH$^+$na), even though they have led to improved results on consecutive image pairs, are not invariant to large rotations, scale changes or perspective changes. To illustrate the need for geometrically invariant data term computation, consider the rectangular neighborhood centered on a pixel p in image I_i (Figure 3.2a), as used in (WDBH$^+$na)[2]. In the successive image I_{i+1}, size and shape of this window stays relatively similar, as the perspective transformation is mainly translational (Figure 3.2b). This allows for an accurate similarity comparison between homologous pixels, computed within constant windows. However, in a non-consecutive image $I_{j \gg i}$, taken several seconds later when the cystoscope is re-visiting this location, the corresponding shape has significantly changed due to the different viewpoint of the instrument (Figure 3.2c). This viewpoint change leads to the number of pixels (and their spatial distribution) being very different in the homologous region, and image similarity clearly cannot be computed very accurately in this situation using constant windows.

In addition to the lack of invariance for data term computation, pairwise regularization (see Equation (2.15)) leads to implicit over-smoothing for strong transformations. Translation-dominated transformations have a pairwise regularization energy close to 0 (see also Figure 3.4a), while strong rotations or perspective changes lead to much higher regularization

[1]In fact, due to local warping and the bladder's spherical surface, the transformation between non-consecutive images is often non-linear. While the vector field computed using the proposed methods can be used to recover non-linear deformations, we will nonetheless assume that a perspective transformation correctly approximates the link between overlapping images in bladder cartography, as discussed in Chapter 1.

[2]The method proposed in (WDBH$^+$na) uses an 11x11 neighborhood. For illustration, a much larger neighborhood is drawn in Figure 3.2.

(a)	(b)	(c)
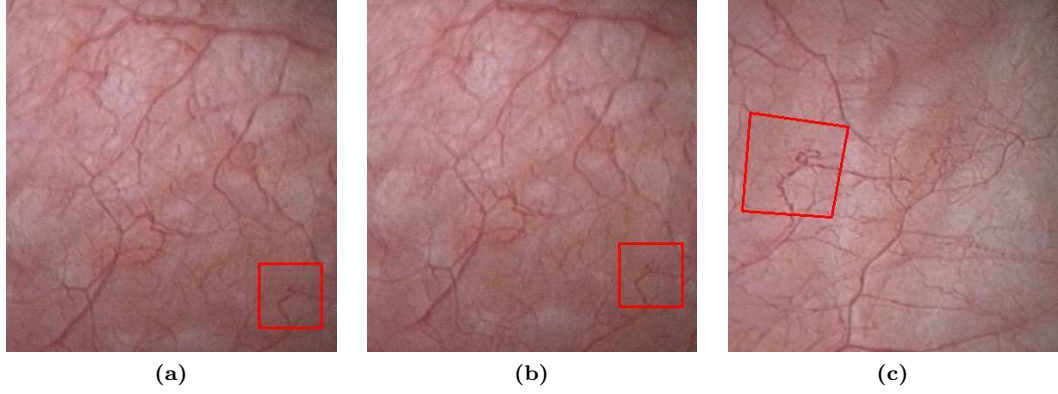
Figure 3.2: Data terms determined in rectangular image regions are not invariant to perspective transformations. (a-b) Consecutive images of a cystoscopic video-sequence. The geometric transformation relating these images is mainly translational, so that a fixed shape window (red rectangles) can be used to compare similarity between homologous pixels. (c) Image taken after the cystoscope has returned to a previously visited location. The instrument is now significantly closer and has a different orientation towards to the bladder surface, as indicated by the quadrangle that corresponds to those of a) and b).

energies (Figure 3.4b), even though both transformations are valid representations of the underlying transformation model (see Equation (1.4)). Therefore, data and regularization terms must be invariant to the geometric transformations linking partly overlapping cystoscopic images.

3.3.1 Data Term

As illustrated in Figure 3.2, measuring homologous image region similarity independently of the underlying projective transformation is not possible using constant window regions. Indeed, the window's geometry (in the target image I_j) would have to be adapted to the given transformation $\mathrm{T}^{2\mathrm{D}}_{i \to j}$, which of course is not known in advance. However, higher-order terms allow to incorporate shape into the energy function itself. First introduced in (GHN$^+$10), second-order terms can be used to compare image similarity in triangular texture patches located in the source and target images. Let $\triangle_{p,q,r}$ be a triangular shape defined by vertices p, q and r, and let $\triangle_{p',q',r'}$ be the corresponding triangular shape defined by $p' = p + x_p, q' = q + x_q$ and $r' = r + x_r$. Then these two triangles are related by an affine transformation $\mathrm{T}^{2\mathrm{D}^{\triangle}}_{pqr}$, and any position u inside $\triangle_{p,q,r}$ can be mapped to its corresponding (sub-pixel) position inside $\triangle_{p'q'r'}$ via $\mathrm{T}^{2\mathrm{D}^{\triangle}}_{pqr} \, u$. This enables to compare image similarity for arbitrary affine transformations $\mathrm{T}^{2\mathrm{D}}_{i \to j}$

relating I_i and I_j. The data terms are then computed using

$$E^\triangle(\mathrm{x}_{i \to j}) = \sum_{(p,q,r) \in \mathcal{C}^\triangle} E^\triangle_{pqr}(x_p, x_q, x_r) \text{ with}$$

$$E^\triangle_{pqr}(x_p, x_q, x_r) = \frac{1}{|\triangle_{pqr}|} \sum_{u \in \triangle_{pqr}} \left\| I_i(u) - I_j(\mathrm{T}^{2\mathrm{D}^\triangle}_{pqr}\ u) \right\|_2, \tag{3.4}$$

where the set of cliques $\mathcal{C}^\triangle$ consists of triplets located in a regularly spaced grid $\mathcal{V}^r \subset \mathcal{V}$, and $I_i : \mathcal{V} \to \mathbb{R}^3$. Colors $I_j(x + x_p)$ at sub-pixel locations are obtained via bi-cubic interpolation and Dirichlet boundary conditions, so $I_j : \mathbb{R}^2 \to \mathbb{R}^3$. Each $E^\triangle_{pqr}(x_p, x_q, x_r)$ is normalized by the number of discrete sample positions $|\triangle_{pqr}|$ inside $\triangle_{pqr}$. The geometric relationship between $\triangle_{pqr}$ and $\triangle_{p'q'r'}$ for different types of transformations is illustrated in Figure 3.3. While the geometric transformation relating the entire images I_i and I_j is usually projective (i.e. not globally affine), if the triangles are made sufficiently small, the perspective transformation $\mathrm{T}^{2\mathrm{D}}_{i \to j}$ can be approximated by several locally affine transformations $\mathrm{T}^{2\mathrm{D}^\triangle}_{pqr}$.

There is however a drawback since too small (i.e. too numerous) triangles will lead to many of them lying in homogeneous areas (i.e. with poor texture information), making the data terms less distinctive. On the other hand, too large triangles will impede the correct estimation of the fully projective transformation and lead to globally affine approximations. This issue is illustrated in Figure 3.3. As long as the images are only related by translations, rectangular windows, as used in (WDBH⁺na), are sufficient (see Figure 3.3b). The triangular data terms allow to compute an exact similarity for rigid and affine transformations (see Figure 3.3c-d). However, when the underlying transformation is fully projective, triangular data terms will only allow for an approximative data comparison, as illustrated in Figure 3.3e. While the three triangle vertices are perfectly transformed using the affine approximation, positions inside the triangles are misplaced because the actual transformation is fully projective. This can be seen when comparing the position of the triangle's center (intersection of the three blue lines) in Figure 3.3a and Figure 3.3e.

Therefore, we propose an extension to the idea of (GHN⁺10). Third-order terms can be used to compute a similarity between quadrangular neighborhood shapes, allowing fully perspective transformations:

$$E^\square(\mathrm{x}_{i \to j}) = \sum_{(p,q,r,s) \in \mathcal{C}^\square} E^\square_{pqrs}(x_p, x_q, x_r, x_s) \text{ with}$$

$$E^\square_{pqrs}(x_p, x_q, x_r, x_s) = \frac{1}{|\square_{pqrs}|} \sum_{u \in \square_{pqrs}} \left\| I_i(u) - I_j(\mathrm{T}^{2\mathrm{D}^\square}_{pqrs}\ u) \right\|_2. \tag{3.5}$$

The set of of cliques $\mathcal{C}^\square$ consists of quadruples, located in the same regularly spaced grid $\mathcal{V}^r$ than used for $\mathcal{C}^\triangle$. Again, each $E^\square_{pqrs}(x_p, x_q, x_r, x_s)$ is normalized by the number of discrete sample positions $|\square_{pqrs}|$ inside the quadrangle $\square_{pqrs}$. The fully projective geometric relationship between $\square_{pqrs}$ and $\square_{p'q'r's'}$ allows to set the size of the quadrangles tailored to white light
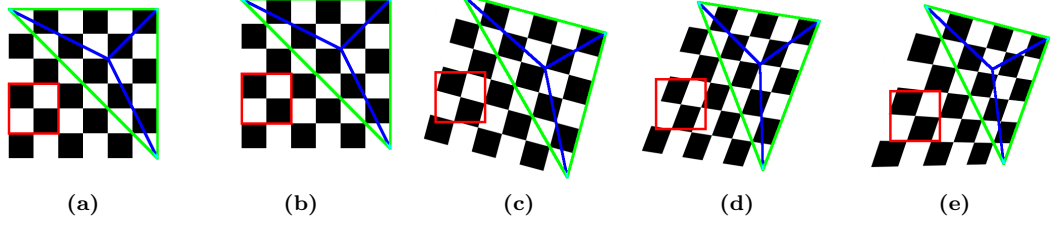
Figure 3.3: Invariance of data term windows. (a) Artificial source image I_i. (b) Target image I_j, related to I_i by pure translations. The rectangular window (red) is invariant to transformations, so it is sufficient to compare image similarity. (c) I_j, related to I_i by a rigid 2D transformation. The rectangular window is no longer sufficient. However, the affine transformation that warps the triangular vertices from I_i to I_j can be used to compute the similarity exactly. (d) Affine transformation relating I_i and I_j. Triangular windows are also sufficient to compute an invariant data term. (e) Fully projective transformation. While the three triangular vertices are perfectly transformed onto I_j using the affine approximation, positions inside the triangle are incorrectly transformed. This can be seen at the intersection of the blue lines (which meet at the center of the green triangle), which is at a different position than in a)-d).

cystoscopic images (e.g. large enough to include textured areas in all quadrangles), without risking affine approximations to $T^{2D}_{i \to j}$.

The set of cliques $\mathcal{C}^{\triangle}$ (Equation (3.4)) and $\mathcal{C}^{\square}$ (Equation (3.5)) are selected from the regular grid $\mathcal{V}^r$, which is illustrated in Figure 3.7, together with the regularization cliques defined in the next section. A 10×10 grid is used for the experiments in Section 3.5.

3.3.2 Regularization Term

Pairwise regularization terms are generally well suited to obtain energy minima without outliers. Intuitively, they penalize strong displacement vector differences between neighbouring vertices, therefore leading to smooth displacement fields:

$$E^{\leftrightarrow}(x_{i \to j}) = \sum_{(p,q) \in \mathcal{N}^r} \frac{1}{\|p - q\|_2} \|x_p - x_q\|_2^2, \tag{3.6}$$

where $\|\cdot\|_2^2$ is the squared L2 norm[1] of the difference of displacement vectors assigned to vertices p and q. The neighborhood system $\mathcal{N}^r$ corresponds to the 8-connectivity in $\mathcal{V}^r$, as shown in Figure 3.7. However, when $T^{2D}_{i \to j}$ consists of displacements of large magnitude and deviates from pure translations, even smooth displacement vector transitions between neighbouring vertices will contribute significantly to the energy cost. This phenomenon is illustrated in Figure 3.4. Consecutive images are related by transformations of small magnitude and dominated by translations. Figure 3.4a shows one such image pair. For this example, the average pairwise cost value between vertex pairs, computed with Equation (3.6), is 3.2. The total pairwise regularization energy contributes only by small fraction to the entire energy, allowing the energy

---

[1] The L1 norm is better suited when discontinuities in the displacement vector field are expected (e.g. due to moving objects or depth discontinuities), which is not the case in cystoscopy.
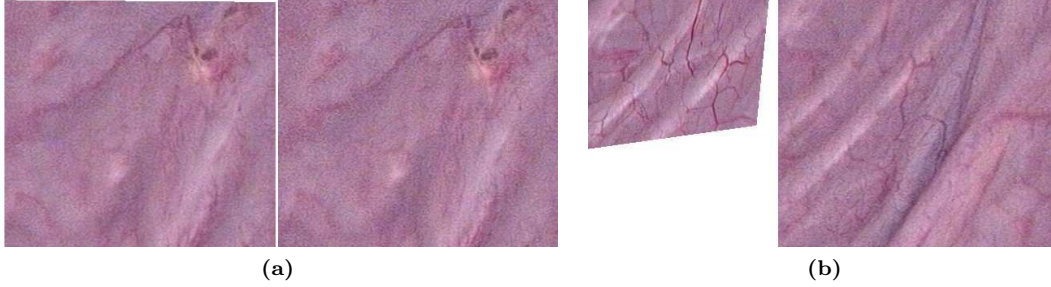
Figure 3.4: Varying regularization influence on the global cost function. (a) Visual representation of the estimated transformation between consecutive images. The relative small regularization energy (3.2 on average per vertex pair) due to the low magnitude of the translation-dominated displacements. (b) Illustration of the estimated transformation between non-consecutive images. The pairwise regularization energy is two orders of magnitude larger (313.7 on average) than that of a) due to the strong perspective relationship between the images.

minimum to correspond to optimal superimposition of the iconic data. This is not the case for many non-consecutive image pairs, such as the one shown in Figure 3.4b. The average regularization energy per vertex pair is by two orders of magnitude larger (313.7 per pair) than for the image pair shown in Figure 3.4a, and the total regularization energy contributes significantly to the entire energy. This is equivalent to an implicit over-regularization compared to transformations of moderate magnitude, and will lead to piecewise constant displacement fields in homogeneous (i.e. without texture) areas (see Figure 3.5c). Because in such areas, data terms are not very distinctive (i.e. return similar costs for several possible displacements), a locally constant displacement field (with a local regularization cost of 0) is less expensive than smooth transitions. In cases of severe transformations, the implicit over-regularization may even prevent a correct estimation.

Again, higher-order terms can be used to overcome this problem. Regularization should penalize displacement fields that deviate from the perspective transformation model, independent of magnitude of the dominant perspective transformation parameters of Equation (1.4). This can be achieved by using a fourth-order regularization term. Consider four vertices $k, l, m, n \in \mathcal{V}^r$ and their corresponding locations k', l', m', n' induced by the displacement vector field $\mathrm{x}_{i \to j}$. These four correspondences exactly define a perspective transformation $\mathrm{T}_{klmn}^{2\mathrm{D}^\diamond}$. The following regularization cost is then computed:

$$E^\diamond(\mathrm{x}_{i \to j}) = \sum_{(p,k,l,m,n) \in \mathcal{C}^\diamond} E_{pklmn}^\diamond(x_p, x_k, x_l, x_m, x_n) \text{ with}$$

$$E_{pklmn}^\diamond(x_p, x_k, x_l, x_m, x_n) = \left\| \mathrm{T}_{klmn}^{2\mathrm{D}^\diamond} p - (p + x_p) \right\|_2^2. \tag{3.7}$$

To ensure that this regularization has effect on all vertices jointly, the vertices (k, l, m, n) are fixed as the four corner vertices in $\mathcal{V}^r$. All remaining vertices p will then form a fourth-order clique $(p, k, l, m, n) \in \mathcal{C}^\diamond$. As all of these cliques share the same four reference vertices, the set
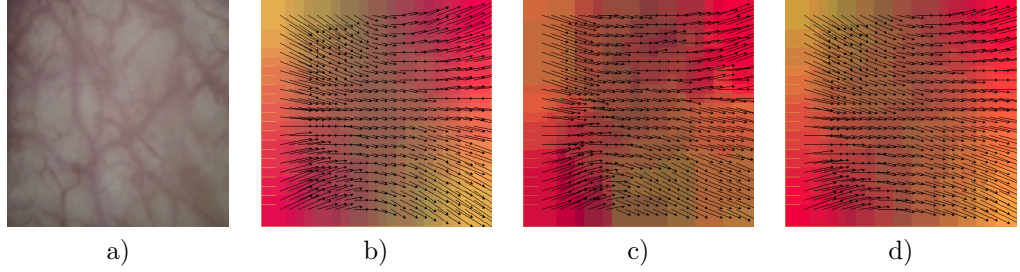
a)   b)   c)   d)

Figure 3.5: Illustration of the advantages of higher-order regularization terms. (a) Source image I_i, showing an image extracted from a cystoscopic video-sequence. The target image I_j was artificially created and is related to I_i by translations $(t_x, t_y) = (5, 1)$ and perspective changes (rotation around the cystoscope's X-axis) $h_x = 2.5e^{-4}$, as defined in Equation (1.4). (b) Displacement vector field $\mathrm{x}_{i \to j}$ obtained using pairwise regularization. (c) Estimated displacement vector field when strong Gaussian noise ($\sigma = 30$) is added to the artificial source and target images. As data terms become less distinctive, the displacement vector field consists of several piecewise constant patches, and results in inaccurate estimation, most evident in the bottom half of c). (d) Estimated displacement vector field using the proposed perspective invariant higher-order regularization term of Equation (3.7). No piecewise constant displacements are estimated, and the resulting displacement vector field conforms with the ground truth.

of vertices is implicitly linked. Intuitively, the data terms ensure that distinctive triangular or quadrangular patches drive the solution towards the optimal data superimposition, while the fourth-order regularization ensures a perspective transformation everywhere. The method was first proposed in (WDWRum), where we applied increasing noise to two input images which were related by random perspective transformations. The proposed regularization term leads to estimated displacement fields that are conform with a perspective transformation (Figure 3.6a), as well as to more accurate registration in general when images suffer from degradations (Gaussian noise was used in (WDWRum), and the results are shown in Figure 3.6b). The geometry of the proposed regularization term is illustrated in Figure 3.7.

3.3.3 Cost Function and Coarse-To-Fine Minimization Scheme

The final energy function to is given by

$$E(\mathrm{x}_{i \to j}) = \alpha \underbrace{E^{\triangle}(\mathrm{x}_{i \to j})}_{2^{\text{nd}}\text{-order data term}} + \beta \underbrace{E^{\square}(\mathrm{x}_{i \to j})}_{3^{\text{rd}}\text{-order data term}} + \gamma \underbrace{E^{\leftrightarrow}(\mathrm{x}_{i \to j})}_{1^{\text{st}}\text{-order regularization}} + \delta \underbrace{E^{\diamond}(\mathrm{x}_{i \to j})}_{4^{\text{th}}\text{-order regularization}} . \quad (3.8)$$

The parameters $(\alpha, \beta, \gamma, \delta)$ are used to weigh the relative importance of each term. Two weight-parameter sets are used according the image pair type to be registered (consecutive or non-consecutive image pairs), which are described in Section 3.5.2. All higher-order terms (Equations (3.4),(3.5),(3.7)) are reduced to their equivalent first-order representation using the method of (Ish09, Ish10) (see Chapter 2 for details). The values of α, β, γ and δ are discussed in detail in Section 3.5.2. As shown by the results, the weights can be constant for patient data.
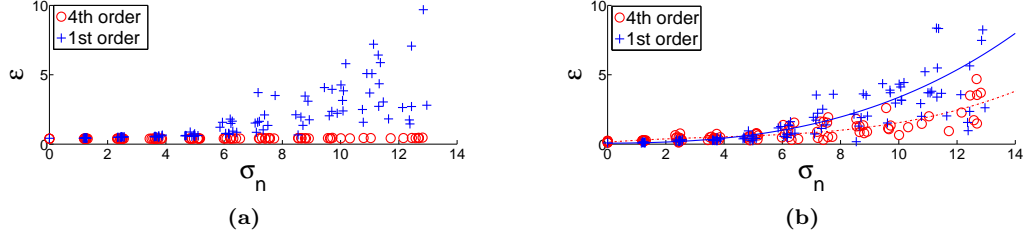
Figure 3.6: Effect of the perspective invariant higher-order regularization term. For both a) and b), the x-axis denotes the standard deviation σ_n of the noise added to the images, while the y-axis represents the registration error ϵ. The error measure ϵ is the mean difference between the estimated displacement vectors and their position as induced by a perspective transformation. (a) With increasing noise level applied to source (I_i) and target (I_j) images, the estimated transformation $\mathrm{T}_{i \to j}^{\mathrm{2D}}$ deviates more and more from the perspective transformation fitted on the displacement vector field (blue crosses). Using the proposed higher-order regularization term, the obtained displacement vector field is always conform with a perspective transformation (red circles). (b) This also leads to statistically more accurate registration when computing ϵ using the ground truth transformation. In Equation (3.15), ϵ is properly defined.

The energy of Equation (3.8) can be minimized using alpha-expansion (Section 2.3.1) and the BHS algorithm (Section 2.2.3). However, the set of potential displacement vectors is very large. For consecutive image pairs, the overlap can be expected to be no less than 90%. Even then, this corresponds to displacements of 40 pixels, which in turn leads to a label set

$$\mathcal{L} = \{(-40, -40), (-40, -39), ..., (40, 39), (40, 40)\}.$$

This would require the computation of $|\mathcal{L}| = 6561$ st-mincuts for one cycle of alpha-expansion. In addition, the higher-order terms add a significant amount of auxiliary variables to the graph. The computation time for one image pair would range in multiples of ten minutes, clearly not suitable for a video-sequence with many hundreds of images. Non-consecutive image pairs may have percentages of overlap less than 50% and stronger transformations, leading to much larger label sets. Therefore, to allow for a second diagnosis some minutes after the examination, a coarse-to-fine energy minimization scheme is required to reduce the computation time.

Image Pyramids

First, the input (source and target) images I_i and I_j are sub-sampled $k_{\max}$ times to form two image pyramids, where levels $k_{\max}$ and k_1 correspond to the original resolution and the lowest resolution, respectively. The size of an image I_i^k at level k corresponds to a fraction of $\omega_k = 0.7^{k_{\max}-k}$ of the original image resolution. Images at level k are obtained by first applying a Gaussian low-pass filter to the original input images (at level $k_{\max}$). The kernel size σ_k for the filter is determined with the formula $\sigma_k = 1.6/(2\omega_k)$, which is known to produce very little discretization artefacts (MY09). The image is then resized by the factor ω_k using bilinear
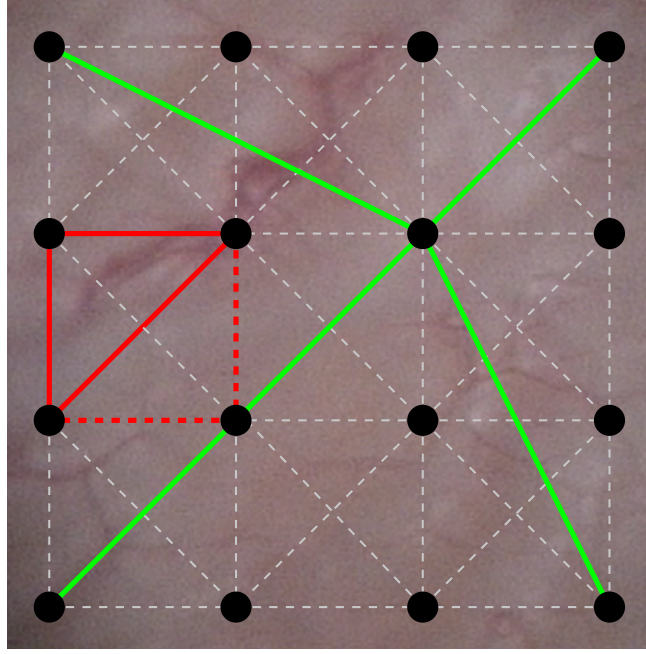
Figure 3.7: Graph structure used for image registration. Black dots represent the regular grid $\mathcal{V}^r$. Dashed grey lines show vertex pairs for which the first-order regularization costs are evaluated (Equation (3.6)). Green lines illustrate a higher-order clique for which the perspective enforcing regularization term (Equation (3.7)) is computed. The red triangle shows a triplet of vertices for which the second-order data term (Equation (3.4)) is computed. If fully perspective data terms need to be computed, the vertex connected to the triangle by a dashed red line forms a third-order clique with the triangle vertices (Equation (3.5)).

interpolation. The number of images in the pyramids directly influences the computation time, as only the coarsest level is searched for the entire range of expected displacements $r_1 = r_{\max}\omega_k$, with $r_{\max}$ being the largest magnitude of expected displacement vectors. For the remaining levels in the pyramid, the range of displacements r_k is strongly reduced. When fewer pyramid levels are chosen, computation time will increase. If too many levels are chosen, the minimization might get trapped in a poor local minima at (very low resolution) level k_1. We will discuss the choice of level numbers in more detail in Section 3.5. Figure 3.8 shows an example of an image pyramid with $k_{\max} = 4$.

Minimization Scheme

The minimization starts at the coarsest level with an initial solution (displacement vector field) $x_{k=1}$. For easier notation, we use $x = x_{i \to j}$. This solution is created from an initial guess of the underlying geometric transformations. For consecutive image pairs, the initial

Figure 3.8: Image pyramid illustration with $k_{\max} = 4$. From (a) lowest resolution at level $k = 1$ to (d) original image resolution at level $k = k_{\max}$.

Algorithm 2: Coarse-to-fine minimization scheme

Input: Initial $\mathrm{T}^{2\mathrm{D}}_{i \to j}$
Output: Final $\mathrm{T}^{2\mathrm{D}}_{i \to j}$
Create x_1 from $\mathrm{T}^{2\mathrm{D}}_{i,j}$;
for $k = 1$ **to** k_{max} **do**
$\quad \hat{\mathrm{x}_k} \leftarrow \mathrm{x}_k$;
$\quad$ **repeat**
$\quad\quad$ **for** $(r_x, r_y)^T \in [-r_k : 1 : r_k, -r_k : 1 : r_k]^T$ **do**
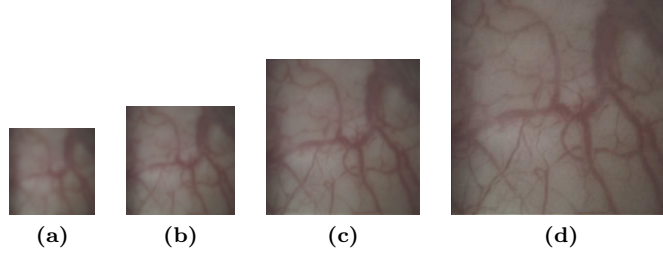$\quad\quad\quad \mathrm{x}_k^P \leftarrow \mathrm{x}_k + (r_x, r_y)^T$;
$\quad\quad\quad \hat{\mathrm{x}_k} \leftarrow \mathrm{Fuse}(\mathrm{x}_k^P, \hat{\mathrm{x}_k})$;
$\quad$ **until** *convergence* ;
$\quad \mathrm{x}_k \leftarrow \hat{\mathrm{x}_k}$;
$\quad$ **if** $k < k_{max}$ **then**
$\quad\quad \mathrm{x}_{k+1} \leftarrow \mathrm{Upsample}(\mathrm{x}_k)$;
$T^{2\mathrm{D}}_{i \to j} \leftarrow \mathrm{LeastSquares}(\mathrm{x}_{k_{\max}})$;

---

guess is the identity matrix[1], while for non-consecutive image pairs, it is created using the initial global transformations $\mathrm{T}^{2\mathrm{D}}_{0 \to j}{}^{-1} \mathrm{T}^{2\mathrm{D}}_{0 \to i}$, which are computed using Equation (3.1) after all consecutive transformations have been estimated. Based on this initial guess, a region of interest is determined, and within this region, the set of vertices $\mathcal{V}^r$ is selected. The region of interest consists of vertices which have a displacement vector pointing to a valid position in I_j. The steps of the coarse-to-fine scheme are illustrated in Algorithm 2 and described below.

The initial solution is then iteratively refined using fusion moves until convergence. Propositions x_k^P are created by adding a set of constant 2D displacement offsets to each element of x_k. The initial magnitude of these offsets is determined by the maximal displacement magnitude r_1 that may relate I_i and I_j. For consecutive images, $r_1 = 75\omega_1$ pixels is used. Non-consecutive images may be related by much larger displacements, so $r_1 = 250\omega_1$ pixels is chosen. The final

---

[1]Here, one could also choose the transformation estimated from the previous image pair, or predict the transformation using a Kalman filter. This may decrease computation time, but has no effect on registration accuracy and robustness, as own tests have shown.

solution $\hat{x}_k$ after each level is then up-scaled to the next level in the pyramid, where it serves as the input x_{k+1}. Again, a region of interest is then computed to select the vertices. For the remaining pyramid levels $k = 2, ..., k_{\max}$, r_k is independent of the underlying transformation fixed to $r_k = 2$[1]. Finally, the solution obtained on the original resolution is then used in a least squares estimation to compute $T_{i \to j}^{2D}$ (see Section 1.3.2).

3.4 Contrast-Enhancing Map Compositing

Once all global transformations $T_{0 \to i}^{2D}$ have been estimated, the final textured map can be created by superimposing the N images on a global planar surface (map coordinate system $\mathcal{V}$). For simplicity, in the remainder of this section, it is assumed that the images are already transformed into the global coordinate system, i.e.

$$I_i = T_{i \to 0}^{2D}(I_i), \ \forall i \in \{0, ..., N-1\}.$$

Previous contributions either perform this superimposition directly (MLHMD$^+$04, MLDB$^+$08, BRM$^+$09), i.e. by overwriting the map image by image, or perform (non-)linear blending techniques to remove/minimize vignetting and exposure related artifacts (WRS$^+$05, HMBD$^+$10, BGS$^+$10). If all images are perfectly aligned and of the same (visual) quality, these approaches will work well. However, as stated in the first section of this chapter, the globally transformed images may still show small misalignments due to local warping of the bladder surface, and in general due to the spherical shape of the bladder projected onto a planar surface. Even after the global map correction of Section 3.2, these small misalignments remain. Additionally, many images suffer from motion blur or de-focus and significantly decrease the visual appearance of the map. Blending techniques therefore, while leading to visually pleasing panoramic images at the first glance, in fact reduce contrast of the underlying images by linearly interpolating between slightly misaligned overlapping parts and by ignoring the images' quality.

The aim of this section is to correct the effects of these small misalignments, while increasing contrast and visual quality of the map. The proposed algorithm consists of two steps, which are formulated as energy minimization problems and solved using graph-cuts:

- First, optimal borders in regions defined by overlapping image parts are determined. These borders, which we refer to as *seams*, are classically used to suppress texture misalignments by choosing transitions where textured structures (e.g. blood vessels) overlap (where misaligned structures intersect). In addition, we extend the graph-cut formulation to include a cost function based on the images' quality, so that pixels in contrasted images are preferred over pixels in blurry images. Unlike previous contributions to bladder

---

[1]Sub-pixel accuracy can easily be integrated by setting the step size to a non-integer value (e.g. $[-r_k : 0.5 : r_k]$ in Algorithm 2) at the expense of increasing computation time. As triangle or quadrangle cliques are already computing image dissimilarity at sub-pixel levels, we found that this did not increase registration accuracy noticeably.

cartography, no blending (linear interpolation between overlapping images) is performed, leading to much more contrasted panoramic images with higher visual quality.

- Then, in the second step, exposure and vignetting related color gradients across the previously found seams are removed. This is achieved without blending (blurring), so that the contrast obtained using the previous step is retained.

3.4.1 Seam Localization

Unlike images for which classical seam detection methods (KSE[+]03b, ADA[+]04) are usually adapted, overlapping images extracted from cystoscopic video-sequences vary significantly in levels of exposure due to the instrument's auto-exposure mode and varying distance to the bladder surface. These differences introduce a strong bias to the optimal seam placement in the classical energy functional. Indeed, a seam connecting a strongly exposed region in one image with a less bright peripheral region in another image induces strong brightness gradients, even if the images are precisely aligned. This in turn will prevent accurate (e.g. seamless) superimposition of vascular structures when the images are slightly misaligned. Since these vascular structures represent only a small percentage of the entire image texture, misaligned vascular structures contribute much less to the overall energy cost than exposure differences do. This bias is illustrated in Figure 3.9c. The general idea of the proposed method is to favor seam positions in image regions with constant colors/brightness so that textures (e.g. vascular structures) have a non negligible impact (in comparison to color gradients) during the seam detection. The advantage of this idea is twice: on the one hand texture discontinuities can be minimized and misaligned vascular structures can be seamlessly stitched, and on the other hand the contrast of the map can be maximized.

As brightness gradients, due to exposure and vignetting, typically correspond to low frequency changes, the seam localization is applied in the high-pass frequency domain by creating high-pass filtered versions of the input (original) images:

$$I_i^{\text{hp}} = I_i - I_i \star G_\sigma, \ \forall i \in \{0, ..., N-1\}, \tag{3.9}$$

where $\star$ denotes the convolution operator, and G_σ the Gaussian convolution kernel. As illustrated in Figure 3.9d, these filtered images effectively ensure that seam positions are not biased by low frequency gradients. Thus, by minimizing an appropriate energy function, vascular structures can be optimally superimposed (e.g. coherently aligned), even if they are slightly misaligned in the overlapping images. This energy function is written as

$$E^{\text{seam}}(\text{x}) = \lambda_{\text{seam}} \sum_{(p,q) \in \mathcal{N}^8} E_{pq}^{\text{seam}}(x_p, x_q) + \sum_{p \in \mathcal{V}} E_p^{\text{seam}}(x_p), \tag{3.10}$$

where $\text{x} : \mathcal{V} \to \{0, ..., N-1\}$ assigns an image index to each pixel in the map. In other words, the color for a pixel p is to be taken from the image I_{x_p}. Correct alignment of vascular structures
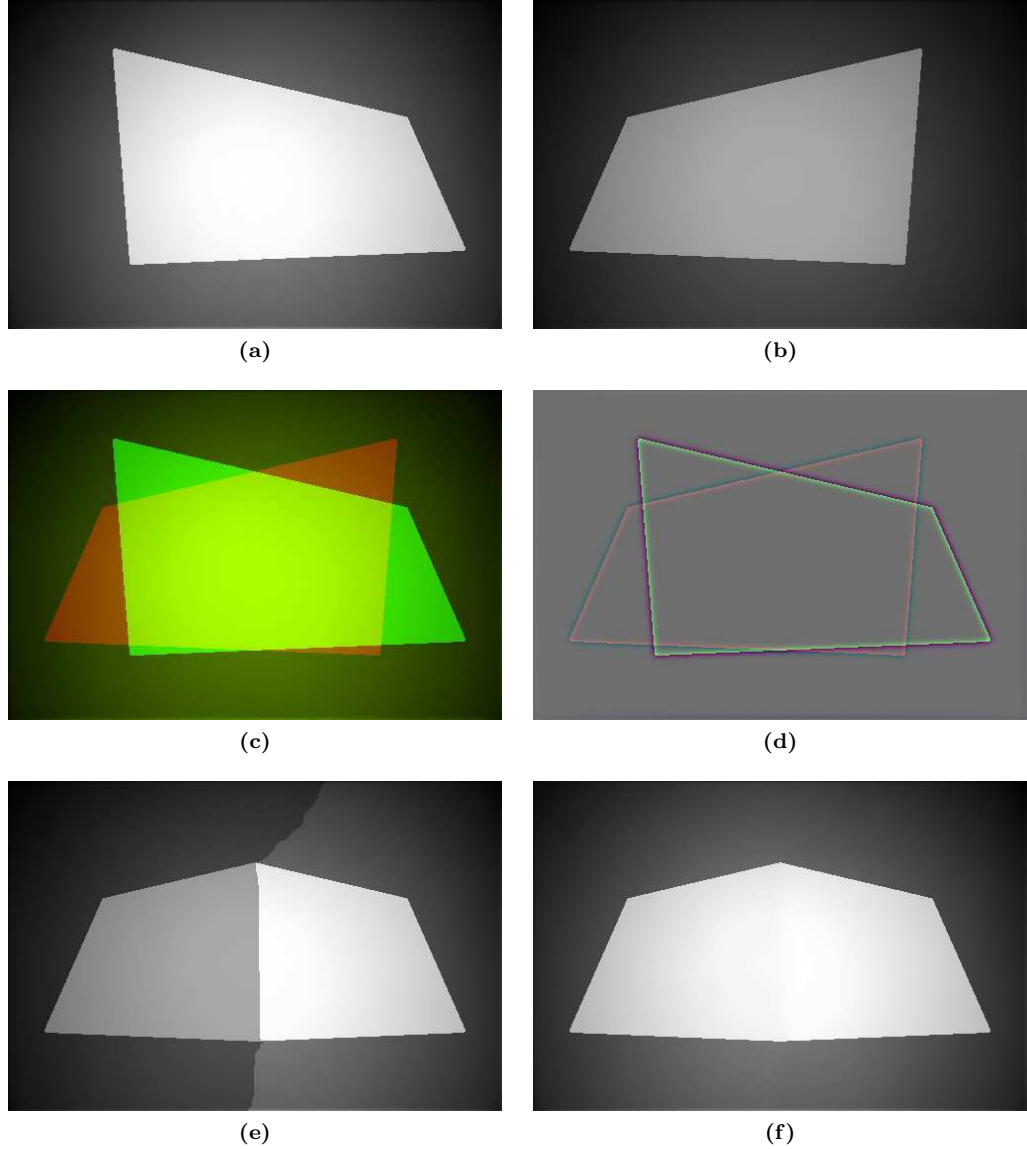
Figure 3.9: Seam detection and exposure correction. (a)-(b) Two input images, (mis-)aligned in a common coordinate system. (Mis-)aligned here means that the images represent globally transformed images affected by errors (as for bladder images, the image superimposition is usually not perfect after the registration, so that small texture discontinuities remain visible in the global map). The error in this example is much larger than for bladder maps for illustration purposes. Vignetting and different levels of exposure is visible. (c) Images overlaid in the red and green channel. The strong exposure difference impedes finding appropriate seam locations. (d) Like c), but using high-pass-filtered images. Potential costs of seams are strongly diminished (i.e. grey pixels) after filtering, except at positions where the object boundaries do not overlap. (e) Seams found using the images of d). (f) After exposure correction.

is encapsulated in the regularization term

$$E_{pq}^{\mathrm{seam}}(x_p, x_q) = \left\| I_{x_p}^{\mathrm{hp}}(p) - I_{x_q}^{\mathrm{hp}}(q) \right\|_2^2 \cdot T(x_p \neq x_q), \tag{3.11}$$

which minimizes gradients along seam lines. As always, $T(\cdot)$ is equal to 1 if its argument is true, else 0. This formulation, similarly used in (KSE$^+$03b, ADA$^+$04), will prefer seams in homogeneous areas (e.g. each connected vascular structure is preferably taken from a single image). If structures are not completely observed in a single image, the seam will likely go through the intersecting region, in case the images do not perfectly align this structure.

However, blurry images tend to be preferred, as the gradients between those is less strong than between contrasted images. This leads to a loss in contrast in the final map. In order to retain as much information from the video-sequence as possible, we introduce a contrast-enhancing data term, formally given by

$$E_p^{\mathrm{seam}}(x_p) = \exp\left(-\frac{\max\limits_{p' \in \mathcal{N}_p^{11}} I_{x_p}^{\mathrm{hp}}(p') - \min\limits_{p' \in \mathcal{N}_p^{11}} I_{x_p}^{\mathrm{hp}}(p')}{\max\limits_{p' \in \mathcal{N}_p^{11}} I_{x_p}^{\mathrm{hp}}(p') + \min\limits_{p' \in \mathcal{N}_p^{11}} I_{x_p}^{\mathrm{hp}}(p')} \right). \tag{3.12}$$

This term computes the contrast in image I_{x_p} using Michelson's formula in an 11x11 neighborhood $\mathcal{N}_p^{11}$ for a pixel p. A high contrast corresponds to well a focused image and leads to a low energy, and vice-versa.

Equation (3.10) is minimized via alpha-expansion until convergence. The pairwise terms (Equation (3.11)) are not necessarily submodular with regard to alpha-expansion. While $E_{pq}(\alpha, \alpha)$ is always equal to zero, $E_{pq}(x_p, x_q)$ may be larger than $E_{pq}(x_p, \alpha) + E_{pq}(\alpha, x_q)$ at some point. However, the number of non-submodular terms is very small (always less than 0.1%, but mostly exactly 0%) in all experiments, so the BHS algorithm drives the solution to a strong local minimum.

3.4.2 Exposure and Vignetting Correction

Minimizing Equation (3.10) ensures that vascular structures are seamlessly superimposed (even if the images are initially not perfectly aligned). In addition, loss of information is minimized by preferring contrasted images over blurry ones. When applying the obtained solution (image index x_p for each pixel $p \in \mathcal{V}$) to the original images, stitching induced color gradients due to exposure and vignetting are strongly noticeable (see Figure 3.9e). These effects can be significantly attenuated using blending techniques (see again Section 1.3.4). However, classical blending methods affect the contrast and seamless alignment obtained by the method of the previous section. Instead, exposure related differences (across seams) must be removed while retaining contrast and alignment. Removing these differences should also not lead to drastic (and unnatural) color appearance changes. This last constraint can be formulated using the following data term:

$$E_p^{\mathrm{exp}}(m_p) = \left\| \frac{I_{x_p}(p)}{||I_{x_p}(p)||} - \frac{m_p}{||m_p||} \right\|_2, \tag{3.13}$$

where now the solution m $: \mathcal{V} \rightarrow \mathcal{L} \subset \mathbf{R}^n$ assigns n-dimensional color vectors m_p ($n = 3$ for RGB color space) to each pixel p in the map. Equation (3.13) ensures that a color vector m_p points in the same direction[1] (in the n-dimensional color space) than the original color vector of the input image $I_{x_p}(p)$, as given by the solution x of Equation (3.10) obtained in the previous step. Since the intensities of colors may change without penalty, but strong changes in hue and saturation are penalized, the natural aspect of the epithelium is preserved. Removing color gradients along the previously determined seam lines (i.e. when $x_p \neq x_q$) should also ensure that the contrast of the original images is retained. This is achieved by penalizing gradient differences within connected image segments (e.g. when $x_p = x_q$):

$$E_{pq}^{\exp}(m_p, m_q) = (T(x_p = x_q) \cdot ||I_{x_p}(p) - I_{x_q}(q)|| - ||m_p - m_q||)^2,$$

where $T(\cdot)$ equals 1 when its arguments are true, and 0 otherwise. Combining both exposure correction terms leads to the following energy function:

$$E_{\exp}(m) = \sum_{p \in \mathcal{V}} E_p^{\exp}(m_p) + \lambda_{\exp} \sum_{(p,q) \in \mathcal{N}^4} E_{pq}^{\exp}(m_p, m_q), \tag{3.14}$$

where the use of the $\mathcal{N}^4$ is necessary, as previous seams were determined using the complementary $\mathcal{N}^8$. If both seam detection and exposure correction were based on the same connectivity, certain exposure differences could not be corrected without inferring new ones. Equation (3.14) is iteratively minimized using fusion-moves. In each iteration, the propositions m^p are generated by multiplying each color channel of the current solution m^c with a constant value. These n values (one for each color channel) are generated as follows. First, a random number in the interval $[0.9, 1.1]$ is generated. To this number, smaller random values $[\pm 0.01]$ are added for each color channel. The large variation between m^c and m^p ensures that both darker and brighter regions may converge to a common brightness level, while the small variations between color channels allow for seamless transitions between different images in case of slight color differences (e.g. due to auto white balance). As there is no guaranteed number of iterations until convergence (as opposed for instance with alpha-expansions), the algorithm is said to converge when the energy decrease within a fixed interval of fusion moves drops below a threshold.

3.5 Results

The proposed methods will be evaluated both quantitatively on realistic phantom data, as well as qualitatively on clinical data. In Section 3.5.1, the registration and cartography accuracy quantified with phantoms will be discussed and compared with state-of-the-art white light cartography algorithms. Then, Section 3.5.2 will briefly recapitulate each step of the proposed

---

[1]In the special case of grey value images ($n = 1$), which we only consider in the example shown in Figure 3.9, every grey value points to the same direction (i.e. RGB color cube diagonal), so Equation (3.13) will always return 0.
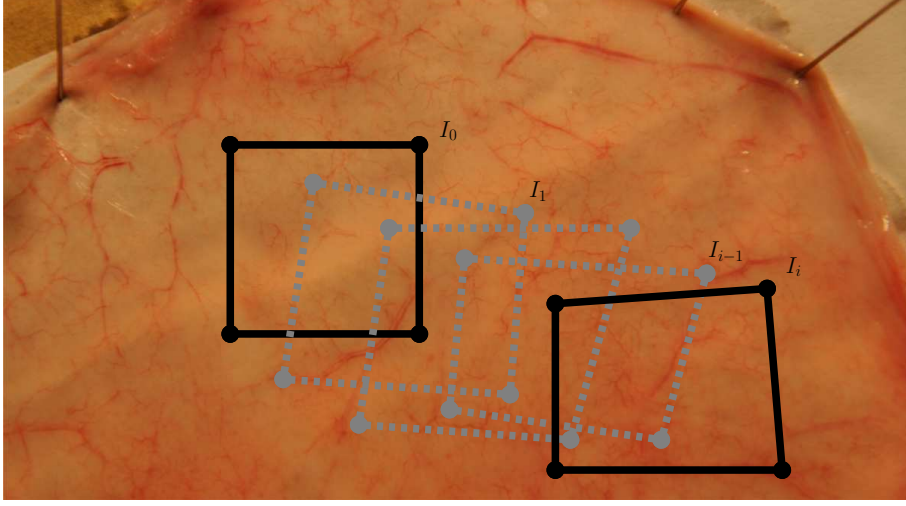
Figure 3.10: Illustration of phantom video-sequence generation. The incised and flattened pig bladder is fixed by needles and photographed in high resolution (for illustration only a small portion of the image is shown). Even for urologists it is difficult to distinguish pig bladder texture from human bladder texture. The reference image $I_{i=0}$ is first selected as a rectangular sub-figure of the high resolution pig bladder photograph. Successive images I_{i+1} are then generated by applying known local transformations $T_{i \to i+1}^{2D^{\star}}$ to the location (borders) of the current image I_i.

algorithm and show qualitative (and where possible quantitative) results obtained for clinical patient data. The advantage over existing methods will also be demonstrated. In addition, several panoramic images of clinical data will be shown and discussed. Finally, in Section 3.5.3 the proposed methods will be applied to non-medical applications to demonstrate their general applicability.

3.5.1 Quantitative Evaluation on Phantom Data

Ground truth transformations (i.e. the true $T_{i \to j}^{2D^{\star}}$ matrices) are impossible to obtain from clinical data because the endoscope is displaced freely (with unknown trajectories) inside the organ during a cystoscopic examination. Therefore, in order to quantitatively assess the proposed registration method, a set of phantom test sequences were generated, similar to those used in (HSB$^+$09).

Three pig bladders were incised, opened up, and photographed with a camera. These high resolution pictures are used to create phantom image sequences with typical cystoscope displacements. To do so, a reference image I_0 is first chosen on the map (i.e. it is a 400×400 pixel sub-image of the high resolution picture). The image sequence is then created by choosing local transformations $T_{i \to i+1}^{2D^{\star}}$, which are used to update the global ground truth transformations $T_{0 \to i}^{2D^{\star}}$. These are used to extract each image I_i from the high resolution pictures. Figure 3.10 illustrates the procedure of generating phanom data for three pig bladders. The cystoscope's

ϕ	$S_x = S_y$	s_x, s_y	h_x, h_y	t_x, t_y
$\pm 5°$	$[0.95, 1.05]$	$[0.95, 1.05]$	$\pm 10^{-5}$	≈ 50 pixels

Table 3.1: Intervals for parameters of Equation (1.4) for the phantom simulations. The maximum values rarely occur between consecutive images in real sequences, particularly when they are combined.

translation (i.e. the parameters t_x, t_y of Equation (1.4)) was simulated by moving the mouse along the high resolution phantom images and capturing images at a fixed timed interval. The average 2D translation displacement corresponds to a radius of about 50 pixels[1]. The other parameters of Equation (1.4) (in-plane rotation ϕ, scale factor (S_x, S_y), shearing parameters (s_x, s_y), and perspective parameters h_x and h_y) were chosen randomly from a set of intervals. The interval limits were determined heuristically by decomposing transformations from clinical data. The maximum values, as shown in Table 3.1, rarely occur in practise. This leads to realistic simulated cystoscope displacements with known $T_{i \to j}^{2D^\star}$ perspective transformations.

Three different trajectory types were assessed with the phantoms. In the first sequence, a "zigzag"-path is simulated. As shown in Figure 3.11a, the endoscope trajectory leads to two sections of overlap. The second sequence simulates a single loop (see Figure 3.11b), while the third sequence corresponds to a loop sequence with two sections of sufficient overlap (see Figure 3.11c). These three types of overlapping scenarios often occur during clinical examinations, as will be seen in Section 3.5.2.

The registration error is quantified using the mean endpoint error (Euclidean distance) in pixels ([px] in Figures 3.11d-i), as used in the Middlebury optical flow database (BSL+11):

$$\epsilon_{i \to j}^{2D} = \frac{1}{|\mathcal{V}|} \sum_{p \in \mathcal{V}} \left\| T_{i \to j}^{2D^\star} p - T_{i \to j}^{2D} p \right\|_2. \tag{3.15}$$

$T_{i \to j}^{2D^\star}$ is the ground truth transformation, and $T_{i \to j}^{2D}$ corresponds to the estimated transformation. The distance $\epsilon_{i \to j}^{2D}$ is the mean distance between pixels placed into the coordinate system of image I_j ($T_{i \to j}^{2D} p$) and the corresponding true position $T_{i \to j}^{2D^\star} p$, whereas $|\mathcal{V}|$ is the number of pixels in I_i. The global cartography errors $\epsilon_{0 \to i}^{2D}$ are also computed using Equation (3.15). Ideally, $\epsilon_{i \to j}^{2D}$ is null.

The average local registration error for consecutive image pairs is constantly low in all three sequences, as can be seen in Figures 3.11d-f (green curves, with a mean $\epsilon_{i \to i+1}^{2D} \approx 0.2$ pixels). The corresponding global cartography errors $\epsilon_{0 \to i}^{2D}$ are given in Figures 3.11g-i. The red curves indicate cartography errors without map correction (i.e. only consecutive (I_i, I_{i+1}) image pairs are registered and the global matrices $T_{0 \to i}^{2D}$ are obtained via concatenation).

The detected additional non-consecutive image pairs are indicated using white lines in Figures 3.11a-c. Registering these pairs led to an average local registration error of $\epsilon_{i \to j \neq i+1}^{2D} = 0.32$,

---

[1]In a 24 images/second cystoscopic video-sequence, the displacement is much smaller than 50 pixels. As will be discussed later, in order to reduce computation time and decrease accumulation of errors, only every tenth image is extracted from the videos. This usually corresponds to an image pair overlap of $\simeq 90\%$, or $\simeq 40$ pixels.
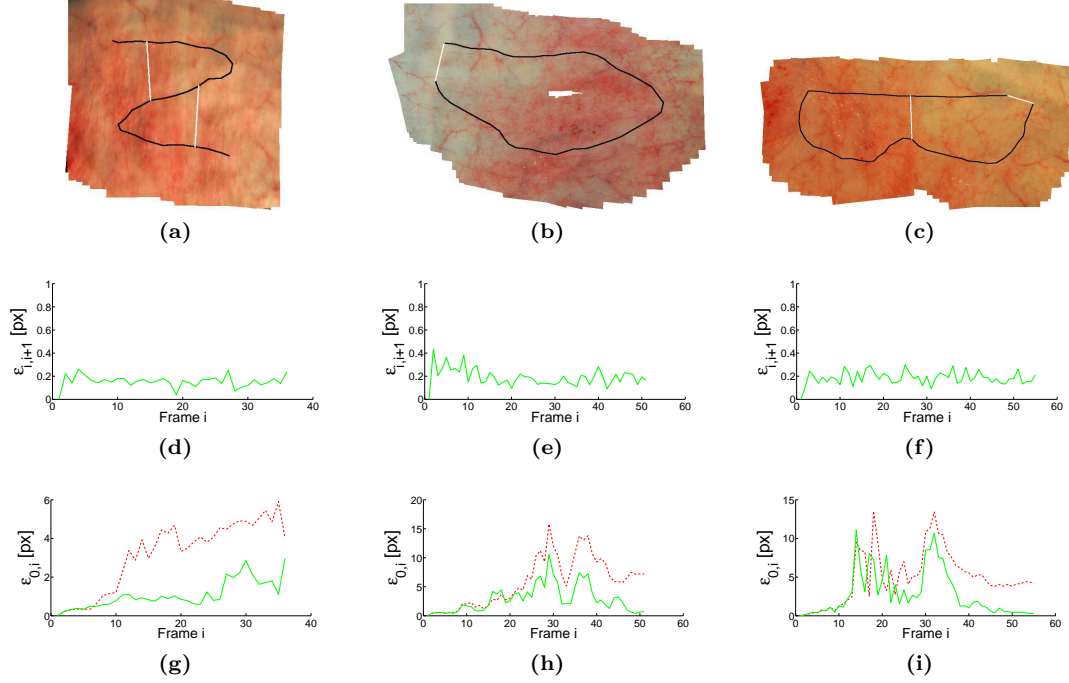
Figure 3.11: Results on phantom data. (a)-(c) Final (corrected) maps with the cystoscope trajectory (the dots of the blue curves indicate images centers on the global map) and additional transformations (white lines) overlaid. (d)-(f) Mean local registration errors, computed respectively for images (a), (b) and (c). (g)-(i) Mean global cartography errors for initial (non-corrected) maps (red dotted lines) and corrected maps (green lines), again computed for (a) to (c). It is noticeable that the points of the green curves are systematically below the red curves.

which comes close to the errors for registering consecutive image pairs. The combined set of consecutive and non-consecutive local transformations matrices $T_{i \to j}^{2D}$ were then used to compute corrected global transformations $T_{0 \to i}^{2D}$, as explained in Section 3.2. The corrected global cartography errors are shown as green curves in Figures 3.11g-i, where global errors diminish in regions were loops are closed. On image Figure 3.11b, it is noticeable that loop beginning and loop end correspond respectively to the first and last images of the sequence. In Figure 3.11h, at image number 50 on the x-axis, it can be seen on the red curve that the cartography error at the sequence end is large (about 10 pixels). After map correction (green curve), the cartography error at the sequence end is almost null leading to a closed loop region without texture discontinuities. In Figure 3.11c, the almost horizontal white line located on the right of the map represents also a closing loop. Figure 3.11i gives again the cartography error before (5 pixels) and after (≈ 0 pixels) loop correction.

Moreover, the global correction is not performed at the expense of the local registration quality. In fact, the local registration errors, shown in Figures 3.11d-f, correspond to errors

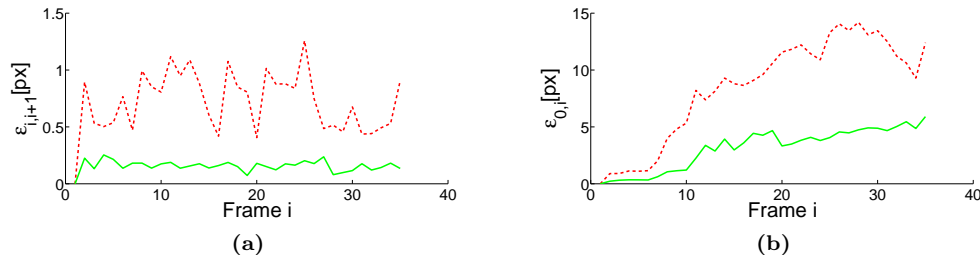**Figure 3.12:** Comparison of the new method (green lines) with the sparse graph-cut method (red dotted lines) described in Chapter 2 and (WDBH⁺na). (a) Registration error comparison. (b) Global cartography error comparison. It is noticeable that both the registration and cartography results are more accurate for the algorithms presented in this chapter. Moreover, the registration algorithm performs similar for each image pair, demonstrating its robustness and invariance to the perspective transformation parameters.

after global correction, but are almost similar to those before global correction. The "zigzag" sequence (Figure 3.11a) does not contain loops, so the global cartography errors increases with time even after global optimization, and cannot be null at the sequence end. However, due to the two additional transformations (white lines in Figure 3.11a) that link the three almost rectilinear cystoscope trajectory parts, these global errors are strongly diminished.

For all three sequences, the errors between overlapping regions are low, leading to visually coherent panoramic maps of the phantom data.

To put the performances of the proposed registration methods in perspective, they could be compared to the different existing methods for white light bladder image registration, namely the mutual information based method (MLHMD⁺04, MLDB⁺08), the optical flow method of Baker and Matthews (HMBD⁺10), and the sparse graph-cut method described in Section 2.5 and published in (WDBH⁺na). However, in (WDBH⁺na), it was shown on phantom data (see also Figure 2.17) that the sparse graph-cut method is by far the most accurate in comparison to the mutual information and Baker and Matthews methods, independent of the parameters of the tested perspective transformations. In other words, the results of (WDBH⁺na) let us reason that the methods of (MLHMD⁺04, MLDB⁺08, HMBD⁺10) will lead to even higher global cartography errors. For this reason, the registration algorithm described in this chapter is only compared to sparse graph-cuts.

Tests performed in Chapter 2 have shown that the registration accuracy of the sparse graph-cut method is very high (errors of some few tenths of a pixel) and almost independent of the parameter values of the underlying perspective transformation. It is noticeable on Figure 3.12a that the registration errors of this method is now by far larger (between 0.5 and 1 pixel error). The reason for this drop in performance of the method of (WDBH⁺na) lies in the fact that the simulated transformations were stronger than those tested in (WDBH⁺na). In (WDBH⁺na), not only the perspective transformation changes were by far smaller, but the parameters did also not change strongly in a simultaneous way.

To compare the sparse graph-cut approach and the new method proposed in this chapter we have computed the map of Figure 3.11a with both methods. To be able to compare both algorithms, no map corrections with additional non-consecutive image pairs was used. As can be seen in Figure 3.12a, the registration error of (WDBH⁺na) is roughly between twice and thrice as large in comparison to the errors of the method proposed in this chapter. The other important result of the new registration method is that the registration error remains constant (independent of the perspective transformation), and the images are robustly superimposed, even for stronger perspective changes. It is also noticeable on Figure 3.12b that, for the sparse graph-cut approach, the varying local registration errors lead to much higher global cartography errors (twice as high after 25-30 images) than those of the method proposed in this chapter. It should be noted that it was still possible to detect additional overlapping image pairs for the sequence in Figure 3.11a. However, registering these additional pairs using the method of (WDBH⁺na) did not lead to satisfying results. The energy got stuck in poor local minima due to the strong perspective transformations involved. For the other phantom (and patient) sequences, even some consecutive image pairs failed to register correctly with the sparse graph-cut method, while such failures were not observed with the method described in this chapter.

Even if the registration and cartography algorithms presented in this chapter are very accurate and robust, the comparison with (WDBH⁺na) justifies the statements made initially. Globally accumulated cartography errors must be kept as low as possible, in order to be able to detect sections of overlap and correct these errors. As robustly detecting non-consecutive image pairs is required to build visually coherent maps, we can conclude that projectively invariant energy formulation is an important step towards accurate registration and global cartography. This helps to keep accumulated errors low for accurate overlap detection, and allows to register non-consecutive image pairs, which are related by much stronger perspective transformations. Registration of such non-consecutive image pairs is impossible with state-of-the-art white light registration algorithms proposed in (MLHMD⁺04, MLDB⁺08, HMBD⁺10) and with the sparse graph-cut method (WDBH⁺na).

3.5.2 Qualitative Evaluation on Clinical Data

Having quantitatively justified the improvements of the proposed registration methods on simulated phantom data in the previous section, this section will present results obtained on clinical data. Six cystoscopic video-sequences acquired at the comprehensive cancer center of Nancy (Institut de Cancérologie de Lorraine, ICL) were processed to assess the applicability of the proposed methods on patient data. The purpose of the each individual algorithm step will be briefly recapitulated and discussed using the results.
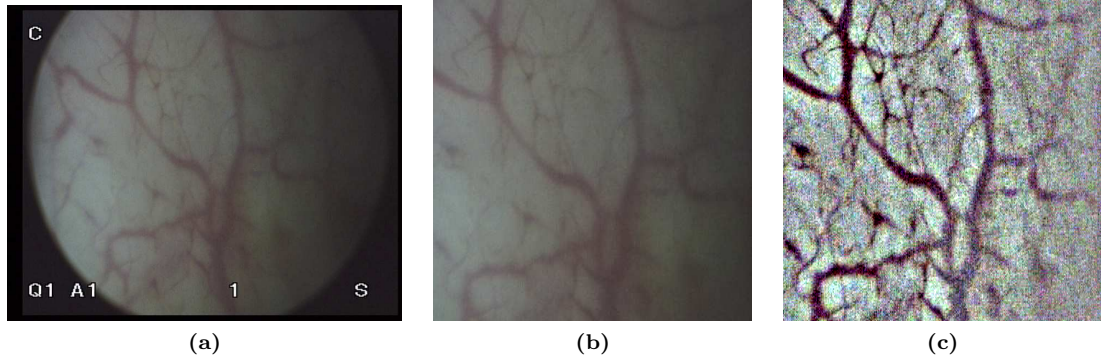
Figure 3.13: Image pre-processing. (a) Original image, de-interlaced. (b) Cropped sub-image, where distortions can be neglected. Illumination gradients are visible. (c) Illumination corrected image, as used for the registration data terms of Section 3.3.1 and the contrast-enhanced seam localization described in Section 3.4.1. Note that the image of c) has been normalized for viewing. The visible noise is also present in the image of b), but not as visible in the original image.

Video Pre-Processing

Pre-processing is necessary to prepare the original cystoscopic video-sequences for robust cartography. First, the videos, recorded with the PAL standard, have to be de-interlaced. Then, a 400×400 pixel sub-image is extracted from each image, where image distortions are negligible (HMBD$^+$10). The last step consists of removing illumination differences due to vignetting and non-orthogonal angle of the cystoscope towards the epithelium. This is achieved by subtracting a bandpass-filtered image from the de-interlaced and cropped input image, similar to the method proposed in (HMBD$^+$10), which was described in Section 1.3.1. Figure 3.13 shows these pre-processing steps, and the illumination corrected images (Figure 3.13c) are used as input for both the registration data terms (see Section 3.3.1), as well as for the contrast-enhanced seam detection method (Section 3.4.1). Finally, from the initial 25 images per second video, a subset of images depending on the overall speed of the cystoscope movement is extracted. In our experiments, we extracted every tenth image.

Registration of Consecutive Image Pairs

For consecutive image pairs, the percentage of overlap is quite large and the translation components of the perspective transformation are usually the dominant parameters. For instance, when every tenth image is extracted from the video-sequence, consecutive images have a typical overlap of 85% or more of the image area. In order to minimize the computation time, different parameter sets were used for consecutive image pairs on the one hand, and for non-consecutive image pairs on the other hand. The parameters given in Table 3.2 (see Equation (3.8)) are used for the registration of consecutive image pairs.

α	β	γ	δ	$k_{\max}$	r_1
1	0	1	0	8	75 pixels

Table 3.2: Constant parameters used for consecutive image registration. These parameters correspond to those of Equation (3.8). Due to translation dominated perspective transformations linking consecutive images (see also Figure 3.14), it is sufficient to use second-order data and first-order regularization terms. This leads to potential costs easier to minimize and consequently to faster convergence time, as opposed to the parameter set necessary for non-consecutive image pairs (Table 3.3).
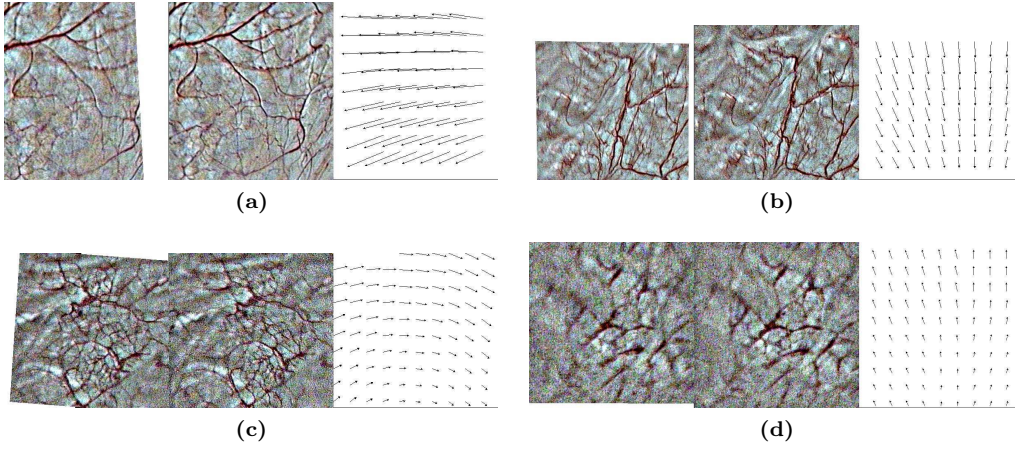
Figure 3.14: Examples of the registration of consecutive images pairs. The images usually share a large percentage of overlap, and while the contrast of the images varies throughout the video-sequence, it is similar between successive images. In each sub-figure, from left to right: image I_i transformed to the coordinate system of I_j; I_j; estimated displacement vector field.

Constant parameters were used for all consecutive pairs, but were not exhaustively fine-tuned. In turn, variations between $50 - 200\%$ of the parameter γ (pairwise regularization of Equation (3.6)) do not change the resulting displacement field noticeably, which emphasizes the robustness of the second-order data terms. Figure 3.14 shows a few examples of registered consecutive image pairs. The geometric relationship is dominated by translations, while rotation and scale changes are also often observed, especially when the cystoscope's direction changes.

As only second-order data terms and pairwise regularization terms are used for the registration of consecutive images, computation time is significantly lower than the time needed to superimpose non-consecutive images. A pair of consecutive images is registered in ten to twenty seconds[1]. While the BHS algorithm itself is difficult to parallelize[2], the registration of different

---

[1] All experiments were computed on a quad-core 3.3GHz desktop computer with 16 GB of RAM, running Ubuntu 12.04.

[2] There are parallel graph-cut implementations available (e.g. (VN08)), but they are only suitable for regular grids. Auxiliary variables induced by higher-order terms do not fit in this formulation, neither do irregular graph structures.

α	β	γ	δ	$k_{\max}$	r_1
1	0	1	0	6	125 pixels

(a) Parameter set for $k = 1$

α	β	γ	δ
1	0	0	500

(b) Parameter set for $k > 1$

Table 3.3: Constant parameters used for non-consecutive image registration, corresponding to Equation (3.8). (a) At the coarsest pyramid level ($k = 1$), higher-order regularization may lead to a large number of non-submodular terms when the initial transformation deviates from the true transformation. To prevent poor local minima, pairwise regularization is used at the initial pyramid level. (b) Parameter set for the remaining levels ($k > 1$). Due to the large number of non-submodular terms when using third-order data terms (Equation (3.5)) and fourth-order regularization (Equation (3.7)), these two terms cannot be used simultaneously.

(a)

(b)

(c)

(d)
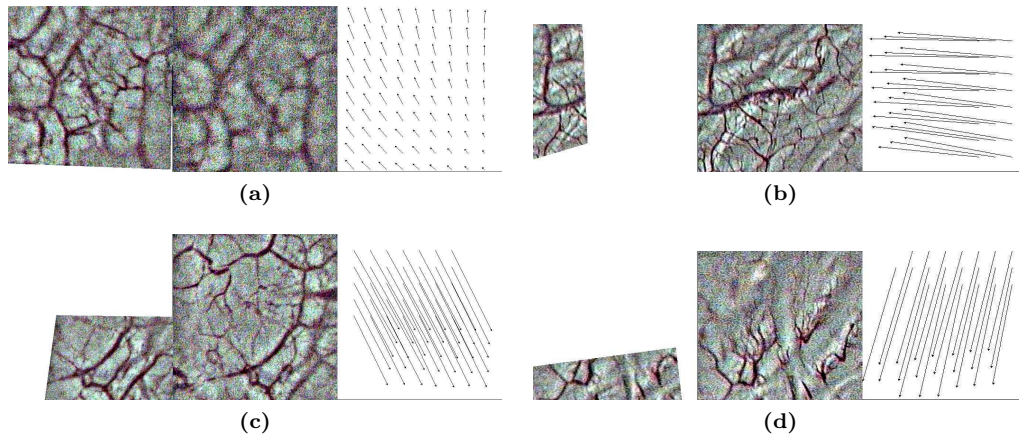
Figure 3.15: Examples of the registration of non-consecutive images pairs. Note the varying contrast between non-consecutive images (e.g. in a)) and the low percentage of overlap (b-d). These image pairs cannot be registered using state-of-the-art white light registration methods (MLHMD+04, MLDB+08, HMBD+10, WDBH+na). Using the proposed higher-order data and regularization terms, approximately invariant to projective transformations, allows to register such image pairs robustly.

image pairs can be easily distributed to several cores, as each CPU can process a pair of images in parallel. When every tenth image is extracted from the video (as done in the experiments), one second of a cystoscopic video can be processed in 7-14 seconds using four CPUs.

Registration of Non-Consecutive Image Pairs

Non-consecutive image pairs are registered using the constant parameters given in Table 3.3. Some examples of registered non-consecutive images pairs are given in Figure 3.15. As can be seen there, such image pairs may share a low percentage of overlap (e.g. Figures 3.15b-d), may be related by strong variations in the displacement vector field, and often differ in contrast (see

Figure 3.15a).

Due to potential displacements of large magnitude and low overlap, the fully projective third-order data term and the perspective-enforcing fourth-order regularization term seem to be the best choice for accurate registration of non-consecutive image pairs. Unfortunately, using both Equation (3.5) and Equation (3.7) (i.e. $\beta > 0$ and $\delta > 0$) leads to a very low percentage of labeled vertices due to the large number of non-submodular terms after reduction to pairwise interactions. While roughly 40% of image pairs could be accurately registered, it was not systematically possible (i.e. for the majority of non-consecutive image pairs, the solution got trapped in poor local minima). However, the second-order data terms of Equation (3.4) lead to a valid approximation of the perspective transformation model. For this reason, we have discarded the fully perspective data terms in favour of the perspective-enforcing fourth-order regularization terms, which are crucial for robustly registering non-consecutive image pairs.

It is noticeable that Equation (3.7) still leads to a significant number of non-submodular terms at the initial level in the proposed coarse-to-fine minimization scheme. If the initial transformation is inaccurate and deviates strongly from the transformation to be found at the coarsest pyramid level, both $E_{pq}(x_p^c, x_q^c)$ (i.e. initial solution) and $E_{pq}(x_p^p, x_q^p)$ (proposed solutions) will have large costs[1]. These costs will violate the submodularity constraint of Equation (2.8) and lead to many vertices being unlabeled. In such cases, the solution obtained after the coarsest level will be far from the true transformation to be found, and consequently, the minimization will get trapped in poor local minima. In order to prevent wrong initial registration at the coarsest pyramid level, the parameters given in Table 3.3a are used at the initial pyramid level. For the remaining levels, the parameters given in Table 3.3b are used. This ensures that an initial solution close to the global minima is reached and enough variables can be labeled when using Equations (3.4) and (3.7) in the remaining pyramid levels.

These terms lead to computation times significantly longer (30 - 60 seconds per pair and CPU) than those for registering consecutive image pairs. However, the number of non-consecutive image pairs is much smaller than the set of consecutive pairs, so the increase of computation time has less influence on the computation time of the entire sequence. For instance, for the patient data of Figure 3.16, 75 images are linked by consecutive $T_{i \to i+1}^{2D}$ matrices, while only 6 non-consecutive image pairs were selected. The computation time of the 75 consecutive images is about 1000 seconds, while the non-consecutive images are registered in $6 \times 45 = 270$ seconds. Such processing times are compatible with a second diagnosis and patient interview shortly after the examination.

Global Map Correction

After all consecutive image pairs have been registered, the subset of additional overlapping image pairs can be determined (i.e. the non-consecutive image pairs that have to be registered).

---

[1] After reduction of higher-order potentials to their equivalent pairwise form.
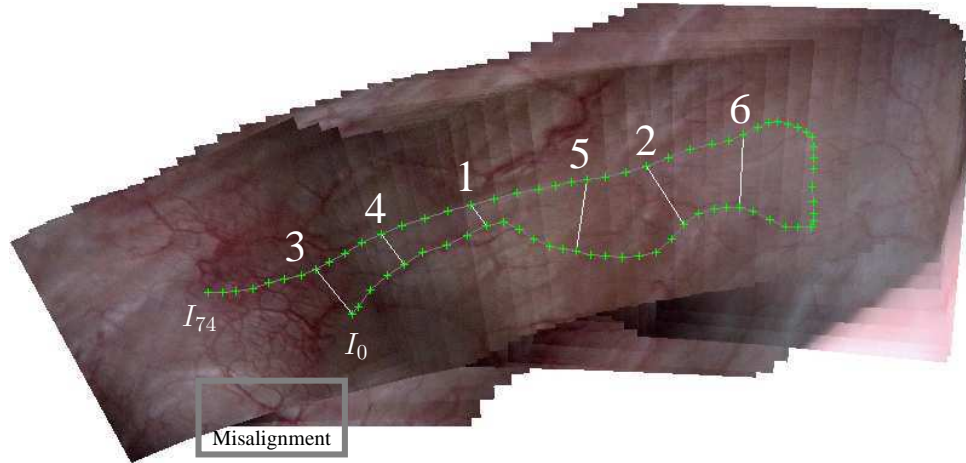
Figure 3.16: Determining a subset of overlapping, non-consecutive image pairs. The cystoscope trajectory (grey lines) and the image centers (green dots) are overlaid on the initial (uncorrected) map. The accumulated cartography error is visible between first (I_0) and last (I_{74}) images of the sequence near the bottom left hand side, as indicated by the grey rectangle. The additional image pairs are indicated by white lines, and the chronological order in which they have been determined is indicated by the numbers. The corrected map can also be seen in Figure 3.18.

Figure 3.16 represents a map built only using consecutive transformations (i.e. no map correction was applied), and illustrates how and in which chronological order additional pairs are found. The cystoscope trajectory (grey lines) is projected on the map, and the center of each image is indicated with a green cross. The global cartography error is visible in the bottom left part of the map (indicated by the grey rectangle) between first I_0 and last I_{74} images of the sequence, but low enough to be able to correctly detect additional overlapping image pairs. These are indicated by white lines, and the corresponding number indicates in which chronological order these pairs have been determined.

Whether the search for additional image pairs will be successful or not depends on the amount of accumulated error during the cartography process. This error is often directly connected to the number of images acquired before returning to a previously visited location. Indeed, the more images are registered, the more the global errors accumulate. However, errors also increase quickly when a few pairs of images are inaccurately registered. When accumulated errors become too large, non-consecutive images that actually capture a common region on the bladder surface might not overlap at all in the estimated initial global transformations. An example for this situation is shown in Figure 3.17d. The cystoscope trajectory is overlaid with black lines, and found additional image pairs are indicated by white lines. The map is constructed using the optimized global transformations, so visible misalignments due to accumulated errors are already removed. It is noticeable however that no additional pair was found in the top left part of the map. This is due to the fact that in this video-sequence, the images are degraded by tissue floating in front of the camera. This influences the registration

(a)   **(b)**   **(c)**

(d)   **(e)**
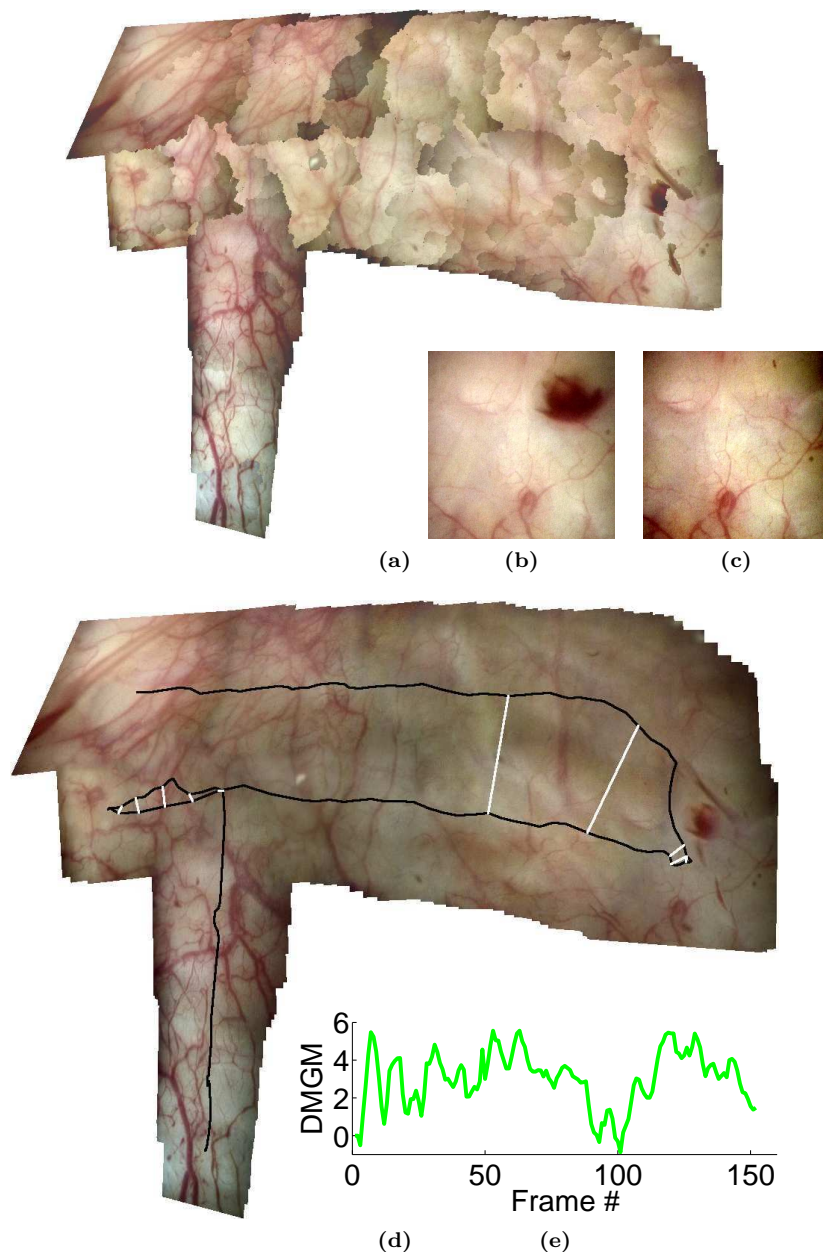
Figure 3.17: Exposure correction and the effects of floating tissue degradation on image registration accuracy and overlap detection. (a) Images placed into the global map coordinate system using the found seams. While all vascular structures are well aligned, exposure related artefacts are strongly noticeable. After exposure correction, the map in (d) shows visually coherent transitions. (b),(c) Consecutive image pair, degraded by floating bladder tissue. Such degradations lead to less accurate image registration when using first-order regularization. The thus accumulated errors led to the top cystoscope trajectory being estimated further to the top in the intial map, and no additional pairs with enough overlap could be detected in the top left part of the map coordinate system. However, the errors were low enough to detect the four additional transformation on the right hand side (after the 180 degree trajectory change). The perspective-invariant higher-order regularization terms are robust against floating tissue, and the obtained shortcut transformations significantly reduced accumulated errors. For this reason, the map could still be stitched seamlessly, and even in the top left hand side, all vascular structures are well aligned.

accuracy, leading to larger local registration errors. An example for a consecutive image pair where floating tissue complicates registration[1] is shown in Figures 3.17b-c. Local errors in this map region led to the top cystoscope trajectory improperly estimated further to the top. Consequently, no overlap could be detected in that region. However, the error was still low enough to detect the four additional pairs near the trajectory direction change (white lines at the right side). As these corresponding non-consecutive image pairs were registered using the perspective-invariant higher-order regularization term, the floating tissue did not have a noticeably degrading influence on the local registration accuracy. Thus, the obtained "shortcut" transformations led to much lower accumulated errors, and the map could be stitched seamlessly (as can be seen in Figure 3.17d). Using these optimized transformation matrices, additional overlapping image pairs could be detected in a second iteration of the algorithm.

For all experiments, the parameters of Algorithm 1 were set to $t_\delta = 0.2$ and $t_\vartheta = 0.7$.

Map Compositing

After all consecutive and selected non-consecutive image pairs have been successfully registered, and global map correction has been applied, the images can be placed into the common map coordinate system to compose the final panoramic image. As stated earlier, small movements of the bladder surface and small errors due to the non-flat surface of the organ will still lead to small (but visible) misalignments of vascular structures, especially for overlapping cystoscope trajectory parts. At the same time, cystoscope de-focus and motion blur vary throughout the sequence. The goal of the contrast-enhancing seam correction method proposed in this chapter is to correct these small misalignments, and select the sharpest images for each region of the panoramic map. Figure 3.18 demonstrates the efficiency of the proposed method when using different regularization weights. Higher regularization weight ($\lambda_{\mathrm{seam}} = 1$ of Equation (3.10)) leads to relatively small seam lengths, as shown in Figures 3.18b&f. Small misalignments are removed, but contrast enhancement is not optimal. Using a lower regularization weight (Figures 3.18c&g) of $\lambda_{\mathrm{seam}} = 0.01$ leads to both seamless alignment and visibly enhanced contrast. For all cystoscopic video-sequences processed, the parameter λ_{seam} of Equation (3.10) was set to 0.01 and led to visually coherent and contrasted maps.

In order to evaluate the advantages of the proposed compositing method, it is compared with distance based feathering (see again Section 1.3.4), which was used in several contributions to bladder cartography (WRS+05, HMBD+10, BGS+10)[1]. The major part of the images of the cystoscopic sequence used to generate the panoramic map shown in Figure 3.19 consists of blurry images, mostly due to cystoscope de-focus. One example of a very blurry image is shown

---

[1] It is recalled that for the registration of consecutive images, first-order regularization is employed to reduce computation time. Perspective-invariant higher-order regularization do not suffer from floating tissue, and could potentially be used also for consecutive image pairs when floating tissue is detected.

[1] It is recalled that the method proposed in (BGS+10) uses feathering based on the intensity of the input images, as the fluorescence emitted by tumorous cells corresponds to high intensities decays rapidly. Nevertheless, contrast or structure misalignments are not considered there neither, so the results of this section also apply for intensity based feathering.
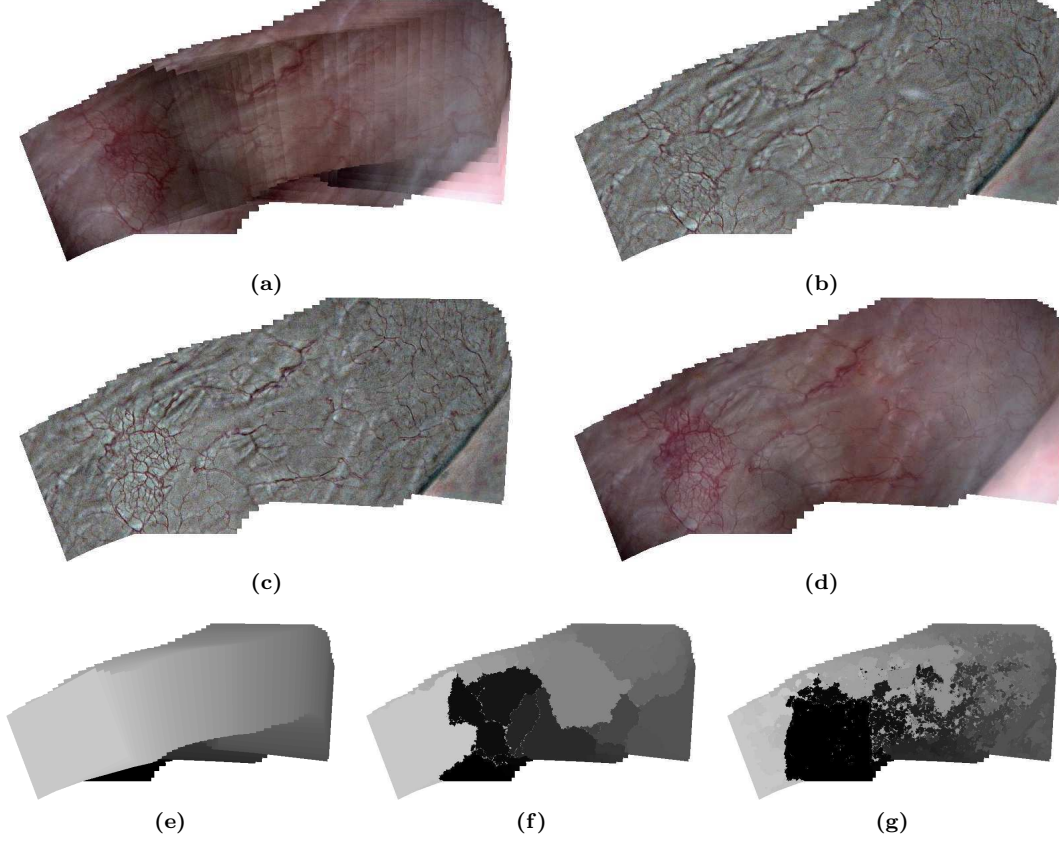
Figure 3.18: Contrast-enhancing seam localization. (a) Map composed by stacking the images on top of each other (BRM⁺09, MLHMD⁺04, MLDB⁺08). Motion blur and small misalignments degrade the visual appearance drastically, and exposure related artefacts are visible. (e) Corresponding label map. It is recalled that a label corresponds to the image number from which a given pixel color will be extracted to be placed in the map. (b) Map after seam localization with $\lambda_{\text{seam}} = 1$ (composed with high-pass filtered images for better contrast perception) (f) The corresponding label map is now composed of much less images, leading to seamless alignment of vascular structures. (c) Map after seam localization with $\lambda_{\text{seam}} = 0.01$. While the label map, shown in g), appears noisy, vascular structures are well aligned and the contrast is stronger compared to b). (d) Exposure correction using the label map of g) and the original input images.

in Figure 3.19d, and its corresponding location in the map is indicated by the blue quadrangle in Figure 3.19a. However, for most regions of the panoramic map, a few sharp images are available (see Figure 3.19e and the corresponding location indicated by a red quadrangle in Figure 3.19a). The distance blending algorithm does not distinguish between sharp and blurry images however. This explains why distance blending often results in blurry maps, as shown in Figure 3.19a (this map has to be visually compared to that of Figure 3.19b). The cystoscope displacement is indicated with black lines, while additional image pairs used for global correction are shown with white lines. The proposed contrast enhancing seam detection algorithm
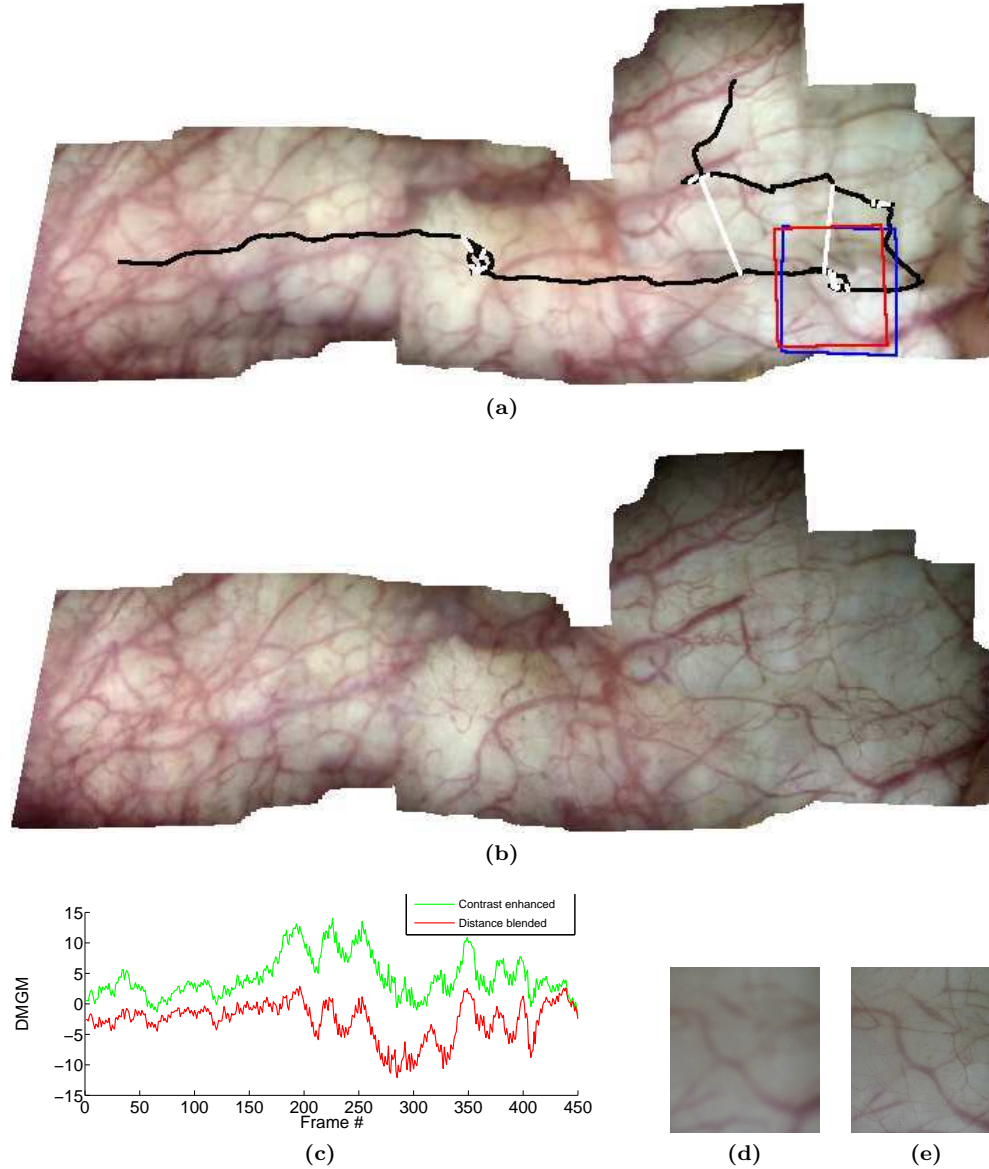
Figure 3.19: Contrast-enhancing compositing versus distance blending. (a) Map composed using distance blending. Vignetting and exposure related artefacts are removed, but the map is blurry because the majority of images of the sequence suffer from de-focus and motion blur. Black lines indicated the endoscope movement, while white lines depict additional image pairs used for global correction. (b) Map composed using the proposed method. Finer vascular structures are visible, and blur is significantly reduced. (c) This can be quantified using the difference of mean gradient magnitude (DMGM, see text). The proposed method creates a map that is mostly sharper than the individual input images (green line), while the distance blended map is mostly blurrier than the input images (red line). (d) Blurry image from the sequence, its position in the map coordinate system is indicated by the blue quadrangle in a). (e) Sharp image from the sequence, located at the red quadrangle in a). Using the contrast enhanced method, the texture of d) is used for the corresponding map region, discarding the other blurry images.

on the other hand stitches the panoramic map using as much contrast as possible without mis-aligning vascular structures. The result, shown in Figure 3.19b, shows even very fine vascular structures and is overall more contrasted than the map of Figure 3.19a. This observation can also be quantified using a simple measurement, which we refer to as difference of mean gradient magnitude (DMGM). It is computed by subtracting the mean gradient magnitude of each input image from the mean gradient magnitude of the corresponding region in the map. The green curve of Figure 3.19c shows that this difference is positive for almost all images of the sequence when computed for the map shown in Figure 3.19b. In other words, the contrast of most images' regions in the map is stronger than for the corresponding images themselves. For instance, the peak at image number 250 in Figure 3.19c corresponds to the image shown in Figure 3.19d. As this image is very blurry, the contrast enhancement in the map is high. If an input image is well contrasted, the enhancement is very low (i.e. the valley at image number 272 corresponds to a DMGM of ≈ 0), which means that this image contributed strongly to the final map. The DMGM for the distance blended map (red curve in Figure 3.19c) on the other hand is mostly below 0, indicating the visual degradation induced by simple blending without considering the images' quality.

When optimal seam positions have been determined, illumination and color differences across seams need to be removed. The parameter for the proposed exposure correction methods was set to $\lambda_{\exp} = 1$ (see Equation (3.14)), and lead to satisfying results for all sequences. Figure 3.17a shows the map before exposure correction, where the different exposure of the individual input images is clearly visible. After exposure correction, the map shown in Figure 3.17d is visually coherent (i.e. no visible exposure artefacts can be seen), while retaining the contrast obtained after seam detection. This is backed by the DMGM, plotted in Figure 3.17e. The green curve is again mostly positive, confirming that the map maximizes the contrast available in the redundant data of the sequence.

Additional Map Examples

In Figure 3.20a, the ureter opening is visible and can act as an anatomical landmark. When the map is archived and used later (some weeks or months after the examination) by another urologist, maps with such landmarks can facilitate navigation towards regions of interests. The map of Figure 3.20b includes a lesion. Showing lesions in a large field of view facilitates diagnosis and follow up (lesion evolution assessment) by comparing maps computed at a given time interval. It is visible on both figures that the maps are visually coherent (i.e. no texture or color discontinuities are visible). Moreover, the the maps are well contrasted in every region and without blur.

Ureter opening

(a)

Lesions

(b)
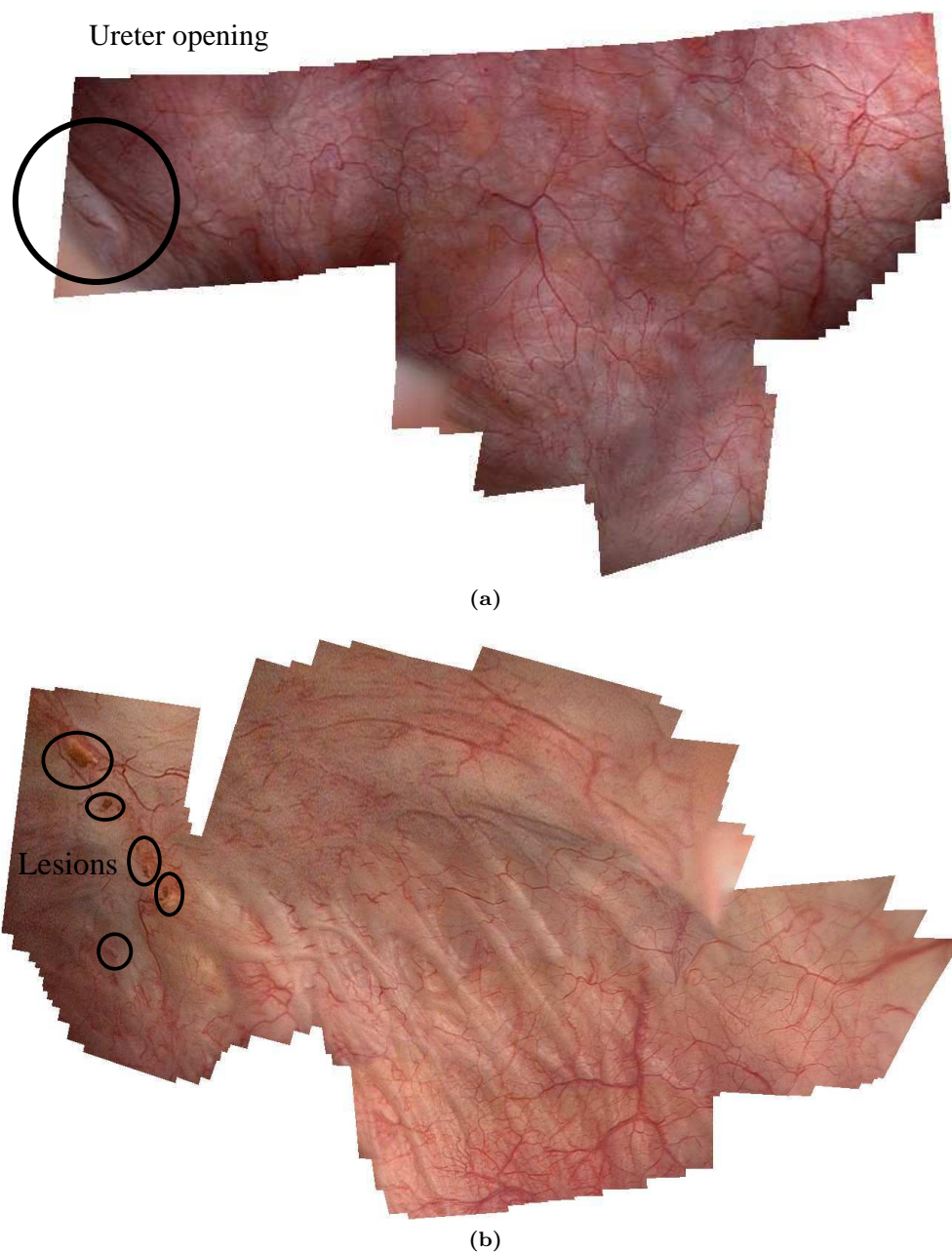
Figure 3.20: Contrast-enhanced panoramic images for two additional cystoscopic video-sequences. (a) The ureter opening in visible. Such an anatomical landmark facilitates navigation during a cystoscopy, and mental orientation weeks or months after the examination when preparing for follow-up. (b) Map showing lesions. This large FOV image can be used to assess lesion evolution over time, either by comparing with another map, or during the cystoscopy itself.

3.5.3 Results on Traditional Applications

While the methods developed and proposed in this chapter were specifically tailored to create large FOV maps from cystoscopic image sequences, they are also usable in more general applications. This section will show two examples, namely a set of images of a tourist attraction stitched seamlessly, and high dynamic range images composed from partly overlapping images with very different exposure levels.

Consumer Photography Stitching

An example for tourist stitching using the methods proposed in this chapter is shown in Figure 3.21, which has been composed from a sequence of 16 partly overlapping images. Consecutive images overlap by $\approx 50\%$. While this is much less than in a cystoscopic video-sequence, the images contain sufficient image primitives. Both consecutive and non-consecutive image pairs could consequently be robustly registered. However, as the large FOV leads to strongly distorted transformed images (see again Figure 1.9 in Chapter 1), the images were transformed to spherical coordinates after registration in order to produce a better scaled panoramic image.

While the result may not impress at first glance (and in fact, when watching semi-closely, misalignments can be observed), stitching the transformed input images seamlessly is not trivial. The registration of both consecutive and non-consecutive images leads to visually coherent image superimposition, as shown in Figures 3.22a-b. However, the spherical projection model induces bending of straight lines in the peripheral image regions, and as the images overlap only by about 50%, this leads to oppositional bending in the overlapping image regions, as shown in Figures 3.22c-d. Consequently, finding seams that align all images without visible discontinuities is much more difficult when using spherical coordinates and sparsely overlapping images. However, it is visible in Figure 3.21 that these seams were found and led to a visually coherent panoramic image, especially when compared to the initial map, as shown in the top left hand side of Figure 3.21.

High-Dynamic Range Images

The methods proposed in this chapter may also be used to create high-dynamic range (HDR) images. An example is shown in Figure 3.23. HDR imaging aims at creating higher dynamic range than a camera is able to capture from a single exposure level. In a single image, loss of detail in dark (Figure 3.23a) or bright (Figure 3.23b) regions is evident. An HDR algorithm allows to reduce such loss of detail by combining multiple images taken with different exposure levels. The resulting image should be well exposed in both dark and bright image regions. The methods proposed in this chapter are also capable of producing HDR images. The two input images of Figures 3.23a-b were taken with a hand-held smartphone camera, and registered using

Figure 3.21: Panoramic image composed of a tourist scene using spherical coordinates. Due to the spherical projection model used and the low percentage of image overlap (about 50%), superimposed images are distorted oppositionally (see also Figure 3.22). This complicates the search for seams that align the images in a coherent fashion, and consequently the panoramic image shows slight misalignments. Nonetheless, it is overall visually coherent, expecially when compared with a simple successively overwritten map, as shown in small at the top left hand side.

the algorithm of Section 3.3. Because over- and undersaturated image regions show less contrast than well exposed regions do, the contrast-enhancing seam localization algorithm results in a label map that represents mostly well exposed parts of the input images, as shown in Figure 3.23c. Black regions correspond to input image shown in Figure 3.23a, grey regions to that of Figure 3.23b. The proposed exposure correction then corrects any remaining inconsistencies, and produces the result as shown in Figure 3.23d. Note that the proposed algorithms were not

(a)

(b)

(c)

(d)
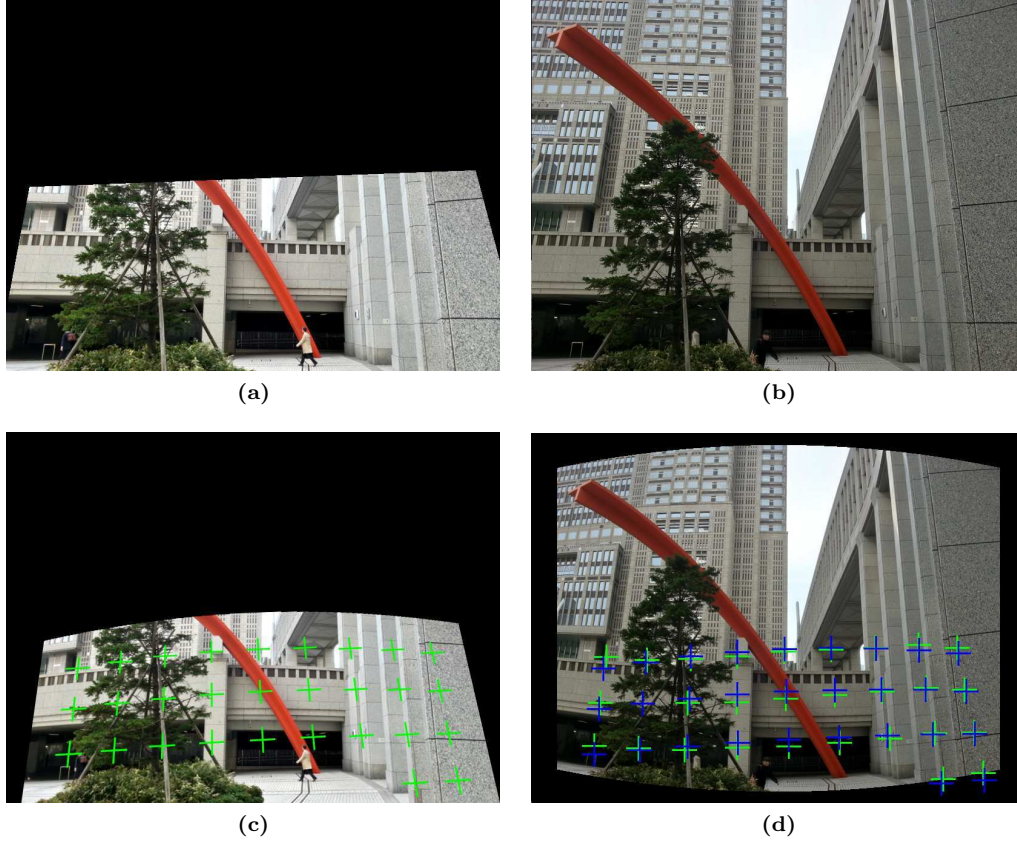
Figure 3.22: Image misalignment due to spherical warping. (a) Image I_i, transformed into the coordinate system of image I_{i+1}. (b) Image I_{i+1}. The images are adequately aligned. (c)-(d) Like a) and b), but using a spherical projection model. (c) A green cross denotes the position of a vertex after transformation into spherical coordinates. (d) A green cross shows the corresponding position (again, in spherical coordinates), as estimated by the registration algorithm. The estimated correspondences still correspond to homologous positions, but the spherical projection violates the assumption of a perspective transformation. This is illustrated by a blue cross in d), which corresponds to a green cross in c), transformed using $T_{i \to i+1}^{2D}$.

designed to produce HDR images, and consequently, we did not perform a comparison with state-of-the-art techniques. It is however straightforward to integrate data and regularization terms better suited for HDR imaging.
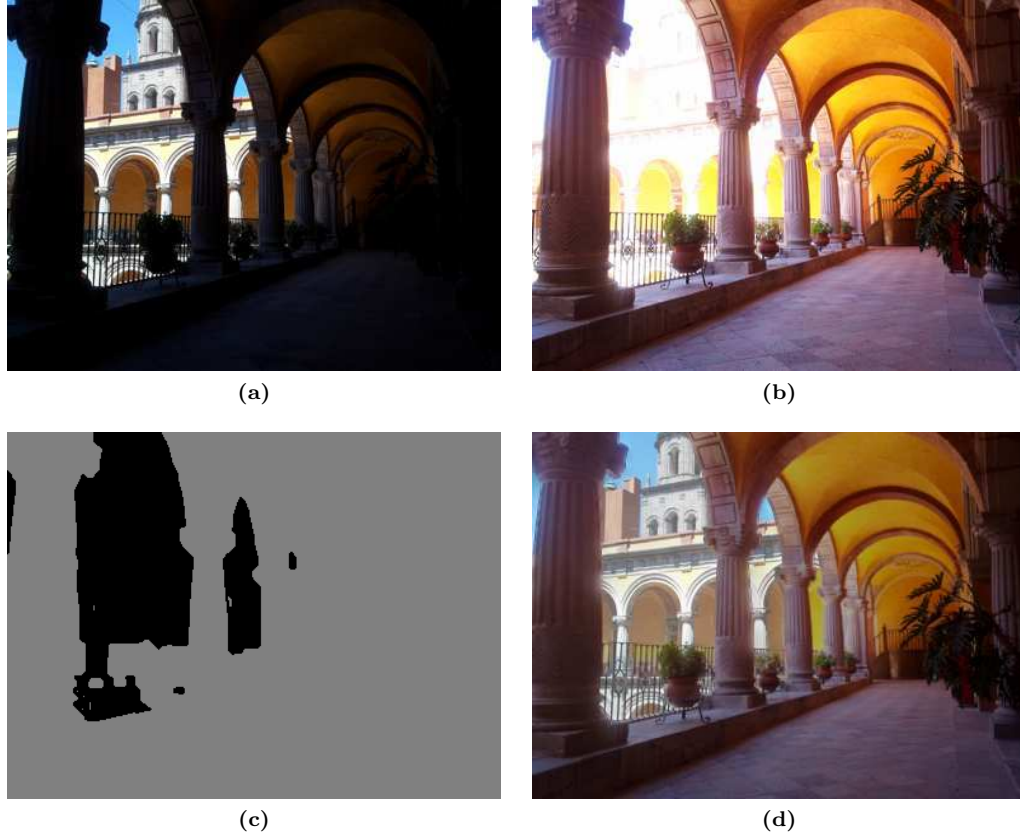
Figure 3.23: High-dynamic range image composition. (a) First input image, captured with short exposure time. (b) Second input image, captured with long exposure time. (d) Composed high-dynamic range image. As over- and under-saturated image regions have a lower contrast than well exposure regions, the contrast-enhanced seam localisation algorithm is able to assign each pixel a corresponding, well-exposed image index, as shown in c). After exposure correction, the dynamic range of the image is much larger than for each individual input image.

3.6 Discussion and Perspectives

3.6.1 Practical and Scientific Contributions

The methods proposed in this chapter allow to construct real large field of view panoramic images from cystoscopic video-sequence. The term "real" stands in opposition to those algorithms which are only able to construct band-shaped maps with a large FOV in one main direction without visible accumulated errors. Indeed, previous contributions did not consider the problem of accumulated errors, and presented registration algorithms that are not suitable

to systematically register non-consecutive image pairs. Consequently, only strip-shape maps (such as the one shown in Figure 1.5) constructed from consecutive image transformations were presented before. An exception is the method proposed in (BTGA11), where gaps in the map are detected using a frame-graph structure. This is potentially useful for clinicians, as they can immediately assess whether they have missed to scan parts of the epithelium. However, this method does not consider accumulated errors neither, and only results on phantom data are given, where error accumulation is significantly lower.

In the following, we will summarize the main contributions of this chapter.

Automatic Detection of Cystoscopic Trajectory Crossings and Correction of Globally Accumulated Cartography Errors

Accumulated cartography errors have to be corrected for crossing endoscope trajectories and for loop scenarios. Image registration is generally computationally intensive for the white light modality because image primitives cannot be systematically extracted, which makes iconic data registration necessary. Due to time constraints, registering all possible consecutive and non-consecutive image pairs is infeasible. Therefore, in order to correct accumulated errors, we use a specific graph structure that represents the images and their relationship in the global coordinate system. This allows to automatically select a meaningful subset of overlapping non-consecutive images, and the transformations relating these pairs are used to correct accumulated errors using sparse non-linear least squares.

Invariant Energy Functions for Image Registration

Non-consecutive image pairs are often linked by image displacements of large magnitude and small image overlap. To deal with this we have proposed data and regularization terms which compute energy costs invariantly to the perspective transformation parameter values that link overlapping images. This is possible using higher-order interaction between pixels, which are reduced to an equivalent pairwise form using reduction by minimum selection. In addition, a coarse-to-fine minimization scheme which significantly reduces the computation time compared to classical iterative minimization methods was proposed. Both consecutive as well as non-consecutive image pairs for six clinical datasets could systematically be registered. The registration was performed using constant parameter sets (a separate set for consecutive and non-consecutive image pairs), which demonstrates the robustness of the proposed method. This robustness is important for potential clinical use, as clinicians should not have to adjust algorithm parameters in order to obtain usable maps.

Contrast-Enhancing Map Compositing

Unlike previous contributions, which use blending techniques to compose the textured panoramic image, we have proposed an energy minimization based seam detection algorithm. This method allows to correct small misalignments of vascular structures when stitching the map. At the same time, it maximizes the map's quality by favouring contrasted images over blurry ones. In

a second step, exposure related artefacts are removed without interpolation across seams, while contrast and hue of the original input images are retained. The thus constructed panoramic images are generally of better or equal quality than the individual input images. This allows clinicians to see the scanned parts of the epithelium in a single high-resolution image.

3.6.2 Limits of the Methods and Perspectives

While all of the proposed methods have theoretical limits, the global and practical limit of the cartography process is the accumulation of local registration errors to global cartography errors. Even with the proposed registration method, which systematically (i.e. robustly) registers consecutive images with high accuracy, errors still accumulate. Even if both perspective-invariant data and regularization terms cannot be used jointly due to the large number of non-submodular terms, the accuracy of registering non-consecutive image pairs is still acceptably close to that of consecutive registration. So as long as accumulated errors are low enough to detect valid additional non-consecutive image pairs, the proposed registration algorithm is able to superimpose these images with satisfying accuracy. Possibly, the order reduction method proposed in (GBP11) might be able to obtain less non-submodular pairwise terms, so that both perspective-invariant data and regularization terms can be used jointly.

However, as was shown in Figure 3.17, when overlapping parts of the map cannot be detected because accumulated errors are too large, the corresponding map regions cannot be accurately corrected. As previously discussed, it was still possible to correct the accumulated errors with the help of two additional transformations and the higher-order potential functions, but this cannot always be guaranteed. An obvious solution is a semi-automatic implementation, where missed trajectory overlaps can be manually selected by the clinician. Exhaustive search of overlapping map regions is also a possibility. This will, however, increase computation time significantly, and it is not straightforward to reject image pairs that do not overlap. In other words, the question whether two images show homologous bladder texture remains an open problem, as all iconic based image registration techniques (existing state-of-the-art methods, as well as those presented in this chapter) will return a local transformation matrix.

Another practical limit is the distortion observed when the FOV is large due to the perspective transformation model used. For instance, in Figure 3.17d, the size of the first image of the sequence (bottom most image) is much smaller than the last image of the sequence. Similar observations can be made in relevant publications concerning bladder cartography. A spherical projection model would be ideal, but without knowledge of the cystoscope position and orientation relative to the surface, the obtained cystoscope path will be incorrect and prevent accurate detection of overlapping trajectories. As we shall see in the next chapter, with such knowledge, it is possible to construct panoramic surfaces with accurate geometry, independently of the field of view. Without such knowledge, a possibility is to allow the clinicians to select an appropriate reference image on the fly. This will minimize perspective distortions

in regions around the point of interest. However, when a change of reference coordinate system infers a strong change in local panoramic resolution, the map compositing process must be re-computed, adding additional computation time.

Finally, the greatest potential in reducing the computation time of the cartography process lies in image registration. The methods proposed in this chapter represent an approach focused on both robustness and accuracy, and outperform state-of-the-art algorithms in these terms. This registration quality comes with the disadvantage of longer computation times, compared for instance with feature based approaches. These can potentially be used in real-time, but cannot guarantee robust registration for the entire video-sequence. Future research should be targeted at selecting an appropriate registration algorithm based on the texture quality of the input images I_i and I_j. Indeed, many consecutive image pairs can be accurately registered with faster algorithms, such as feature based approaches, sparse graph-cuts, or fast optical flow algorithms. If an image texture analysis algorithm can robustly predict the probability of a successful registration for a given algorithm, the computation time can be significantly reduced by choosing the fastest applicable algorithm. Furthermore, a Kalman filter can be used to predict the cystoscope displacement $T_{i \to i+1}^{2D}$ based on the previous registration result $T_{i-1 \to i}^{2D}$. This could allow to select the number of images that can be skipped without jeopardizing a successful registration, potentially leading to a much smaller number of consecutive images to be registered.

3.6.3 Publications

International Journal

- T. Weibel, C. Daul, D. Wolf, R. Rösch, and F. Guillemin. Graph based construction of textured large field of view mosaics for bladder cancer diagnosis. *Pattern Recognition*, 45(12):4138 – 4150, 2012

International Conferences

- T. Weibel, C. Daul, D. Wolf, and R. Rösch. Planarity-enforcing higher-order graph cut. In *18th IEEE International Conference on Image Processing (ICIP)*, pages 41–44, September 2011. Brussels, Belgium (Oral presentation)

- T. Weibel, C. Daul, D. Wolf, R. Rösch, et al. Contrast-enhancing seam detection and blending using graph cuts. In *21st International Conference on Pattern Recognition (ICPR)*, pages 2732–2735, November 2012. Tsukuba, Japan (Oral presentation)

National Conference

- T. Weibel, C. Daul, D. Wolf, and R. Rösch. Customizing graph cuts for image registration problems. In *XXIIIe Colloque GRETSI Traitement du Signal & des Images (GRETSI)*, September 2011. Bordeaux, France (Oral presentation)

Chapter 4

3D Cartography: a Proof of Concept

4.1 Introduction and Chapter Overview

In the previous chapter, it was shown how two-dimensional textured maps of the epithelium can be built from cystoscopic video-sequences. The cartography process was divided into several steps and processed sequentially. First, consecutive image pairs (I_i, I_{i+1}) were registered, and the estimated local transformations $T^{2D}_{i \to i+1}$ gave an initial estimate of the global transformations $T^{2D}_{0 \to i}$. In the next step, accumulated cartography errors were automatically corrected. This step required the development of a robust registration algorithm for non-consecutive image pairs, which state-of-the-art algorithms are unable to register robustly. In the last step, small remaining texture misalignments and exposure differences were corrected while simultaneously maximizing the contrast of the map. The purpose of this chapter is to demonstrate that the proposed two-dimensional cartography steps can be modified to build three-dimensional maps (textured surfaces) when additional three-dimensional information is available.

However, while in Chapter 3 it was shown that the 2D cartography algorithm is applicable on patient data, the work described in this chapter is limited to a proof of concept. Indeed, phantom data, provided by prototypes simulating the acquisition principle of potential 3D-endoscopes, are used as a first validation of the proposed 3D cartography method. Section 4.1.1 will first recapitulate the advantages of such three-dimensional textured surfaces over two-dimensional maps for clinical diagnosis. Then, Section 4.1.2 presents the particular choice of 3D cartography principle used in this chapter. More details on previous contributions to 3D endoscopic cartography were given in Section 1.4.

Available acquisition prototypes are described in Section 4.2. In essence, these prototypes can be used to obtain additional three-dimensional information for each acquired color image. This additional data allows for modifying the 2D cartography approach of the previous chapter. It is important to stress that these prototypes are not yet applicable in clinical examinations. Consequently, no clinical data sets are available. Nonetheless, the results on realistic phantom

data demonstrate the potential of the proposed algorithms to three-dimensional cartography. Moreover, to highlight the flexibility (interest of the method for non-medical scenes), the algorithm was not only applied to bladder phantoms. To do so, the algorithm was used for the cartography of indoor datasets acquired with a Microsoft Kinect sensor, which is described in Section 4.2.3.

Section 4.3 will outline the steps of the three-dimensional cartography algorithm (which are individually described from Sections 4.3.2 to 4.3.4), with a focus on the differences between two- and three-dimensional cartography. The proposed algorithms are tested on several data sets in Section 4.4. The chapter concludes with a discussion and potential perspectives in Section 4.5.

4.1.1 Motivation and Projection Geometry

Clinicians try to mentally visualize the bladder's three-dimensional structure while they scan the epithelium for potential lesions. In other words, when clinicians observe the video-sequence, each currently observed FOV (two-dimensional projection in form of the image I_i) is intuitively perceived at (or re-projected onto) its corresponding location on the surface of the epithelium. The aim of a three-dimensional cartography algorithm is to automatically carry out this re-projection, i.e. to reconstruct the three-dimensional texture representation of the observed bladder surface from a video-sequence.

Technically, each observed small FOV is a two-dimensional projection of a part of the organ's internal wall onto the plane of image I_i (see Figure 4.1). Let $\mathcal{P}_i^{3D}$ be a finite (sub-)set of three-dimensional points on the epithelium, expressed in the (local) coordinate system of acquisition i. As before, a subscript $i = 0$ indicates the global and common reference 3D coordinate system of the map. A video-sequence consists of N acquistions, with $i \in \{0, ..., N-1\}$. The homogeneous coordinates of a point $p_{i,k}^{3D} \in \mathcal{P}_i^{3D}$ with index k, expressed in the coordinate system of viewpoint i, are defined by $[X_{i,k} \ Y_{i,k} \ Z_{i,k} \ 1]^T$. This point is transformed into the local coordinate system of acquisition number j by the rigid transformation $T_{i \to j}^{3D}$, whose 3D rotation matrix $R_{i \to j}^{3D}$ and translation vector $t_{i \to j}^{3D}$ are defined in Equation (1.3):

$$p_{j,k'}^{3D} = T_{i \to j}^{3D} \ p_{i,k}^{3D} = \left[\begin{array}{cc} R_{i \to j}^{3D} & t_{i \to j}^{3D} \\ \vec{0} & 1 \end{array} \right]_{i \to j} p_{i,k}^{3D}. \tag{4.1}$$

In the remaining parts of this chapter, indices k and k' represent homologous points displaced from the coordinate system of acquisition i into that of acquisition j. We will also use the notation $T_{i \to j}^{3D}(\mathcal{P}_i^{3D})$, which transforms all $p_{i,k}^{3D} \in \mathcal{P}_i^{3D}$ to the coordinate system of viewpoint j using Equation (4.1). The corresponding two-dimensional homogeneous projection $p_{j,k'}^{2D} = [x_{j,k'} \ y_{j,k'} \ 1]^T \in \mathcal{P}_j^{2D}$ in the coordinate system of image I_j is then obtained by

$$p_{j,k'}^{2D} = \nu_k \ \left[K\vec{0} \right] \ \left(T_{i \to j}^{3D} \ p_{i,k}^{3D} \right). \tag{4.2}$$
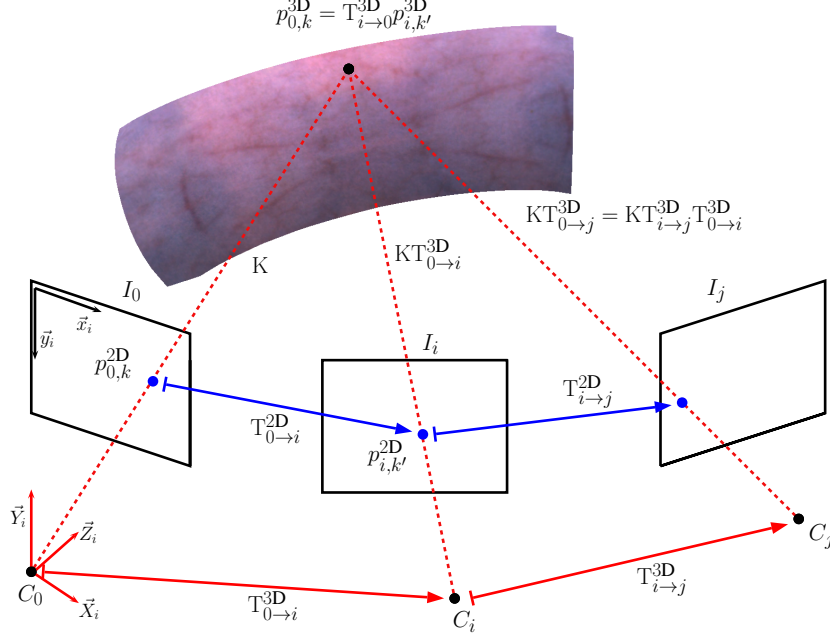
Figure 4.1: Illustration of the image projection geometry. The rigid transformation $\mathrm{T}_{i\to j}^{\mathrm{3D}}$ relates the coordinate systems of two acquisitions i and j. Points $\mathcal{P}_i^{\mathrm{3D}}$ on the epithelium, expressed in the coordinate system of acquisition i, are projected onto the image plane of acquisition j via $\mathrm{KT}_{i\to j}^{\mathrm{3D}}$. When global transformations $\mathrm{T}_{0\to i}^{\mathrm{3D}}$ are known for each acquisition i, the surface can be constructed by placing all $\mathcal{P}_i^{\mathrm{3D}}$ into the coordinate system of the reference acquisition $i=0$. C_0, C_i, and C_j correspond to the location of the camera's optical centers in global coordinate system, and define the (local) 3D coordinate system origin for viewpoints 0, i and j, respectively. The local 2D and 3D coordinate systems are illustrated for viewpoint 0, which also correspond to the global coordinate systems.

where $\mathcal{P}_j^{\mathrm{2D}}$ is a set of valid projections in the coordinate system of image I_j, K is the intrinsic camera parameter matrix defined in Equation (1.1)[1]. The normalizing factor ν_k ensures that the third element of $p_{j,k'}^{\mathrm{2D}}$ is equal to 1. The color vector at a (sub-pixel) position $I_i(p_{i,k}^{\mathrm{2D}})$ is extracted from I_i using bilinear interpolation. If there exists a three-dimensional measurement in acquisition i that can be associated with a pixel p, it will be addressed by $p_{i,p}^{\mathrm{3D}}$ for simplicity.

As in two-dimensions, the global transformation $\mathrm{T}_{0\to i}^{\mathrm{3D}}$ relating the local coordinate system of acquisition i with the common global coordinate system (without loss of generality, assumed to be identical with the first acquisition $i=0$) is obtained via concatenation:

$$\mathrm{T}_{0\to i}^{\mathrm{3D}} = \prod_{k=0}^{i-1} \mathrm{T}_{k\to k+1}^{\mathrm{3D}}. \tag{4.3}$$

When 3D points $\mathcal{P}_i^{\mathrm{3D}}$ and global transformations $\mathrm{T}_{0\to i}^{\mathrm{3D}}$ are known for each acquisition i, three-dimensional textured surfaces can be constructed. The advantages of such 3D maps are manifold:

---

[1]The images are assumed to be distortion-corrected beforehand.

- In comparison to two-dimensional maps, textured surfaces correspond more naturally to the clinicians' mental representation of the organ. Such a 3D representation should therefore facilitate diagnosis and follow-up preparations.

- Two-dimensional maps are prone to strong perspective "deformations" between images acquired with large instrument displacements and viewpoint changes (see Figure 1.9 and the cartography results of the previous chapter). Therefore, map resolution varies with time and cystoscope trajectory, but not necessarily with respect to the scale of the observed bladder surface. Three-dimensional maps do not exhibit these degradations, as $T_{0 \to i}^{\mathrm{3D}}$ is a rigid transformation that preserves scale and shape of the observed scene. Accumulated errors may still lead to inaccurate rigid displacements when returning to previously visited locations, but do not affect either scale or shape of each viewpoint's observed surface.

- A second "virtual" examination can be performed on the computer, allowing the clinicians to navigate freely inside the textured three-dimensional map.

In the next section, we will briefly recapitulate existing approaches towards three-dimensional cartography of endoscopic data and motivate the particular choice of reconstruction principle used in this chapter.

4.1.2 Choice of 3D Map Reconstruction Principle

As discussed in Section 1.4, there are several potential approaches for constructing three-dimensional surfaces from endoscopic video-sequences. Due to the quasi-planar surface part observed in each small FOV, three-dimensional structure can only be recovered with the aid of a priori information, or by using modified endoscopes. Indeed, as discussed in Section 1.4.3, quasi-planar surfaces represent poor geometrical information (depth variations), which impedes direct 3D-3D point registration algorithms, such as iterative closest points approaches (BM92, Zha94, SHT09).

Moreover, the works described in Sections 1.4.1 and 1.4.2 show that neither 2D images combined with a priori knowledge about the organ's surface (CS09), nor SfM methods (SPS12) are suitable for 3D bladder cartography.

As will be explained in the next section, additional three-dimensional data can be obtained with devices that capture (sparse or dense) three-dimensional point sets $\mathcal{P}_i^{\mathrm{3D}}$ for each viewpoint i. Since the quasi-planar FOVs of cystoscopic images impede a direct 3D-3D data registration due to a lack of geometrical surface information, the only solution is to use simultaneously the 2D image texture and 3D point information to compute 3D maps. Such a strategy was successfully applied in (BHDS$^+$10), where the 3D surface construction was guided by 2D image registration, and geometrical constraints allowed to converge towards the rigid 3D transformation effectively linking two consecutive viewpoints i and i + 1 of a cystoscope prototype.

Two recent contributions (SFS$^+$12, ANKB13) used additional external navigation systems to facilitate the cystoscope position determination for each acquisition. The rigid cystoscope displacement is estimated by tracking markers located on the external part of the cystoscope with a stereo-camera system. Such a system allows to compute the cystoscope's viewpoint in a global coordinate system, relative to the stereo camera coordinate system (i.e. the coordinate system is located in the examination room, not in the bladder). The approach proposed in (SFS$^+$12) also reconstructs the surface seen in each FOV using an active stereo-vision endoscope. Similar to (CLZQ03, BHSD$^+$10), a set of 49 projected laser points is reconstructed in each acquisition's local coordinate system. These three-dimensional measurements are then transformed into a common coordinate system via the estimated rigid cystoscope displacement. The patient must remain still during the entire examination, as the rigid cystoscope displacement is only measured via external tracking. Furthermore, no means of applying the texture onto the reconstructed point cloud is proposed (no texture images were acquired). The objective of the approach proposed in (ANKB13) is merely to document the position of lesions in order to quickly navigate to this position in a follow-up examination. As the bladder's three-dimensional structure is not reconstructed (i.e. no cartography algorithm is proposed), clinicians do not benefit from extended FOV (showing lesions and anatomical landmarks), which does not facilitate diagnosis. Both approaches require special equipment (including an external tracking system present in the examination room), which infers additional costs and technical problems. Moreover, as shown in (BHSD$^+$10), 3D maps can be build without such additional navigation systems.

We can conclude with the observation that robust three-dimensional cartography of cystoscopic video-sequences is feasible with a combination of two-dimensional image and additional three-dimensional data (points on the bladder surface). External navigation systems (as used in (SFS$^+$12, ANKB13)) may facilitate the estimation of local rigid cystoscope displacements, but are not sufficient alone to robustly compute global displacements in the organ's coordinate system. The methods developed in the remainder of this chapter therefore assume that modified cystoscopes allow to simultaneously capture color images I_i and a set of three-dimensional measurements $\mathcal{P}_i^{3D}$ of the observed scene for each acquisition i. The advantage is that such cystoscopes can be constructed using existing hardware (i.e. by modifying one- or two-channel endoscopes). The next section will describe the available data of such modified cystoscopes and present existing prototypes developed at the CRAN laboratory.

4.2 Data Acquisition

The prototypes available at the CRAN laboratory allow to capture a color image I_i (distortion-corrected) and a set of (local) three-dimensional points $\mathcal{P}_i^{3D}$ on the surface in view. The following subsection presents these prototypes in detail.

4.2.1 Laser-Based Cystoscope Prototype

An endoscope typically consists of two channels, while cystoscopes are one-channel systems. For cystoscopes (and some two-channel endoscopes), the light source illuminates the observed scene through a bundle of optical fibers, and the acquisition channel captures the reflected light using a camera connected to the instrument. In (CLZQ03), the first channel of a two-channel endoscope was used to project a dense laser dot matrix onto the observed surface, while the second channel was used for image acquisition. The dot matrix was created by a collimated laser beam falling on a diffractive optics. After accurate camera and dot matrix projector calibration, the three-dimensional positions $\mathcal{P}_i^{\text{3D}}$, corresponding to the dots $\mathcal{P}_i^{\text{2D}}$ of the matrix, can be calculated in the color camera coordinate system. The sub-millimeter reconstruction accuracy is remarkable, given the small baseline of about 2.2 millimeters (the baseline corresponds to the distance between the optical centers of camera and projector). However, as argued in Chapter 1, due to the planar appearance in each image, robust 3D-3D registration using only $\mathcal{P}_i^{\text{3D}}$ and $\mathcal{P}_j^{\text{3D}}$ is not possible due to poor depth variations on the bladder surface. Even if $\text{T}_{i \to j}^{\text{3D}}$ could be estimated robustly, the valuable texture information needed in the context of cytoscopy is lost due to the dense dot-matrix projection.

To robustly reconstruct the observed surface together with the bladder texture, the method proposed in (BHDS$^+$10) uses eight projected laser points. By projecting only eight points (ideally near the peripheral regions of the circular FOV of the cystoscope), the major part of the texture is preserved, and visual inconveniences are minimized. The authors also proposed a flexible camera-projector calibration technique (BHSD$^+$10) that does not require expensive calibration equipment. The method proposed in (BHSD$^+$10, BHDS$^+$10) can potentially by implemented on one channel endoscopes (e.g. cystoscopes), and this one-channel solution can be briefly described as follows.

The prototype (see Figure 4.2a) consists of a cylindrical tube, through which a cystoscope is inserted. In addition, a green laser beam passes inside the tube and falls onto a diffractive optics, located at the instrument distal tip (the laser beam is currently guided by mirrors inside the cylindrical tube). This diffractive optics projects eight beams onto the surface. An image acquired with this prototype is shown in Figure 4.2b. As illustrated in Figure 4.2d, a triangulation technique can be used to compute the 3D coordinates of the laser dot centers (BHSD$^+$10). Tests with the prototype of figure Figure 4.2a have shown that the error on the z coordinate is always smaller than a millimeter for a distance measure lying between 20 and 40 mm. This reconstruction is accurate for a baseline of 3 mm, and is sufficient when 3D shapes have to recovered (as in cystoscopy) without the aim to perform exact dimensional measurements. The reconstructed points corresponding to the laser dots of Figure 4.2b are shown in Figure 4.2c. Even if this prototype cannot be used directly in clinical conditions, its geometry and scale (very small baseline of 3mm) is close to that of a cystoscope, and can be potentially built by manufacturers.
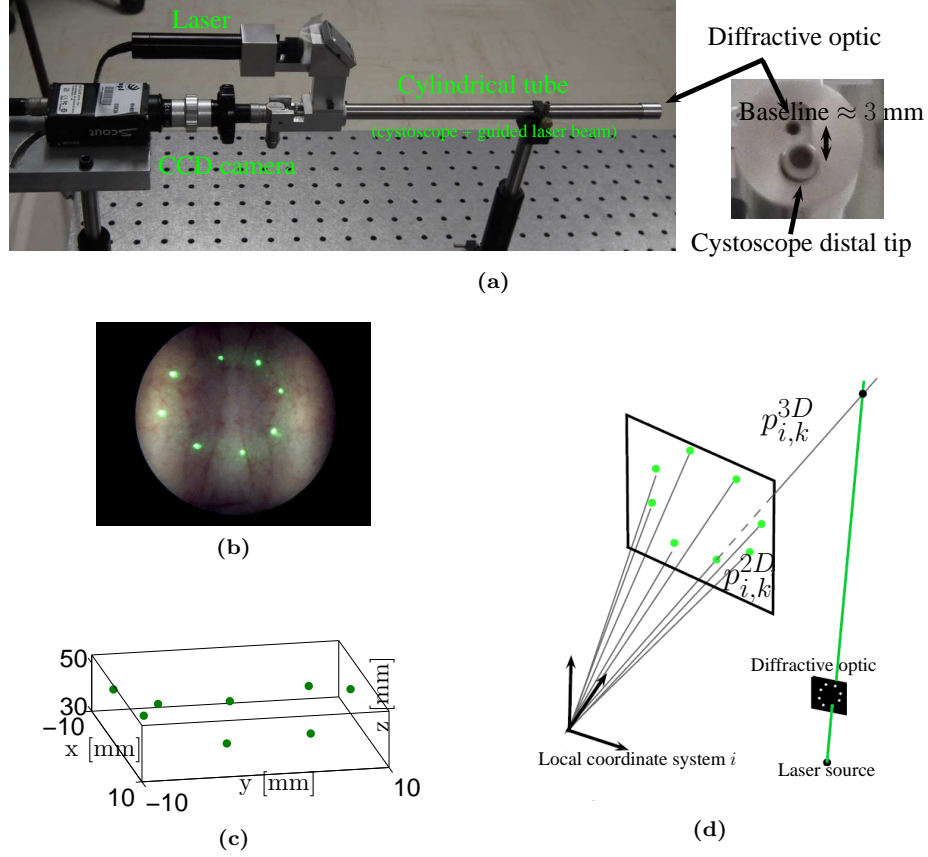
Figure 4.2: Active stereo-vision principle of the laser cystoscope prototype. (a) Instrumentation prototype. (b) A set of eight laser rays is projected onto the color image. This allows to simultaneously capture most of the bladder's texture and (c) a set of eight three-dimensional positions, reconstructed in the camera coordinate system. (d) Geometry of this acquisition system. Only one of the eight diffracted laser beams is illustrated.

4.2.2 Time-of-Flight Prototype

The advantage of the method of (BHDS$^+$10) compared to (CLZQ03) is that texture information is not lost, but implies the disadvantage that only a very sparse set $\mathcal{P}_i^{3D}$ is available for each acquisition. As shown in Section 4.4, dense point clouds acquired for each acquisition can facilitate the 3D map construction in comparison to sparse 3D data per viewpoint. On the other hand, the solution of (CLZQ03) was designed for two-channel endoscopes and is not applicable with one-channel cystoscopes (a second channel is required for the pattern projection). For the prototype of Figure 4.2, the diffractive optics is placed at the output of the cylindrical tube, and an optical fiber can illuminate this optics with a laser light, avoiding the need of a second channel. However, only manufacturers can decide if such a solution is feasible for commercial
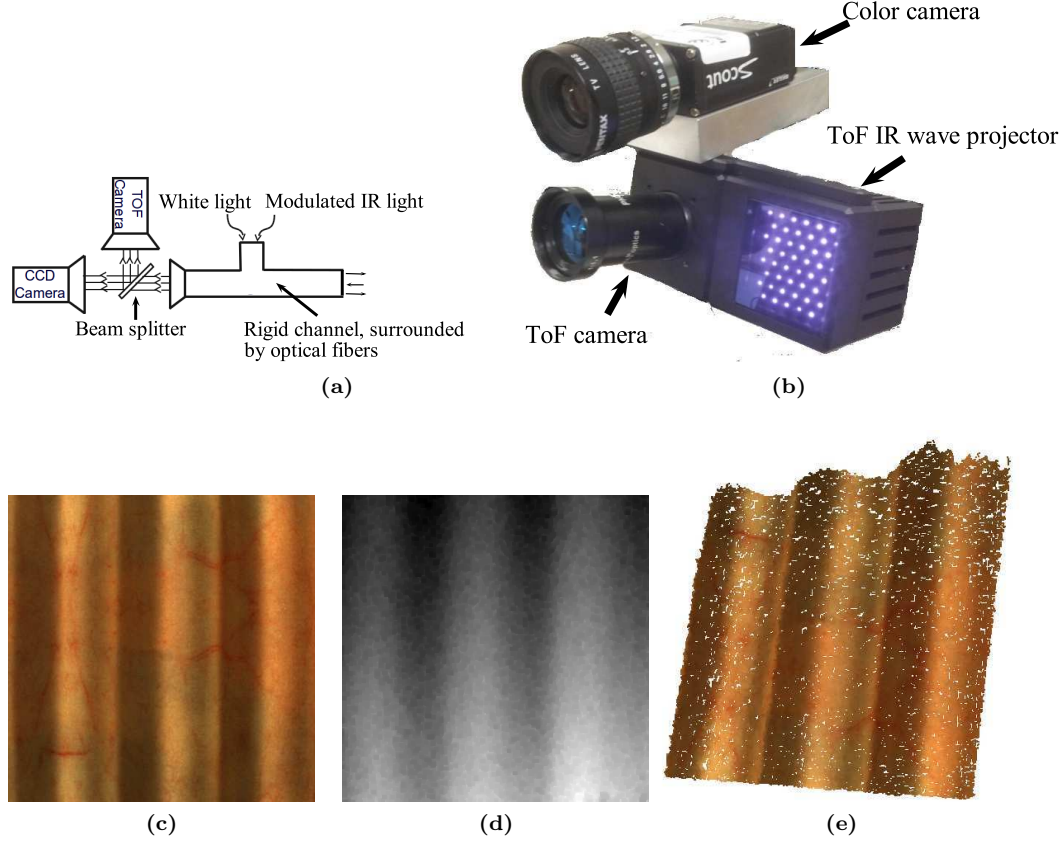
Figure 4.3: Time-of-flight prototype and data obtained for an acquisition of a wave-shape phantom. (a) Schematic illustration of the prototype currently being developed. (b) Simple prototype used for the experiments. (c) Color image. (d) Corresponding depth map (transformed into the color camera coordinate system). The intensity is proportional to the distance to the camera. (e) 3D point cloud representation of d) using the colors of c).

production.

Another potential solution to obtain both texture *and* a dense point cloud is to integrate a time-of-flight (ToF) camera into the color image acquisition channel of the cystoscope (PHS+09). In (PHS+09), such an approach was proposed for a laparoscope, even if no 3D textured surface was built since the authors limited their work to 3D measurement tests. A ToF camera is a range sensing device that measures the time of flight of emitted light from the camera to the object (PMD13). The phase difference between emitted infra-red (IR) waves and those reflected by the surface and absorbed by the sensor is used to compute a distance from the surface for each pixel of the sensor. When the equations of the ToF camera rays are known (they can by computed with classical camera calibration methods), the measured distanced along these rays allow for computing 3D coordinates in the camera coordinate system. ToF cameras usually work at a high frame rate (up to 100 Hz), and recent chipsets allow for spatial resolutions of up to 320x240 pixels. Because the light emitted by a commercial ToF camera

is infra-red, it is possible to modify an existing cystoscope for simultaneous acquisition of two images (color and distance) through one unique channel. This acquisition principle is sketched in Figure 4.3a. Both white light source and the ToF camera can use the same endoscope channel using commercially available beam splitters. The 20 mega Hertz wave IR light can be emitted through one of the fibers of the bundle used for the white light scene illumination. Such a prototype is currently being developed at the CRAN laboratory, but was not available at the time of the experimental stage. In order to show the feasibility of 3D cartography with ToF-based cystoscopes, a simplified prototype was used for the experiments in this chapter. This prototype, shown in Figure 4.3b, consists of a color and a ToF-camera (with a resolution of 200×200 pixels), which are calibrated for both intrinsic and extrinsic camera parameter. While the prototype does not utilize a beam splitter or a common channel for both cameras, it can be used to assess the feasibility of the proposed methods. Each pixel of the color image can be associated with a distance to the observed sequence, as can be seen when comparing Figure 4.3c with Figure 4.3d. The pixel-wise depth information and the known geometry (intrinsic and extrinsic calibration parameters) allow to reconstruct a dense set $\mathcal{P}_i^{3D}$, as shown in Figure 4.3e.

4.2.3 RGB-Depth Cameras

RGB-Depth cameras are commercially available acquisition systems (Pri13) that simultaneously capture color images and pixel-wise depth information. Such systems usually rely on active-stereo vision (Kon10) to estimate pixel-wise disparity maps, while a separate color camera captures the texture of the observed scene. The two (color and depth) camera systems are calibrated so that each pixel in the color camera can be associated with a depth value. RGB-Depth cameras may also be constructed using passive stereo-vision or time-of-flight sensors. In fact, the ToF prototype described in the previous section is a custom built version of an RGB-Depth camera. Consequently, the data acquired with an RGB-Depth camera consists also of a color image I_i and a pixel-wise corresponding set $\mathcal{P}_i^{3D}$. For the evaluation in this chapter, a Microsoft Kinect device (Mic13), which captures 640x480 color images and corresponding depth maps at 30 frames per second, was used. An example of the data acquired with this device is shown in Figure 4.4. It is noticeable that the depth map acquired with the Kinect sensor contains missing data along object borders corresponding to depth discontinuities, which is a typical problem for stereo-vision based disparity estimation. Furthermore, the noise levels in the depth map depend on IR-reflectivity of objects, and some materials might not reflect IR at all. These issues can be neglected in general for the registration algorithm, as these are guided by the texture obtained from the color camera. However, the estimated point cloud $\mathcal{P}_i^{3D}$ might contain "holes" due to occlusions. This can be overcome if the scene is captured from different viewpoints, and more observations of the the same scene portion allow to average out noise, for instance using (truncated) signed distance functions (CL96, NDI+11, IKH+11).
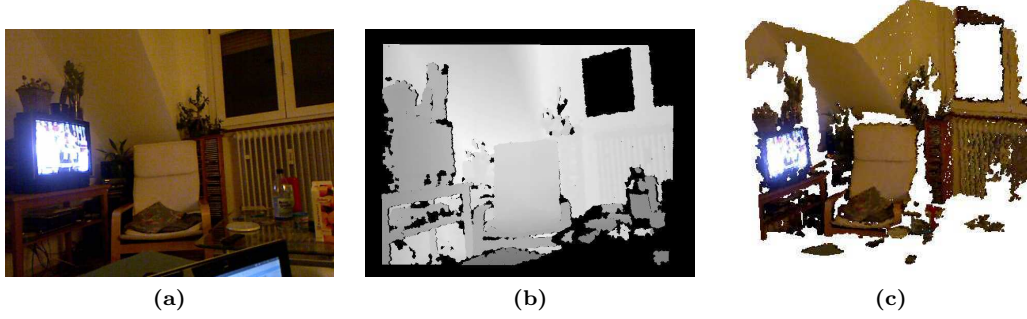
(a)　　　　　　　　　**(b)**　　　　　　　　　**(c)**

Figure 4.4: RGB-Depth camera. (a) Color image. (b) Depth map in the color camera coordinate system. (c) Point cloud representation of b) using the colors of a).

4.3 3D Cartography Approach

The aim of the proposed extensions to the algorithms presented in Chapter 3 is to be able to build 3D maps independently of the 3D point density (i.e. the algorithm must be able to handle the data of all three acquisition systems). This section will begin with a description of the different steps of the three-dimensional cartography process, and emphasize similarities as well as differences to its two-dimensional counterpart. Implementation details follow in Sections 4.3.2 to 4.3.4.

4.3.1 Overview of the 3D Cartography Steps

Link between 2D and 3D Data of Two Acquisitions

The two-dimensional cartography process started with the registration of consecutive image pairs. The obtained local transformations $T^{2D}_{i \to i+1}$ were then simply concatenated to obtain (initial) global transformations $T^{2D}_{0 \to i}$. These two-dimensional projective transformations displace points from the image plane of each acquisition i to the plane of the common coordinate system, leading to two-dimensional planar maps. To obtain three-dimensional maps instead, the depth data of each acquisition must be placed into a global three-dimensional coordinate system, which requires three-dimensional transformations. However, to obtain these 3D transformations, the 2D registration algorithm is not changed. Instead, the dense 2D correspondences (obtained from $x_{i \to j}$) are used to solve for $T^{3D}_{i \to j}$. In fact, $T^{2D}_{i \to j}$ were estimated from $x_{i \to j}$ by minimizing a least squares criterion (recall Section 1.3.2.4). As described in Section 4.3.2.1, combining $\mathcal{P}^{3D}_i$ and $x_{i \to j}$ allows to estimate $T^{3D}_{i \to j}$ without modifications to the two-dimensional registration algorithm proposed in the previous chapter. Independently of the number of 3D measurements (eight points given by the laser prototype, or dense point cloud provided by

the ToF-prototype and the Kinect), the computation method of the 3D transformation will be the same. However, when dense point clouds are available, the computation of the 2D optical flow $x_{i \to j}$ can be improved with this 3D data, independently of the 3D cartography problem. Indeed, the dense points sets $\mathcal{P}_i^{3D}$ and $\mathcal{P}_j^{3D}$ can be integrated into the energy minimization framework used to optimize $x_{i \to j}$. This allows for first-order regularization without implicit over-smoothing, which was a problem in two dimensions and required computationally expensive higher-order regularization terms.

To sum up, for the data of all acquisition prototypes, the 2D registration of two images (first step) and the 3D transformation computation of the corresponding data are two sequential and independent steps. Only for dense point clouds, the 2D registration step can be facilitated by using the additional 3D points information.

Global 3D Map Correction

In the 2D cartography algorithm, global transformations $T_{0 \to i}^{2D}$ were adjusted to correct accumulated errors. This required an automated selection of a (small) subset of additional non-consecutive image pairs. This selection was achieved using a graph structure, where each image was represented by its polygon shape in the two-dimensional global coordinate system. The amount of image overlap was computed using the area of polygon intersection. In three dimensions, the representation of each image in the three-dimensional global coordinate system and the computation of image overlap has to be adapted. These modifications are explained in Section 4.3.3, together with the (minor) modifications to the global bundle adjustment step.

Surface Compositing

As the last step of the two-dimensional cartography process, the optimal color for each pixel in the global map was selected from the available images. This goal was formulated as an energy minimization problem, and allowed to simultaneously maximize the contrast while correcting small image misalignments and exposure differences. This concept will be extended to three dimensions in Section 4.3.4. Instead of pixel-wise map colouring, the optimal texture is determined by analysing the projections of triangular faces onto the image planes. As in 2D, this approach allows for simultaneous contrast-enhancement and texture misalignment correction.

4.3.2 Three-Dimensional Data Registration

Estimating $T_{i \to j}^{3D}$ from $x_{i \to j}$

As explained in Section 1.3.2.4, given a set of homologous pixel positions in images I_i and I_j (via the displacement vector field $x_{i \to j}$), the two-dimensional perspective transformation $T_{i \to j}^{2D}$ can be estimated by minimizing a least squares error criterion. Each two-dimensional correspondence $p \leftrightarrow p + x_p$ gives two equations that are linear with respect to the parameters of $T_{i \to j}^{2D}$, so that an over-determined linear equation system can be solved.

When a set of three-dimensional correspondences $p_{i,k}^{3D} \leftrightarrow p_{j,k'}^{3D}$ is available, similar SVD-based techniques exist (AHB87, HHN88) that minimize E^2 of Equation (4.4). The aim is to find the six parameters of $T_{i \rightarrow j}^{3D}$, encapsulated in the translation vector $t_{i \rightarrow j}^{3D}$ and the rotation matrix $R_{i \rightarrow j}^{3D}$.

$$E^2 = \sum_{k=1}^{|\mathcal{P}_i^{3D}|} \left\| p_{j,k'}^{3D} - R_{i \rightarrow j}^{3D} \; p_{i,k}^{3D} - t_{i \rightarrow j}^{3D} \right\|_2^2. \tag{4.4}$$

Other techniques use quaternion representations (i.e. (Hor87, WSV91)). As systematically analyzed in (ELF97), all these approaches achieve comparable robustness and accuracy for both simulated and real data.

However, this approach can only be employed when a set of homologous three-dimensional point correspondences $p_{i,k}^{3D} \leftrightarrow p_{j,k'}^{3D}$ can be established. Both the ToF-prototype and the Kinect sensor capture dense depth measurements $\mathcal{P}_i^{3D}$, which allows to obtain such a set of correspondences via the displacement vector field $x_{i \rightarrow j}$. Indeed, the elements of $x_{i \rightarrow j}$ give two-dimensional point correspondences between pixels of acquisitions i and j, and the correspondence of 3D points and their 2D projections is known in the 3D acquisition coordinate system. With this knowledge, and due to the dense 3D point clouds, 3D homologous point correspondences can be established for two acquisitions i and j.

The laser cystoscope prototype however captures only a sparse set of eight three-dimensional positions for each acquisition i, and there exists no corresponding three-dimensional measurement at the homologous pixel positions[1] in acquisition j. In this case, we have to solve for $T_{i \rightarrow j}^{3D}$ using an approach often referred to as *camera pose estimation*, which is based on Equation (4.2). The least squares error criterion is given by

$$E^2 = \sum_{k=1}^{|\mathcal{P}_i^{3D}|} \left\| p_{j,k'}^{2D} - \nu_k \left[K \vec{0} \right] \; \left(T_{i \rightarrow j}^{3D} \; p_{i,k}^{3D} \right) \right\|_2^2, \tag{4.5}$$

where ν_k and K are, as in Equation (4.2), the normalization factor and the intrinsic camera parameter matrix, respectively. Equation (4.5) is overdetermined for 5 or more correspondences. As this latter approach is applicable for all three prototypes described in Section 4.2, we employ the robust linear n-point method presented in (QL99), which does not degenerate for co-planar point correspondences, to estimate $T_{i \rightarrow j}^{3D}$ via $x_{i \rightarrow j}$ and $\mathcal{P}_i^{3D}$ for both dense and sparse point clouds.

Integrating 3D Measurements into the 2D Registration Framework

This section describes how three-dimensional measurements $\mathcal{P}_i^{3D}$ and $\mathcal{P}_j^{3D}$ can be integrated into the two-dimensional image registration framework, as described in Section 3.3. The cost functions defined in the following two sections can be added to Equation (3.8), i.e. they can be

---

[1]The laser points move on the surface when the prototype is displaced. Therefore, laser points of two acquisitions do not represent the same 3D positions.

used in any combination with the cost functions defined in the previous chapter. The particular cost functions used for the results of this chapter are given in Section 4.4.1. However, the energy cost function extentions for the $\mathrm{x}_{i \rightarrow j}$ vector field determination is only feasible when dense point clouds (i.e. homologous three-dimensional measurements) are available. Both ToF-prototype and the Kinect capture such dense point clouds, while for the laser cystoscope prototype, the following two extensions are not exploitable.

Enforcing Rigid Transformations

The problem of explicit over-smoothing of pairwise regularization terms was addressed in Section 3.3.2. A fourth-order potential function allowed to enforce a perspective transformation globally on the estimated displacement field $\mathrm{x}_{i \rightarrow j}$. A similar approach that enforces a rigid 3D transformation can be implemented when (dense) three-dimensional measurements are available:

$$
\begin{aligned}
E^{\diamond \mathrm{3D}}(\mathrm{x}_{i \rightarrow j}) &= \sum_{(p,k,l,m,n) \in \mathcal{C}^{\diamond}} E_{pklmn}^{\diamond \mathrm{3D}}(x_p, x_k, x_l, x_m, x_n) \text{ with} \\
E_{pklmn}^{\diamond \mathrm{3D}}(x_p, x_k, x_l, x_m, x_n) &= \left\| \mathrm{T}_{klmn}^{\mathrm{3D}^{\diamond}} \, p_{i,p}^{\mathrm{3D}} - p_{j,p+x_p}^{\mathrm{3D}} \right\|_2^2.
\end{aligned}
\tag{4.6}
$$

$\mathrm{T}_{klmn}^{\mathrm{3D}^{\diamond}}$ in this case is the rigid transformation that transforms the three-dimensional measurements of acquisition i associated with vertices (k, l, m, n) to the three-dimensional measurements of acquisition j associated with positions (k', l', m', n'). Again, k, l, m and n are chosen to be the corner vertices in $\mathcal{V}^r$, and all remaining vertices p form fourth-order cliques $(p, k, l, m, n) \in \mathcal{C}^{\diamond}$, where $\mathcal{C}^{\diamond}$ is the same set of cliques used for the perspective-enforcing higher-order term of Equation (3.7). As for the two-dimensional regularization, this ensures a global interaction between variables. Equation (4.6) will ensure that the displacement vector field $\mathrm{x}_{i \rightarrow j}$ corresponds to a rigid transformation $T_{i \rightarrow j}^{\mathrm{3D}} : \mathcal{P}_i^{\mathrm{3D}} \rightarrow \mathcal{P}_j^{\mathrm{3D}}$.

Scale-Consistent Regularization

Similar to its two-dimensional counterpart $E^{\diamond}(\mathrm{x})$, the higher-order terms of Equation (4.6) lead to several non-submodular pairwise terms after reduction. Using three-dimensional measurements $\mathcal{P}_i^{\mathrm{3D}}$ and $\mathcal{P}_j^{\mathrm{3D}}$, it is possible to use pairwise regularization, avoiding the problem of over-smoothing and non-submodular terms. This will lead to an energy function much easier to minimize. This *scale-consistent* regularization term is defined as

$$
\begin{aligned}
E^{\mathrm{scale}}(\mathrm{x}_{i \rightarrow j}) &= \sum_{(p,q) \in \mathcal{N}^r} E_{pq}^{\mathrm{scale}}(x_p, x_q) \text{ with} \\
E_{pq}^{\mathrm{scale}}(x_p, x_q) &= \left(\left\| p_{i,p}^{\mathrm{3D}} - p_{i,q}^{\mathrm{3D}} \right\|_2 - \left\| p_{j,p+x_p}^{\mathrm{3D}} - p_{j,q+x_q}^{\mathrm{3D}} \right\|_2 \right)^2.
\end{aligned}
\tag{4.7}
$$

It ensures that the Euclidean distance between the three-dimensional measurements $p_{i,p}^{\mathrm{3D}}$ and $p_{i,q}^{\mathrm{3D}}$ is similar to the corresponding Euclidean distance between $p_{j,x+x_p}^{\mathrm{3D}}$ and $p_{j,q+x_q}^{\mathrm{3D}}$. This ensurse the preservation of the scale of the observed surface parts when passing from one viewpoint to another.

Interpolating Missing Measurements

Both selected vertices p, as well as corresponding positions $p + x_p$ might not have valid 3D measurements in acquisitions i and j. This is the case for non-overlapping parts (i.e. $p + x_p$ lies outside the valid domain of image I_j), and in general for noisy measurements. Such missing measurements $p_{i,p}^{3D}$ and $p_{j,p+x_p}^{3D}$ are interpolated by fitting a plane equation to the n nearest available measurements in $\mathcal{P}_i^{3D}$ and $\mathcal{P}_j^{3D}$ with respect to p and $p + x_p$, respectively. In all experiments, $n = 10$ was chosen.

4.3.3 Global Map Correction

As argued in Section 3.2, registration of all possible overlapping image pairs in infeasible for iconic data superimposition algorithms due to time constraints. For this reason, we employ an extension of the two-dimensional map correction approach to compensate globally accumulated errors in three-dimensional maps.

First, assuming all consecutive acquisitions have already been registered, global transformations $T_{0 \to i}^{3D}$ are obtained via concatenation of local transformation matrices $T_{i \to i+1}^{3D}$ (see Equation (4.3)). Then, a subset of additional, non-consecutive image pairs is selected, which allow to maximize the "material shortcut" (see also Section 3.2). These pairs are then registered using the algorithm described in Section 3.3 (and potentially with the extensions described in Section 4.3.2.2 when dense point measurements are available). The combined set of local (consecutive and non-consecutive) transformations $T_{i \to j}^{3D}$ are then used to equally distribute accumulated 3D point position errors in the global coordinate system.

The following subsections describe only the changes to the algorithm presented in Section 3.2.

Detecting Additional Acquisition Pairs

In Equation (3.2), $\delta_{i,j}^{2D}$ depicted the percentage of image area overlap between I_i and I_j in the global two-dimensional coordinate system. Each image was represented by a polygon (rectangle image domain transformed by $T_{i \to 0}^{2D}$) in the global coordinate system, and $\delta_{i,j}^{2D}$ was computed using the area of polygon overlap. Here, we can compute the overlap $\delta_{i,j}^{3D}$ between acquisitions i and j in three-dimensions by projecting the point cloud $\mathcal{P}_i^{3D}$ into the coordinate system of acquisition j via $T_{i \to j}^{3D}$, and vice-versa:

$$\delta_{i,j}^{3D} = \min \left(\frac{|T_{i \to j}^{3D}(\mathcal{P}_i)|^{\text{valid}_j}}{|\mathcal{P}_i|}, \frac{|T_{j \to i}^{3D}(\mathcal{P}_j)|^{\text{valid}_i}}{|\mathcal{P}_j|} \right). \tag{4.8}$$

In Equation (4.8), $|T_{i \to j}^{3D}(\mathcal{P}_i)|^{\text{valid}_j}$ is the number of 3D points of acquisition i, whose projections are valid (i.e. visible) in the two-dimensional coordinate system of I_j, and $T_{i \to j}^{3D} = T_{0 \to j}^{3D} {T_{0 \to i}^{3D}}^{-1}$. All other steps of the algorithm (see Section 3.2.1) remain identical to its two-dimensional

counterpart, except that the edge weights and the "material shortcut" are computed with $\delta_{i,j}^{3D}$ instead of $\delta_{i,j}^{2D}$. The result is a set of additional non-consecutive acquisition pairs $(i \to j \neq i)$ that have to be registered. Then, all available $T_{i \to j}^{3D}$ can be used to find again the shortest path transformation $T_{0 \to i}^{3D}$ for each acquisition in the common coordinate system. The edges of this second graph are also weighted by the SDD between superimposed images I_i, I_j (via $T_{i \to j}^{2D}$ as in Section 3.2.2).

Bundle Adjustment

After global 3D transformations have been updated, errors due to different shortest paths are present and must be corrected[1]. In the two-dimensional case, a set of regularly placed grid points $\mathcal{G}$ was created in the global coordinate system of the map. This led to a sparse set of non-linear equations that allowed to optimize all $T_{0 \to i}^{2D}$ while minimizing registration errors jointly for all (consecutive and non-consecutive) $T_{i \to j}^{2D}$.

In three dimensions, creating an equivalent set of regular surface points is not straightforward due to the sparsity of the point cloud and a lack of neighborhood connectivity[2]. However, a set of points $\mathcal{P}_i^{3D}$ is already available for each acquisition i. These are transformed into the global coordinate system via $T_{i \to 0}^{3D}(\mathcal{P}_i^{3D})$. A simple modification of Equation (3.3) leads to

$$E^2 = \sum_{i=0}^{N-1} \sum_{k=1}^{|\mathcal{P}_i^{3D}|} \left(\frac{1}{|L_k|} \sum_{(i,j) \in L_k} \left\| p_{0,k'}^{3D} - T_{j \to 0}^{3D} T_{i \to j}^{3D} T_{0 \to i}^{3D} \ p_{0,k'}^{3D} \right\|_2^2 \right), \qquad (4.9)$$

where, as usual, the notation $k \leftrightarrow k'$ indicates that the points expressed in the local coordinate systems were transformed to the global coordinate system. Equation (4.9) is sparse ($20 - 30\%$ non-zero elements in the Hessian matrix), as each global point $p_{0,k'}^{3D} \in T_{i \to 0}^{3D}(\mathcal{P}_i^{3D})$ is projected to valid image coordinates only in a small subset of acquisition pairs I_i and I_j ($(i,j) \in L_k$). The cost for each point is normalized by the number of acquisitions $|L_k|$. Again, the parameters of all global transformation matrices $T_{0 \to i}^{3D}$ are optimized to minimize the errors induced by all available local transformations $T_{i \to j}^{3D}$. Just as Equation (3.3), the equation system based on Equation (4.9) is minimized using a sparse Levenberg-Marquardt routine (Lou10), and the Jacobian matrix is computed using automatic differentiation (GJM$^+$99).

4.3.4 Contrast-Enhanced Surface Compositing

In Section 3.4, the final textured map was composed by two successive steps, which were both formulated as energy minimization problems. The first step was designed to correct small misalignments between overlapping images (by minimizing texture gradients/discontinuities

---

[1] For instance, when two point clouds of consecutive acquisitions i and $i + 1$ are placed into the global coordinate system using two different shortest paths, small alignment errors appear between $T_{i \to 0}^{3D}(\mathcal{P}_i^{3D})$ and $T_{i+1 \to 0}^{3D}(\mathcal{P}_{i+i}^{3D})$.

[2] One could fit a surface onto the global point cloud, and extract equidistant points.

across seams) and to maximize the contrast (by selecting the best possible image index for each pixel). In the second step of the algorithm, exposure related gradients were attenuated while retaining contrast and hue of the original images. The discrete two-dimensional domain of the map allowed to formulate the corresponding equations directly on a pixel-level using the $\mathcal{N}^4$ and $\mathcal{N}^8$ complementary neighborhood configurations in Equations (3.10) and (3.14).

The point clouds $\mathcal{P}_i^{3D}$ obtained with the ToF-prototype and the Kinect sensor are generally noisy and contain holes (see Figure 4.4c and Figure 4.3c). Consequently, it is not straightforward to extend the compositing algorithm of Section 3.4 to a voxel-level and three-dimensional complementary neighborhood systems (e.g. $\mathcal{N}^6$ and $\mathcal{N}^{26}$). This is even more of a problem for the laser cystoscope prototype, as it captures only data for eight three-dimensional point measurements for each acquisition. This leads to a very sparse global point cloud, and many areas of the observed scene are not covered.

Therefore, to texture the observed three-dimensional measurements, the global point cloud must first be transformed to an appropriate surface representation. A polygon mesh (consisting of vertices, edges and faces) is a common representation of (locally) waterproof surfaces that can be textured. The following section will show how, for N acquisitions, the noisy global point cloud

$$\mathcal{P}^{3D} = \sum_{i=0}^{N-1} \mathrm{T}_{i \to 0}^{3D}(\mathcal{P}_i^{3D})$$

can be converted to such a polygon mesh, which is known as surface rendering (HDD$^+$92, OS09).

Converting Point Clouds into Meshes

Polygon meshes have been studied extensively in computer graphics and geometric modelling, and generally different applications require different representations of these meshes. Technically, faces of a polygon mesh may be represented by triangles, quadrilaterals, simple convex polygons, or by more general concave polygons (with holes). In this medical application context, it is sufficient to convert the global point cloud $\mathcal{P}^{3D}$ into a triangular mesh, as this simplifies the texturing process. Let $\mathcal{M}^{3D} = \left\{ \mathcal{V}^{3D}, \mathcal{E}^{3D}, \mathcal{F}^{3D} \right\}$ be the polygon representation of the surface map to be textured, consisting of a set of vertices $\mathcal{V}^{3D}$, edges $\mathcal{E}^{3D}$, and triangular faces $\mathcal{F}^{3D}$. Depending on the observed scene, different algorithms have to be used to obtain $\mathcal{M}^{3D}$ from $\mathcal{P}^{3D}$. Smooth surfaces without depth discontinuities (such as the bladder phantoms acquired with the laser cystoscope prototype) allow to compute the polygon mesh $\mathcal{M}^{3D}$ using Poisson reconstruction (KBH06), which yields a very smooth mesh. The algorithm used is available through the open source system Meshlab (CNR). Required vertex normals are computed using plane-fitting on each vertex's nearest neighbors. For scenes that show depth discontinuities (for instances as shown in Figure 4.4c), Poisson reconstruction is not adequate as it does not handle sharp discontinuities or multiple objects. For such $\mathcal{P}^{3D}$, we use the classic Marching-Cube algorithm (LC87). Figure 4.5 shows the estimated surface meshes obtained for both scene types.
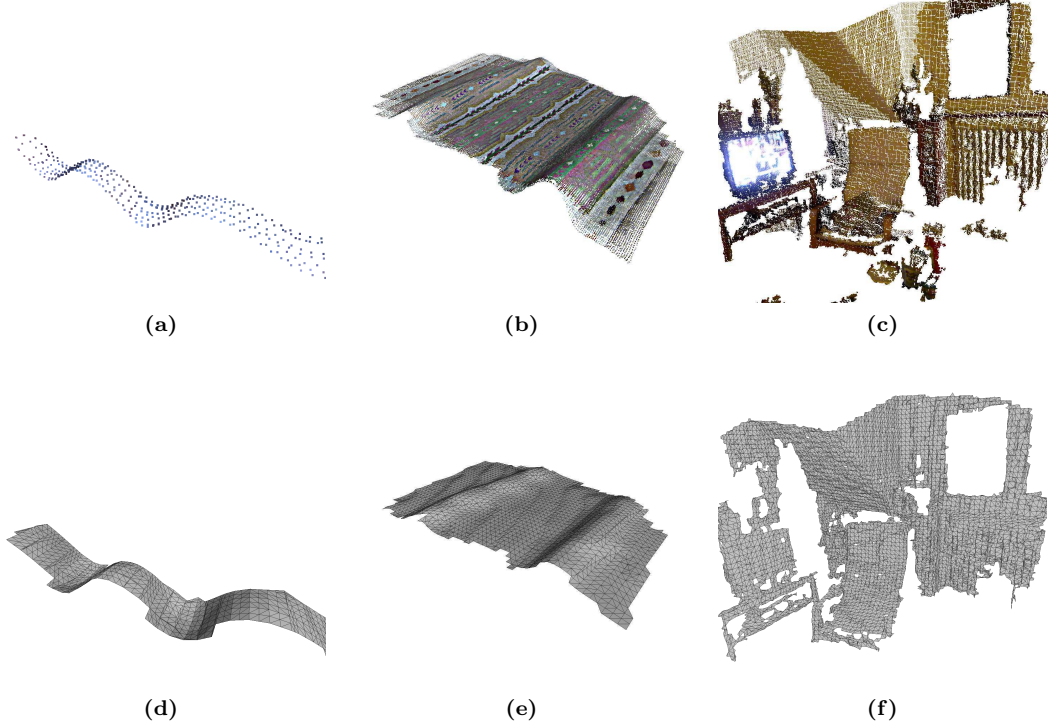
Figure 4.5: Surface meshes for different scene types. (a) Sparse point cloud, acquired with the laser cystoscope prototype for a video-sequence of 45 images of a wave phantom. (b) Dense point cloud of a carpet with waves (35 images), acquired with the Kinect sensor. (c) Dense point cloud for a scene with discontinuities (single image), acquired with the Kinect sensor. (d)-(e) For scenes without depth discontinuities (i.e. smooth surfaces), Poisson reconstruction (KBH06) is used to extract surface meshes. (f) Scenes with depth discontinuities are meshed using marching cubes (LC87). Multiple acquisitions from different viewpoints are necessary to produce a more accurate mesh with less holes.

Note that for scenes with depth-discontinuities, the mesh of a single image contains many holes and is in general very noisy. Multiple acquisitions from different viewpoints allow to reduce noise and fill missing surface parts.

Seam Localization on Triangular Meshes

After converting noisy (and potentially locally misaligned due to bladder movement) global point clouds $\mathcal{P}^{3D}$ to a polygon mesh $\mathcal{M}^{3D}$, it is now possible to compute optimized texture. Similar to Section 3.4.1, the energy function to be minimized is defined as

$$E^{\text{seam}^{3D}}(\mathbf{x}) = \sum_{f \in \mathcal{F}^{3D}} E_f^{\text{seam}^{3D}}(x_f) + \lambda_{\text{seam}} \sum_{(f,w) \in \mathcal{E}^{3D}} E_{fw}^{\text{seam}^{3D}}(x_f, x_w), \qquad (4.10)$$

with the configuration

$$\mathrm{x} : \mathcal{F}^{3D} \to \{0, ..., N-1\}$$

assigning an image index x_f to each face $f \in \mathcal{F}^{3D}$. As in the two-dimensional algorithm, this index indicates that the texture for face f is extracted from image I_{x_f}, chosen from the N images of the sequence. The vertices of f are projected into the images' coordinate system via $\mathrm{KT}^{3D}_{0 \to x_f}$, leading to a projected triangle $f^{2D}_{x_f}$ in image I_{x_f}. Similar to Equation (3.12), the contrast of such a triangle projection can then be computed. Instead of using a fixed shape neighborhood to compute the contrast for a pixel p in the two-dimensional map, Michelson's contrast is now evaluated directly within a discrete approximation of $f^{2D}_{x_f}$ in image I_{x_f}:

$$E^{\mathrm{seam}^{3D}}_f(x_f) = \exp\left(-\frac{\max\limits_{p \in f^{2D}_{x_f}} I_{x_f}(p) - \min\limits_{p \in f^{2D}_{x_f}} I_{x_f}(p)}{\max\limits_{p \in f^{2D}_{x_f}} I_{x_f}(p) + \min\limits_{p \in f^{2D}_{x_f}} I_{x_f}(p)} \right), \tag{4.11}$$

where $p \in f^{2D}_{x_f}$ denotes a discrete sampling within the projected face in image I_{x_f}. Like in two dimensions, a projection with a large contrast will yield a small energy cost, and vice versa.

Texture misalignments are attenuated by minimizing color gradients along the common edge of neighboring faces. If two faces $f, w \in \mathcal{F}^{3D}$ share a common edge $e_{fw} \in \mathcal{E}^{3D}$, the amount of texture misalignment can be computed by the sum of squared color differences at the corresponding projected locations along this edge:

$$E^{\mathrm{seam}^{3D}}_{fw}(x_f, x_w) = \sum_{p^{3D}_{0,k} \in e_{fw}} \left\| I^{\mathrm{hp}}_{x_f}(p^{2D}_{x_f,k'}) - I^{\mathrm{hp}}_{x_w}(p^{2D}_{x_q,k'}) \right\|^2_2 \cdot T(x_f \neq x_w). \tag{4.12}$$

The notation $p^{3D}_{0,k} \in e_{fw}$ denotes a discrete 3D point sampling along edge e_{fw}, and $p^{2D}_{x_f,k'}$ corresponds to the position of each sample projected into image I_{x_f}. As before, the notation k and k' indicate the correspondence of a point in different coordinate systems. When two faces are assigned the same image indices ($x_f = x_w$), the truncation function $T(\cdot)$ is null and $E^{\mathrm{seam}^{3D}}_{fw}(x_f, x_w)$ does not contribute to the regularization costs. The use of high-pass filtered images I^{hp} (computed with Equation (3.9)) ensures that only texture misalignments are penalized, while exposure related gradients are treated separately in the next section. It is recalled that in the high-pass filtered images, the texture remains visible, while exposure gradients are strongly attenuated (for details see Section 3.4.1). Equation (4.10) is minimized using alpha-expansion until convergence, usually requiring two full cycles over $\mathcal{L} = \{0, ..., N-1\}$.

A similar approach was first published in (LI07). While the authors employ the same strategy for the regularization term, the data term for each face is based on a different quality criterion. In (LI07), a projection is assumed to be of good quality (i.e. low $E^{\mathrm{seam}^{3D}}_f(x_f)$) when the angle between face normal and local (in x_f) camera viewing direction (i.e. Z-axis of the camera) is small. While this approach can be useful for arbitrary viewpoints, it can be neglected for bladder cartography, as the camera's Z-axis is close to perpendicular for most acquisitions. Furthermore, the data term proposed in Equation (4.11) evaluates the quality of a projection

directly from the image texture. This allows to discard blurry images, and to maximize the contrast of the textured surface. Similar to two-dimensional seam localization, the method of (LI07) neglects the problem of motion blur and de-focus and assumes a sequence of well-contrasted images with small upto moderate exposure differences. As shown in Chapters 1 and 3, this assumption is not valid in cystoscopy.

Exposure and Vignetting Correction

Similar to the two-dimensional case, exposure related color gradients across neighboring faces can be corrected using blending/feathering techniques (RCMS99, LHS01, Bau02), seam-leveling (LI07), or total-variation based super-resolution techniques (GC09). However, these approaches correct exposure differences at the expense of loss of contrast, or can only be used to correct small exposure differences. As exposure differences are strong in a cystoscopic video-sequence (see Section 1.3.4), related color gradients are attenuated by a modified version of the methods proposed in Section 3.4.2.

The energy function to be minimized is given by Equation (4.13):

$$E^{\mathrm{exp^{3D}}}(\mathrm{m}) = \sum_{f \in \mathcal{F}^{\mathrm{3D}}} E_f^{\mathrm{exp^{3D}}}(m_f) + \lambda_{\mathrm{exp}} \sum_{(f,w) \in \mathcal{E}^{\mathrm{3D}}} E_{fw}^{\mathrm{exp}}(m_f, m_w), \tag{4.13}$$

where the configuration $\mathrm{m} : \mathcal{F}^{\mathrm{3D}} \to \mathcal{L} \subset \mathbb{R}^3$ assigns each face a multiplicative RGB vector to correct exposure. This means that the texture for a face $f \in \mathcal{F}^{\mathrm{3D}}$ is obtained by point-wise multiplication, i.e. the color vector $I_{x_f}(p)$ at each pixel $p \in f_{x_f}^{\mathrm{2D}}$ is point-wise multiplied by m_f, with x_f being the image index assigned to each face f in the previous section. This point-wise multiplication is expressed with the Hadamard (or Schur) product (Dav62) $I_{x_f}(p) \circ m_f$. The data term $E_f^{\mathrm{exp^{3D}}}$ is used to adjust the "face brightnesses", while the regularization term E_{fw}^{exp} ensures that the edges of neighbouring faces have no color discontinuities. For clarity, the regularization term is described prior to the data term.

Visible exposure differences across the common edge of two faces are attenuated using

$$E_{fw}^{\mathrm{exp^{3D}}}(m_f, m_w) = \sum_{p_{0,k}^{\mathrm{3D}} \in e_{fw}} \left\| I_{x_f}(p_{x_f,k'}^{\mathrm{2D}}) \circ m_f - I_{x_w}(p_{x_q,k'}^{\mathrm{2D}}) \circ m_w \right\|_2^2. \tag{4.14}$$

Equation (4.14) is similar to Equation (4.12), except that the original images instead of high-pass filtered images are evaluated and the indicator function is omitted. The L_2 norm allows for smooth transitions (i.e. small differences in m_f and m_w) across faces f and w having been textured from the same image (i.e. $x_f = x_w$), while larger exposure differences across faces textured from different images (i.e. $x_f \neq x_w$) are attenuated. To ensure that m does not change the hue of the original images noticeably, the following data term is used:

$$E_f^{\mathrm{exp^{3D}}}(m_f) = \left\| \operatorname*{mean}_{p \in f_{x_f}^{\mathrm{2D}}} \frac{I_{x_f}(p) \circ m_f}{|I_{x_f}(p) \circ m_f|} - \operatorname*{mean}_{p \in f_{x_f}^{\mathrm{2D}}} \frac{I_{x_f}}{|I_{x_f}|} \right\|_2. \tag{4.15}$$

Equation (4.15) ensures that the mean color vector of the original image texture points in the same direction (in the RGB color cube) than the modified mean color vector. Equation (4.13) is minimized using fusion-moves, with the same brightness and color variations used in Section 3.4.2, and converges when the energy decrease within a fixed interval of fusion-moves drops below a threshold.

4.4 Results

This section presents results obtained for the three prototypes with the methods proposed in this chapter. First, in Section 4.4.1, data registration robustness and accuracy (in two and three dimensions) is assessed. In the remainder of this chapter, the term "registration" corresponds to the estimation of both $T_{i\rightarrow j}^{2D}$ and $T_{i\rightarrow j}^{3D}$. Similar, registration accuracy corresponds to deviations of the estimated transformation matrices from the ground truth transformations. The influence of depth sensor noise (3D point reconstruction errors along the Z-axis of the sensor) and the number of available reconstructed three-dimensional measurements (per acquisition) on registration quality are evaluated on simulated phantom data. Global map accuracy is then assessed in Section 4.4.2 on data sets acquired with the sensors described in Section 4.2, as well as on non-medical scenes, acquired with the Kinect. Furthermore, the efficiency of the proposed global map correction algorithm is assessed. In Section 4.4.3, the effectiveness of the proposed contrast-enhancing surface compositing algorithm is evaluated. This chapter concludes with a discussion of the contributions made in Section 4.5.

Bladder Phantoms

For the medical prototypes (ToF-prototype and laser cystoscope prototype), two phantoms with different geometry are used to evaluate the proposed registration and map correction algorithms. The first phantom (shown in Figure 4.6b) has a cylindrical shape (radius of 3.5 cm), and allows to simulate the bladder's curvature in a realistic fashion orthogonal to the cylinder's main axis (the ideal bladder is ovoidal with a radius of 4-5cm). The second phantom, consisting of several waves (see Figure 4.6c), simulates extreme cases of local deformation due of other organs warping the bladder. Indeed, without other organs pushing on the bladder, its shape is ideally convex (when it is filled with isotonic saline solution). When another organ pushes against the bladder, its shape becomes concave. The wave simulates an extreme surface warping with several convex deficit parts. The texture for both medical phantoms consists of a standard paper printout of a pig bladder photograph (as discussed in Chapter 3, pig and human bladder tissue is visually very similar).
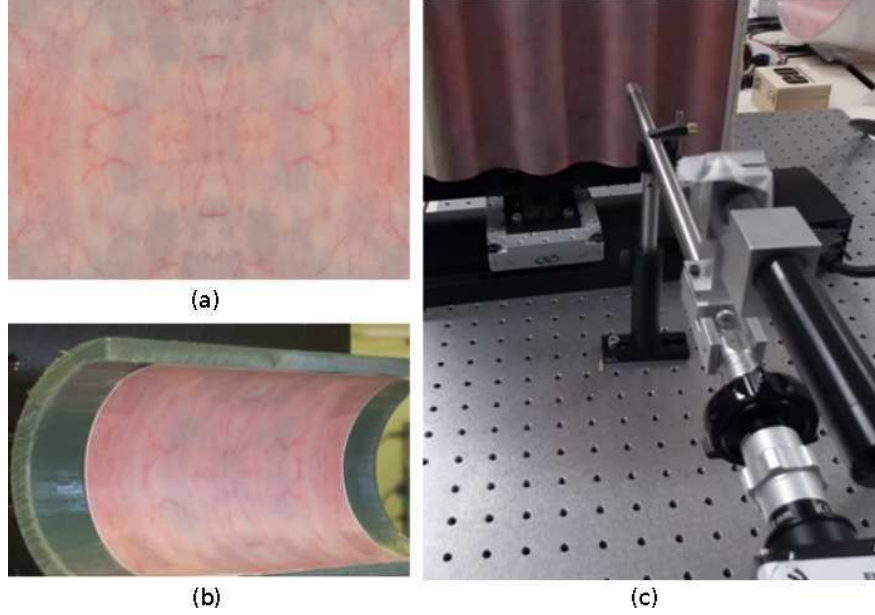
Figure 4.6: Medical phantoms for the assessment of three-dimensional cystoscopic cartography. (a) Pig bladder photograph used to texture the phantoms. The bladder photography corresponds to the upper left quarter of the image. The whole textured image was obtained by using the symmetries of the photography. (b) Cylindrical phantom with radius of 3.5cm, simulating the curvature of the bladder orthogonal to the cylinder's main axis. (c) Wave-shaped phantom and the laser cystoscope prototype, simulating extreme situations of local deformations. The wavelength corresponds to 8 cm, and the amplitude measures 1 cm.

4.4.1 2D and 3D Registration Robustness and Accuracy on a Simulated Phantom

As discussed in detail in Section 3.5, the proposed higher-order data and regularization terms allowed for robust and accurate estimation of the two-dimensional displacement vector field $\mathrm{x}_{i \to j}$. The fitted perspective transformations $\mathrm{T}^{2\mathrm{D}}_{i \to j}$ led to very small image registration errors $\epsilon^{2\mathrm{D}}_{i \to j}$ of about 0.25 pixels (defined in Equation (3.15)) for both consecutive ($j = i + 1$) and non-consecutive ($j > i$) image pairs. Three-dimensional registration accuracy of the estimated transformations $\mathrm{T}^{3\mathrm{D}}_{i \to j}$ can be similarly quantified by the mean three-dimensional registration error $\epsilon^{3\mathrm{D}}_{i \to j}$, which measures the accuracy of placing 3D points from viewpoint i into the coordinate system of viewpoint j:

$$\epsilon^{3\mathrm{D}}_{i \to j} = \frac{1}{|\mathcal{P}^{3\mathrm{D}}_i|} \sum_{p^{3\mathrm{D}}_{i,k} \in \mathcal{P}^{3\mathrm{D}^\star}_i} \left\| \mathrm{T}^{3\mathrm{D}^\star}_{i \to j} p^{3\mathrm{D}}_{i,k} - \mathrm{T}^{3\mathrm{D}}_{i \to j} p^{3\mathrm{D}}_{i,k} \right\|_2 . \tag{4.16}$$

In Equation (4.16), $\epsilon^{3\mathrm{D}}_{i \to j}$ is a straightforward extension of the two-dimensional registration error $\epsilon^{2\mathrm{D}}_{i \to j}$, where $\mathrm{T}^{3\mathrm{D}^\star}_{i \to j}$ is the ground truth transformation matrix, and $\mathcal{P}^{3\mathrm{D}^\star}_i$ is a set of known and
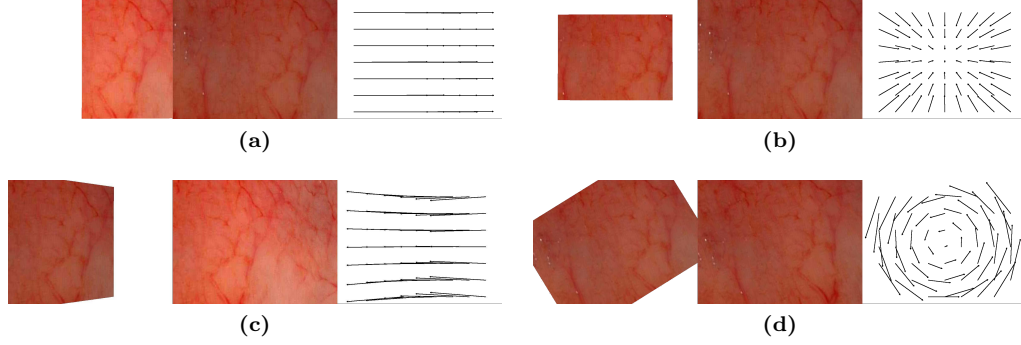
Figure 4.7: Examples of the simulated transformations for robustness and accuracy tests. These transformations depict those with the largest parameter values of (a) translations, (b) zooming, (c) out-of-plane rotations, and (d) in-plane rotations. The displacement vector fields were obtained by minimizing Equation (4.18).

noise-free 3D points in the coordinate system of acquisition i. As in Equation (3.15), the error measure is normalized by the number of points $|\mathcal{P}_i^{3D^\star}|$ and is ideally null.

Like in Section 3.5.1, a set of local transformations were simulated in order to assess robustness and accuracy of the proposed methods with regard to two- and three-dimensional registration. The set consists of 60 simulated acquisition pairs of a planar phantom with realistic bladder texture (see Figure 4.6a). Each acquisition pair consists of two color images I_i and I_j and two dense point sets $\mathcal{P}_i^{3D}$ and $\mathcal{P}_j^{3D}$. The point set $\mathcal{P}_i^{3D}$ of the first acquisition of each pair corresponds to a plane parallel to the image plane I_i in 20mm distance to the camera origin. The planar shape allows for assessing both the accuracy of the 2D image registration and 3D point displacement from one coordinate system to another. Gaussian noise with standard deviation $\sigma_{\text{color}} = 5$ was added to both images of the acquisition pair to simulate color camera noise between acquisitions, and vignetting is simulated based on the camera viewpoints. The first 10 acquisition pairs are linked by translations along the X-axis with increasing magnitude: $t_X \in \{1\text{mm}, -2\text{mm}, ..., 9\text{mm}, -10\text{mm}\}$. The next 20 acquisition pairs alternate between zooming in and zooming out, which is equivalent to translations along the Z-axis ($t_Z \in \{\pm 0.6\text{mm}, ..., \pm 6\text{mm}\}$). Perspective changes correspond to rotations around the Y-axis, and are simulated in the following 20 acquisition pairs ($r_Y \in \{\pm 2°, ..., \pm 20°\}$). The last set of acquisitions consist of rotations around the Z-axis ($r_Z \in \{3.5°, -7°, ..., 31.5°, -35°\}$), which correspond to in-plane image rotation. Figure 4.7 shows the strongest transformations for each type. Such strong transformations do not occur (between consecutive pairs) in a cystoscopic video-sequence, but may arise in other (non-medical) acquisition scenarios. Non-consecutive acquisition pairs are however often related by such strong transformations, as shown in Chapter 3.
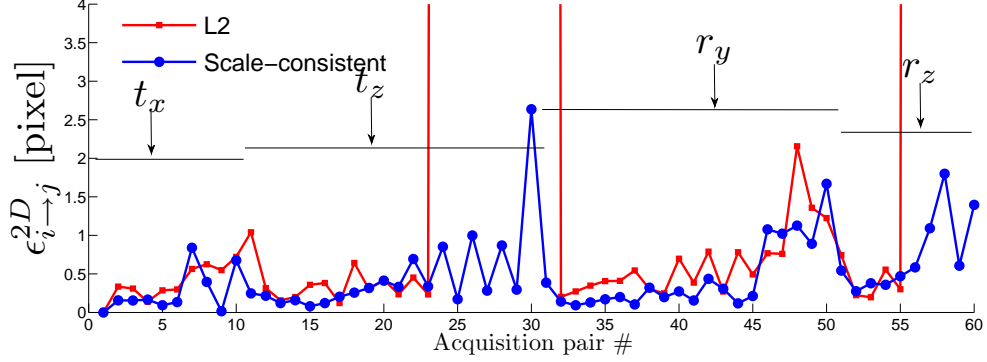
Figure 4.8: Accuracy and robustness of different pairwise regularization terms. The horizontal labeled lines depict the acquisition pair indices for which a particular rigid three-dimensional transformation type (t_Z, t_Z, r_y or r_Z) is applied. For transformations without large displacement differences between neighboring vertices, 2D data registration accuracy is comparable. For strong zooming or in-plane rotations however, the pairwise regularization of Equation (3.6) converges to poor local minima, which leads to high out-of-chart registration errors. The scale-consistent regularization term of Equation (4.7) does not lead to pool local minima, and robustly registers even strong transformations.

Registration Robustness with and without 3D Measurements

In this test, the robustness of the L2 pairwise regularization term of Equation (3.6), as used for consecutive images in Chapter 3, is compared with that of the scale-consistent pairwise regularization, formulated in Equation (4.7). For this comparison, Equation (4.17) corresponds to the energy computed with the L2 pairwise registration term $E^{\leftrightarrow}(x_{i \to j})$, while Equation (4.18) represents the energy computed with the scale consistent term $E^{\text{scale}}(x_{i \to j})$. For both energies, the second-order data term $E^{\triangle}(x_{i \to j})$ of Equation (3.4) is used.

$$E^{\text{reg2D}}(x_{i \to j}) = E^{\triangle}(x_{i \to j}) + \lambda_{\text{L2}} \ E^{\leftrightarrow}(x_{i \to j}) \tag{4.17}$$

$$E^{\text{reg3D}}(x_{i \to j}) = E^{\triangle}(x_{i \to j}) + \lambda_{\text{scale}} \ E^{\text{scale}}(x_{i \to j}) \tag{4.18}$$

The parameter $\lambda_{\text{L2}} = 1$ is set to the constant value used for all results in Chapter 3, while the parameter $\lambda_{\text{scale}} = 5$ will be used for the experiments in the remainder of this chapter. For this test, Gaussian noise (standard deviation $\sigma_{\text{depth}} = 1$mm) was applied to $\mathcal{P}_i^{\text{3D}}$ to simulate depth sensor noise. This noise level is representative of the three-dimensional point reconstruction errors of both the ToF-prototype and the laser cystoscope prototype. Looking at Figure 4.8, it can be seen that the accuracy of 2D registration is comparable for both regularization terms. A blue curve depicts the registration error $\epsilon_{i \to j}^{\text{2D}}$ when using scale-consistent regularization (Equation (4.18)), while the red curve corresponds to registration errors using L2 pairwise regularization (Equation (4.17)). It is noticeable that for both curves, the ϵ^{2D} values are mostly smaller than 1 pixel, which is not visually perceptible between two images. For

135

transformations with small magnitudes, the errors are similar (i.e. $\epsilon^{2D}_{i \to j} < 0.4$ pixels) to those obtained on simulated two-dimensional phantoms (see Section 3.5.1).

However, the transformations tested here also correspond to strong transformations, which often occur between non-consecutive images (notably for large scale and perspective changes). For transformations that involve large pairwise L2 regularization costs, such as strong zooming (acquisitions 24-31) or in-plane rotation (acquisitions 55-60), the registration converges to very incorrect local minima, indicated by the out-of-chart high values of the red curve. Such transformations are often observed for non-consecutive image pairs, as shown in Chapter 3. This fact led to the development of perspective-invariant higher-order regularization in Section 3.3.2. Instead of higher-order terms, the scale-consistent pairwise regularization term can be used when dense three-dimensional point measurements are available. This leads to faster computation and less non-submodular terms. The red curve of Figure 4.8 indicates the best results which can be obtained when dense point measurements are not available for each acquisition, and the L2 pairwise regularization term of Equation (3.6) has to be used. This is the case for the laser cystoscope prototype. These results suggest that the higher-order perspective-invariant regularization of Equation (3.7) should be employed when it is not possible to register non-consecutive image pairs using dense three-dimensional point measurements, but can be avoided when such information is available. In fact, using the three-dimensional rigid-enforcing version of Equation (3.7), as defined in Equation (4.6), leads to very similar results than those obtained with pairwise three-dimensional regularization. Because of this, and the increased algorithmic complexity and number of non-submodular terms, Equation (4.6) was not used in the experiments.

Registration Accuracy with Varying Sensor Noise Levels

For the second test, increasing Gaussian noise ($\sigma_{\text{depth}} = 1, 2, ..., 5$ mm) was applied to $\mathcal{P}^{3D}_i$ and $\mathcal{P}^{3D}_j$ to simulate (strong) depth sensor inaccuracies. Figure 4.9 shows the effect of this noise on image registration (ϵ^{2D}) as well as on 3D point alignment (ϵ^{3D}) accuracy between two viewpoints. For this test, only the result of minimizing the energy of Equation (4.18) is evaluated, as Equation (4.17) is not based on three-dimensional measurements. Increasing depth noise σ_{depth} leads to monotonically increasing $\epsilon^{3D}_{i \to j}$ registration errors, as shown in Figure 4.9a. Dashed lines depict the median registration error for all acquisition pairs of the sequence. However, noise with a standard deviation of 2 mm or more (in 20 mm distance to the surface) is very high. The ToF-prototype has, for instance, an error with standard deviation of 0.5 cm (along the Z-axis) at a distance of 25 cm to the surface, while for the laser cystoscope prototype, $\sigma_{\text{depth}} = 1$ mm at a distance of 35 mm. It is noticeable on Figure 4.9, that the $\epsilon^{3D}_{i \to j}$ value is small for $\sigma_{\text{depth}} = 1$mm (median $\epsilon^{3D} = 0.25$ mm) and remains sub-millimetric for $\sigma_{\text{depth}} = 2$mm (at a distance of about 20mm). Moreover, depth sensor noise does not have a strong influence on 2D data registration. As can be seen in Figure 4.9b, the 2D registration error $\epsilon^{2D}_{i \to j}$ does not increase
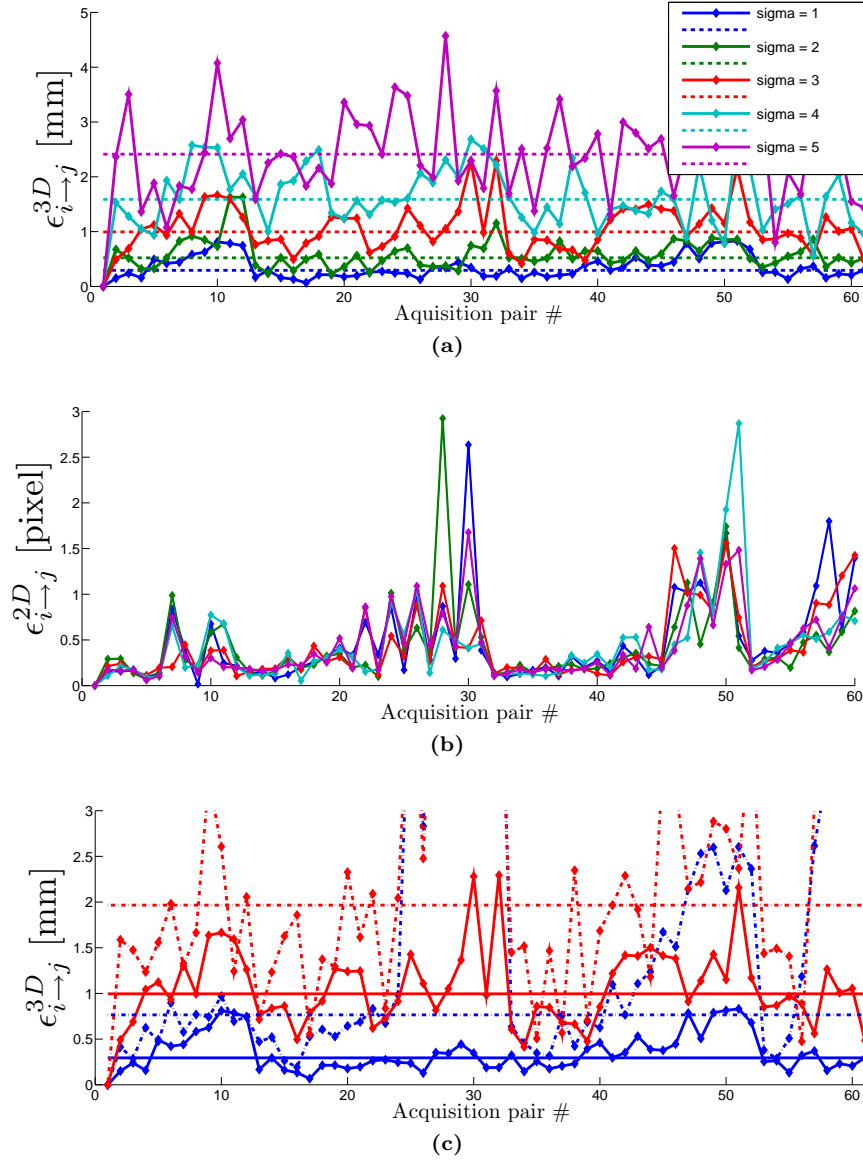
Figure 4.9: Influence of depth sensor noise on registration accuracy. (a) Effect of increasing Gaussian noise applied to the (dense) depth measurements on three-dimensional point alignment accuracy. Dashed lines indicate the median ϵ^{3D} of all acquisition pairs of the sequence. (b) Two-dimensional registration error does not increase linearly with σ_{depth}. (c) Registration accuracy $\epsilon^{3D}_{i \to j}$ comparison of dense (solid lines) and sparse (dashed lines) depth measurements for $\sigma_{depth} \in \{1(blue), 3(red)\}$. While two-dimensional registration accuracy (i.e. the displacement vector field $\mathbf{x}_{i \to j}$) is comparable (unlike robustness, see Figure 4.8), three-dimensional inaccuracy grows exponentially for sparse measurements relative to depth measurements with increasing noise σ_{depth}.
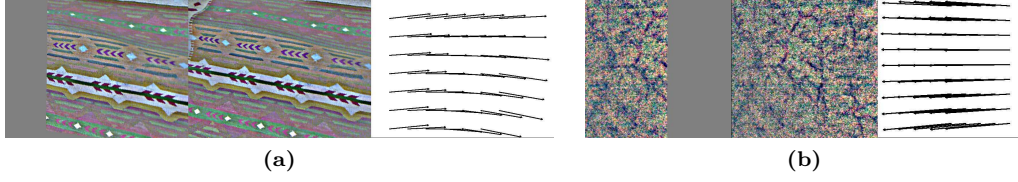
Figure 4.10: Registration of non-consecutive acquisition pairs using scale-consistent regularization. (a) Example of a registered non-consecutive pair, acquired with the Kinect sensor, showing a curved carpet. (b) Example of a registered pair of a wave phantom, acquired with the ToF-prototype. The displacement vector fields $x_{i \to j}$ are smooth, and two-dimensional image superimpositions are accurate for both sensor types. The three-dimensional registration error depends mainly on the quality and quantity of depth measurement.

monotonically, and is mostly influenced by the magnitude of the transformations, as it is the case for L2 regularization terms. This result indicates that the scale-consistent regularization is robust against sensor noise with regard to 2D registration accuracy, while being more robust with regard to registration success compared to L2 regularization (see also Figure 4.8).

Registration Accuracy of Dense and Sparse Depth Measurements

The final test evaluates the influence of the number of depth measurements (per acquisition) on three-dimensional registration accuracy for varying depth sensor noise. As can be seen in Figure 4.9c, the three-dimensional registration error increases exponentially with the noise level when using sparse measurements (dashed lines), while for dense point measurements (solid lines), this increase is less severe. For this test, the displacement vector field obtained from minimizing Equation (4.18) was used to obtain $T_{i \to j}^{3D}$ for dense measurements, while the displacement vector field of minimizing Equation (4.17) has to be used for sparse measurements. The sparse set of measurements corresponds to a spatially well distributed subset of the dense simulated measurements (see Figure 4.2b).

Conclusions

These results allow to reason that the scale-consistent regularization term is well suited for the registration of RGB-Depth images (acquired with dense depth measuring prototypes, such as the Kinect or the ToF-prototype). Even strong transformations (such as zooming, or in-plane rotations) can be robustly registered (as opposed to image registration with L2 regularization), which makes this term especially suitable for the registration of non-consecutive image pairs. At the same time, for moderate transformations, the 2D registration accuracy with the scale-invariant regularization term is comparable with that of L2 regularization, and the registration is not particularly sensitive to depth measurement noise. In other words, depth noise does not have a significant effect on the estimated displacement vector field $x_{i \to j}$ obtained by minimizing

Equation (4.18), as shown in in Figures 4.7 and 4.10. The displacement vector fields are smooth, and correctly superimpose the image pairs in two dimensions. Despite all these advantages, the three-dimensional registration accuracy strongly depends on the quality of the reconstructed depth measurements, as these are used to fit $\mathrm{T}_{i \to j}^{\mathrm{3D}}$. This is especially critical for the laser cystoscope prototype, as the small number of reconstructed point leads to exponentially larger inaccuracies, especially when local scene geometry is poor, as will be shown in the next section.

4.4.2 Global Map Reconstruction Accuracy

As in the two-dimensional cartography process, global transformations $\mathrm{T}_{0 \to i}^{\mathrm{3D}}$ are obtained by concatenation of local consecutive transformations $\mathrm{T}_{i \to i+1}^{\mathrm{3D}}$. These global transformations allow to place each local point cloud $\mathcal{P}_i^{\mathrm{3D}}$ into the global coordinate system via $\mathrm{T}_{i \to 0}^{\mathrm{3D}}(\mathcal{P}_i^{\mathrm{3D}})$. The accuracy of a two-dimensional global panoramic image is directly related to the accuracy of the displacement vector field $\mathrm{x}_{i \to j}$. As shown in the previous section, the (local and global) accuracy of three-dimensional point alignment mainly depends on sensor noise, as well as the number of depth measurements per acquisition. Increasing noise levels lead to monotonically increasing $\epsilon_{i \to j}^{\mathrm{3D}}$, and a sparse set of measurements infers exponentially larger errors than dense measurements. In this section, the effects of accumulated errors on map reconstruction accuracy and the efficiency of the global map correction technique are evaluated.

Wave Phantom and ToF-Prototype

The first example corresponds to a scan of the wave-shape phantom, recorded with the ToF-prototype. Figure 4.11a shows the phantom and the acquisition geometry for this setup. The sequence corresponds to a loop scenario, and consists of 70 manually displaced acquisitions, with varying translations along X- and Z-axis, as well as rotations around the Y-axis. Acquisition beginning (image I_0), trajectory and ending (image I_{N-1}) are annotated in Figure 4.11a. The initial point cloud without global correction (only $\mathrm{T}_{i \to i+1}^{\mathrm{3D}}$ were used) in Figure 4.11c shows clearly the globally accumulated error when the prototype returns close to the initial position. Between the three-dimensional points of the first and the last acquisition of the sequence, this accumulated error corresponds roughly to 1.5 cm, at a distance of 22 cm between optical center and surface. An area of 20×13 cm^2 is observed during the sequence. After a subset of additional acquisition pairs has been detected and global map correction has been performed, the corrected global point cloud, as shown in Figure 4.11d, is free of misalignments. The final textured surface is shown in Figure 4.11b, which corresponds to the observed surface part of the phantom, as indicated by the black rectangle in Figure 4.11a. The used ToF-prototype exhibits a depth measurement error with standard deviation of roughly ± 0.5cm at 25 cm distance to

the surface. However, due to dense (pixel-wise) measurements and strong depth variations[1] seen in each FOV, local errors are relatively small and do not lead to strong inaccuracies when fitting $T_{i \to j}^{3D}$. In particular, the reconstructed wave is not "bent", and the measured wavelength of Figure 4.11b corresponds to 78.6 mm (average taken from several manual measurements), whereas the true wavelength is known to be 80 mm. The measured amplitude corresponds to about 9.2 mm, compared to the true amplitude of 1cm. Such errors are insignificant, as the deformations of the bladder between (and locally during) examinations are larger and therefore impede very exact measurements.

---

[1]The term "strong depth variations" means here that for each viewpoint, the sensor acquires "rich" geometrical information, as the amplitude of the wave phantom is 1cm and at least one wave period is visible in each FOV. As shown later, local alignment errors are larger for shapes with less depth variations visible in the FOV.

(a)

(b)

(c)

(d)
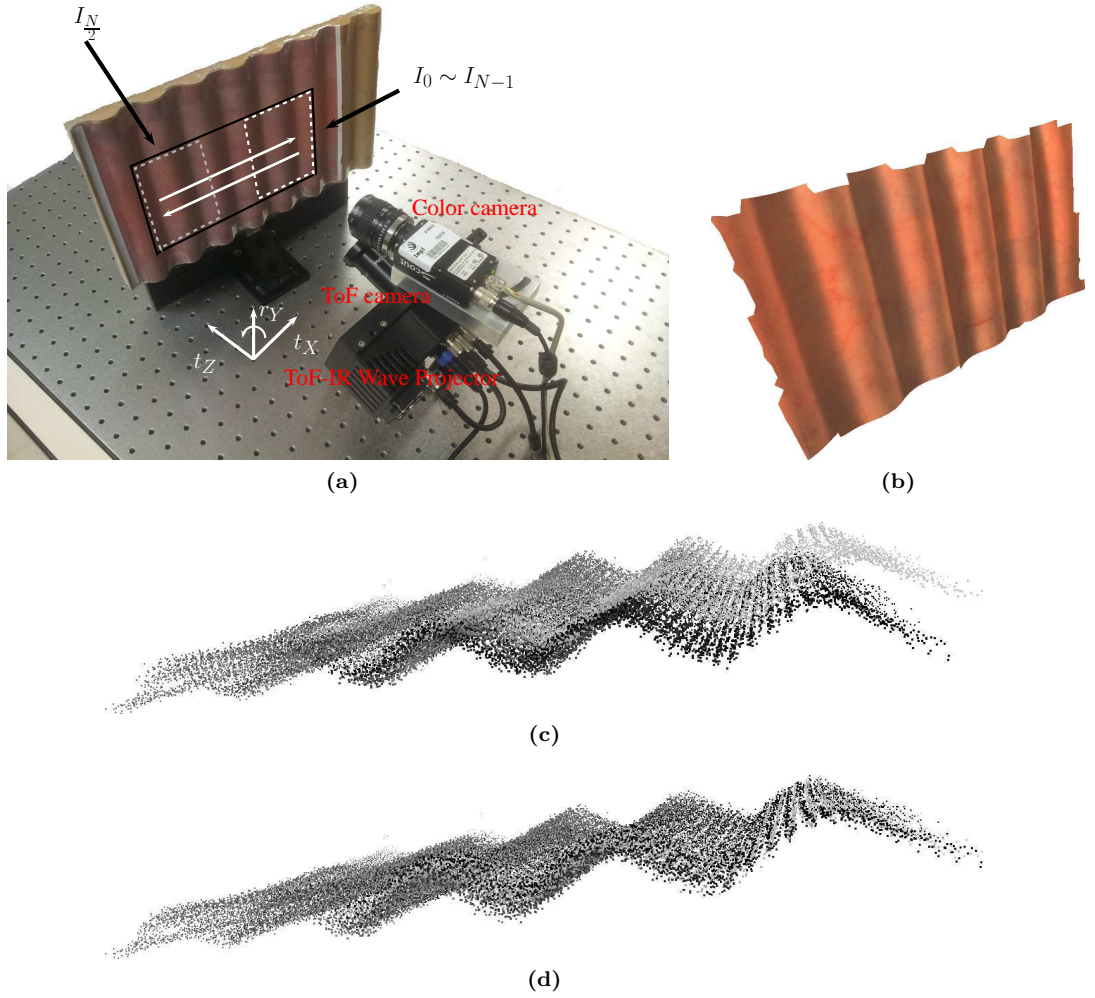
Figure 4.11: Global surface construction for the wave phantom and the ToF-prototype. (a) Acquisition setup, showing the prototype and the phantom. The sequence consists of translations along the X- and Z-axis, as well as rotations r_Y, and performs two overlapping scans, as indicated. (b) Reconstructed textured surface after global map correction and texture compositing. (c) Initial non-corrected global point cloud. Each point's intensity is proportional to the acquisition number. The globally accumulated error is visible between starting (dark) and ending (bright) position of the sequence, and is roughly measured as 1.5 cm. (d) After global correction, accumulated errors are attenuated. The optimized point cloud is correctly superimposed, and the reconstructed surface, shown in b), is coherent with the observed part of the phantom.

Cylinder Phantom and Laser Cystoscope Prototype

Scenario 1 - Scan Orthogonal to the Surface

This experiment simulates the typical scanning procedure during a cystoscopic examination: the half-cylinder phantom is scanned while keeping the cystoscope's viewing angle close to orthogonal relative to local surface of each viewpoint. This requires a combination of rotation and translation, which was performed by placing the phantom on a rotation table (the rotation center being between cystoscope and phantom)[1]. Two fully overlapping scans (forward and backward scan) were acquired, which is illustrated in Figure 4.12a. Figures 4.12d-f plot the parameter values of the estimated perspective transformation $T^{2D}_{i \to i+1}$ for the forward scan (the parameters for the backward scan are inverted, but otherwise very similar). The estimated parameters change smoothly during the scan, which confirms that the proposed registration algorithm of Chapter 3 achieves robust and accurate image registration. In particular, the dominant parameters of the estimated $T^{2D}_{i \to i+1}$ correspond to t_x and h_x, which correlates with the performed displacements. All other parameters, such as in-plane rotation ϕ or scale changes S_x, S_y are without effect. However, the parameter values of the estimated rigid transformation $T^{3D}_{i \to i+1}$, plotted in Figures 4.12g-h, fluctuate strongly during the scan (they should also change smoothly). This confirms the observations made on simulated data: even a very accurate displacement vector field $x_{i \to i+1}$ leads to noticeable three-dimensional registration errors when only a small number of noisy reconstructed depth measurements are available. The initial (uncorrected) global point cloud is shown in Figure 4.12b. The noise of the individual depth measurements are comparable with those of the ToF-prototype (compare with Figures 4.11c-d). A similar observation can be made with regard to globally accumulated errors, which corresponds to 3.3 mm between first and last acquisition in Figure 4.12b. After global correction, the three-dimensional measurements of both scans are superimposed (i.e. the accumulated errors are corrected). However, the small number of depth measurements leads to an error of 0.8cm for the line drawn in Figure 4.12i. Indeed, in 3D, the true length of the yellow line drawn in Figure 4.12i is 50mm, while the corresponding distance measured in the 3D map is 58mm. A larger image can also be seen in Figure 4.14b. Consequently, the resulting textured surface is "less" bent than the true phantom shape. This indicates that individual measurement errors for two similar scan patterns do not lead to very strong accumulated errors (thus allowing a global correction via additional acquisition pairs), but the global reconstruction itself becomes less accurate (deviates from the true surface shape) when sparse noisy depth measurements are used (compared with the accurate measurements obtained with the ToF prototype in the previous section).

---

[1]Displacing the phantom instead of the laser cystoscope prototype is performed for practical reasons. From an algorithmic point of view, the problem remains unchanged.

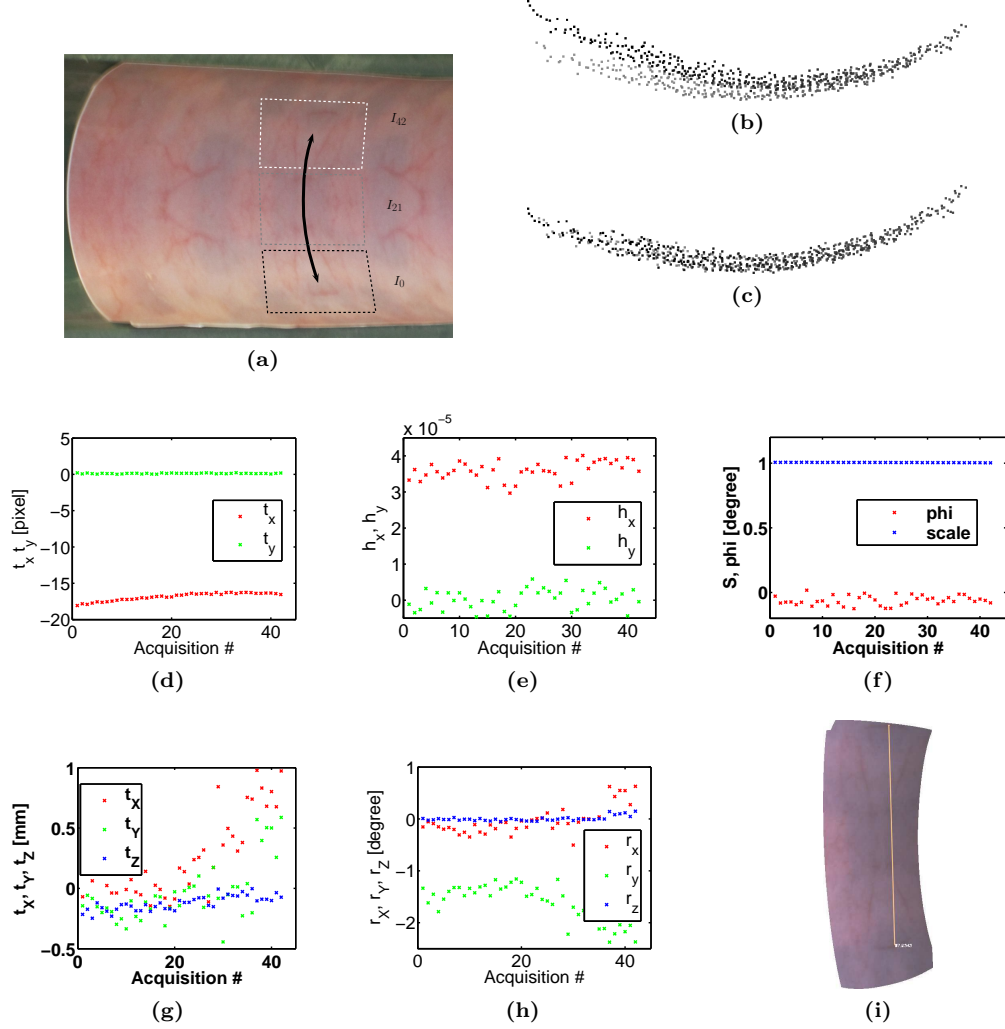**Figure 4.12:** Global surface construction for the half cylinder phantom and the laser cystoscope prototype. (a) Acquisition setup. The prototype displacements correspond to a combination of rotation around the Y-axis and translation along the X-axis. The viewpoint is close to perpendicular during the sequence, which simulates the scanning procedure of clinicians. (b) Uncorrected global point cloud. The visible gap between first and last acquisition has an error of 3.3 mm. (c) Corrected point cloud. (d) Estimated two-dimensional translation parameters t_x and t_y (for the first scan upto acquisition $i = 42$). (e) Estimated two-dimensional perspective parameters h_x and h_y, and (f) in-plane rotation ϕ and scale change $S = S_x + S_y$. The plots of d)-f) illustrate that two-dimensional image registration is performed robustly and accurately throughout the sequence. (g) Estimated three-dimensional displacements t_X, t_Y and t_Z and (h) rotation parameters r_X, r_Y and r_Z. Due to point reconstruction inaccuracies and the low number of reconstructed points per acquisition, the estimation of the three-dimensional transformation parameters is less accurate and varies strongly during the sequence. (i) Reconstructed surface from c) (see also Figure 4.14b). While locally accumulated errors are comparable with the ToF-prototype, the overall reconstruction accuracy is worse. The error along the line drawn in i) is 8 mm (58mm measured, true distance 50mm), resulting in a cylinder that is slightly less bent than that of the original phantom.

Scenario 2 - Scan Parallel to the Cylinder's Main Axis

The second experiment illustrates these inaccuracies. Instead of performing two almost identical forward and backward scans, the phantom is now scanned by two zig-zag patterns parallel to the cylinder's main axis, as shown in Figure 4.13a. The prototype displacements correspond to four partly overlapping linear trajectory scans, with a total of 288 acquisitions. Each of the four trajectory parts consists of 69 translations of $t_X = 1$mm along the X-axis, which are performed with a micrometer translation table. Translations t_Y along the Y-axis (which link overlapping linear trajectory scans) have been performed manually, because only one translation table was available. Within each individual trajectory line, the observed three-dimensional geometry is identical (i.e. noise-free depth measurements would be reconstructed at the same local coordinates), while it changes between each trajectory. In the first two trajectories (first zig-zag, acquisition numbers 1 - 150), the observed three-dimensional geometry is relatively "rich". As the prototype's viewing angle is not orthogonal to the surface, visible curvature (as illustrated by the strong perspective FOVs in Figure 4.13a) leads to depth variations between the eight reconstructed three-dimensional measurements. These variations impede large inaccuracies when estimating $T^{3D}_{i\rightarrow i+1}$, and the estimated parameters of the rigid transformations correspond effectively to $|t_X| = 1$ mm, as shown in Figures 4.13c-d. The other five parameters $(t_Y, t_Z, r_X, r_Y, r_Z$, see caption of Figure 4.13) of $T^{3D}_{i\rightarrow i+1}$ remain close to 0 (except for t_Y at the trajectory turnings).

However, local registration/data alignment errors become stronger when the FOV observes less three-dimensional structure/depth variations, as is the case for the second zig-zag (acquisition numbers 151-288). These two trajectory scans observe the surface almost orthogonally to the local viewing direction along the Z-axis, so that the reconstructed depth measurements do not exhibit strong variations (reconstructed points are situated on a "quasi-planar" local surface orthogonal to the Z-axis of the camera). Inaccuracies of local depth measurements now have a stronger influence on the parameters of the estimated $T^{3D}_{i\rightarrow i+1}$. As can be seen in Figures 4.13c-d, the parameter t_X is increasingly underestimated in the last two linear trajectory scans (i.e. $|t_X| < 1$mm). In turn, this is compensated by an overestimation of r_Y ($|r_Y| > 0°$).

The increasing errors on the estimated rigid transformations $T^{3D}_{i\rightarrow i+1}$ correlate with the initial (uncorrected) global point cloud, as shown in Figure 4.13b. As before, the intensity of the points are proportional to the acquisition index. Accumulated errors between the trajectory parts of the first zig-zag scan are relatively low (i.e. comparable with the results obtained with the ToF-prototype and the orthogonal forward-backward scan), the corresponding parts of the global point cloud reflect the linear (translation-only) scan paths. However, the points corresponding to the third and fourth trajectory lines exhibit increasingly stronger deviations from a linear shape, and accumulated errors become significantly larger (between second and third trajectory line). Furthermore, the global point cloud is affected by a "bending"-effect due to the overestimation of r_Y. As with the forward-backward scan example in the previous section, accumulated errors between trajectories that observe similar three-dimensional structure (i.e.
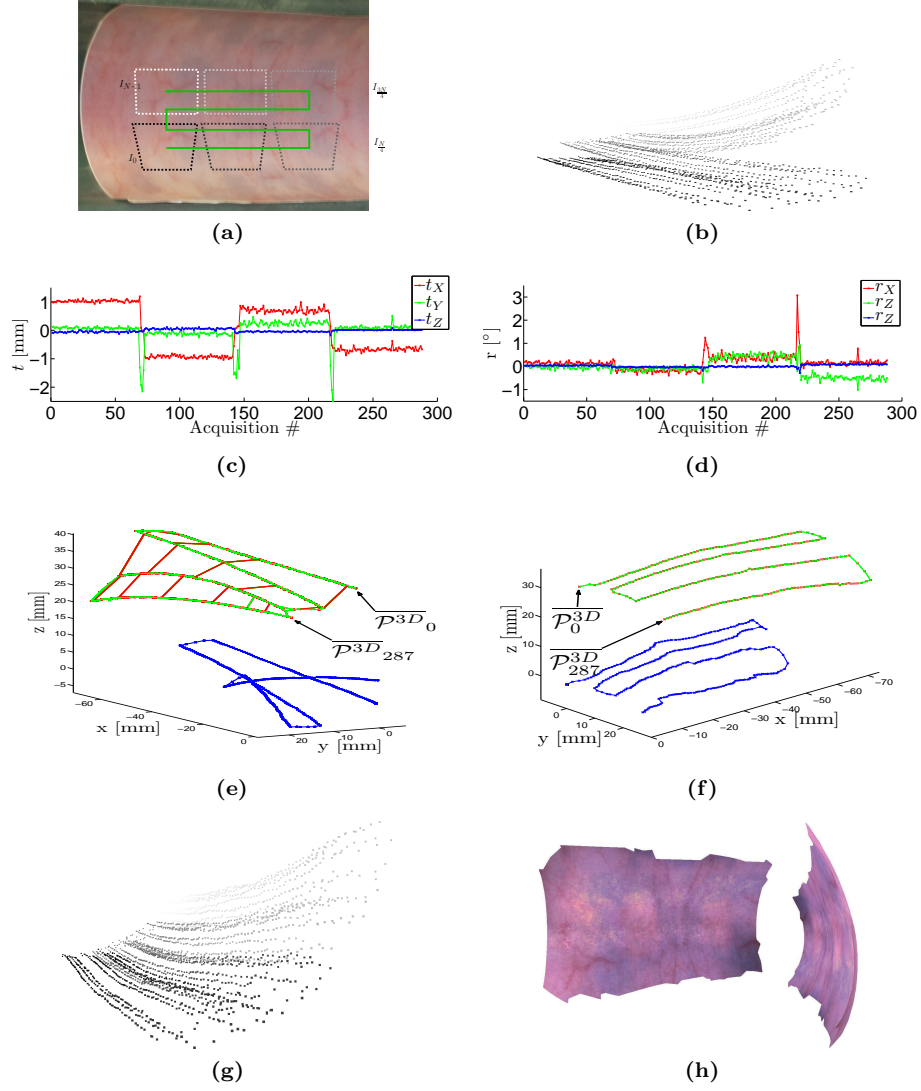
Figure 4.13: Global surface construction for a cylindrical bladder phantom and the laser cysto-scope prototype. (a) The sequence simulates two zig-zag paths, as indicated by the green lines. The last two scan-lines exhibit poor local depth information (the reconstructed points lie in a plane orthogonal to the camera's Z-axis) (b) Initial (non-corrected) global point cloud, exhibiting large accumulated errors. (c) Translation parameters of the estimated transformations. (d) Rotation parameters. As can be seen in c) and d), with decreasing depth variation in the FOV, translations are underestimated, while rotations are overestimated. (e) Additional pairs (thick red lines) used for global map correction are nonetheless found. (d) Scene geometry after global correction. (g) Corrected point cloud: accumulated errors are attenuated. (h) Left image: reconstructed textured surface viewed roughly from the same viewpoint than a). Right image: half-cylinder part viewed from the side. The cylindrical shape is clearly visible, and sufficient for the medical application context.

first and second, respectively third and fourth trajectories) are lower than those between second and third trajectory scans. This indicates that when using the laser cystoscope in a clinical situation, relative errors between partly overlapping trajectory scans can be kept (relatively) low, as long as the cystoscope is displaced at a similar angle towards the observed surface. While this is usually the case (as clinicians mostly navigate orthogonally to the surface), clinical examinations are required in order to verify the observations made here.

Despite the relatively strong alignment errors between the different trajectories of this experiment (compared to the previous experiments), correct additional acquisition pairs were found (see Figure 4.13e). After global correction, the corresponding point cloud is free of local misalignments, as shown in Figures 4.13f-g. The textured surface is shown in Figure 4.13h, and corresponds visually to the part of the observed cylinder phantom (see Figure 4.13a), both in texture and shape. As explained previously, an exact reconstruction of the bladder is not required in cystoscopy, as the shape of the bladder changes between (and locally during) examinations. It is only important to preserve the overall shape and texture continuities.

Comparison with (BHDS$^+$10)

Figure 4.14 shows that, for moderate cystoscope displacements and depth variations visible in the FOV[1], the method proposed in (BHDS$^+$10) is unable to accurately estimate the rigid three-dimensional transformation $T_{i \rightarrow j}^{3D}$. The assumptions made in (BHDS$^+$10) about the two-dimensional perspective relation between overlapping images do not hold in the phantom acquisition scenario, previously assessed and shown in Figure 4.12. The images do show minor depth variations of the cylinder phantom (see the FOV illustration in Figure 4.12a), so a perspective transformation $T_{i \rightarrow j}^{2D}$ only approximates the actual non-linear transformation between consecutive image pairs. As the method of (BHDS$^+$10) optimizes the parameters of $T_{i \rightarrow j}^{3D}$ by minimizing image dissimilarity between I_j and $T_{i \rightarrow j}^{2D}(I_i)$, the simplex-driven optimization estimates mainly translations, unable to recover also the rotation part of the underlying prototype displacements, as can be seen in Figure 4.14a. The displacement vector field $x_{i \rightarrow j}$ is estimated independently of any assumptions about 2D image geometry. This allows to estimate both rotation and translation of the prototype displacements. It should be noted that the method proposed in (BHDS$^+$10) registers every image pair of the 24fps video-sequence, whereas the methods proposed in this thesis use only every tenth image. Consequently, the method of (BHDS$^+$10) will work more accurately for very low displacements (large image overlap), and/or when the cystoscope is closer to the epithelium. However, this cannot be always guaranteed, and non-consecutive acquisition pairs cannot be robustly and accurately registered with this method.

---

[1]During a cystoscopic examination, the endoscope is often, but not systematically, displaced slightly closer to the epithelium. Only for short distances between cystoscope and epithelium, the FOV is small and corresponds to weak depth variations.
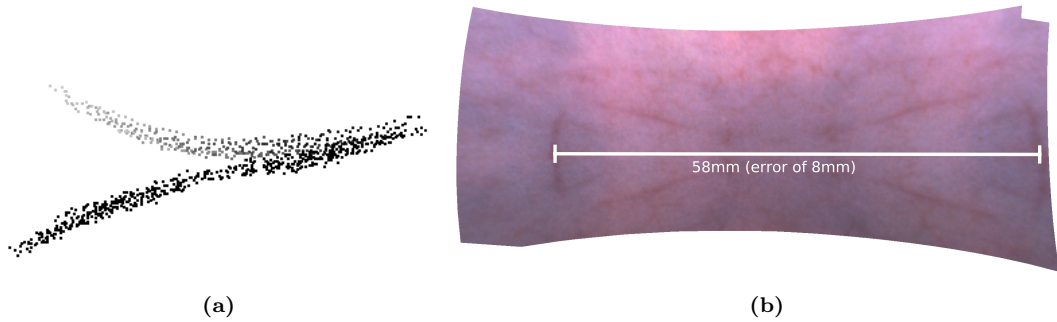
<div align="center">(a)   (b)</div>

Figure 4.14: Comparison with the method proposed in (BHDS$^+$10). (a) Point cloud aligned with the proposed method (increasing grey values) and with the method of (BHDS$^+$10) in black for the forward scan of Figure 4.12, shown in the same global coordinate system of acquisition $i = 0$. The assumptions made in (BHDS$^+$10) concerning the two-dimensional geometry between overlapping acquisitions does not hold (i.e. the FOV corresponds to non-planar surface parts). The simplex-driven optimization method of (BHDS$^+$10) is unable to estimate the rotation part of the prototype displacements and estimates only translations. The point cloud consequently is not bent. Our method makes no assumptions about 2D geometry, and the non-linear deformation field $x_{i \to j}$ allows for estimating both translations and rotations (see Figure 4.12 and text for the performed prototype displacements). (b) Larger view of the final textured surface shown in Figure 4.12i.

Non-Medical Scene Reconstruction with the Kinect Sensor

A flat textured carpet is captured with the Kinect sensor as the first example, being of similar locally smooth appearance than the bladder phantoms. The initial (non-corrected) point cloud, shown in Figure 4.15a, is less noisy than those obtained with the ToF prototype (see Figure 4.11) or the laser cystoscope prototype (Figure 4.13). Even without global map correction, the points of different acquisitions are already well aligned and of planar appearance (i.e. without visible misalignments). In fact, the globally corrected point cloud and the non-corrected one are visually almost indistinguishable, so we choose to show only the latter here. Figure 4.15b shows the same cloud, viewed from the top. The density of the cloud indicates which areas were captured from several trajectory parts (viewpoints). For instance, the top-left part is visited several times, while the central part is visited by two trajectories (central trajectory, plus the top and bottom parts, respectively). The complete acquisition path is shown in Figure 4.15c. Found additional pairs are again indicated by thick red lines (refer to Figure 4.13 for explanations).

Finally, a full 360° scan of the author's living room was acquired with the Kinect sensor. To do so, the Kinect was rotated manually in the center of the room. Figure 4.16 shows a few viewpoints of the reconstructed, globally corrected point cloud.
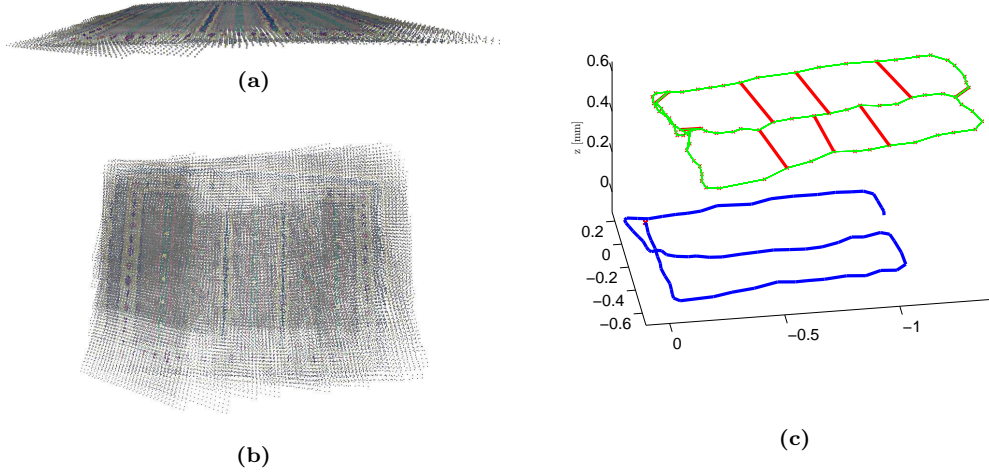
Figure 4.15: Global map example for the Kinect sensor and a planar scene. (a) Initial point cloud, reconstructed for a textured carpet. The depth measurement of the Kinect sensor is more accurate than that of the laser cystoscope and the ToF-prototype. Coherently with the results of Section 4.4.1, estimated $T_{i\rightarrow i+1}^{3D}$ are very accurate. Consequently, the initial global point cloud shows very little misalignments. (b) Point cloud of a), viewed from the top. To illustrate overlapping regions, the cloud has been sub-sampled by a factor of 10. (c) Scene geometry, showing the path of the acquisition device (blue lines) and additional pairs found (in red).

4.4.3 Surface Compositing

Contrast-Enhancement

To evaluate the performance of the three-dimensional contrast-enhancing surface compositing step, a subset of 12 acquisitions is selected from the sequence used to construct the point cloud of Figure 4.15. Every second image is blurred ($\sigma_{\text{blur}} = 2$) to demonstrate the effects of the proposed technique in comparison to classical approaches. Figures 4.17a-c show the first three images of the sequence. Simple first-come-first-serve stitching[1] leads to an alternation between sharp and blurry textured regions, as shown in Figure 4.17d. Figure 4.17e shows the resulting texture mapping obtained without contrast-enhanced data term (i.e. only $E_{fw}^{\text{seam}^{3D}}$ of Equation (4.12) is minimized). As regularization is less costly for blurry texture transitions, the obtained solution extracts texture from the blurry images. The data terms proposed in (LI07) are based on the normal vector of each face towards the camera orientation (the more parallel, the lower the cost). As the Kinect's orientation towards the carpet is roughly similar for all

---

[1] Equivalently to the 2D case, each face is textured by the first (in time) image where all three vertices of the face are projected to valid coordinates.
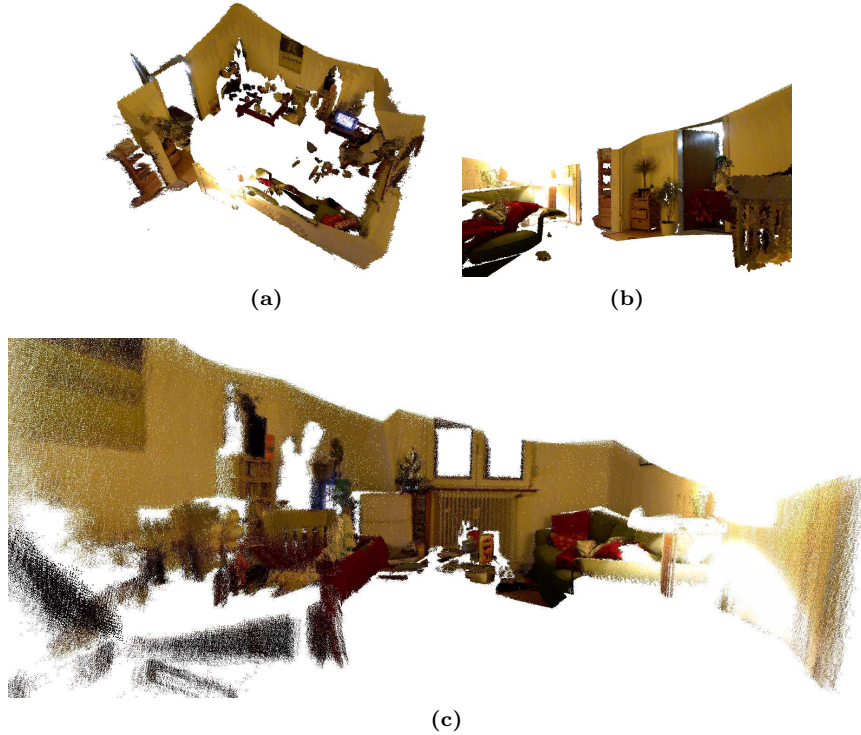
Figure 4.16: Full 360 degree scan of a living room with a hand-held Kinect. (a) Globally corrected global point cloud viewed from the top. The points are globally well aligned (i.e. the room is rectangular, and all walls are connected). (b) Same cloud, viewed from the position of the television. (c) Viewed from the right door seen in b).

12 acquisitions, the method of (LI07) can be assumed to produce a comparable, blurry texture mapping. After minimizing both regularization and contrast-enhanced data terms proposed in this chapter, the texture is taken from the sharp images of the sequence, while at the same time being visually coherent, as can be seen in Figures 4.17f-g.

Comparison with the Kinect-Fusion Algorithm

The proposed surface texturing approach is also suitable for more general 3D scenes. We demonstrate this on a scan of a desktop, reconstructed with the Kinect-Fusion algorithm (NDI$^+$11, IKH$^+$11). The implementation of this algorithm was taken from the open source Point Cloud Library (PCL) (RC11). In essence, the Kinect-Fusion algorithm performs real-time registration of each current $\mathcal{P}_i^{3D}$ into a fixed-size 3D volume via ICP running on the GPU. The volume itself is represented as a truncated signed distance function (CL96) and kept in GPU memory throughout the acquisition. Each registered point cloud is used to iteratively update the volume. The main limitation of this real-time implementation is the relatively low
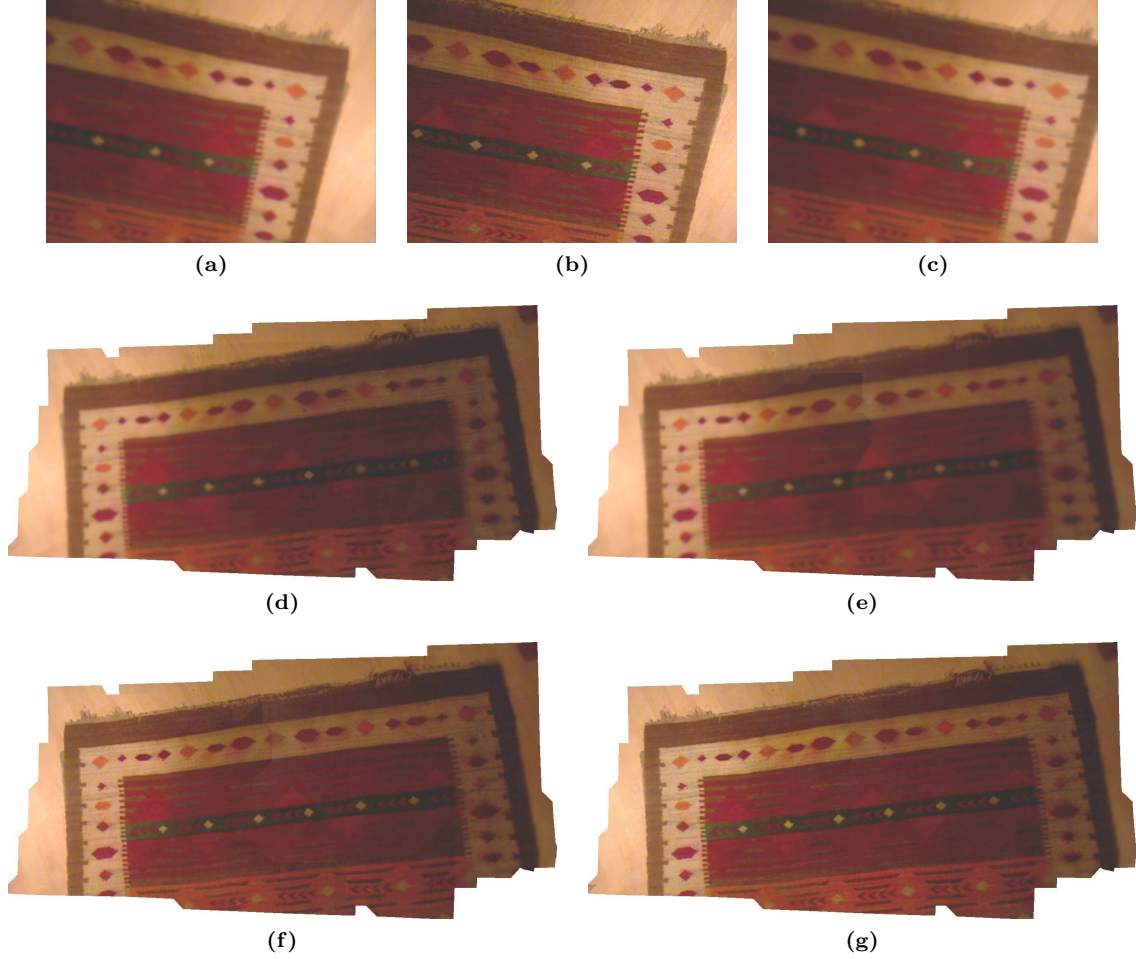
Figure 4.17: Contrast enhancement for textured surfaces. (a)-(c) Three of 12 input images of the carpet sequence used to construct the map of Figure 4.15. Every second image is strongly blurred to demonstrate the effects of the proposed method. (d) Initial surface texture (first come, first serve). Note how blurry and contrasted images are interlaced. (e) Surface texture determined without contrast-enhancing data term. Color gradients are less strong in blurry images. (f) Surface textured using contrast-enhancing data term. Most of the texture is obtained from the sharp images of the sequence. (g) Exposure correction of f).

spatial resolution of the volume, which is limited by the memory of the graphics card. In our experiments, the largest resolution that could be used[1] was a $256 \times 256 \times 256$ voxel volume.

Figures 4.18a-c show three of 36 images of the RGB-Depth sequence used. During the acquisition stage, the Kinect was moved around the desktop, leading to a great variability in viewpoints. The PCL implementation offers to triangulate a surface mesh on the reconstructed point cloud. This reconstructed mesh, the images and the camera viewpoints (i.e. $T_{0 \to i}^{3D}$) are

---

[1]Using an NVIDIA Quadro 600 graphics card with 1GB RAM.

used as the input for the proposed contrast-enhancing surface compositing algorithm, which is compared qualitatively with both the PCL texturing implementation and a first-come-first-serve approach. Figure 4.18d shows the texture of the PCL implementation, which chooses the texture for each face from the first image I_i that projects this face to valid image coordinates. This allows to push occluded faces to the next acquisition $i+1$, eventually allowing to label faces that cannot be projected to valid coordinates in any image as being occluded. As can be seen in Figure 4.18d, this approach does not necessarily lead to neighboring faces being textured by consecutive acquisitions. For instance, the checkerboard pattern, the monitors, and most prominently the keyboard, show visible misalignments due to incorrect estimation of $T_{0 \rightarrow i}^{3D}$ by the Kinect-Fusion algorithm. Alternatively, the mesh can be iteratively over-textured by the image of the next consecutive acquisition (first-come-first-serve). This approach is shown in Figure 4.18e. As local registration errors between consecutive acquisitions are smaller compared to global transformation inaccuracies, texture misalignments are noticeably reduced. Nonetheless, seam locations are arbitrary (with respect to scene geometry and texture) and pass through objects (e.g. the monitors), and still exhibit smaller misalignments. The proposed contrast-enhancing seam detection algorithm chooses seams in mostly homogeneous areas, as shown in Figure 4.18f. The monitors and the checkerboard are now textured by single images, leading to overall visually more coherent texture transitions.
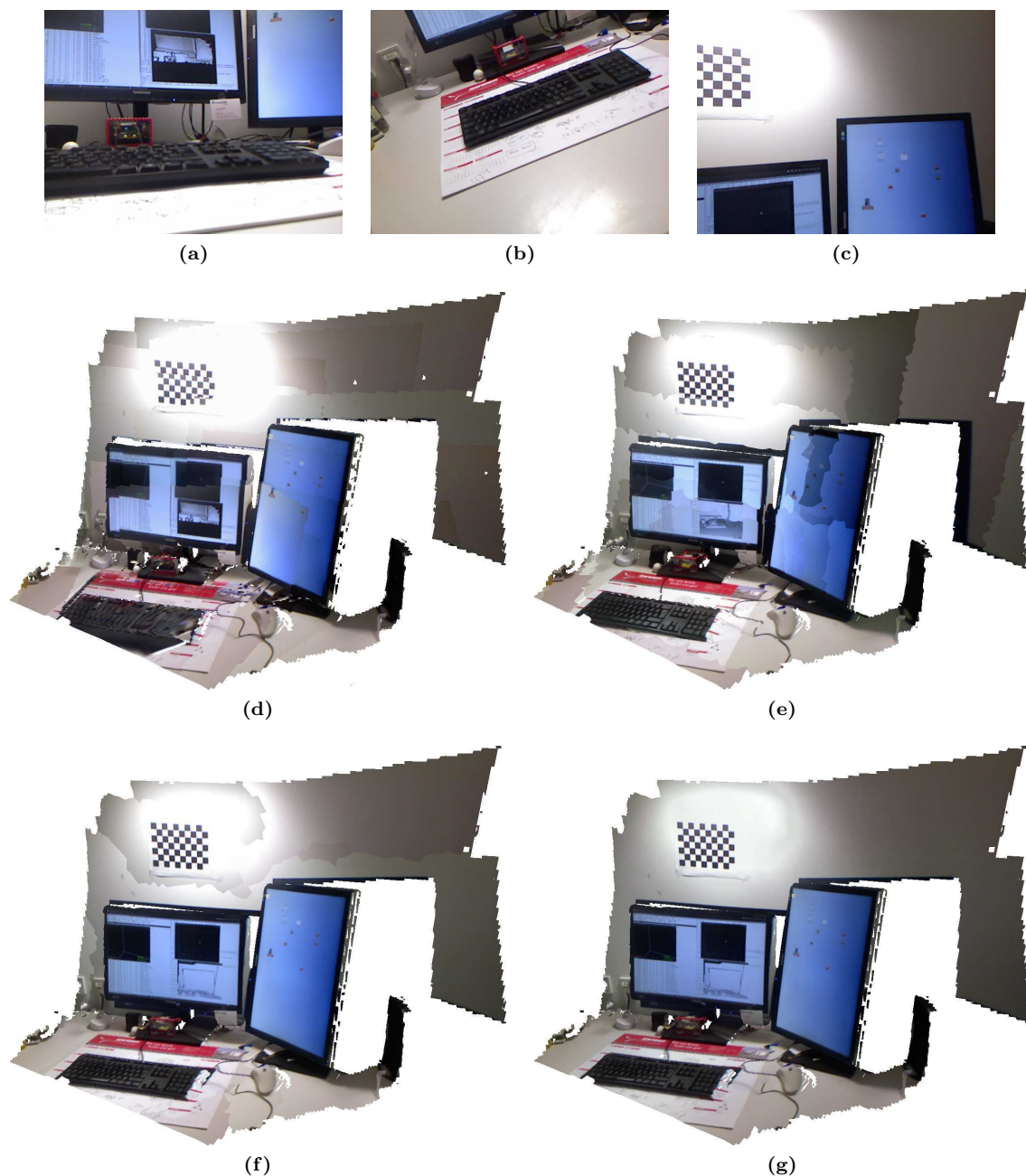
Figure 4.18: Contrast-enhancing surface compositing example on a scene constructed with the Kinect-Fusion algorithm (NDI+11, IKH+11). (a)-(c) Three of 36 images of the sequence showing a desktop, illustrating the strongly varying viewpoints. (d) Textured scene output of the PCL implementation (RC11). Note that this texture generation is part of PCL, not the Kinect-Fusion publication. Each face is textured by the first acquisition that correctly projects this texture into its image plane. This leads to many misaligned neighboring faces (e.g. the checkerboard pattern, the monitors and the keyboard). Occlusions checks are also performed, leading to holes noticeable on the desktop. (e) Textured using first-come-first-serve strategy. As registration errors are small(er) between consecutive images, visible misalignments are reduced (see checkerboard), but still present (monitor edges, screen content). (f) Texture after seam localization. Textures are now correctly aligned (except for the mouse cable), seams pass homogeneous areas where possible. (g) Exposure correction.

4.5 Conclusions and Perspectives

The methods developed in this chapter correspond to modifications of the two-dimensional cartography process, as proposed in Chapter 3. As argued in Sections 1.4 and 4.1.2, without additional sensor information, estimating the rigid instrument displacement is not possible due to the small FOV and the poor local geometry (depth variation) of cystoscopic video-sequences. The methods therefore assume that modified instruments (which were introduced in Section 4.2) allow to capture local three-dimensional information in addition to the color images. As these prototypes are not yet available in clinical examinations, the results of this chapter are limited to a proof of concept. Nonetheless, the results obtained for quite realistic (with regard to shape and texture) phantom data show the potential of the proposed methods. As in Section 3.5, constant parameters were used for all experiments, demonstrating the robustness of the proposed algorithms. Additionally, the methods can also be applied to more general acquisition scenarios, which was demonstrated for a set of scenes acquired with the Kinect sensor.

In the following sections, we present the main scientific contributions made in this chapter, and discuss their limitations and potential future work.

4.5.1 Main Scientific Contributions

Robust Data Registration

In Chapter 3, the perspective transformation $T^{2D}_{i \to j}$ that links two images of a cystoscopic video-sequence was computed by solving an over-determined linear system. The rigid transformation $T^{3D}_{i \to j}$, required for three-dimensional cartography, is similarly estimated. In other words, both equation systems are based on the two-dimensional displacement vector field $x_{i \to j}$, which gives a set of correspondences between two acquisitions. Consequently, the data registration algorithm used to estimate $T^{3D}_{i \to j}$ inherits the robustness of its two-dimensional version, described in Section 3.3. Robustness and accuracy of the method of (BHDS+10) depend on an initial estimate of $T^{3D}_{i \to j}$ and can therefore only handle consecutive acquisition pairs with small displacements. The proposed method allows to register both consecutive and non-consecutive acquisition pairs (needed for global map correction) pairs robustly. In addition, compared to (BHDS+10), the proposed method does not assume that the acquisition pairs are related by a perspective two-dimensional transformation $T^{2D}_{i \to j}$. In turn, more general surface geometry can be registered, such as non-planar scenes (strong local bladder deformations, non-medical scenes).

Compared to classical approaches, the proposed method is able to register acquisition pairs that exhibit both poor local depth variations and poor texture quality. Poor depth variations impede the use of classic 3D-3D point registration techniques, such as ICP based algorithms, while poor texture quality prevents a robust use of feature-based 2D registration algorithms

combined with depth sensor measurements. This situation (poor geometry and texture) is often observed in cystoscopic video-sequences, and the experimental results indicate that a combination of the registration algorithm proposed in Chapter 3 and modified cystoscopes allow to robustly estimate viewpoint changes of the cystoscope during the examination. Furthermore, it was shown that the depth measurements can be integrated in form of pairwise regularization into the energy minimization framework of Section 3.3. Unlike classic pairwise L1 or L2 regularization, the integration of dense depth measurements allow to register acquisition pairs related by arbitrary viewpoint changes without implicit oversmoothing. Therefore, it is not necessary to use either 2D or 3D higher-order regularization when registering non-consecutive acquisition pairs.

Global Map Correction

In order to correct globally accumulated cartography errors, the automatic detection of trajectory crossings (zig-zag paths, loops, see Section 3.2) was modified to work on data acquired with the prototypes used in this chapter. The modified algorithm allows for detecting a meaningful subset of additional, non-consecutive acquisition pairs. The amount of acquisition overlap is computed using multiple view geometry formulations. After these additional acquisition pairs are registered using the method discussed previously, global transformation parameters are optimized jointly while minimizing local registration errors.

Contrast-Enhanced Surface Compositing

The pixel-based contrast-enhanced map stitching technique, as proposed in Chapter 3, was extended to a mesh-based surface compositing method. As in the two-dimensional case, blurring induced by blending techniques, is avoided. At the same time, the quality of the textured surface is greatly enhanced. This is achieved by preferring contrasted regions in the original images over blurry ones. The resulting three-dimensional maps are visually coherent and do not exhibit texture or exposure discontinuities. The two-step compositing approach allows to first maximize the contrast of the global surface, and attenuate exposure related gradients in a second step. Compared to state-of-the-art techniques, this allows to reconstruct high contrasted meshes of the epithelium in the presence of motion blur, and is able to attenuate even very strong exposure differences.

4.5.2 Limits and Perspectives

As it is the case for the two-dimensional cartography algorithm, the proposed three-dimensional cartography process requires accumulated errors to be low enough in order to detect additional, non-consecutive overlapping acquisition pairs. As long as this (moderate) constraint is met, large FOV textured surfaces can be constructed automatically. When accumulated errors are too large, a solution is to allow the clinicians to manually select additional overlapping acquisition pairs that cannot be detected automatically from the uncorrected initial map. Such a
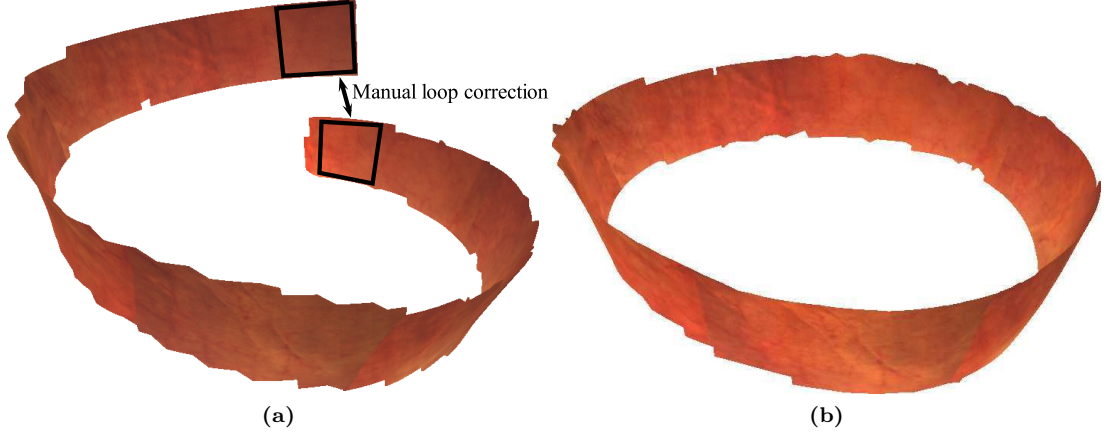
Manual loop correction

(a)   (b)

Figure 4.19: Manual loop correction. (a) In extreme situations, overlapping parts cannot be detected, such as in this full 360 degree scan, performed with the ToF prototype inside a full cylinder phantom. (b) After manual selection of loop beginning and loop ending, the cylinder can be reconstructed in a coherent fashion with regards to texture and shape. Note that the visible vertical texture discontinuities correspond to different sheets of paper with bladder texture.

situation is shown in Figure 4.19. The ToF prototype was manually displaced in a combination of rotations and translations inside a full cylinder phantom. As can be seen in Figure 4.19a, the accumulated errors after a full 360 degree scan are too strong. Consequently, loop beginning and loop ending do not overlap at all, and the section of overlap cannot be detected automatically. After manually choosing the first and the last acquisition as an additional overlapping acquisition pair, the full cylinder can be reconstructed in a visually coherent fashion, as shown in Figure 4.19b. Even in such an extreme scenario[1], the required user input is much less than needed by the method of (BTGA11), and furthermore does not restrict the clinicians accustomed fashion of scanning the epithelium.

Concerning computation time improvements, the remarks made in Section 3.6 also apply here. Depending on the images textures, different algorithms for image registration could be selected. When sufficient image primitives can be extracted, fast feature based approaches could be used to decrease the overall computation time, while the method proposed in this chapter may be used as a fall back solution when faster algorithms fail. Prediction techniques, such as a Kalman filter, could also help to decrease computation time by limiting the search range or by supplying an initial estimate, depending on the registration algorithm employed.

---

[1]The bladder cannot be scanned in such a way with a rigid cystoscope.

Conclusion

The main objective of this thesis was to facilitate bladder cancer diagnosis using discrete energy minimization techniques. The proposed large (two- and three-dimensional) FOV maps of the epithelial surface of the bladder enable clinicians to see multi-focal bladder lesions in their entirety and with respect to anatomical landmarks. Furthermore, such maps allow for archiving the examination in an intuitive, re-usable format. Compared to archiving video-sequences, these maps greatly reduce redundancy, and enable clinicians to compare lesion evolution side-by-side when preparing for lesion follow-ups. Several previous contributions focused on the creation of such large FOV maps from cystoscopic video-sequences, including three previous dissertations at the CRAN laboratory. In the following, the main contributions and perspective of this thesis are summarized.

Medical Contributions

From a clinician's point of view, the methods proposed in this thesis lead to several improvements over previous contributions towards bladder cartography. For the first time, large FOV maps can be constructed from multiple overlapping cystoscope trajectories. Previous contributions presented only "strip"- or "band"-shaped maps with a large FOV in only one main direction, which severely limits the applicability in clinical situations. The approach proposed in this thesis is able to create large FOV maps from multiple scan trajectories, thereby extending the FOV in two directions. Strip-shaped maps, obtained with state-of-the-art methods, require similar scan-paths for a direct comparison of larger parts of the epithelium. The maps constructed with the proposed methods potentially enable to compare larger parts of the epithelium from different examinations, without enforcing clinicians to follow a similar scanning path in a follow-up examination. Furthermore, we have proposed a map compositing approach that increases the visual quality of the constructed maps. From the redundant data of the video-sequence, the map texture is composed by a maximum of information and contrast. Motion blur and camera de-focus is greatly attenuated, and the constructed maps show finer vascular structures than those presented by previous contributions.

Scientific Contributions

These medical contributions required to solve several algorithmic challenges. The corresponding scientific contributions are summarized in the following paragraphs.

Automatic Global Map Correction. Previous contributions constructed large FOV maps by concatenating successive images of the video-sequence into the coordinate system of a reference acquisition. However, as the cystoscope returns to previously visited areas, globally accumulated errors lead to visible texture misalignment. We have proposed a graph-based approach to detect such trajectory crossings. Furthermore, our method automatically selects a small subset of all overlapping non-consecutive acquisition pairs. This greatly reduces the number of acquisition pairs that need to be registered, while ensuring that all parts of the map can be corrected. A sparse non-linear bundle adjustment approach then simultaneously adjusts all transformation parameters, leading to a globally aligned set of acquisitions. This approach was successfully applied in Chapter 3 for two-dimensional cystoscopic cartography. Results on simulated and clinical datasets showed that the proposed map correction technique works robustly, even in the case of larger accumulated errors. Furthermore, the approach was designed to be extendible to three-dimensional cartography. In Chapter 4, we showed that merely one equation has to be adapted, namely the computation of acquisition overlap percentage.

Invariant Energy Functions for Data Registration. In Chapter 3, we have proposed data and regularization cost functions which are invariant to the perspective transformation model that links overlapping images of a cystoscopic video-sequence. These allow, for the first time in bladder cartography, for robustly and accurately registering non-consecutive image pairs, related by arbitrary (and often large) viewpoint changes. Such images have to be registered in order to achieve global map correction, as described in the previous paragraph. It was shown quantitatively on simulated phantom data that consecutive image registration accuracy is superior to state-of-the-art registration techniques. The registration of non-consecutive image pairs is similarly accurate, while previous contributions cannot even robustly register such image pairs. The proposed method was successfully applied to several clinical data sets, and constant algorithm parameters demonstrated the registration robustness. In Chapter 4, it was shown that the proposed registration approach is also suitable to robustly estimate the rigid cystoscope displacements when additional sensor information is available. Hence, the method can directly be used for three-dimensional cartography. Additionally, the cost functions can be extended to include additional three-dimensional sensor measurements, removing the need for higher-order regularization. This leads to cost functions that are easier to minimize, which decreases computation time and algorithmic complexity. Furthermore, no assumption on the two-dimensional relationship between overlapping images is made. Consequently, the proposed registration technique is able to estimate the rigid transformation between local acquisition

systems even for (locally) non-planar scenes. This was demonstrated using the commercially available Kinect sensor.

Contrast-Enhancing Map Compositing. We have proposed a two-step map compositing approach in Chapter 3, which enables to compensate three major problems typical of cystoscopic video-sequences. First, small texture misalignments due to local and temporal bladder deformations remain perceptible after global map alignment. These lead to ghosting and blur when blending techniques are used, and overall suppress fine vascular structures. Second, motion blur and camera de-focus are often observed in cystoscopic video-sequence. These lead to a loss of information (additional blur) in the map when blending techniques are used. Third, due to vignetting and different viewing angles of the cystoscope towards the epithelium, exposure differences are strong between overlapping images, especially for non-consecutive image pairs. The proposed cost functions allow for correcting small misalignments and exposure differences, while simultaneously minimize the loss of information by choosing the most contrasted images from the redundant video-sequence. Results on clinical datasets show, both quantitatively and qualitatively, the improvements compared to previous contributions. Furthermore, the cost functions were adapted to work on triangular meshes in Chapter 4. On both medical phantom data sets, as well as more general scenes acquired with the Kinect, the method is able to construct seamless and visual coherent textured surfaces with a maximum of contrast.

Perspectives

As pointed out in the previous section, the proposed techniques contribute in several ways to the state-of-the-art of constructing two- and three-dimensional large FOV maps of the epithelium. Nevertheless, some problems remain, and the proposed methods open a few new perspectives. The criterion that was least considered when developing the cartography algorithms was computation time. Instead, the focus was laid on the development of robust and accurate algorithms, enabling to compute maps of high visual quality. For these reasons, the proposed methods, especially the registration part, cannot be used in a real-time application. However, the computation times allow for a second diagnosis or patient interview after the examination. Nonetheless, it can be desirable to construct large FOV maps in real-time[1], under the restriction that map accuracy and quality does not suffer drastically. One possible solution to decrease computation time is to use fast registration techniques whenever possible, and use the proposed method only for difficult (e.g. strong motion blur, non-consecutive, etc.) image pairs. Such an approach to decrease registration time is currently being evaluated at the CRAN laboratory. Furthermore, in a real-time application, the proposed sequential cartography approach is also not directly usable. For instance, global map correction must be

---

[1]Processing times of one or two frames per second should suffice, as in all experiments of this thesis, the cystoscope displacement allowed to process only every tenth image from the 24 fps video-sequences with sufficient overlap between consecutive image pairs.

performed during the acquisition and consecutive image registration stage. Trajectory crossings have to be detected and global transformations must be corrected "on the fly". However, the proposed method can easily be modified to work in such a way. The frame structure graph can be incrementally updated, while re-using most of the already computed edge weights and shortest-paths. Likewise, the proposed map compositing technique can be modified to work on a frame-by-frame base. By decreasing the map sections to be corrected (i.e. only update the map texture in a small region around the current image to be placed in the map), it is possible to update the map in less than a second. Although shortest path search, global map correction, and map compositing can be modified to be performed "on the fly", reaching real-time will remain a challenge. Nevertheless, these algorithm parts could be processed in a separate thread (and updated less frequently), while registration and simple map updating can be performed at faster processing speed.

References

[ADA+04] A. Agarwala, M. Dontcheva, M. Agrawala, S. Drucker, A. Colburn, B. Curless, D. Salesin, and M. Cohen. Interactive digital photomontage. In *ACM Transactions on Graphics (TOG)*, volume 23, pages 294–302. ACM, 2004.

[ADG09] C. Albitar, C. Doignon, and P. Graebling. Calibration of vision systems based on pseudo-random patterns. In *Intelligent Robots and Systems, 2009. IROS 2009. IEEE/RSJ International Conference on*, pages 321–326. IEEE, 2009.

[AFG08] A. Ali, A. Farag, and G. Gimelfarb. Optimizing binary mrfs with higher order cliques. *Computer Vision–ECCV 2008*, pages 98–111, 2008.

[AHB87] K Somani Arun, Thomas S Huang, and Steven D Blostein. Least-squares fitting of two 3-d point sets. *Pattern Analysis and Machine Intelligence, IEEE Transactions on*, (5):698–700, 1987.

[ANKB13] Michelle Agenant, Herke-Jan Noordmans, Wim Koomen, and JLH Ruud Bosch. Real-time bladder lesion registration and navigation: A phantom study. *PloS one*, 8(1):e54348, 2013.

[B+67] H. Blum et al. A transformation for extracting new descriptors of shape. *Models for the perception of speech and visual form*, 19(5):362–380, 1967.

[Bau02] Adam Baumberg. Blending images for texturing 3d models. In *Proceedings of the British Machine Vision Conference*, pages 404–413, 2002.

[BBS+10] Alexander Behrens, Michael Bommes, Thomas Stehle, Sebastian Gross, Steffen Leonhardt, and Til Aach. A multi-threaded mosaicking algorithm for fast image composition of fluorescence bladder images. In *Medical Imaging 2010: Visualization, Image-Guided Procedures, and Modeling*, volume 7625, page 76252S, San Diego, USA, February 13–18 2010. SPIE.

REFERENCES

[Bes74] J. Besag. Spatial interaction and the statistical analysis of lattice systems. *Journal of the Royal Statistical Society. Series B (Methodological)*, pages 192–236, 1974.

[Bes86] J. Besag. On the statistical analysis of dirty pictures. *Journal of the Royal Statistical Society. Series B (Methodological)*, pages 259–302, 1986.

[BFL06] Y. Boykov and G. Funka-Lea. Graph cuts and efficient nd image segmentation. *International Journal of Computer Vision*, 70(2):109–131, 2006.

[BGS+10] A. Behrens, M. Guski, T. Stehle, S. Gross, and T. Aach. Intensity based multi-scale blending for panoramic images in fluorescence endoscopy. In *Biomedical Imaging: From Nano to Macro, 2010 IEEE International Symposium on*, pages 1305–1308. IEEE, 2010.

[BGS+11] A. Behrens, M. Guski, T. Stehle, S. Gross, and T. Aach. A non-linear multi-scale blending algorithm for fluorescence bladder images. *Computer Science - Research and Development*, 26:125–134, 2011.

[BH02] E. Boros and P.L. Hammer. Pseudo-boolean optimization. *Discrete applied mathematics*, 123(1):155–225, 2002.

[BHDS+10] A. Ben Hamadou, C. Daul, C. Soussen, A. Rekik, and W. Blondel. A novel 3d surface construction approach: Application to three-dimensional endoscopic data. In *Image Processing (ICIP), 2010 17th IEEE International Conference on*, pages 4425–4428. IEEE, 2010.

[BHS91] E. Boros, PL Hammer, and X. Sun. Network flows and minimization of quadratic pseudo-boolean functions. *RUTCOR Research Report, RRR*, pages 17–1991, 1991.

[BHSD+10] A. Ben Hamadou, C. Soussen, C. Daul, W. Blondel, and D. Wolf. Flexible projector calibration for active stereoscopic systems. In *17th IEEE International Conference on Image Processing (ICIP)*, pages 4241–4244, 2010.

[BHT06] E. Boros, P.L. Hammer, and G. Tavares. Preprocessing of unconstrained quadratic binary optimization. *RUTCOR Research Report, RRR*, pages 10–2006, 2006.

[BJ01] Y.Y. Boykov and M.P. Jolly. Interactive graph cuts for optimal boundary & region segmentation of objects in nd images. In *Computer Vision, 2001. ICCV 2001. Proceedings. Eighth IEEE International Conference on*, volume 1, pages 105–112. IEEE, 2001.

[BK04] Y. Boykov and V. Kolmogorov. An experimental comparison of min-cut/max-flow algorithms for energy minimization in vision. *Pattern Analysis and Machine Intelligence, IEEE Transactions on*, 26(9):1124–1137, 2004.

[BKR11] A. Blake, P. Kohli, and C. Rother. *Markov Random Fields for Vision and Image Processing*. Mit Pr, 2011.

[BL03] M. Brown and D.G. Lowe. Recognising panoramas. In *Proceedings of the Ninth IEEE International Conference on Computer Vision*, volume 2, page 5, 2003.

[Bli94] J.F. Blinn. Jim blinns corner: Compositing, part 1: Theory. *IEEE Computer Graphics and Applications*, 14(5):83–87, 1994.

[BM92] P.J. Besl and N.D. McKay. A method for registration of 3-D shapes. *IEEE Transactions on Pattern Analysis and Machine Intelligence*, pages 239–256, 1992.

[BMG10] T. Botterill, S. Mills, and R. Green. Real-time aerial image mosaicing. In *Proceedings of Image and Vision Computing New Zealand*, pages 1–6, 2010.

[BRB⁺04] A. Blake, C. Rother, M. Brown, P. Pérez, and P. Torr. Interactive image segmentation using an adaptive gmmrf model. *Computer Vision-ECCV 2004*, pages 428–441, 2004.

[BRM⁺09] T. Bergen, S. Ruthotto, C. Munzenmayer, S. Rupp, D. Paulus, and C. Winter. Feature-based real-time endoscopic mosaicking. In *Image and Signal Processing and Analysis, 2009. ISPA 2009. Proceedings of 6th International Symposium on*, pages 695–700. IEEE, 2009.

[Bro92] L.G. Brown. A survey of image registration techniques. *ACM computing surveys (CSUR)*, 24(4):325–376, 1992.

[BSGA09] A. Behrens, T. Stehle, S. Gross, and T. Aach. Local and global panoramic imaging for fluorescence bladder endoscopy. In *31st International Conference of the IEEE Engineering in Medicine and Biology Society (EMBC)*, pages 6690–6693, 2009.

[BSL⁺11] S. Baker, D. Scharstein, JP Lewis, S. Roth, M.J. Black, and R. Szeliski. A database and evaluation methodology for optical flow. *International Journal of Computer Vision*, pages 1–31, 2011.

[BSW05] M. Brown, R. Szeliski, and S. Winder. Multi-image matching using multi-scale oriented patches. In *International Conference on Computer Vision and Pattern Recognition (CVPR)*, volume 1, pages 510–517, 2005.

REFERENCES

[BTGA11] A. Behrens, M. Takami, S. Gross, and T. Aach. Gap detection in endoscopic video sequences using graphs. In *Engineering in Medicine and Biology Society, EMBC, 2011 Annual International Conference of the IEEE*, pages 6635–6638. IEEE, 2011.

[BTVG06] H. Bay, T. Tuytelaars, and L. Van Gool. Surf: Speeded up robust features. In *European Conference on Computer Vision (ECCV).*, pages 404–417, 2006.

[BVZ98] Y. Boykov, O. Veksler, and R. Zabih. Markov random fields with efficient approximations. In *Computer Vision and Pattern Recognition, 1998. Proceedings. 1998 IEEE Computer Society Conference on*, pages 648–655. IEEE, 1998.

[BVZ01] Y. Boykov, O. Veksler, and R. Zabih. Fast approximate energy minimization via graph cuts. *Pattern Analysis and Machine Intelligence, IEEE Transactions on*, 23(11):1222–1239, 2001.

[Cap04] D. Capel. *Image mosaicing and super-resolution.* Springer-Verlag New York Inc, 2004.

[CB90] P.B. Chou and C.M. Brown. The theory and practice of bayesian image labeling. *International Journal of Computer Vision*, 4(3):185–210, 1990.

[CG06] D. Cremers and L. Grady. Statistical priors for efficient combinatorial optimization via graph cuts. *Computer Vision–ECCV 2006*, pages 263–274, 2006.

[CL96] B. Curless and M. Levoy. A volumetric method for building complex models from range images. In *Proceedings of the 23rd annual conference on Computer graphics and interactive techniques*, pages 303–312. ACM, 1996.

[CLZQ03] M. Chan, W. Lin, C. Zhou, and J.Y. Qu. Miniaturized three-dimensional endoscopic imaging system based on active stereovision. *Applied optics*, 42(10):1888–1898, 2003.

[CM00] C.G.L. Cao and P. Milgram. Disorientation in minimal access surgery: A case study. In *Proceedings of the Human Factors and Ergonomics Society Annual Meeting*, volume 44, pages 169–172. SAGE Publications, 2000.

[CMFO06] F. Caballero, L. Merino, J. Ferruz, and A. Ollero. Improving vision-based planar motion estimation for unmanned aerial vehicles through online mosaicing. In *Robotics and Automation, 2006. ICRA 2006. Proceedings 2006 IEEE International Conference on*, pages 2860–2865. IEEE, 2006.

[CNR] Visual Computing Lab ISTI CNR. Meshlab. http://meshlab.sourceforge.net/.

[Cor01] T.H. Cormen. *Introduction to algorithms.* The MIT press, 2001.

[CQWS97] J.S. Chou, J.Z. Qian, Z. Wu, and H.F. Schramm. Automatic mosaic and display from a sequence of peripheral angiographic images. In *Proceedings of SPIE*, volume 3034, page 1077, 1997.

[CS09] R.E. Carroll and S.M. Seitz. Rectified surface mosaics. *International journal of computer vision*, 85(3):307–315, 2009.

[CSRT02] A. Can, C.V. Stewart, B. Roysam, and H.L. Tanenbaum. A feature-based, robust, hierarchical algorithm for registering pairs of images of the curved human retina. *Pattern Analysis and Machine Intelligence, IEEE Transactions on*, 24(3):347–364, 2002.

[CZ03] D. Capel and A. Zisserman. Computer vision applied to super resolution. *Signal Processing Magazine, IEEE*, 20(3):75–86, 2003.

[Dav62] Chandler Davis. The norm of the schur product operation. *Numerische Mathematik*, 4(1):343–344, 1962.

[Dij59] E.W. Dijkstra. A note on two problems in connexion with graphs. *Numerische mathematik*, 1(1):269–271, 1959.

[Din70] E.A. Dinic. Algorithm for solution of a problem of maximum flow in networks with power estimation. In *Soviet Math. Dokl*, volume 11, pages 1277–1280, 1970.

[DT05] N. Dalal and B. Triggs. Histograms of oriented gradients for human detection. In *Computer Vision and Pattern Recognition, 2005. CVPR 2005. IEEE Computer Society Conference on*, volume 1, pages 886–893. Ieee, 2005.

[d07] P. dAngelo. Radiometric alignment and vignetting calibration. *Proc. Camera Calibration Methods for Computer Vision Systems*, 2007.

[EK72] J. Edmonds and R.M. Karp. Theoretical improvements in algorithmic efficiency for network flow problems. *Journal of the ACM (JACM)*, 19(2):248–264, 1972.

[ELF97] David W Eggert, Adele Lorusso, and Robert B Fisher. Estimating 3-d rigid body transformations: a comparison of four major algorithms. *Machine Vision and Applications*, 9(5):272–290, 1997.

[FB81] M.A. Fischler and R.C. Bolles. Random sample consensus: a paradigm for model fitting with applications to image analysis and automated cartography. *Communications of the ACM*, 24(6):381–395, 1981.

REFERENCES

[FD05] D. Freedman and P. Drineas. Energy minimization via graph cuts: Settling what is possible. In *Computer Vision and Pattern Recognition, 2005. CVPR 2005. IEEE Computer Society Conference on*, volume 2, pages 939–946. IEEE, 2005.

[FF56] L.R. Ford and D.R. Fulkerson. Maximal flow through a network. *Canadian Journal of Mathematics*, 8(3):399–404, 1956.

[FF62] LR Ford and DR Fulkerson. Flows in networks. 1962.

[FFKM02] D. Fedorov, L.M.G. Fonseca, C. Kenney, and B.S. Manjunath. Automatic registration and mosaicking system for remotely sensed imagery. In *SPIE 9th International Symposium on Remote Sensing*. Citeseer, 2002.

[GBP11] A.C. Gallagher, D. Batra, and D. Parikh. Inference for order reduction in markov random fields. In *Computer Vision and Pattern Recognition (CVPR), 2011 IEEE Conference on*, pages 1857–1864. IEEE, 2011.

[GC09] Bastian Goldluecke and Daniel Cremers. Superresolution texture maps for multiview reconstruction. In *Computer Vision, 2009 IEEE 12th International Conference on*, pages 1677–1684. IEEE, 2009.

[GG84] S. Geman and D. Geman. Stochastic relaxation, gibbs distributions, and the bayesian restoration of images. *Pattern Analysis and Machine Intelligence, IEEE Transactions on*, (6):721–741, 1984.

[GHN+10] B. Glocker, T.H. Heibel, N. Navab, P. Kohli, and C. Rother. Triangleflow: optical flow with triangulation-based higher-order likelihoods. In *European Conference on Computer Vision (ECCV)*, pages 272–285, 2010.

[GJM+99] Andreas Griewank, David Juedes, H. Mitev, Jean Utke, Olaf Vogel, and Andrea Walther. ADOL-C: A package for the automatic differentiation of algorithms written in C/C++. Technical report, Institute of Scientific Computing, Technical University Dresden, 1999. Updated version of the paper published in *ACM Trans. Math. Software* 22, 1996, 131–167.

[GKT+08] B. Glocker, N. Komodakis, G. Tziritas, N. Navab, and N. Paragios. Dense image registration through mrfs and efficient linear programming. *Medical Image Analysis*, 12(6):731–741, 2008.

[GR70] G.H. Golub and C. Reinsch. Singular value decomposition and least squares solutions. *Numerische Mathematik*, 14(5):403–420, 1970.

[GT88] A.V. Goldberg and R.E. Tarjan. A new approach to the maximum-flow problem. *Journal of the ACM (JACM)*, 35(4):921–940, 1988.

[HC71] J.M. Hammersley and P. Clifford. Markov fields on finite graphs and lattices. 1971.

[HDD+92] Hugues Hoppe, Tony DeRose, Tom Duchamp, John McDonald, and Werner Stuetzle. *Surface reconstruction from unorganized points*, volume 26. ACM, 1992.

[HHN88] Berthold KP Horn, Hugh M Hilden, and Shahriar Negahdaripour. Closed-form solution of absolute orientation using orthonormal matrices. *JOSA A*, 5(7):1127–1135, 1988.

[HLCB+04] J.M. Holzbeierlein, E. Lopez-Corona, B.H. Bochner, H.W. Herr, S. Donat, P. Russo, G. Dalbagni, and P.C. Sogani. Partial cystectomy: a contemporary review of the memorial sloan-kettering cancer center experience and recommendations for patient selection. *The Journal of urology*, 172(3):878–881, 2004.

[HM07] Y. Hernandez-Mier. Construction rapide d'images panoramiques applicables à l'exploration cystoscopique et à l'endoscopie de fluorescence en cancérologie, 2007.

[HMBD+10] Y. Hernández-Mier, W. Blondel, C. Daul, D. Wolf, and F. Guillemin. Fast construction of panoramic images for cystoscopic exploration. *Computerized Medical Imaging and Graphics*, 34(7):579–592, 2010.

[Hor87] Berthold KP Horn. Closed-form solution of absolute orientation using unit quaternions. *JOSA A*, 4(4):629–642, 1987.

[HS88] C. Harris and M. Stephens. A combined corner and edge detector. In *Alvey vision conference*, volume 15, page 50. Manchester, UK, 1988.

[HSB+09] A.B. Hamadou, C. Soussen, W. Blondel, C. Daul, and D. Wolf. Comparative study of image registration techniques for bladder video-endoscopy. In *European Conference on Biomedical Optics*. Optical Society of America, 2009.

[HZ03] R. Hartley and A. Zisserman. *Multiple view geometry in computer vision*. 2003.

[IKH+11] S. Izadi, D. Kim, O. Hilliges, D. Molyneaux, R. Newcombe, P. Kohli, J. Shotton, S. Hodges, D. Freeman, A. Davison, et al. Kinectfusion: real-time 3d reconstruction and interaction using a moving depth camera. In *Proceedings of the 24th annual ACM symposium on User interface software and technology*, pages 559–568. ACM, 2011.

[Ish03] H. Ishikawa. Exact optimization for markov random fields with convex priors. *Pattern Analysis and Machine Intelligence, IEEE Transactions on*, 25(10):1333–1336, 2003.

REFERENCES

[Ish09] H. Ishikawa. Higher-order gradient descent by fusion-move graph cut. In *International Conference on Computer Vision (ICCV)*, pages 568–574, 2009.

[Ish10] H. Ishikawa. Transformation of general binary MRF minimization to the first-order case. *IEEE Transactions on Pattern Analysis and Machine Intelligence*, pages 1234–1249, 2010.

[JJ06] P.K. Jain and C.V. Jawahar. Homography estimation from planar contours. In *3D Data Processing, Visualization, and Transmission, Third International Symposium on*, pages 877–884. IEEE, 2006.

[JMHL96] A. Jalink, J. McAdoo, G. Halama, and H. Liu. Ccd mosaic technique for large-field digital mammography. *Medical Imaging, IEEE Transactions on*, 15(3):260–267, 1996.

[JSH12] O. Jamriska, D. Sykora, and A. Hornung. Cache-efficient graph cuts on structured grids. In *Computer Vision and Pattern Recognition (CVPR), 2012 IEEE Conference on*, pages 3673–3680. IEEE, 2012.

[KBH06] Michael Kazhdan, Matthew Bolitho, and Hugues Hoppe. Poisson surface reconstruction. In *Proceedings of the fourth Eurographics symposium on Geometry processing*, 2006.

[KGJV83] S. Kirkpatrick, C.D. Gelatt Jr, and M.P. Vecchi. Optimization by simulated annealing. *science*, 220(4598):671–680, 1983.

[Kon10] K. Konolige. Projected texture stereo. In *Robotics and Automation (ICRA), 2010 IEEE International Conference on*, pages 148–155. IEEE, 2010.

[KR07] V. Kolmogorov and C. Rother. Minimizing nonsubmodular functions with graph cuts-a review. *Pattern Analysis and Machine Intelligence, IEEE Transactions on*, 29(7):1274–1279, 2007.

[KSE$^+$03a] V. Kwatra, A. Schodl, I. Essa, G. Turk, and A. Bobick. Graphcut textures: Image and video synthesis using graph cuts. *ACM Transactions on Graphics*, 22(3):277–286, 2003.

[KSE$^+$03b] Vivek Kwatra, Arno Schödl, Irfan Essa, Greg Turk, and Aaron Bobick. Graphcut textures: Image and video synthesis using graph cuts. *ACM Transactions on Graphics, SIGGRAPH 2003*, 22(3):277–286, July 2003.

[KZ01] V. Kolmogorov and R. Zabih. Computing visual correspondence with occlusions using graph cuts. In *Computer Vision, 2001. ICCV 2001. Proceedings. Eighth IEEE International Conference on*, volume 2, pages 508–515. IEEE, 2001.

[KZ02] V. Kolmogorov and R. Zabih. Multi-camera scene reconstruction via graph cuts. *Computer VisionECCV 2002*, pages 8–40, 2002.

[KZ04] V. Kolmogorov and R. Zabih. What energy functions can be minimizedvia graph cuts? *IEEE Transactions on Pattern Analysis and Machine Intelligence*, 2004.

[LC87] William E Lorensen and Harvey E Cline. Marching cubes: A high resolution 3d surface construction algorithm. In *ACM Siggraph Computer Graphics*, volume 21, pages 163–169. ACM, 1987.

[LHS01] Hendrik Lensch, Wolfgang Heidrich, and Hans-Peter Seidel. A silhouette-based algorithm for texture registration and stitching. *Graphical Models*, 63(4):245–262, 2001.

[Li95] S.Z. Li. *Markov random field modeling in computer vision*. Springer-Verlag New York, Inc., 1995.

[LI07] V. Lempitsky and D. Ivanov. Seamless mosaicing of image-based texture maps. In *Computer Vision and Pattern Recognition, 2007. CVPR'07. IEEE Conference on*, pages 1–6. IEEE, 2007.

[LKK03] A. Litvin, J. Konrad, and W.C. Karl. Probabilistic video stabilization using kalman filtering and mosaicking. In *Proceedings of SPIE Conference on Electronic Imaging*, pages 663–674, 2003.

[Lou10] Manolis I.A. Lourakis. Sparse non-linear least squares optimization for geometric vision. In *European Conference on Computer Vision*, volume 2, pages 43–56, 2010.

[Low99] D.G. Lowe. Object recognition from local scale-invariant features. In *International Conference on Computer Vision (ICCV)*, volume 2, pages 1150–1157, 1999.

[LRR08] V. Lempitsky, S. Roth, and C. Rother. Fusionflow: Discrete-continuous optimization for optical flow estimation. In *International Conference on Computer Vision and Pattern Recognition (CVPR)*, pages 1–8, 2008.

[LRRB10] V. Lempitsky, C. Rother, S. Roth, and A. Blake. Fusion moves for markov random field optimization. *Pattern Analysis and Machine Intelligence, IEEE Transactions on*, 32(8):1392–1405, 2010.

[LSC07] H. Lombaert, Y. Sun, and F. Cheriet. Landmark-based non-rigid registration via graph cuts. *Image Analysis and Recognition*, pages 166–175, 2007.

REFERENCES

[LSKK10] M. Lindner, I. Schiller, A. Kolb, and R. Koch. Time-of-flight sensor calibration for accurate range sensing. *Computer Vision and Image Understanding*, 114(12):1318–1328, 2010.

[MFM04] R. Marzotto, A. Fusiello, and V. Murino. High resolution video mosaicing with global alignment. In *International Conference on Computer Vision and Pattern Recognition (CVPR)*, volume 1, pages I–692, 2004.

[Mic13] Microsoft, 2013.

[MLDB+08] R. Miranda-Luna, C. Daul, W.C.P.M. Blondel, Y. Hernandez-Mier, D. Wolf, and F. Guillemin. Mosaicing of bladder endoscopic image sequences: Distortion calibration and registration algorithm. *IEEE Transactions on Biomedical Engineering*, 55(2):541–553, 2008.

[MLHMD+04] R. Miranda-Luna, Y. Hernandez-Mier, C. Daul, W. Blondel, and D. Wolf. Mosaicing of medical video-endoscopic images: data quality improvement and algorithm testing. In *International Conference on Electrical and Electronics Engineering*, pages 530–535, 2004.

[MOG+06] Y. Matsushita, E. Ofek, W. Ge, X. Tang, and H.Y. Shum. Full-frame video stabilization with motion inpainting. *Pattern Analysis and Machine Intelligence, IEEE Transactions on*, 28(7):1150–1163, 2006.

[MV98] J.B. Maintz and M.A. Viergever. A survey of medical image registration. *Medical image analysis*, 2(1):1–36, 1998.

[MWC+06] L. Merino, J. Wiklund, F. Caballero, A. Moe, J.R.M. De Dios, P.E. Forssen, K. Nordberg, and A. Ollero. Vision-based multi-uav position estimation. *Robotics & Automation Magazine, IEEE*, 13(3):53–62, 2006.

[MY09] J.M. Morel and G. Yu. Asift: A new framework for fully affine invariant image comparison. *SIAM Journal on Imaging Sciences*, 2(2):438–469, 2009.

[MYW05] T. Meltzer, C. Yanover, and Y. Weiss. Globally optimal solutions for energy minimization in stereo vision using reweighted belief propagation. In *Computer Vision, 2005. ICCV 2005. Tenth IEEE International Conference on*, volume 1, pages 428–435. IEEE, 2005.

[NDI+11] R.A. Newcombe, A.J. Davison, S. Izadi, P. Kohli, O. Hilliges, J. Shotton, D. Molyneaux, S. Hodges, D. Kim, and A. Fitzgibbon. Kinectfusion: Real-time dense surface mapping and tracking. In *Mixed and Augmented Reality (ISMAR), 2011 10th IEEE International Symposium on*, pages 127–136. IEEE, 2011.

[OS09] Joachim Ohser and Katja Schladitz. *3D images of materials structures: processing and analysis*. Wiley-VCH, 2009.

[Ots75] N. Otsu. A threshold selection method from gray-level histograms. *Automatica*, 11:285–296, 1975.

[PD84] T. Porter and T. Duff. Compositing digital images. *ACM Siggraph Computer Graphics*, 18(3):253–259, 1984.

[Pea88] J. Pearl. *Probabilistic reasoning in intelligent systems: networks of plausible inference*. Morgan Kaufmann, 1988.

[PHS+09] J. Penne, K. Höller, M. Stürmer, T. Schrauder, A. Schneider, R. Engelbrecht, H. Feußner, B. Schmauss, and J. Hornegger. Time-of-flight 3-D endoscopy. *Medical Image Computing and Computer-Assisted Intervention (MICCAI)*, pages 467–474, 2009.

[PKG99] M. Pollefeys, R. Koch, and L.V. Gool. Self-calibration and metric reconstruction inspite of varying and unknown intrinsic camera parameters. *International Journal of Computer Vision*, 32(1):7–25, 1999.

[PMD13] PMDTec, 2013.

[PMR+03] T.J. Pearson, BS Mason, ACS Readhead, MC Shepherd, JL Sievers, PS Udomprasert, JK Cartwright, AJ Farmer, S. Padin, ST Myers, et al. The anisotropy of the microwave background to l= 3500: mosaic observations with the cosmic background imager. *The Astrophysical Journal*, 591:556, 2003.

[PMV03] J.P.W. Pluim, J.B.A. Maintz, and M.A. Viergever. Mutual-information-based registration of medical images: a survey. *Medical Imaging, IEEE Transactions on*, 22(8):986–1004, 2003.

[Pri13] PrimeSense, 2013.

[QL99] Long Quan and Zhongdan Lan. Linear n-point camera pose determination. *Pattern Analysis and Machine Intelligence, IEEE Transactions on*, 21(8):774–780, 1999.

[RC11] Radu Bogdan Rusu and Steve Cousins. 3D is here: Point Cloud Library (PCL). In *IEEE International Conference on Robotics and Automation (ICRA)*, Shanghai, China, May 9-13 2011.

[RCMS99] Claudio Rocchini, Paolo Cignoni, Claudio Montani, and Roberto Scopigno. Multiple textures stitching and blending on 3d objects. In *Eurographics Rendering Workshop 1999*, pages 119–130. Springer-Verlag. Berlin-Heidelberg, 1999.

REFERENCES

[RKB04] C. Rother, V. Kolmogorov, and A. Blake. Grabcut: Interactive foreground extraction using iterated graph cuts. In *ACM Transactions on Graphics (TOG)*, volume 23, pages 309–314. ACM, 2004.

[RKKB05] C. Rother, S. Kumar, V. Kolmogorov, and A. Blake. Digital tapestry [automatic image synthesis]. In *Computer Vision and Pattern Recognition, 2005. CVPR 2005. IEEE Computer Society Conference on*, volume 1, pages 589–596. IEEE, 2005.

[RKLS07] C. Rother, V. Kolmogorov, V. Lempitsky, and M. Szummer. Optimizing binary MRFs via extended roof duality. In *IEEE International Conference on Computer Vision and Pattern Recognition (CVPR)*, pages 1–8, 2007.

[Rou84] P.J. Rousseeuw. Least median of squares regression. *Journal of the American statistical association*, pages 871–880, 1984.

[RRKB11] E. Rublee, V. Rabaud, K. Konolige, and G. Bradski. Orb: an efficient alternative to sift or surf. In *Computer Vision (ICCV), 2011 IEEE International Conference on*, pages 2564–2571. IEEE, 2011.

[SA11] M. Schmidt and K. Alahari. Generalized fast approximate energy minimization via graph cuts: Alpha-expansion beta-shrink moves. *arXiv preprint arXiv:1108.5710*, 2011.

[SC09] R. So and A. Chung. Multi-level non-rigid image registration using graphcuts. In *Acoustics, Speech and Signal Processing, 2009. ICASSP 2009. IEEE International Conference on*, pages 397–400. IEEE, 2009.

[SC10] R.W.K. So and A.C.S. Chung. Non-rigid image registration by using graphcuts with mutual information. In *Image Processing (ICIP), 2010 17th IEEE International Conference on*, pages 4429–4432. IEEE, 2010.

[Sch07] D. Schlesinger. Exact solution of permuted submodular minsum problems. In *Energy Minimization Methods in Computer Vision and Pattern Recognition*, pages 28–38. Springer, 2007.

[SF06] D. Schlesinger and B. Flach. *Transforming an arbitrary minsum problem into a binary one*. TU, Fak. Informatik, 2006.

[SFS+12] Nikita Shevchenko, Johannes A Fallert, Herbert Stepp, Hichem Sahli, Alexander Karl, and Tim C Lueth. A high resolution bladder wall map: Feasibility study. In *Engineering in Medicine and Biology Society (EMBC), 2012 Annual International Conference of the IEEE*, pages 5761–5764. IEEE, 2012.

[SHT09] A. Segal, D. Haehnel, and S. Thrun. Generalized-icp. In *Proc. of Robotics: Science and Systems (RSS)*, volume 25, pages 26–27, 2009.

[Soc08] American Cancer Society. *Cancer facts & figures*. The Society, 2008.

[Soi03] P. Soille. *Morphological image analysis: principles and applications*. Springer, 2003.

[SPS05] D. Steedly, C. Pal, and R. Szeliski. Efficiently registering video into panoramic mosaics. In *Computer Vision, 2005. ICCV 2005. Tenth IEEE International Conference on*, volume 2, pages 1300–1307. IEEE, 2005.

[SPS12] T.D. Soper, M.P. Porter, and E.J. Seibel. Surface mosaics of the bladder reconstructed from endoscopic video for automated surveillance. *Biomedical Engineering, IEEE Transactions on*, 59(6):1670–1680, 2012.

[SS97] R. Szeliski and H.Y. Shum. Creating full view panoramic image mosaics and environment maps. In *Proceedings of the 24th annual conference on Computer graphics and interactive techniques*, pages 251–258. ACM Press/Addison-Wesley Publishing Co., 1997.

[SSSB96] RJ Sault, L. Staveley-Smith, and WN Brouw. An approach to interferometric mosaicing. *Astronomy and Astrophysics Supplement Series*, 120:375–384, 1996.

[ST94] T. Saito and J.I. Toriwaki. New algorithms for euclidean distance transformation of an n-dimensional digitized picture with applications. *Pattern recognition*, 27(11):1551–1565, 1994.

[STR03] C.V. Stewart, C.L. Tsai, and B. Roysam. The dual-bootstrap iterative closest point algorithm with application to retinal image registration. *Medical Imaging, IEEE Transactions on*, 22(11):1379–1394, 2003.

[Sze06] R. Szeliski. Image alignment and stitching: A tutorial. *Foundations and Trends® in Computer Graphics and Vision*, 2(1):1–104, 2006.

[SZS⁺08] R. Szeliski, R. Zabih, D. Scharstein, O. Veksler, V. Kolmogorov, A. Agarwala, M. Tappen, and C. Rother. A comparative study of energy minimization methods for markov random fields with smoothness-based priors. *Pattern Analysis and Machine Intelligence, IEEE Transactions on*, 30(6):1068–1080, 2008.

[TC07] T.W.H. Tang and A. Chung. Non-rigid image registration using graph-cuts. In *Proceedings of the 10th international conference on Medical image computing and computer-assisted intervention-Volume Part I*, pages 916–924. Springer-Verlag, 2007.

REFERENCES

[TMHF00] B. Triggs, P. McLauchlan, R. Hartley, and A. Fitzgibbon. Bundle adjustmenta modern synthesis. *Vision algorithms: theory and practice*, pages 153–177, 2000.

[TP03] JE Tyczynski and DM Parkin. Bladder cancer in europe. *ENCR Cancer Fact Sheets*, 3:1–4, 2003.

[Vek08] O. Veksler. Star shape prior for graph-cut image segmentation. *Computer Vision–ECCV 2008*, pages 454–467, 2008.

[VN08] V. Vineet and PJ Narayanan. Cuda cuts: Fast graph cuts on the gpu. In *Computer Vision and Pattern Recognition Workshops, 2008. CVPRW'08. IEEE Computer Society Conference on*, pages 1–8. IEEE, 2008.

[VPPA05] T. Vercauteren, A. Perchant, X. Pennec, and N. Ayache. Mosaicing of confocal microscopic in vivo soft tissue video sequences. *Medical Image Computing and Computer-Assisted Intervention–MICCAI 2005*, pages 753–760, 2005.

[VWI97] P. Viola and W.M. Wells III. Alignment by maximization of mutual information. *International journal of computer vision*, 24(2):137–154, 1997.

[WAB03] J. Wills, S. Agarwal, and S. Belongie. What went where [motion segmentation]. In *Computer Vision and Pattern Recognition, 2003. Proceedings. 2003 IEEE Computer Society Conference on*, volume 1, pages I–37. IEEE, 2003.

[WDBH+na] T. Weibel, C. Daul, A. Ben Hamadou, D. Wolf, and R. Rösch. Endoscopic bladder image registration using sparse graph cuts. In *17th IEEE International Conference on Image Processing (ICIP)*, pages 157–160, September 2010. Hong Kong, China.

[WDW+12] T. Weibel, C. Daul, D. Wolf, R. Rösch, and F. Guillemin. Graph based construction of textured large field of view mosaics for bladder cancer diagnosis. *Pattern Recognition*, 45(12):4138 – 4150, 2012.

[WDW+an] T. Weibel, C. Daul, D. Wolf, R. Rösch, et al. Contrast-enhancing seam detection and blending using graph cuts. In *21st International Conference on Pattern Recognition (ICPR)*, pages 2732–2735, November 2012. Tsukuba, Japan.

[WDWRce] T. Weibel, C. Daul, D. Wolf, and R. Rösch. Customizing graph cuts for image registration problems. In *XXIIIe Colloque GRETSI Traitement du Signal & des Images (GRETSI)*, September 2011. Bordeaux, France.

[WDWRum] T. Weibel, C. Daul, D. Wolf, and R. Rösch. Planarity-enforcing higher-order graph cut. In *18th IEEE International Conference on Image Processing (ICIP)*, pages 41–44, September 2011. Brussels, Belgium.

[WJW02] M. Wainwright, T. Jaakkola, and A. Willsky. Map estimation via agreement on (hyper) trees: Message-passing and linear programming approaches. In *PROCEEDINGS OF THE ANNUAL ALLERTON CONFERENCE ON COMMUNICATION CONTROL AND COMPUTING*, volume 40, pages 1565–1575. The University; 1998, 2002.

[WPM+12] O. Woodford, M.T. Pham, A. Maki, R. Gherardi, F. Perbet, and B. Stenger. Contraction moves for geometric model fitting. *Computer Vision–ECCV 2012*, pages 181–194, 2012.

[WRS+05] D. Wald, M. Reeff, G. Székely, P. Cattin, and D. Paulus. Fließende überblendung von endoskopiebildern für die erstellung eines mosaiks. *Bildverarbeitung für die Medizin 2005*, pages 287–291, 2005.

[WSV91] Michael W Walker, Lejun Shao, and Richard A Volz. Estimating 3-d location parameters using dual number quaternions. *CVGIP: image understanding*, 54(3):358–367, 1991.

[WTRF08] O.J. Woodford, P.H.S. Torr, I.D. Reid, and A.W. Fitzgibbon. Global stereo reconstruction under second order smoothness priors. In *Computer Vision and Pattern Recognition, 2008. CVPR 2008. IEEE Conference on*, pages 1–8. IEEE, 2008.

[YS04] G. Yang and C.V. Stewart. Covariance-driven mosaic formation from sparsely-overlapping image sets with application to retinal image mosaicing. In *Computer Vision and Pattern Recognition, 2004. CVPR 2004. Proceedings of the 2004 IEEE Computer Society Conference on*, volume 1, pages I–804. IEEE, 2004.

[ZF03] B. Zitová and J. Flusser. Image registration methods: a survey. *Image and Vision Computing*, 21(11):977–1000, 2003.

[Zha94] Z. Zhang. Iterative point matching for registration of free-form curves and surfaces. *International journal of computer vision*, 13(2):119–152, 1994.

[Zha00] Z. Zhang. A flexible new technique for camera calibration. *Pattern Analysis and Machine Intelligence, IEEE Transactions on*, 22(11):1330–1334, 2000.

[ZHR04] Z. Zhu, A.R. Hanson, and E.M. Riseman. Generalized parallel-perspective stereo mosaics from airborne video. *Pattern Analysis and Machine Intelligence, IEEE Transactions on*, 26(2):226–237, 2004.

[ZP00] A. Zomet and S. Peleg. Efficient super-resolution and applications to mosaics. In *Pattern Recognition, 2000. Proceedings. 15th International Conference on*, volume 1, pages 579–583. IEEE, 2000.

REFERENCES

[Zwi95] U. Zwick. The smallest networks on which the ford-fulkerson maximum flow procedure may fail to terminate. *Theoretical computer science*, 148(1):165–170, 1995.

Résumé

L'objectif de cette thèse est de faciliter le diagnostic du cancer de la vessie. Durant une cystoscopie, un endoscope est introduit dans la vessie pour explorer la paroi interne de l'organe qui est visualisée sur un écran. Cependant, le faible champ de vue de l'instrument complique le diagnostic et le suivi des lésions. Cette thèse présente des algorithmes pour la création de cartes bi- et tridimensionnelles à large champ de vue à partir de vidéo-séquences cystoscopiques. En utilisant les avancées récentes dans le domaine de la minimisation d'énergies discrètes, nous proposons des fonctions coût indépendantes des transformations géométriques requises pour recaler de façon robuste et précise des paires d'images avec un faible recouvrement spatial. Ces transformations sont requises pour construire des cartes lorsque des trajectoires d'images se croisent ou se superposent. Nos algorithmes détectent automatiquement de telles trajectoires et réalisent une correction globale de la position des images dans la carte. Finalement, un algorithme de minimisation d'énergie compense les faibles discontinuités de textures restantes et atténue les fortes variations d'illuminations de la scène. Ainsi, les cartes texturées sont uniquement construites avec les meilleures informations (couleurs et textures) pouvant être extraites des données redondantes des vidéo-séquences. Les algorithmes sont évalués quantitativement et qualitativement avec des fantômes réalistes et des données cliniques. Ces tests mettent en lumière la robustesse et la précision de nos algorithmes. La cohérence visuelle des cartes obtenues dépasse celles des méthodes de cartographie de la vessie de la littérature.

Mots-clés : Cartographie 2D et 3D, diagnostic du cancer de la vessie, recalage d'images, mosaïquage d'images, minimisation d'énergies discrètes, coupes de graphes.

Abstract

The aim of this thesis is to facilitate bladder cancer diagnosis. The reference clinical examination is cystoscopy, where an endoscope, inserted into the bladder, allows to visually explore the organ's internal walls on a monitor. The main restriction is the small field of view (FOV) of the instrument, which complicates lesion diagnosis, follow-up and treatment traceability. In this thesis, we propose robust and accurate algorithms to create two- and three-dimensional large FOV maps from cystoscopic video-sequences. Based on recent advances in the field of discrete energy minimization, we propose transformation-invariant cost functions, which allow to robustly register image pairs, related by large viewpoint changes, with sub-pixel accuracy. The transformations linking such image pairs, which current state-of-the-art bladder image registration techniques are unable to robustly estimate, are required to construct maps with several overlapping image trajectories. We detect such overlapping trajectories automatically and perform non-linear global map correction. Finally, the proposed energy minimization based map compositing algorithm compensates small texture misalignments and attenuates strong exposure differences. The obtained textured maps are composed by a maximum of information/quality available from the redundant data of the video-sequence. We evaluate the proposed methods both quantitatively and qualitatively on realistic phantom and clinical data sets. The results demonstrate the robustness of the algorithms, and the obtained maps outperform state-of-the-art approaches in registration accuracy and global map coherence.

Keywords: 2D/3D Cartography, Bladder Cancer Diagnosis, Image Registration, Image Compositing, Discrete Energy Minimization, Graph-Cuts.